CRANFIELD UNIVERSITY

SCHOOL OF ENGINEERING

Department of Power, Propulsion and Aerospace Engineering

Ph.D Thesis

Academic Year 2007–2008

Unsteadiness In An Embedded Axial Compressor Stage

Edward NAYLOR

SUPERVISOR: PROF. P. C. IVEY
&
DR. J. A. AMARAL TEIXEIRA

February 2008

Abstract

Previous research on blade boundary layers in turbomachinery have been recognised to crucially influence the stability and performance of the gas turbine components. The interactions between rotating and stationary blade rows inevitably make the flow environment within a multistage axial compressor unsteady. Research conducted at midspan in Low Pressure turbines has shown that patches of transitional flow can withstand higher levels of deceleration, helping the boundary layer stay attached.

An experimental investigation into unsteadiness in a embedded stage was conducted in the third-stage of the Cranfield four-stage Low Speed Research Compressor at two operating points: peak efficiency and near stall. This build of the Cranfield Rig was equipped with three-dimensional blading. A three-hole pressure probe was traversed at the exit of Rotor 3 in the rotating frame of reference and at the exit of Stator 3 in the stationary frame of reference. In addition measurements were made at the exit of both Rotor and Stator 3 using a slanted hotwire rotated about its axis. This measurement technique gave time-resolved three-dimensional velocities. Coupled to the exit traverses a series of boundary layer traverses were performed along Stator 3 suction surface covering the mid-chord region at midspan and close to the casing endwall. To aid in the understanding and interpretation of the experimental campaign, three-dimensional computations of Stator 3 were made at the two operating points using the commercial Computational Fluid Dynamics code ANSYS-CFX . A two-dimensional unsteady calculation of Rotor 3, Stator 3 and Rotator 4 at midspan and peak efficiency was also performed.

The time-resolved measurements downstream of Rotor 3 showed that the rotor wake was characterised by high levels of random unsteadiness and increased incidence onto the stator row. The increase in incidence across the wake was two to three times that experienced with change in flow coefficient. Therefore the increased incidence and turbulence in a rotor wake will have a significant influence on the unsteady development of a downstream boundary layer.

Measurements of the boundary layer at design condition at midspan show evidence of laminar and transitional flow up to 50% of the suction surface length. The boundary layer flow periodically undergoes transition due to the convection of the wake-induced strip that was generated close to the leading edge. Towards the casing the picture is altered slightly due to the stator-casing separation region. Boundary layer transition is completed farther forward and the transition length reduced. At off-design the picture is completely altered. Transition is completed upstream of 25% suction surface length and the flow shows only a modulating variation with blade passing. The stator-casing separation region grows in spanwise extent and the boundary layer flow on the stator surface is completely separated aft of 50% of suction surface length.

Acknowledgement

I would like to thank my supervisor, Prof. Paul Ivey for his advice, guidance and the opportunities presented to me throughout my time at Cranfield. I would also like to give a special thank you to my second supervisor, Dr. Joao Amaral Teixeira, for going above and beyond the call of duty and without whom, this thesis would probably not exist. If at times I drove you mad, I apologise, although I secretly think you enjoyed it.

The project could not have been completed without the help of many, including Bernard Charnley, the technical staff in the test area at Cranfield and everyone in the turbomachinery department who gave some of their time and knowledge. Thanks to Dr Steven Hearing for access to the cobra probe data used in Chapter 4, for which I am very grateful.

Finally I would like to acknowledge the invaluable insight into turbomachinery gained from listening to Chris Freeman.

Nomenclature

Symbols

A	area
C_D	discharge coefficient
C_{P_0}	total pressure coefficient
C_{P_s}	static pressure coefficient
Cp	specific heat at constant pressure
C_u	wall correction factor
E	hot wire voltage
H_{12}	shape factor
H	total enthalpy
L	length
M	number of ensemble, Mach number
P	pressure
Re	Reynolds number
Re_{crit}	critical Reynolds number
Re_θ	momentum thickness Reynolds
S	source terms in the Navier-Stokes equations
S_0	suction surface length
T	temperature
TQ	torque
Tu	turbulence intensity
U	blade speed
V	velocity
W	relative velocity
W, X, Y, Z	boundary layer trajectories drawn at $0.7V_\infty$
a	leading edge celerity
b	trailing edge celerity
c	chord
i	incidence, internal energy
i, j, k	grid indices
k	turbulent kinetic energy, cosine law correction factor, thermal conductivity
$\dot{m}$	massflow
r	radius
s	surface distance, solidity
s_1, s_2, s_3	cobra probe calibration coefficients
q	dynamic head
t	time
u	velocity vector
u, v, w	velocity components
y^+	non-dimensional wall distance
x, y, z	spatial co-ordinates

Greek

α	yaw angle; turbulent spot spreading half angle
β	pitch angle
Γ	diffusion coefficient
γ	intermittency, ratio of specific heats
δ	boundary layer thickness
δ^*	displacement thickness
ε	dissipation rate of kinetic energy
η	torque efficiency
θ	momentum thickness
λ	Pohlhausen pressure gradient parameter
λ_θ	Thwaites pressure gradient parameter
μ	dynamic viscosity
μ_{eff}	effective viscosity
μ_T	turbulent viscosity
ν	kinematic viscosity
ρ	density
σ	spot propagation parameter
τ_0	blade passing period
τ_w	wall shear stress
Φ	dissipation function
ϕ	flow coefficient V_a/U_{mid}
φ	wire angle
χ	blade angle
ψ	pressure coefficient
Ω	wire rotation angle
ω	rotational speed, turbulent frequency

Subscript

∞	free-stream
0	total quantity
a	axial
acq	acquired
$corr$	correction
e	end of transition, edge of boundary layer, effective cooling
i,j,k	wire co-ordinate system
$isen$	isentropic
mid	mid-span
p	perturbation (time-average subtracted)
r	radial
ref	reference
rel	relative
s	start of transition
t	tangential
w	wire

Superscript

$\bar{}$	time mean
$\hat{}$	mass average
$'$	instantaneous value
$\tilde{}$	ensemble

Abbreviations

CFD	computational fluid dynamics
DF	diffusion factor
HP	high pressure
I.D.	internal diameter
IGV	inlet guide vanes
LE	leading edge
LP	low pressure
O.D.	outside diameter
PS	pressure surface
SFC	specific fuel consumption
SS	suction surface
TE	trailing edge
T-S	Tollmien-Schlicting

All other nomenclature used in this thesis is defined where it is introduced.

Contents

Chapter 1

Introduction

The prospect of global climate change is forcing the suppliers of energy consuming machinery to consider how to increase the energy efficiency of their products. Air transport has had for some time the biggest growth of energy consumption of any sector and needs to consider how to improve its energy efficiency. Over the period of 1999 to 2005 airlines have seen a 66% increase in their direct operating cost associated with fuel in the medium and long range market segments (MacBurnie, 2005). Although there has been a small decrease in the price of oil, it still remains around the $60/barrel mark - more than double the price in 2000.

The work done on the aircraft by current generation aero engines amounts to approximately 1/3 of the heat released from the fuel, whilst 1/3 goes to entropy production in the components, and a further 1/3 is lost as waste energy in the thermodynamic cycle. Within these portions the entropy rise in the components is critical in that it significantly influences the cycle and hence the waste energy. Significant improvements in the energy efficiency of aero engines may thus be gained by reducing entropy production.

To this end knowledge of both steady and unsteady flow in turbomachinery is essential for assessment, analysis and design. With increasing emphasis being placed on the requirements of the airline operators for lower specific fuel consumption (SFC), reduced weight and increasing life cycles leading to reduced cost of ownership.

An important trend over the last 30 years has been a marked increase in the overall pressure rise. Significant increases have been achieved compared to only a small increase in engine efficiency (Cumpsty, 1989). Greater understanding of complex aerodynamic flows have been achieved in this period through mathematical modelling and parallel advances in experimental techniques (Penner, 1999). Figure 1.1 provides clear evidence of the trend in pressure ratio with time. The increasing pressure ratio has contributed significantly to a similar reduction of SFC (Fig. 1.2). As higher cycle pressure ratios are achieved, importance is placed on reducing losses, especially as increasing the efficiency of a component

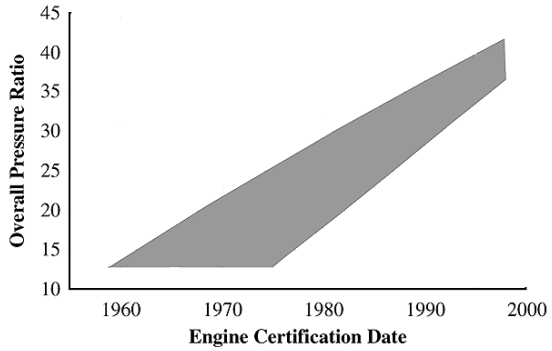

Figure 1.1: Overall pressure ratio with time. (Penner, 1999)

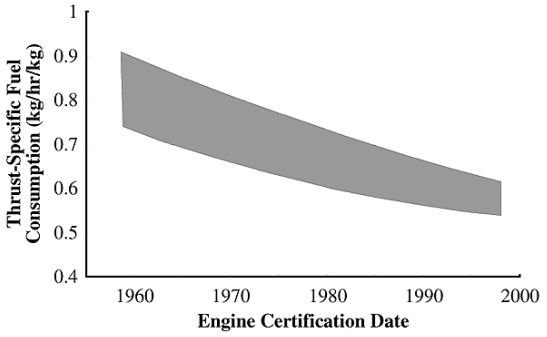

Figure 1.2: Fuel consumption progress with time. (Penner, 1999)

by one percent will improve the engines fuel consumption by an equivalent amount.

A consequence of the high engine pressure ratio is the requirement for higher flame temperature, increasing oxides of nitrogen, NO_x, formation rate and ultimately increased turbine entry temperatures. At altitudes typically flown by large aircraft, emissions of NO_x are particularly effective in forming ozone (O_3). At these altitude NO_x emissions result in greater concentrations of O_3 than surface NO_x emissions. It is for this reason that the Advisory Committee for Aeronautics (ACARE) has called for an 80% reduction by 2020.

This presents compressor design engineers with the dual requirements for high pressure ratios and high compression efficiency, while maintaining adequate surge margin for safe, part speed operation. As the cycle peak pressure and temperature are increased, the optimum bypass ratio increases, so the core engine size for a given thrust reduces and deleterious viscous and blade-row interactions effects make the achievement of high efficiency more difficult (Robinson, 1991), particularly in the latter stages of a high pressure core compressor, where the aspect ratios of unity or less are common.

Modern compressor designs have reached polytropic efficiency levels of greater 90%, with the last 10% being associated with blade interactions and near endwall flow phenomena. One area where the unsteady effects of blade interactions have been shown to be important is the effect that upstream wakes have on boundary-layer transition. Wake-induced transition can have both beneficial and detrimental effects on performance. Studies within low-pressure (LP) turbine blade rows have shown that, the turbulent wake shed from upstream blade rows induce bypass transition upstream of the natural transition point. This increases the turbulent wetted area and therefore the losses (Hodson et al., 1994). The calmed regions which follow the turbulent spots tend to reduce losses compared to the undisturbed boundary layer and help suppress separation. Loss reductions are intimately linked to the relative portions of the blade covered by laminar, turbulent, calmed and separated flow. In the LP turbine case with wake passing the separation is periodically suppressed by the turbulent and calmed flow. Looking at the time average, the losses generated

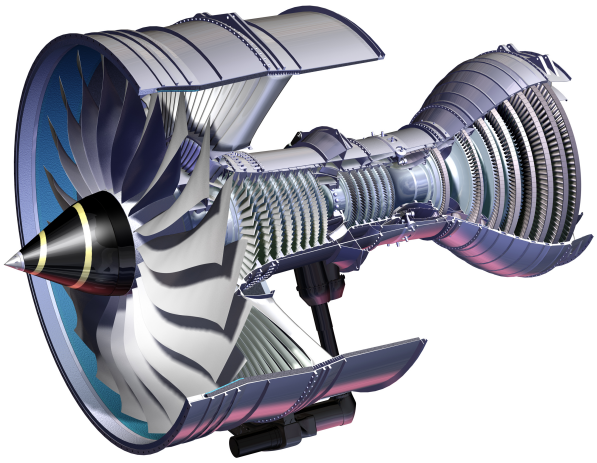

Figure 1.3: A high bypass ratio turbofan

during the turbulent and calmed periods contribute less than the steady separation which leads to loss reduction. High-lift and ultra-high-lift LP turbines designs are now possible (Howell et al., 2000, 2001; Haselbach et al., 2001). The new turbine profiles achieve a blade reduction of approximately 20% whilst still maintaining the same level of loss.

Advances in CFD have produced efficiency gains of at least 2% in the last decade due to improved blade profile and three-dimensional designs (Gallimore, 1998). Further reduction in loss can be found in greater understanding of the unsteady nature, transition and secondary flows. However more significant improvements are available through increased understanding at off-design (i.e. stall inception). This will lead to increased stage-loading to reduce part counts and hence cost without a reduction in efficiency.

1.1 The gas turbine

The core of the basic gas turbine consists of three main parts: The compressor, which mechanically increases the energy of the air (raising the pressure and temperature); the combustor, in which fuel is burned (further raising the temperature of the pressurised air); and the turbine, which mechanically extracts enough energy from the hot compressed gas to drive the compressor (thereby reducing the pressure and temperature of the gas).

A schematic of the typical high bypass turbofan is illustrated in Fig. 1.3. The large diameter fan is clearly evident in the figure. This would typically produce approximately 75% of the engine thrust. The axial compressor stage consists of one row of rotating blades, rotors and a row of stationary blades, stators. The pressure rise results from the energy imparted to the air by the rotor. The air is then passed through the downstream stator, where the swirl is removed and a rise in static pressure is achieved. For a typical

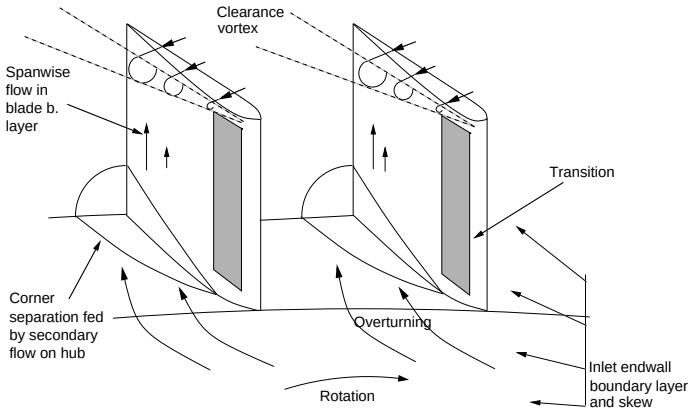

Figure 1.4: Schematic diagram of flows in rotor passage. (Gallimore, 1998)

core compressors, the total pressure ratio across a stage is in the range of 1.3-1.4. The reason for the small pressure increase through the stage is that the rate of deceleration of the airflow through each of the blades must be limited to avoid flow separation and stall. Typically around 12-15 stages are used to achieve an overall pressure ratio of 50:1, and compressor exit temperatures of around 700°C. The resulting high blade count contributes to the engine weight and ultimately to the fuel consumption. One of the primary goals of compressor design is to increase the pressure ratio and the efficiency while reducing the number of blades and stages. This can be achieved by the use of fewer but more highly loaded compressor blades. This requires a detailed physical understanding of the unsteady flow field and the resulting effects on the performance and flow stability.

1.2 Description of the Compressor Flow Field

The flow in a multi-stage compressor is highly unsteady and turbulent. The rotor and stator blades aerodynamically interact due to vortical disturbances produced by the relative motion of wakes from blade rows further upstream and the potential effects of the blades. In addition, the wakes and potential effects of the blades superimpose with other flow patterns, such as secondary flow phenomena and tip clearance vortices. A schematic of the flow inside a compressor blade row is shown in Fig. 1.4 with the unsteady effects ignored.

1.2.1 Endwall Flow

The flow in the endwall regions of a compressor are the most important and least well understood parts of the compressor. This is the most difficult loss component to understand and to predict and virtually all prediction methods are still based on correlations of empirical data, often with very little underlying physics.

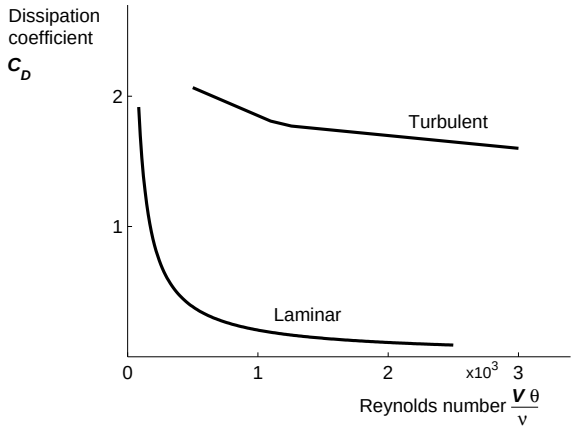

Figure 1.5: Dissipation coefficients for turbulent and laminar flow useful for estimating loss production. (Cumpsty, 1989)

The most important effect is in the corner region formed by the annulus and suction surface, where endwall flow cannot sustain the amount of diffusion required and separates. This separation region is fed by endwall fluid that is overturned by the cross-passage pressure gradient that exists between the pressure surface and suction surface. This separation is responsible for much of the blockage observed in compressor blade rows. Its effects may not be localised and it can interact with the suction surface boundary layers to cause separation over much of the blade span (Denton, 1993).

1.2.2 Blade Boundary Layer

Boundary layers on the blade surface are three-dimensional, as the momentum of fluid in the boundary layer is lower than the free-stream flow, causing the fluid to be centrifuged radially outwards on rotors. In stator blade rows the radial pressure gradient imposed by radial equilibrium tend to force the boundary layer radially inward.

The process of transition is complex and has been the subject of extensive study (Chapter 2). The boundary layer is usually assumed to be fully turbulent from the leading edge when performing CFD calculations. The methodology behind this is due to the high free-stream turbulence intensities present in multi-stage compressors. In addition a leading edge spike is often present in the static pressure distribution close to the leading edge because the stagnation point is not exactly located on the nose of the aerofoil. The leading edge spike is assumed to promote transition due to is large acceleration and deceleration of the boundary layer which usually occurs in 1% of chord. The work of Halstead et al. (1997a) revealed that the transition process is unsteady and heavily influenced by the incoming

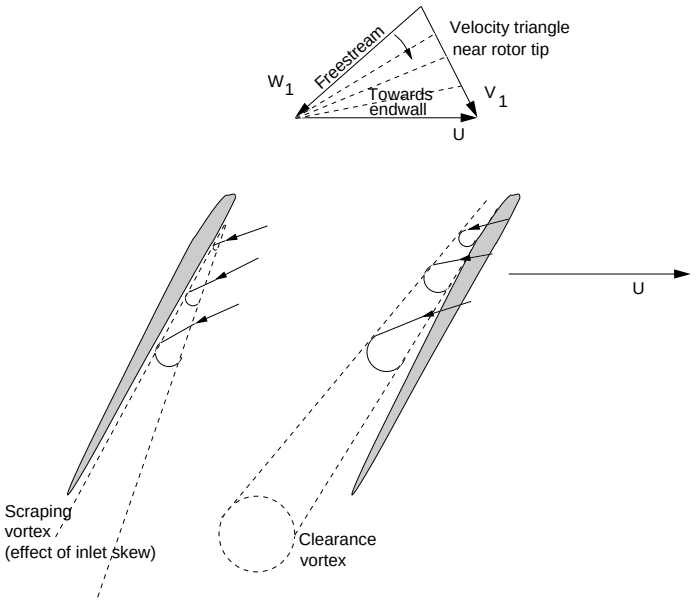

Figure 1.6: Schematic diagram of viscous effects in tip clearance viewed looking down on rotor tips. (Cumpsty, 1989)

wakes from the upstream blade row.

The aerodynamic performance of turbomachinery blading is strongly dependent on the nature of boundary layer development on the blades. The blade boundary layer is responsible for the aerofoil aerodynamic efficiency and thus for the overall performance of the machine. Most blade designers take advantage of the laminar boundary, as the loss produced by a turbulent boundary layer is an order of magnitude greater than that produced by a laminar one (Fig. 1.5), and set the maximum suction surface velocity to around 15-30% of blade chord. This allows for high blade loading in combination to low losses. The large difference in dissipation coefficient highlights the importance of predicting boundary layer transition on turbomachinery blades.

No matter where transition occurs it is clear that since the rate of entropy production is proportional to V_∞^3, the majority of loss generation takes place on those parts of the blade surface where the surface velocity is close to its maximum. Consequently the loss generated on the suction surface is several times greater ($\approx$ 5x) than on the pressure surface.

1.2.3 Tip Clearance Flow

The flow at the free end is dominated by the flow across the tip clearance which is driven by the pressure differential that exists across the blade and the viscous drag of the endwall passing over the blade tip. The tip clearance flow interacts with the flow already in the endwall to produce a complex flow pattern that is typified by a vortex as the tip flow rolls up and passes downstream (Fig. 1.6). Another effect of the tip clearance is the scrapping

vortex. The boundary layer fluid near the tip on the pressure side is 'scrapped up' and piles up forming a vortex.

Tip clearance has an important effect on both the endwall and blade-to-blade flows in its vicinity. Generally increasing clearance leads to reduced efficiency, loss in capacity and deterioration in the stall line. However there is evidence to suggest that an optimum value exists, below which the loss starts to increase.

1.2.4 Summary

The above effects increase as the aspect ratio tends to unity and dominate the behaviour of multi-stage compressor blades. They determine the stall behaviour and are responsible for at least 1/2 the losses. The result of the flow phenomena described above is that the flow field in a compressor blade row is extremely complicated and can be characterised as being unsteady, three-dimensional and dominated by viscous effects. The loss generated by the three components above (endwall, profile and tip leakage) are comparable in magnitude and each accounts for about 1/3 of the total loss in a blade row (Denton, 1993).

1.3 Exploitation of Three-Dimensional Flows in Design

1.3.1 Sweep

Sweep is defined as a change in the position of an endwall section along the chord-line. Sweep induces the axial component of velocity to accelerate on the suction surface and decrease on the pressure surface. The flow near the suction surface is induced towards the endwall, while the opposite occurs near the pressure surface. Due to the opposing motion of the flow either side of the passage the stream surface is no longer-axisymmetric but becomes twisted. At the hub the sweep induced passage vortex opposes the classical cross passage flow and supports it at the casing. Positive sweep is defined as movement of the endwall section upstream and can be used to reduce leading edge loading, resulting in an aft loaded section.

1.3.2 Lean

Lean is defined as a change in the position of the section normal to the chord-line. Positive lean is taken when the section are stacked to produce a concave suction surface. Lean loads the endwall section close to the leading edge but has the effect of reducing the loading over the majority of the chord. Therefore the application of lean can be applied to reduce the possibility of corner separation. Although loading is lowered at the endwall section,

the loading of sections towards midspan is increased. Lean also results in increased flow migration along the span due to the higher pressure on the endwall.

1.3.3 End-bend

Close to the endwall the local incidence onto the blade sections is increased by the reduced meridional velocity of the endwall boundary layers and by overturning due to secondary flow from the upstream blade row. End-bends are used to increase the blade stagger close to the endwall which reduces the incidence through better matching of the blade inlet angle to the local flow direction and reduces the overturning due to secondary flows.

1.4 Thesis Objectives

Previous research on boundary layer flows have essentially used either large scale flat plates, cascades or single-stage compressor rigs. The similarity between these research vehicles is fundamentally the two dimensionality of the flow and blading used. In a modern core compressor the aspect ratio of the blades is close to unity and as such, endwall effects occupy a significant fraction of the span. The blades are often highly three-dimensional, incorporating a mixture of lean, sweep and end-bends in order to improve the efficiency of the blading. The result is that the flow cannot be described as two-dimensional and therefore assumptions made at midspan, employing a two-dimensional model, should be used with care.

The novelty of this research lies primarily in the description of the unsteady development of boundary layers that occur in a modern three-dimensional, highly loaded, low aspect ratio blading which is typical of an embedded stage of a multistage core compressor. The boundary layers that develop on a three-dimensional turbomachinery blade at different radii are strongly coupled it is essential to study the entire surface of the blade in order to appreciate the action of the viscous effects close to the surface. Multistage influences were investigated through an experimental programme focussing on the third-stage of the Cranfield four-stage Low Speed Research Compressor. The ability of three-dimensional steady state and two-dimensional unsteady CFD to predict the flow environment in this class of machines was also investigated. Answers to following questions are sought:

- What is the physical scene of the unsteady boundary layer development along the span of a cantilevered stator in a multistage environment?
- If transition is present, where does it occur and what is the extent of the transition zone?

- How does the picture change towards off-design conditions?
- How well do existing CFD codes predict this development?

1.5 Thesis Overview

The work presented in this thesis seeks primarily to understand the unsteadiness in an embedded stages of three-dimensional blading and its impact on boundary layer development. In particulary how this alters along the span of the blade at design and off design conditions.

Chapter 2 presents a review of the literature on boundary layer transition. The chapter is divided into three main sections that deal with the steady and unsteady physics of boundary layer transition, sources of unsteadiness and the three-dimensional flow field in compressors. The main thrust of the literature review was towards transition in adverse pressure gradients.

Chapter 3 introduces the different experimental and numerical techniques used in this thesis. Detail is given on the main test vehicle of this research, the Cranfield four-stage Low Speed Research Compressor, along with a description of the three-dimensional blading. The different aspects of Computational Fluid Dynamics are introduced and described.

In Chapters 4 and 5 the three-dimensional flow field that exists in the third-stage of the Rig is described. Chapter 4 presents the time-average results, whilst Chapter 5 describes the time-resolved measurements. The numerical calculations are used to aid and interpret the experimental data.

The unsteady boundary layer development on Stator 3 suction surface is described in Chapter 6. Here boundary layer traverses, flow visualisation, surface pressure tappings and steady/unsteady numerical calculations are presented and analysed. The change in boundary layer state with operating point and spanwise height is described.

Each chapter is finished with its own discussion. Chapter 7 initially highlights the main conclusions of Chapters 4, 5 and 6 and then discusses there implications in light of the results. The final section of Chapter 7 suggests recommendations for future work.

Chapter 2

Literature Review

2.1 Introduction

The aim of this chapter is to provide an overview of the published work that is relevant to this thesis. This will involve a discussion of the sources of unsteadiness in a compressor and the areas where the unsteady flows are likely to play an important part.

2.2 Boundary Layer Development

The development of unsteady boundary layers on turbomachinery blading is influenced significantly by laminar to turbulent transition. A critical examination of the transition process in turbomachinery is presented by Mayle (1991) and in compressors by Walker (1993). Parameters influencing the boundary layer development are the properties of: incoming wakes, free-stream turbulence, blade loading, Reynolds number and profile pressure distribution.

2.2.1 Transition in Steady Flow

The transition from laminar to turbulent was first visualised by Reynolds in 1883 through the use of die injected into the flow in his now famous experiments. The generally accepted model of transition which resulted from these observations, was that of an instantaneous change between laminar and turbulent states. The three fundamental processes by which transition occurs in steady flow are also relevant for the unsteady flow in turbomachinery. These are natural, bypass and separated-flow transition.

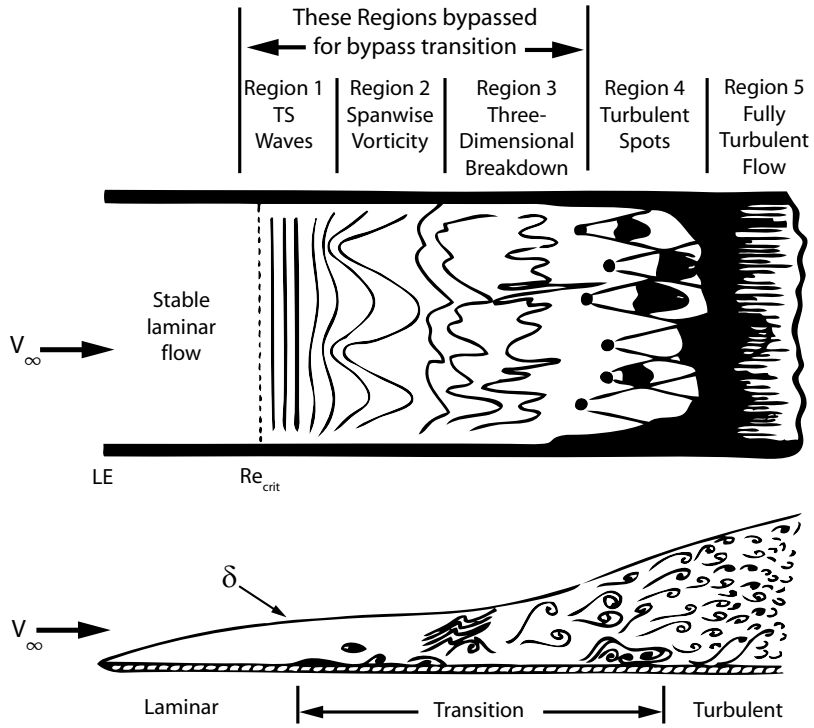

Figure 2.1: Natural boundary layer transition after White (2006)

2.2.1.1 Natural Transition

The early research on transition was based on inviscid-stability theory which obscured the problem of transition. Lord Rayleigh's inviscid theory[1], suggested that all boundary layer flows were only unstable if there was a point of inflexion present in the velocity profile. It was later predicted physically by Prandtl and then proven mathematically by Tollmein, that a laminar boundary layer can be destabilised by the presence of viscous instability waves, known as Tollmien-Schlichting or T-S waves. The existence of T-S waves were initially doubted because the experiments on transition were contaminated by the very turbulence and acoustics of the wind tunnels of the day. The experiments of (Schubauer and Skramstead, 1948) conducted in a newly constructed wind tunnel with extremely low free-stream turbulence level of 0.02% (previously values of 1.2% were common) documented their existence.

White (2006) describes the process of steady flow natural transition on a flat plate, Fig. 2.1. A laminar boundary layer develops linear oscillations of well defined frequency (T-S waves) when the Reynolds number exceeds a critical value. The instability is through a process whereby viscosity destabilises the waves. As the amplitude of the T-S waves increases, three-dimensional instability, which produces periodic spanwise flow distortions,

[1]Theorem 1 (Rayleigh, 1880). It is necessay for instability that the velocity profile have a point of inflection, the so called *point of inflexion criterion*

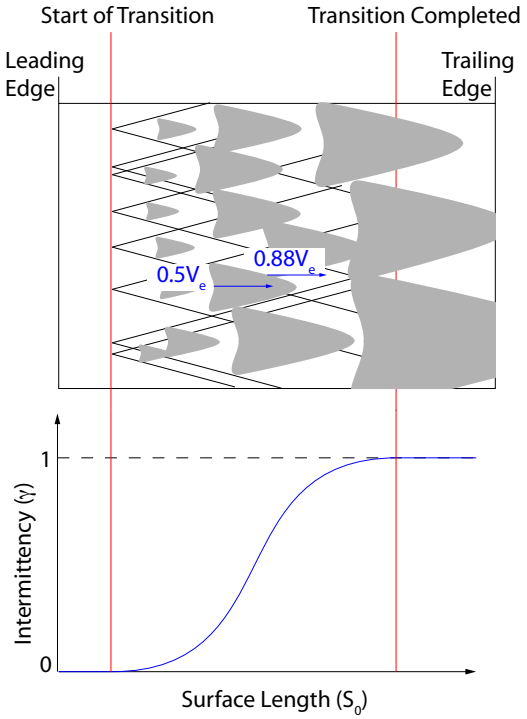

Figure 2.2: Schematic of bypass transition after Dhawan and Narasimha (1958).

start to appear. This introduces streamwise vorticity and causes a rapid non-linear amplification of the spanwise waves into vortex loops, known as hairpin eddies (Klebanoff et al., 1962). At this point, formation of turbulent spots (Emmons, 1951) occur at locally intense fluctuations. Within this region the boundary layer state alternates between a laminar and turbulent state. Turbulent spots eventually coalesce into a fully turbulent boundary layer.

It is generally accepted that natural transition occurs in relatively low disturbance environments ($Tu_\infty < 0.5\%$ Mayle (1991); Hodson and Howell (2005)). In compressors therefore, other modes of transition are believed to dominate. However, Hughes and Walker (2001) have observed natural transition processes in low-speed compressors.

2.2.1.2 Bypass Transition

For transition at high free-stream turbulence levels ($Tu_\infty > 1\%$), the formation and amplification process of two-dimensional T-S waves in natural transition is bypassed such that turbulent spots are directly formed in the boundary layer due to forced disturbances from the free-stream. The high level of turbulence in turbomachinery mean that bypass transition is thought to be the most likely mechanism.

A schematic of bypass transition in steady flow is shown in Fig. 2.2. At some distance from the leading edge turbulent spots form directly. At any instance in time, a point in the transition zone can be instantaneously laminar or turbulent. In Fig. 2.2 the term inter-

mittency, γ, is introduced. Intermittency is the probability that the flow will be turbulent. The probability i.e. intermittency increases towards the rear of the transition zone. Intermittency is zero for laminar flow and is unity for turbulent flow. The intermittency curve, Fig. 2.2 is typically 'S'-shaped in steady flow.

Currently, there does not appear to be any adequate theory for predicting where or when breakdown will occur but correlations are available. The empirical models correlate the momentum thickness Reynolds number at transition inception, $\mathrm{Re}_{\theta ts}$. Among the numerous correlations, those of Mayle (1991), Eqn. 2.1, and Abu-Ghannam and Shaw (1980), Eqn. 2.2, are the ones most frequently cited.

$$\mathrm{Re}_{\theta ts} = 400 Tu^{-0.625} \tag{2.1}$$

$$\mathrm{Re}_{\theta ts} = 163 + \exp\left[F(\lambda_\theta) - \frac{F(\lambda_\theta)}{6.91}\overline{Tu}\right] \tag{2.2}$$

where $\overline{Tu}$ is the average free-stream turbulence level between the leading edge and transition inception location, and $F(\lambda_\theta)$ in Eqn. 2.2 is a function of Thwaites' pressure gradient parameter ($\lambda_\theta = (\theta^2/\nu)\, dV_\infty/dx$), defined as

$$F(\lambda_\theta) = 6.91 + 12.75\lambda_\theta + 64.64\lambda_\theta^2 \qquad \lambda_\theta \leqslant 0 \tag{2.3}$$

$$F(\lambda_\theta) = 6.91 + 12.48\lambda_\theta - 12.27\lambda_\theta^2 \qquad \lambda_\theta \geqslant 0 \tag{2.4}$$

Although the model of Abu-Ghannam and Shaw (1980) has the advantage of accounting for the effects of both free-stream turbulence and streamwise pressure distribution, the correlation imposes transition inception for $\mathrm{Re}_\theta > 163$, which corresponds to the stability limit for zero pressure gradient flows. For free-stream turbulence intensities typical of turbomachinery blade rows, it is known that transition inception in an attached boundary layer is not strongly affected by streamwise pressure distribution (Mayle, 1991).

Mayle and Schulz (1997); Johnson and Ercan (1996) present alternative methods for predicting bypass transition which calculate the effect of free-stream turbulence on the pre-transitional laminar boundary layer. Johnson and Ercan (1996) found that low frequency disturbances were most likely to cause bypass transition, while Mayle and Schulz (1997) suggested that the high frequency pressure fluctuations in the free-stream initiate fluctuations in the laminar boundary layer. These pressure waves propagate into the boundary layer and, similar to the T-S waves, cause the growth of velocity fluctuations until eventually they are large enough that turbulent spots form. All of these correlations are based on steady flow transition. Therefore there applicability to unsteady transition is questionable. Computations based solely on bypass transition criteria cannot capture separation bubble phenomena at all.

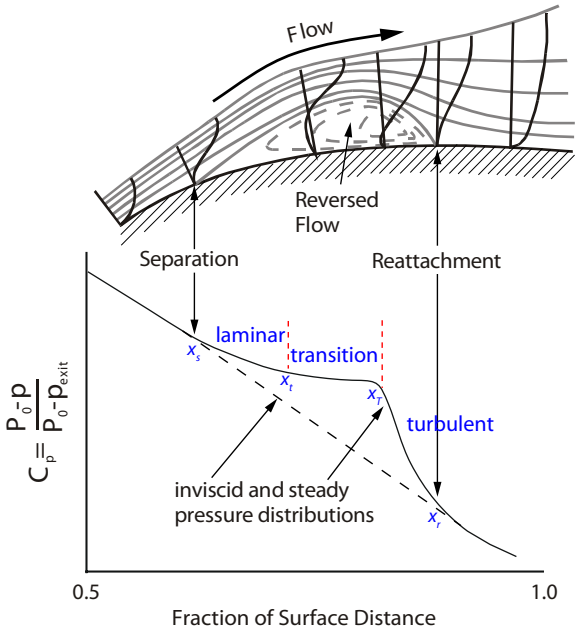

Figure 2.3: Schematic of time mean laminar separation bubble (exaggerated scale) (Hodson and Howell, 2005).

2.2.1.3 Separated Flow Transition

When a laminar boundary layer experiences a strong adverse pressure gradient, the boundary layer fluid may separate from the surface. At separation the pressure gradient according to Thwaites (1949) is given by $\lambda_\theta \approx -0.082$. Transition may occur in the free shear layer flow of the separation due to the result of inviscid instability mechanism. The enhanced mixing generated by the transitioning flow, promotes the shear layer to reattach to the surface.

The schematic of the time-averaged structure of a separation bubble is shown in Fig. 2.3, along with the phases of transition in a laminar separation bubbble with turbulent reattachment. The actual flow is highly three-dimensional and unsteady. After the flow separates at x_s the separation bubble can be divided into two distinct regions: I) an upstream region of nearly constant pressure, and II) a downstream region with a large pressure recovery (Mayle, 1991). At x_t in Fig. 2.3 a turbulent spot is produced ending the laminar shear layer. The laminar shear layer is inherently unstable due to the inflection point in the velocity profile. Transition in the shear layer is usually completed by x_T before the flow reattaches at x_r as a turbulent boundary layer.

Separation bubbles are classified as either being long or short, with the distinction between the two being related to their influence on the overall pressure distribution. Short bubbles, Fig. 2.3, only have a local displacement effect, so that, before and after them, the pressure distribution is close to that predicted for the flow over the surface without

separation. Long separation bubbles interact with the external flow to such an extent that the pressure distribution over the whole surface is appreciably different from that predicted without the separation bubble. The length of the separation bubble depends not on the length of transition, but on the length of the unstable laminar shear layer (Mayle, 1991). Gaster (1969) suggested that the bubble length was a function of momentum thickness Reynolds number at separation and the Thwaites pressure gradient parameter. A sudden change in bubble length is known as bursting. It can result in a dramatic loss of lift and could even cause the blade to stall if the bubble fails to reattach.

In compressor blade rows separated transition commonly occurs near an over-speed region caused by a discontinuity in curvature around the leading edge and in the decelerating pressure gradient downstream of minimum pressure on the suction surface. The size of the leading edge separation bubble is strongly coupled to the free-stream turbulence intensity, the leading edge geometry, the angle of attack and only weakly coupled to the Reynolds number (Walraevens and Cumpsty, 1995). Walraevens and Cumpsty (1995) observed that circular leading edges at zero incidence would have a small separation bubble located at the leading edge, whereas elliptic leading edges remained attached. The separation bubbles reattached as turbulent. Downstream of the reattachment, the momentum thickness for the circular leading edge was found to be 2-3 times that of the elliptic leading edge when a separation bubble was present.

2.2.1.4 Turbulent Spots

In general all transition modes eventually lead to production of turbulent spots. Emmons (1951) first proposed that the transition from laminar to turbulent state was through the formation of turbulent spots, after observations in shallow running water. From Emmons limited data he proposed that 'the presence of a spot anywhere in the flow does not affect the generation or propagation of other spots at other points in the flow'. This is known as the independence hypothesis.

The first quantitative data on the shape, growth and propagation of a turbulent spot was provided by Schubauer and Klebanoff (1955). They observed that turbulent spots are roughly triangular in plan view, although their shape varies across the height of the boundary layer. Figure 2.4 illustrates the general characteristic of a turbulent spot. In zero pressure gradient flow, the leading and trailing edge celerity of turbulent spots were typically 88% and 50% of the free-stream velocity respectively. As the spot propagates across the surface it not only grows in the streamwise direction due to the differential speeds of the leading and trailing edge but it also grows in the spanwise direction with a spreading half-angle of approximately 11 degrees. The leading and trailing edge propagation rates are shown in the space-time diagram in Fig. 2.4. The shaded area represents the area where

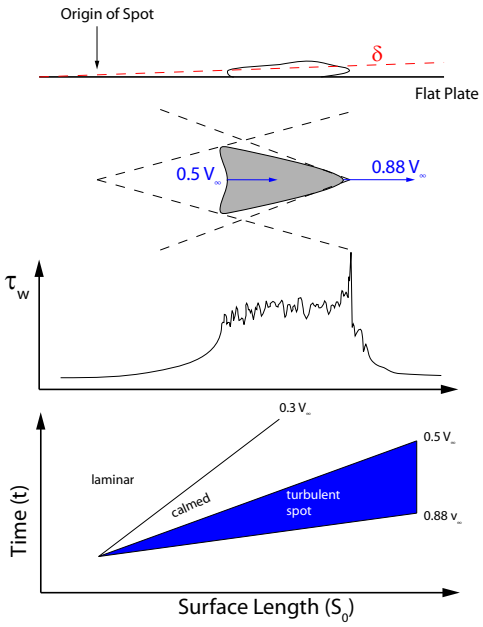

Figure 2.4: Schematic of a turbulent spot.

the turbulent flow exists in space and time as measured along the centreline of a typical turbulent spot.

The work of Solomon et al. (1996); Gostelow et al. (1996); D'Ovidio et al. (2001a,b) showed that the characteristics of a turbulent spot were a function of the local pressure gradient. The spreading half-angle increases strongly as adverse pressure gradient increases, approaching 30 degrees at the point of laminar separation. D'Ovidio et al. (2001b) provided two correlations[2], relating the spot propagation parameter, Eqn. 2.6, and the spot spreading half-angle, Eqn. 2.7, to the Thwaites pressure gradient parameter. The use of the spot propagation parameter, σ, is predicted on the classical Emmons spot propagation model, Eqn. 2.5

$$\sigma = \tan\alpha\left(b^{-1} - a^{-1}\right) \tag{2.5}$$

$$\sigma = 0.024 + \left(0.604/\left(1 + 5.0\exp\left(66\lambda_\theta\right)\right)\right) \tag{2.6}$$

$$\alpha = 4.0 + \left(22.14/\left(0.79 + 2.72\exp\left(47.63\lambda_\theta\right)\right)\right) \tag{2.7}$$

where a and b are the fractions of leading and trailing edge celerities based on free-stream velocity of the turbulent spot respectively.

Schubauer and Klebanoff (1955) observed that a quiescent or 'calmed' region of laminar-like flow trails behind a turbulent spot or turbulent strip (Pfeil et al., 1983; Orth, 1993). The

[2]The original correlation for σ and α was provided by Gostelow et al. (1996). These correlations were extrapolated up to the point of laminar separation. The work by D'Ovidio et al. (2001a,b) extended the experimental database to the point of laminar separation. The new data suggested that α remain unchanged, but a new correlation for σ was required

calmed region is identified as the region of decreasing wall shear stress behind the spot, Fig. 2.4. The calmed region is unreceptive to disturbances. This occurs because the boundary layer profile which is relaxing from a turbulent to laminar level of shear stress, is more stable than the surrounding undisturbed laminar boundary layer. The trailing boundary of the calmed region propagates at typically 20-30% of the free-stream velocity. The calmed region has two important effects on the developing boundary layer: I) it greatly increases the length of transitional flow by delaying transition from other modes, II) it delays the onset of laminar separation because of their elevated levels of shear stress and low shape factors (Howell et al., 2000)

Work on natural transition, in the absence of stimulation of turbulent spot behaviour, has been described in detail by Gostelow et al. (1994). Results based on wavelet analysis by Gostelow et al. (1999), demonstrated similarities between the behaviour of triggered turbulent spots and the turbulent patches caused by wake interactions on compressor and turbine blades. T-S wave activity in compressor stators have been observed by Solomon et al. (1996). Hughes and Walker (2001) used wavelet conditioning to identify the prevalence of T-S instability phenomena in the flow over compressor blades. The dominant wave frequencies were compared with linear stability predictions for the unstable T-S wave frequency having the greatest amplification rate (Walker, 1989). Reasonable agreement was found, providing strong evidence for T-S instability processes retaining a significant role in wake-induced transition.

Isolated triggered spots produced additional data on spot spreading rates permitting extension of the work to highly diffusing conditions conducive to laminar separation. Research into the effect of multiply turbulent spots have been carried out by Gutmark and Blackwelder (1987); Gostelow and Thomas (2005); Thomas and Gostelow (2005); Gostelow et al. (2007). Gutmark and Blackwelder (1987) first investigated interaction effects on triggered turbulent spots. Their research suggested that when the spacing between two turbulent spots became sufficiently low the leading edge celerities and fluctuation levels in the following turbulent spot would be reduced. This did not agree with Emmons independence hypothesis. This was experimentally verified through triggered turbulent spots by Gostelow and Thomas (2005). Thomas and Gostelow (2005) went further and used pairs of rotating bars to simulate wakes interacting with a boundary layer. They observed that the wake leading and trailing boundaries propagated at the same speed but the turbulence level of a following wake induced turbulent patch was reduced, by up to 40%. In addition the calmed region following the turbulent patch induced by wake interaction is stronger than that of an isolated turbulent spot. Gostelow et al. (2007) extended the work of Thomas and Gostelow (2005) for a series of four wakes to better represent a aero-engine environment. The work of Thomas and Gostelow (2005); Gostelow et al. (2007)

highlighted that the calmed region remains at work even when its domain coincides with that of the following turbulent patch. This has the effect of reducing the violence of the turbulence and therefore continuing to stabilise the flow.

2.2.1.5 Concentrated Breakdown

Narasimha (1957) proposed that turbulent spot production would form at a preferred streamwise location randomly in time and in the cross-flow direction. This is known as the concentrated breakdown hypothesis. Narasimha found that this hypothesis agreed with the experimental results of Schubauer and Klebanoff (1955). Later Dhawan and Narasimha (1958) showed with the concentrated breakdown hypothesis, all mean flow properties in a flat plate boundary layer could be predicted with good agreement in the transition zone.

Concentrated breakdown describes the ability of the calmed region to suppress the formation of turbulent spots. As the turbulent part of the spot and the calmed region grow in significance beyond the start of transition, fewer spots can form because the flow will increasingly be either in a calmed state or turbulent. Schulte and Hodson (1998) showed that spot production is effectively inhibited by these effects once the intermittency reached 0.25. Upstream of the start of transition turbulent spots can form but they will not be self-sustaining (Dong and Cumpsty, 1990a).

2.2.2 Transition in Periodically Unsteady Flow

The periodic passing of wakes from upstream blades can cause boundary layer transition through any of the modes described above. It has been experimentally observed that the wakes are so disruptive to the laminar boundary layer that turbulent spots often form in the location where the wakes impinges on the surface (Durbin et al., 2002; Langtry, 2006). It is not clear if transition is caused by the enhanced turbulence in the wake or the free-stream momentum defect and its interaction with the boundary layer.

The conventional picture of wake induced transition in compressors which is based on the work of Cumpsty et al. (1995) is shown in Fig. 2.5. The figure is a schematic of the transition phenomena in the space-time domain. The x-axis indicates the position along the blade chord or suction surface length and the y-axis shows multiples of wake passing periods. Indicated in Fig. 2.5 are trajectories drawn at V_∞, 90% V_∞ and 50% V_∞. The wakes from upstream blades periodically wash over the suction surface of the downstream blade row. At some distance downstream of the leading edge (marked L_B), the high turbulence level in the wake directly forms a turbulent spots. In fact it is assumed that the production of turbulent spots caused by the passing wake is so intense that the spots immediately coalesce into a turbulent strip. The leading boundary of the turbulent strip travels at approximately

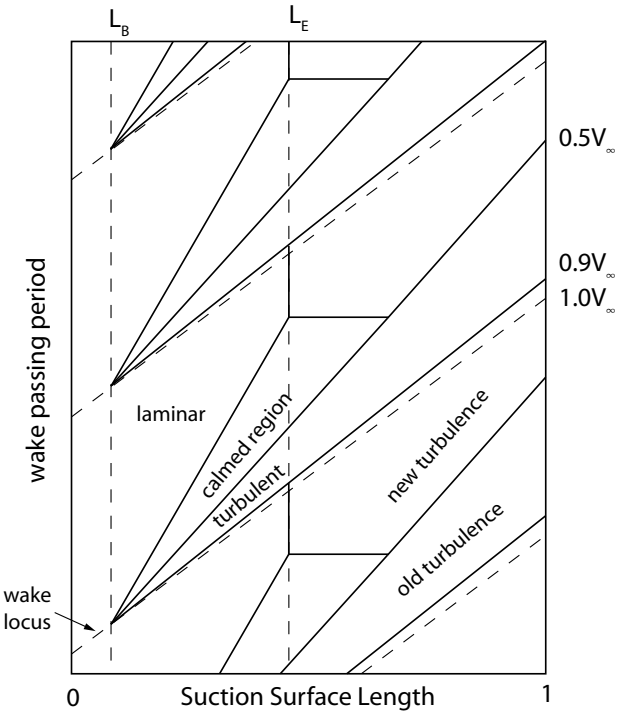

Figure 2.5: Schematic representation of wake induced transition on compressors boundary layer state (Wheeler et al., 2006).

90% V_∞ while the trailing boundary travels at approximately 50% V_∞. Therefore, the period of time that the turbulent strip occupies increases as it propagates downstream. A calmed region follows the turbulent strip, with the trailing boundary travelling at approximately 30% V_∞. Although the edge of the calmed region is rather symbolic, since the process of relaxation is a very gradual one. In between the wake passing events the boundary layer on the compressor blade suction surface undergoes transitions close to the location where transition would have occurred in steady flow (marked L_E). Also marked in Fig. 2.5 are the terms 'old' and 'new' turbulence after Cumpsty et al. (1995). Old turbulence refers to the turbulent region generated by wake induced transition and new turbulence refers to the turbulent regions that form in the absence of wakes. 'Old' turbulent regions are generally thicker and are more strongly affected by adverse pressure gradients than 'new' turbulence.

There have been several studies of wake induced transition in compressors such as, Dong and Cumpsty (1990a,b); Halstead et al. (1997b); Hughes and Walker (2001); Solomon and Walker (2000); Mailach and Vogeler (2003) and others. Originally it was believed that due to the highly turbulent environment and the adverse pressure gradient, that boundary layers on compressor blades would be fully turbulent. A fact that is still used in the modelling of compressors in CFD. Walker (1968, 1974) first established the transitional nature of compressor blades in a 1.5 stage low-speed compressor rig through hot wire studies and provided the first evidence of unsteady transitional phenomena on axial compressor blades

in response to passing rotor wakes. Evans (1978a) carried out a similar study to Walker (1968) but, because the effects of wakes was not separate from the three-dimensional flow influence, the results were inconclusive.

High levels of turbulence in wakes led to the hypothesis that wake induced transition would be bypass transition. That is turbulent spots would be directly produced in the boundary layer through local interactions with the free-stream turbulence (Mayle, 1991). Assuming that wake induced transition occurs in this manner, the onset of transition would be expected to correlate with wake passing trajectory. Pfeil and Herbst (1979) realised that the unsteady passing of wakes causes the boundary layer to become turbulent during the impingement on the surface. If a wake impinges the leading edge of a turbomachine blade the high turbulence of the wake penetrates into the laminar boundary layer (Mayle and Dullenkopf, 1989). In this way, a wake induced transitional and subsequently turbulent strip is formed, which is moving along the blade independently from the propagation of the wake in the blade passage. Thus a time shift between the wakes propagation in the blade passage and its influence on the blade surface can be observed. Solomon et al. (1999) used the MISES code of Youngren and Drela (1991) in a quasi-steady method to predict the unsteady onset of transition on a compressor blade surface. Good agreement with the experimental data was found, if the predicted onset boundary was based on a disturbance speed of 70% of the free-stream velocity. They proposed that the transition process must involve disturbances traveling more slowly than the free-stream.

The most comprehensive and basic research on compressor and turbine transition were carried out by Halstead et al. (1997a,b,c,d). The authors performed extensive studies of wake-induced transition in compressors and turbines at mid-span. They clarified the fundamental effects regarding wake passing: like the early onset of transition in the wake induced path, the suppression of a laminar separation bubble and the existence of a calmed region. The authors found a similarity between compressors and turbines and that wake induced transition can delay separation in compressors

Research by Solomon and Walker (2000); Hughes and Walker (2001); Mailach and Vogeler (2003) have shown that wake-induced transition generally starts very early on the suction surface. The apparent anomaly between empirical correlations and experimental evidence for early start has been addressed in part by Hughes and Walker (2001), who suggested that early transition in compressor blade rows occurs due to the amplification of T-S disturbances. Wheeler et al. (2006) observed that in unsteady flows the leading edge region had a significant effect on the performance of compressor blades in the presence of incoming wakes. They showed that the instantaneous momentum thickness of the early boundary layer was raised by 18% when the wake impinged on the leading edge. This region of increased thickness provided a favourable environment for the formation of

turbulent spots where at other times the boundary layer remained laminar. The thickened turbulent boundary layer was found to propagate over the blade surface. The leading and trailing edge of the structure was observed to travel at 70% and 60% of the free-stream velocity. The interaction of the wake with the leading edge, therefore, caused an increase in the turbulent wetted area on the blade surface and this was found to raise the suction surface profile loss by 13%. Henderson et al. (2006) also highlighted the importance of wakes at the leading edge by showing that it was a key receptivity site for turbulent spot formation.

Work on turbine rotors by Hodson (1984) has shown the significant impact of wakes on the increase of profile loss compared with that in a no-wake flow. In a low pressure turbines Schulte and Hodson (1998); Howell et al. (2001) demonstrated that taking into account the unsteadiness created by the passing wakes of upstream blade rows, it would be possible to design higher lift blades without increasing profile loss. The increases in lift and the resulting reduction in blade count were achieved due to wake induced transition of the boundary layer. Hodson and Howell (2005) showed that wake-induced transition can have both beneficial and detrimental effects on performance. Studies within low pressure turbines have shown that, on the one hand the increase in turbulent wetted area, due to the wake induced transition increase losses, whilst on the other hand, the calmed regions which followed the wake induced transition strips tended to reduce losses compared to the undisturbed boundary layer. The reduction of loss in low pressure turbines is achieved through the following mechanism (Fig. 2.6): the boundary layer separation over the late suction surface of a high lift turbine blade is temporary suppressed by turbulence induced by the incoming wakes. The calmed region that trial wake induced turbulent flows have a full velocity profile and yet are laminar-like in nature. The calmed region does not readily separate, thus delaying the re-establishment of the bubble and because they are laminar-like, they produce lower losses and so counterbalance any extra loss associated with the wake induced turbulence.

Benefits associated with calmed regions have been in investigated in compressors with varying degrees of success. Dong (1988) reported no significant effect on loss for a controlled diffusion aerofoil with associated unsteadiness. However studies on a compressor like flat plate by Ottavg et al. (2004) showed a large impact on loss, with unsteadiness and transition where performance improvements above the steady flow case were achievable at certain flow conditions. Ottavg et al. showed that it should be possible to increase the lift by 35% while keeping the same level of loss as a low lift compressor blade. The balance is between the loss associated with the turbulent regions, old and new turbulence, and the loss reduction mechanisms in the calmed region. If the benefits of the calmed region are stronger than the loss addition due to the early transition generated by upstream wakes then

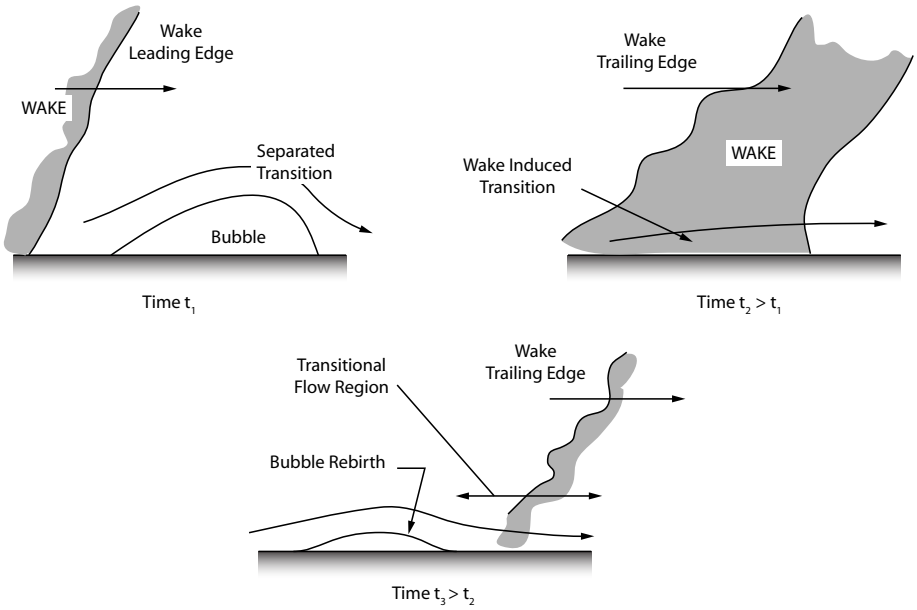

Figure 2.6: Effect of wake induced transition on separation bubbles (Mayle, 1991).

benefits can be had.

2.3 Unsteadiness in Compressors

The flow in a compressor is inevitably unsteady with free-stream disturbances. The free-stream disturbances and unsteadiness are generated by previous blade row wakes, potential fields, endwall boundary layers, secondary flows, tip clearances and blade row interactions. The turbulence level is important since it has a significant consequence on the development of the boundary layers on the blade surfaces. However, the turbulence levels in aero-engines are not well known, but measurements of free-stream turbulence levels within low-speed multistage compressors have ranged from 2-10% (Schlichting, 1959; Wisler et al., 1987; Camp and Shin, 1995). Evans (1978b) was one of the earliest studies that published extensive measurements of the turbulence and unsteadiness levels downstream of an axial flow compressor rotor. Slanted hot wire measurements by Wisler et al. (1987) observed turbulence intensities as high as 20% in endwall regions and wakes in a four-stage low-speed research compressor. Camp and Shin (1995) performed extensive investigations of the turbulence level in several research compressors. They experimentally verified that both turbulence level and turbulence length scale increase with stage loading.

Early analytical studies into the propagation of wakes through compressor blade rows were performed by Kemp and Sears (1955); Meyer (1985); Lefcort (1965). Further detailed investigations on the wake chopping and inter-blade passage transport of the wake segment were done by Kerrebrock and Mikolajczak (1970). The wakes do not only pro-

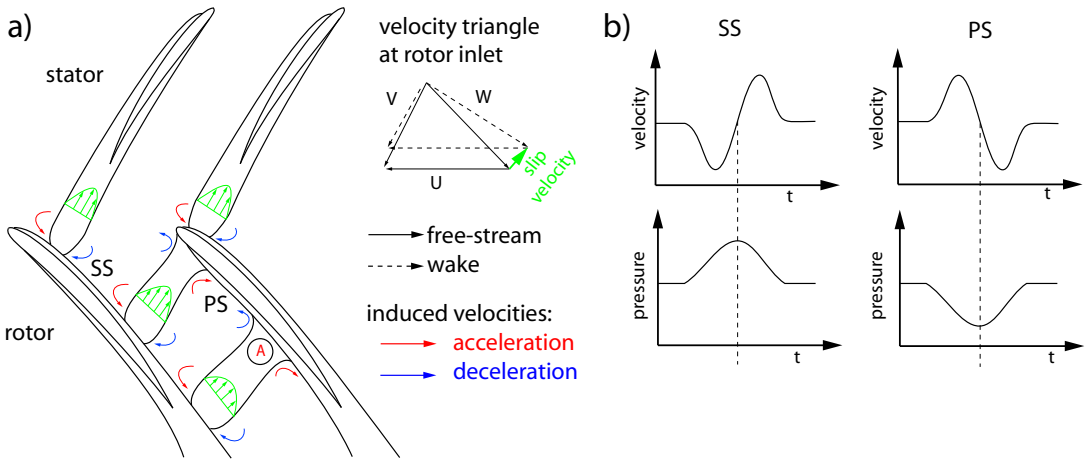

Figure 2.7: Negative-jet effect: a) influence within a compressor blade row, b) effect on velocity and pressure at fixed position near blade surface. (Mailach et al., 2007a)

duce fluctuations in velocity, but in incidence, turbulence and total temperature. The effect of velocity and incidence fluctuations is most acute where the pressure gradients on the blade are the greatest. In general this is near the blade's leading edge. A schematic of the transport of wake fluid during its propagation through a subsequent blade row is illustrated in Fig. 2.7.

Meyer (1985) observed that wakes have a slip velocity relative to the main flow, and hence can be thought of as a negative jet (see, Fig. 2.7). The negative-jet drives the low momentum wake fluid to move along the wake centreline from the suction side through the blade passage to the pressure side. Meyer discussed the unsteady influence of the negative-jet on the boundary layer. Near the suction side at the leading boundary of the wake segment, the negative-jet induces a reduction of velocity. While at the trailing boundary of the wake segment an increase of velocity appears (Fig. 2.7). The opposite is true for the pressure side.

The decay rate of a wake is largely due to both mixing (results in loss) and stretching (no loss accrual). Smith (1966) showed how, in a compressor, the wake segments become stretched, due to the increase in passage area. This leads to a faster decay of the wake and therefore reduces the viscous mixing losses. This is phenomena is termed 'wake recovery'. Van Zante et al. (2002) showed that for the rotor/stator spacing typical of core compressors, wake recovery is the dominant wake decay process within the stator. The authors went on to develop a model for the rotor wake decay process which exhibited good agreement with experimental data.

Wakes hitting the leading edge of the downstream blades are chopped into segments which are rotated through the downstream passage. At exit the initially continuous wakes have been transformed into a sheet of discontinuous segments ('old school tie' effect).

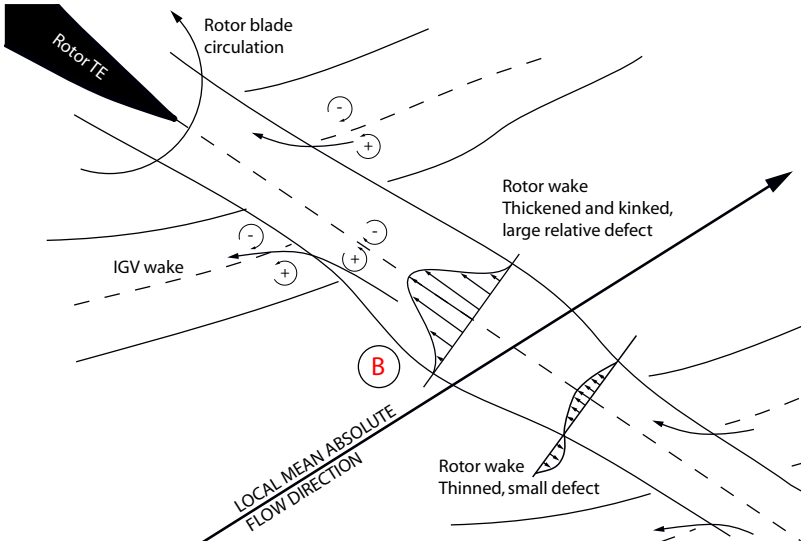

Figure 2.8: Schematic of instantaneous flow pattern with rotor wake kinking

Individual segments are no longer parallel to the local mean flow direction and are terminated by wakes from the rotor. The presence of stator wakes adjacent to the rotor wakes leads to interactions which can significantly modify the rotor wake decay. Chow et al. (2002); Chow and Katz (2003) showed that a discontinuous wake contains a 'kinked region' (Fig. 2.8). The kinked region is characterised by turbulent kinetic energy and concentrated vorticity. There are two significant mechanisms which may modify the relative flow within the rotor wake and reduce the circumferential transport. The first, the mixing due to chopped upstream stator wake segments impinging on the rotor wake acts to restrict the relative flow within the rotor wakes; The avenues of chopped stator wake segments effectively form barriers against which low energy rotor wake fluid accumulates (location B in Fig. 2.8). The relative flow will also be restricted by interposition of downstream stator causing accumulation of rotor wake fluid on the stator pressure surface (location A in Fig. 2.7). Variations on the rotor wake thickness and velocity defect along its trajectory due to wake-wake interactions were observed by previous researchers Lockhart and Walker (1974). They alluded to the kinked wake, describing it as a 'wobbly wake.

2.4 Three-Dimensional Flows in Compressors

The previous sections were primarily concerned with the essentially two-dimensional aspect of unsteady flows in compressors. In reality the flow field in the compressor is highly three-dimensional, due to the development of corner separations, tip clearance flows and the low aspect ratio of core compressors. The low aspect ratio results in the endwall flow occupying a significant proportion of the annulus height.

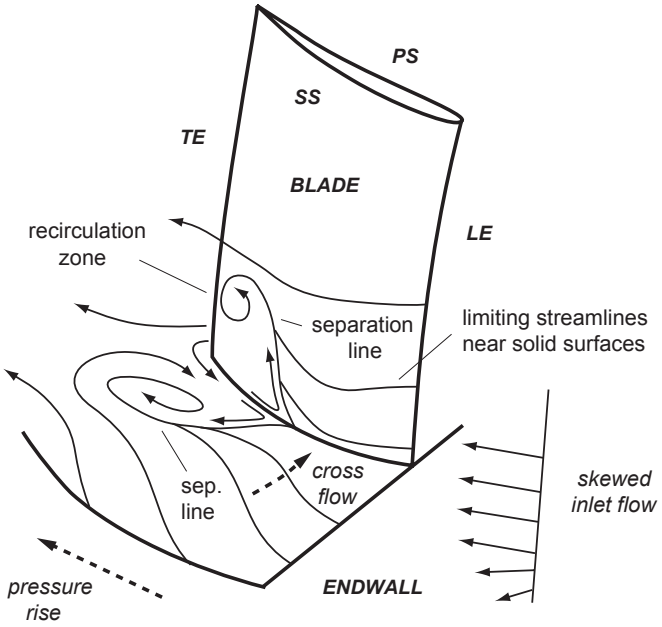

Figure 2.9: Basic processes governing the formation of hub corner stall together with limiting streamlines and separation lines (Lei et al., 2006).

2.4.1 Three-dimensional Separations

Hub corner separation as illustrated in Fig. 2.9 have been observed experimentally by Joslyn and Dring (1985); Dong et al. (1987) in compressor rigs. Schulz and Gallus (1988) experimentally identified the characteristic features of three-dimensional corner stall in annular compressor cascades. These included the stagnation of low momentum fluid in the corner and flow reversal. The stagnation of the low momentum fluid is driven by a combination of the adverse pressure gradient and the the cross-passage pressure gradient. The cross-passage pressure gradient arises due to secondary flow that overturns the lower momentum fluid close to the endwall. This drives the endwall fluid from the pressure surface to the suctions surface, where the flow interacts with the suction surface boundary layer. A detailed description of the mechanisms of secondary flow are given by Horlock et al. (1966). Unlike two-dimensional separations, three-dimensional separations do not require a streamwise pressure gradient. A comprehensive review of corner separations in compressor cascades can be found in Moore and Richardson (1957); Horlock et al. (1966); Salvage (1974). Gbadebo et al. (2005) established topological rules which predict the properties of the limiting streamlines and singularities. As the number of singularities increased, the thickness of the separation region and losses increased as well.

Evans (1978a) highlighted the importance of understanding separations in the presence of rotor-stator interactions. Schulz et al. (1990) presents a detailed interpretation of the effects of upstream wakes on the entire passage flow. Considerable progress has been made

in understanding the nature and extent of wall separation and its dependency on blade loading in isolated blade rows such as cascades, annular cascades and rotors. Measurements suggest that in the presence of rotor wakes, transition starts very close to the leading edge. The rotor-stator interactions also reduced the size of the hub corner stall compared to the isolated stator hub corner stall. This reduction was caused by the upstream rotor wakes, the increased turbulence level and the absence of a laminar separation bubble of the stator. The authors proposed a topology consisting of a stream surface bounded by separation lines on the endwall and the blade surface and separating the stalled flow from the free-stream. A ring vortex, associated with the flow reversal inside the stall region, is suggested to exist in the recirculation zone. This separation topology and the transport of low momentum fluid by secondary flow was confirmed by Hah and Loellbach (1999). The experiments of Schulz et al. (1990) showed that wakes do not penetrate regions of separated flow. The blade boundary layer responds to the imposed velocity fluctuations by a relative breathing of its velocity profile and its momentum thickness. The amplitude of local velocity fluctuations are at a maximum inside the boundary layer. Inside the separated flow regions and close to the laminar sublayer, the rotor wake is damped and hence, only small velocity fluctuations were observed. This was confirmed by the later work of Honen and Gallus (1995). They observed that the centre of the hub separation was unaffected by the rotor flow, but it was at the edges of the separation where the rotor influence was seen. Here the stator hub corner separation could be forced into unsteady periodic motion.

2.4.2 Tip Clearance Vortex

A brief description of the time-averaged tip clearance flow was given in Chapter 1 and Fig. 1.6. The tip clearance flow is of crucial importance for compressor design and operation because of its detrimental impact on the efficiency and the pressure rise due to the blockage effect in the endwall region (Wisler, 1985). An increase in the tip clearance of 1% of span may yield a 1% drop in compressor efficiency (Peacock, 1982). In rotors the leakage flow plays a crucial role in the flow stability and rotating stall inception. The maximum leakage flow over the blade tip can be expected at the position of the maximum profile difference between the pressure and suction surfaces Inoue and Kuroumaru (1989) and can be considered to be the origin of the tip clearance vortex.

Storer (1991) compared linear compressor cascade measurements with numerical solutions of the tip clearance vortex. The mechanisms of the tip clearance vortex was primarily inviscid and in most parts controlled by the static pressure field near the tip region. Mailach et al. (2007b) performed Laser Doppler Anemometry measurements over the third-stage rotor in a four-stage low-speed research compressor. They found that the time-resolved tip clearance vortices were strongly affected by the passing wakes. Due to the wake impact

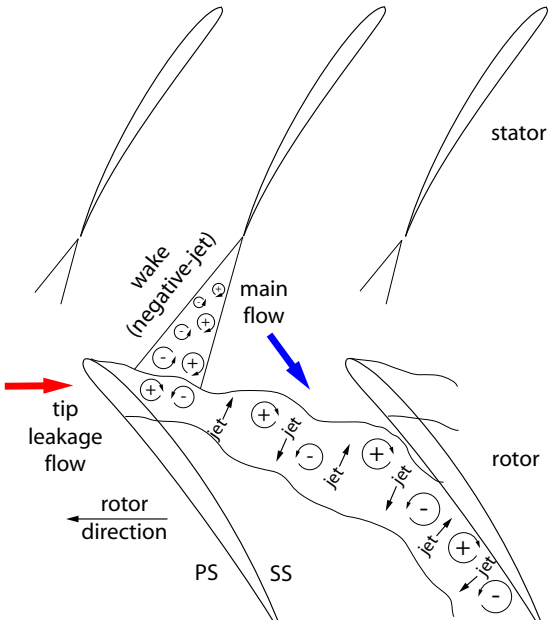

Figure 2.10: Schematic of tip clearance vortex influence by passing wakes after Mailach et al. (2007b)

the position of the maximum leakage massflow, the vortex intensity and consequently the orientation and extension of the tip clearance vortices altered in time. This pulsation was tied to the stator blade passing frequency. Mailach et al. (2007b) observed that the counter-rotating vortices due to the negative-jet in the stator wake induced pairs of counter-rotating vortices in the leakage flow. Between the counter-rotating vortices fluid jets were generated, Fig.2.10.

2.5 Concluding Remarks

This chapter has addressed the wide body of literature covering unsteadiness and transition in axial flow compressors. This body of knowledge is expanding rapidly due to the benefits achieved in low pressure turbine blade designs. It has been demonstrated that the flow in a compressor are highly three-dimensional, unsteady with complicated wake-boundary layer interactions.

The physics of transition has been well documented with fundamental studies performed using flat plates. The unsteady boundary layer development in turbomachinery has been primarily performed using either flat plates with prescribed pressure distributions or cascades with rotating bars to simulate upstream blade rows. Wake affected boundary layer transition has also been observed in single stage low-speed compressor rigs, but the inlet flow is usually clean and does not take into account wake disturbances representative

of an embedded stage or the potential interaction of a downstream blade row. There have been relatively few experiments performed in a multistage environment where the above affects can be captured.

This review has highlighted that wakes can affect the development of the boundary layer in an unsteady manner. At midspan wakes have been observed to cause transition close to the leading edge, but little information is available on how the transition or even development of the boundary layer changes in the spanwise direction. Therefore, this thesis investigates the wake-boundary layer interactions in an embedded blade row away from midspan and determines how this influences the unsteady development of the boundary layer and hence the profile loss.

Chapter 3

Experimental and Numerical Techniques

3.1 Introduction

The experimental facilities, instrumentation, measurements techniques and the CFD code used in obtaining the experimental and numerical results presented in the following Chapters of this thesis are describe here.

The commercial CFD code is described together with details of the turbulence models, boundary conditions and grid considerations. The experimental measurements described in this thesis were performed in the Cranfield University four-stage low-speed research compressor.

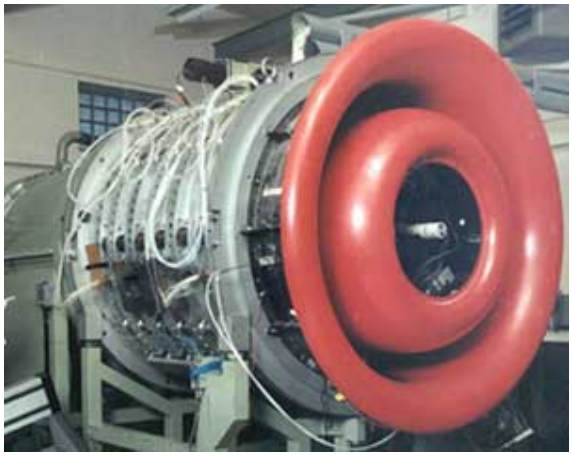

Figure 3.1: The Cranfield four-stage low-speed compressor.

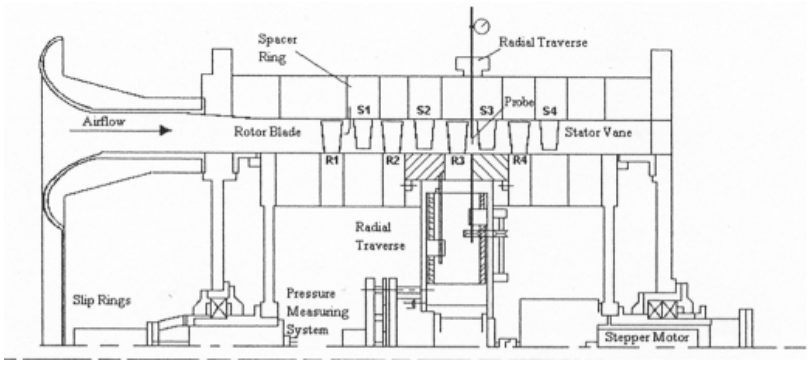

Figure 3.2: Cross-section of LSRC, including location of radial traverse gear.

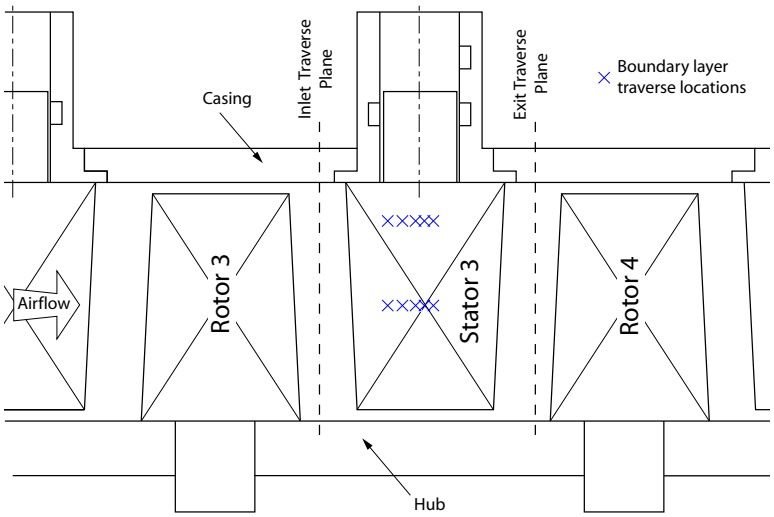

Figure 3.3: Schematic of compressor test stage. Measurement locations are highlighted.

3.2 The Cranfield Four-Stage Rig

The Cranfield 120 kW four-stage rig (Fig. 3.1) is a large-scale model of an embedded, low-aspect ratio high-pressure compressor. The large physical size of the rig allows for detailed measurements of the flow field (Chapters 4 and 5), secondary flows (Chapter 4) and blade boundary layers (Chapter 6). A schematic of the rig and the test-stage are shown in Figs. 3.2 and 3.3[1]. The flow enters the test building via a gauze to remove any asymmetry and particles which could contaminate and or damage the measurement instrumentation. The flow then enters the compressor through a calibrated bellmouth, followed by a small contraction (designed to remove excessive endwall boundary layer growth). The flow then passes through the inlet guide vanes (IGVs) where the flow is turned to ensure correct swirl angle onto the first stage rotors. A parallel annulus of four repeating blade rows then

[1]Note that the test stage has not been drawn to scale. Leading and trailing edge locations are also not accurately represented

Number of Stages	4.5
Corrected Rotor Speed, rpm	1045
Tip Radius, mm	609.6
Hub-to-tip ratio	0.91
Axial Gap, mm	30.3
Midspan Reaction	0.645
Midspan $\Delta H/U^2$	0.494
Peak Efficiency, ϕ	0.450
Near Stall, ϕ	0.400

Table 3.1: General Specifications of LSRC.

follows. The flow is finally exhausted to the atmosphere via a discharge damper, several metres downstream. A throttle located downstream of the compressor is used to control the massflow through the compressor at constant operating RPM. The throttle system was gear driven and operated from the control room for accurate incremental control. The throttle also included a surge control device which activates a quick release feature of the discharge throttle for rapid stall recovery in the event of surge.

The performance of an embedded stage is strongly influenced by those around it and therefore an essential ingredient of the modelling process is to simulate the likely entry and exit conditions (Lyes and Ginder, 1998). This is achieved by using geometrical identical stages. In the Cranfield rig the first two stages set-up repeating flow conditions and appropriate endwall boundary layers so that the axial velocity profile is representative of an embedded stage (Smith, 1969). The third is the study stage and the fourth sets-up appropriate downstream pressure fields.

The details of the stage at the design point are shown in Tab. 3.1. The outer annulus wall has a constant radius of 0.6096 m and a hub/tip-ratio of 0.91. All the stators are cantilevered from the outer annulus wall with a rotating hub.

3.2.1 Blading

All the measurements presented in this thesis were taken from the ANT2 build (Aurifeille, 2003). The ANT2 build was a deviation of a previously tested build, ANT1 (Madden, 2001, 2003). ANT1 was designed to be a low speed aerodynamic equivalent of the blades for the third stage of the five-stage high-pressure compressor of the Affordable Near Term Low Emission (ANTLE) engine.

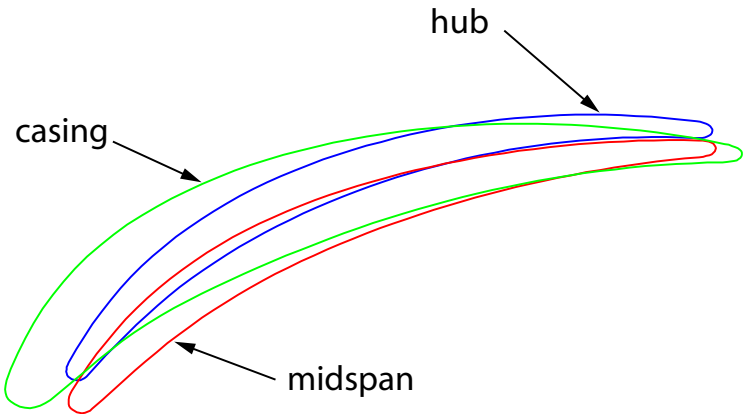

Figure 3.4: ANT1/2 stator profiles at casing, midspan and hub in the ANT2 build.

The main design parameter adjusted in the development of ANT2 was the solidity. It is well known that changes in the pitch, hence the solidity, in rotor blades have a major influence on efficiency. Going to large pitches, and reduced blade count gives improvements in efficiency and reductions in stall and surge margins, but the blading experiences a wider incidence range. By re-cambering the aerofoil at the leading and trailing edge, the problems due to incidence can be reduced and the flow turning and exit whirl angle can be controlled. This resulted in a reduction of rotor blades in ANT2 from 101 to 88. The lean and sweep of the new rotor blades was the same as for ANT1, but the sections were modified to achieve the same turning. ANT2 stators and IGVs were the same as ANT1. CFD analysis performed by Rolls-Royce plc did not show any performance improvement with modification of the stator geometry or blade count.

ANT2 blading is typical of modern designs, with high hub/tip-ratio, low aspect-ratio and high solidity. The mean-line blading design specifications are shown in Tab. 3.2. Representative profiles at hub, mid-span and tip locations for the stator are shown in Fig. 3.4. The aspect ratio for both the rotors and stators are low for this build and as such the secondary flows, and the endwall boundary layers can occupy a significant fraction of the span. The stator blades incorporate three-dimensional design methodologies including lean, sweep and end-bends.

3.2.2 Rig Monitoring

For measurements discussed in this thesis, the rig conditions were monitored to ensure that they remained within a specified tolerance during the acquisition of data. A once-per-revolution signal from an optical switch mounted on the shaft of the rig was used to monitor the rotational speed, which was maintained at 1045 rpm corrected (Eqn. 3.1). The

	Rotor	Stator
No. of Blades	88	134
Chord, mm	70.50	52.78
Axial Chord, mm	49.63	48.91
Aspect Ratio	0.78	1.04
Stagger Angle, deg	46.61	22.07
DeHaller Number	0.62	0.65
DF	0.49	0.52
Solidity	1.7	1.93
Tip clearance, % span	1.18	1.1
Re_{chord}	$3.07x10^5$	$1.67x10^5$

Table 3.2: ANT2 mean-line blading specifications.

rpm value was the average of 48 values taken each time the scani-valves were indexed.

$$\mathrm{RPM}_{Cor} = \overline{RPM}\sqrt{\frac{T_{0\,ISA}}{T_{inlet}}} \tag{3.1}$$

Running of the rig was done under current control, were the current was adjusted in order to hold the non-dimensional speed within $\pm 0.5\%$. The inlet massflow was calculated by,

$$\dot{m} = C_D A \sqrt{2\,\rho_{inlet}\,q_{inlet}} \tag{3.2}$$

where $C_D = 0.988$ is the discharge coefficient for the inlet, A is the inlet area, q_{inlet} is the inlet dynamic head and ρ_{inlet}, is the inlet density. The inlet dynamic head or depression was recorded by directly measuring the difference between the average of 2 NPL total pressure probes and the average of the 10 bellmouth and bullet static pressures measured using a Baratron. The inlet density was calculated from the average temperature recorded on 5 platinum resistance thermometers (assumption that static temperature at inlet is the same as total) and the average total pressure recorded on the two NPL pitot-static probes minus the inlet depression. The torque efficiency of the rig was calculated using,

$$\eta = \left[\left(\frac{P_{04}}{P_{01}}\right)^{\frac{\gamma-1}{\gamma}} - 1\right]\frac{T_{inlet}}{\Delta T} \tag{3.3}$$

where P_{01} and P_{04} are the averaged total pressures recorded by the 8 inlet and exit total

pressure rakes respectively (each total pressure rake has 12 ports). The change in temperature across the four stages was calculated using the measured torque and calculated massflow rate, Eqn. 3.4

$$\Delta T = \frac{\omega \, TQ}{\dot{m} \, \mathbf{Cp}} \tag{3.4}$$

where ω is the rotational speed of the compressor, TQ is the measured torque and **Cp** is the specific heat capacity at constant pressure. The pressure rise coefficient, ψ, based on a four-stage average was calculated by

$$\psi = \frac{\mathrm{Cp} \, \Delta T_{isen}}{4 \, U_{mid}^2} \tag{3.5}$$

where ΔT_{isen} is the isentropic temperature rise across the rig and was calculated from

$$\Delta T_{isen} = \left[\left(\frac{P_{04}}{P_{01}} \right)^{\frac{\gamma-1}{\gamma}} - 1 \right] T_{inlet} \tag{3.6}$$

3.2.3 Data Acquisition

Data acquisition involved the logging of the electronic signal produced by the hotwires. The signals were logged by the Keithley KPCI-3101 12-bit analogue to digital converter. The maximum sampling rate for this card was 225 kHz. A once-per-revolution pick-up was set to trigger the logging of the unsteady signals. The analogue to digital converter was operated in the +5 V range giving a resolution of 1.22 mV. The raw unfiltered output of the anemometer was typically between 1.5 V and 3.0 V.

Steady pressure measurements were logged using two PSI-9010 intelligent pressure scanners connected as master and slave. The PSI-9010 was capable of logging 16 pressure ports simultaneously and was connected to the acquisition PC through a RS232 serial link. All the differential pressure measurement instruments in the stationary frame had their reference pressure ports connected to the same reference volume within the test cell. This volume was connected to the ambient pressure outside the test cell.

The rotating frame instrumentation was connected through a 48 way Scani-valve with integrated Druck PDCR 22 differential pressure transducer. Data was transferred to and from the stationary frame using a 50 way slip ring attached to the front of the rig.

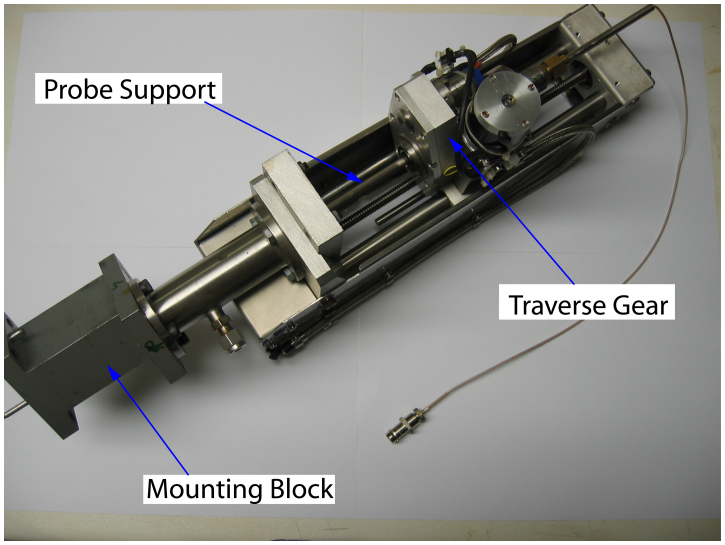

Figure 3.5: RotaData Traverse Gear with hotwire probe support and rig mount.

Rotor 3 Exit (Plane 8)	+35% of rotor axial chord
Stator 3 Exit (Plane 9)	+49% of stator axial chord

Table 3.3: Axial locations of the traverse planes, measured from trailing edge.

3.2.4 Probe Traversing

3.2.4.1 Area Traversing

The Rotadata RTA190 two-axis (radial and yaw) traverse gear (see, Fig. 3.5) was used to traverse the measurement probes (hotwire and cobra probes) within the flow field at two axial locations within the rig. Both radial and yaw drive is provided by miniature stepper motors. The radial drive line is a repeating ball linear ball screw design with a maximum stroke of 190 mm $\pm$0.01 mm. The yaw axis drive line is through a worm and wheel gearing arrangement capable of $\pm 125^{\circ}$ with a tolerance of $\pm 0.1^{\circ}$. The approximate positions of these traverse planes are shown in Fig. 3.3 and detailed in Tab. 3.3. The probes were mounted to the rig and inserted through the casing. The casing rings could be clocked relative to the stators allowing for traversing in the circumferential direction.

3.2.4.2 Boundary Layer Traversing

The boundary layer traverse gear was mounted on a removable cassette that contained two stator blades. Figure 3.6(a) shows the boundary layer traverse gear mounted on the Cranfield rig. The traverse gear was originally designed by Lee (2001) and has been used by Lee (2001) and Shin et al. (2003). The hotwire probe is attached at 90° to a sliding

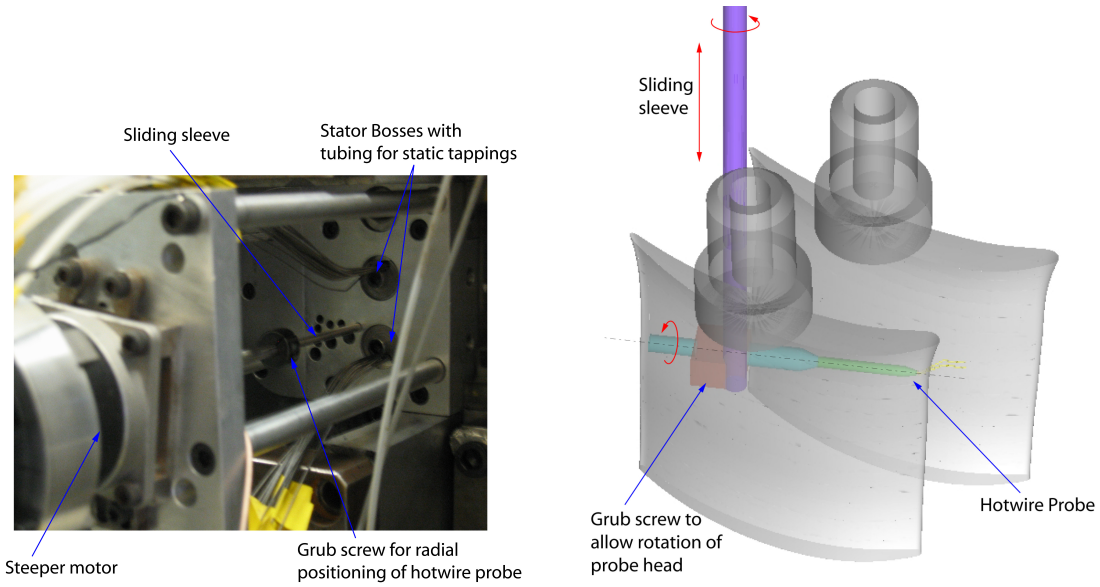

Figure 3.6: Boundary layer traverse mechanism mounted to the Cranfield four-stage rig.

sleeve aligned with the local radius (Fig. 3.6(b)), which is capable of moving up and down the traverse shaft. A small grub screw allows for small axial movements and rotation of the hotwire probe about its axis for alignment with the surface. The hotwire probe is rotated about the traverse shaft, resulting in near perpendicular movement. A series of holes are provided in the cassette to allow for axial movement of the hotwire probe. The location of these holes were calculated so that the tip of the hotwire prongs just made contact with the surface. Radial movement is achieved through varying the length of the traverse shaft.

The stepper motor is controlled by a micro-stepping card, capable of 12800 steps-per-revolution. The position of the probe was determined by a HEIDENHAIN ROD 426 rotary encoder which has 9000 pulses-per-revolution (4500x2 internal interpolation) with TTL square wave output signal. In order to increase the resolution of the encoder the TTL square wave output is routed into a US digital USB1 encoder Data acquisition device that supports four times edge counting (where the counter increments on every quadrature change). This resulted in a positional accuracy of 0.01° which is allowed for the accurate measurement of movement as low as 8 μm. The USB1 encoder was linked to a 7-port US digital Universal Serial Bus in the control room.

The boundary layer was traversed at 50% and 85% annulus heights. In the streamwise direction the probe was traversed at 25%, 35%, 44%, 50% and 56% based on 50% span suction surface length. Measurements upstream of 25% suction surface length were not possible due to the three-dimensional design of the blades and measurements downstream of 56% were not possible due to possible interference with Rotor 4 leading edge. The

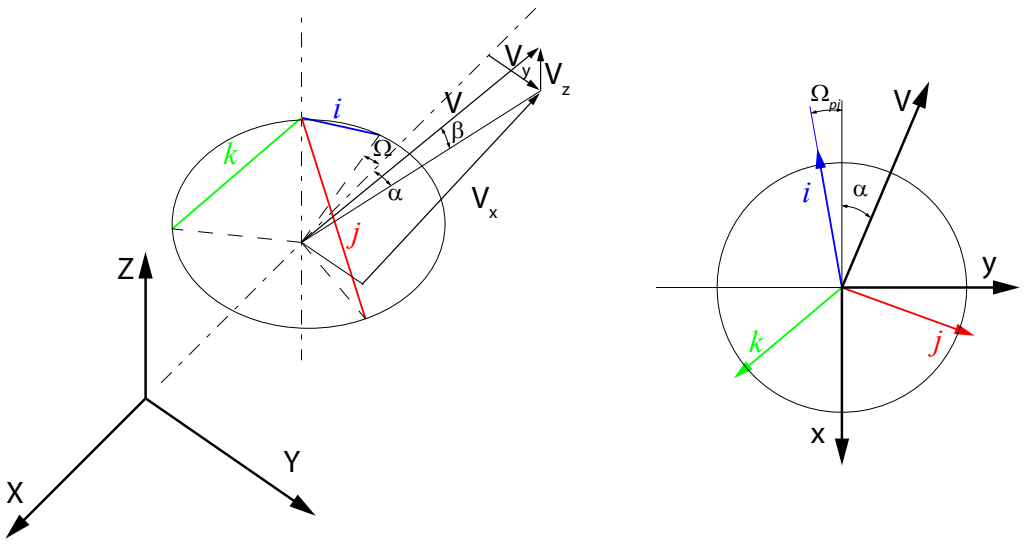

Figure 3.7: Schematic of wire and Rig coordinate frames.

boundary layer and free-stream was discretised into 68 points with clustering applied towards the suction surface. The boundary layer traverse extended approximately 10 mm from the suction surface.

3.3 Experimental Techniques

3.3.1 Hotwire Measurements

Several measurements were performed using hotwire probes. These included flow field measurements and boundary layer measurements. The wires were calibrated for velocity using King's Law and temperature compensated using Eqn. 3.7,

$$E_{corr} = \left[\frac{T_w - T_{ref}}{T_w - T_{acq}}\right]^{0.6} E_{acq} \tag{3.7}$$

For the boundary layer measurements, the near-wall effects were corrected for using the correction by Lange et al. (1999),

$$C_u = \frac{V_0}{V_{meas}} \tag{3.8}$$

where C_u is the correction factor given by Eqn. 3.9, V_{meas} the measured velocity and V_0 the actual velocity.

$$C_u = 1.0 - \exp(-0.4y^{+^2}) \tag{3.9}$$

The frequency response of the hotwires was approximately 30 kHz. The hotwire sig-

nals were sampled at 150 kHz and low-pass filtered at 30 kHz using a Dantec 56N20 to avoid aliasing. The sampling frequency was selected based on the work by Camp and Shin (1995). The ensembled statics were obtained from 500 phase-locked signals. The following sections discuss the hotwire measurements in more detail.

3.3.1.1 Slanted Hotwire Measurements

Measurement of the unsteady free-stream velocity, whirl and pitch angle were performed using a Dantec 55P02 slanted hotwire probe. The probe was modified to give a wire inclination angle of 54.7°[2]. A technique similar to that of Whitfield et al. (1972) was used. Whitefield's method only assumes that first order cooling effects are important. That is, the flow only responds to the flow perpendicular to its axis and therefore, insensitive to the flow parallel to the wire. Adachi and Murakami (1979); Lomas (1986) and Kang (1996) extended this method to take account of the additional flow parallel to the wire.

The three-dimensional flow velocities were obtained at each measurement position as follows. Three angular orientations of the hotwire were selected 120° apart. The initial position, i, was chosen so that the wire was parallel to the mean flow direction (shorter prong upstream). This was performed at each radial height traversed. The mean flow direction was taken from the measured yaw angle obtained from the cobra probe traverses. The directional characteristic of the hotwire was given by the effective cooling velocity, V_e, and Hinze law,

$$V_e = V\left(\cos^2\alpha + k^2\sin^2\alpha\right)^{1/2} \tag{3.10}$$

where α denotes the angle between the flow direction and the normal to the axis of the wire, and k is a correction factor due to deviation from the cosine law. With this correction, the velocity sensed by each orientation of the hotwire is given by,

$$\begin{bmatrix} v_i^2 \\ v_j^2 \\ v_k^2 \end{bmatrix} = \begin{bmatrix} k^2 & 1 & 1 \\ 1 & k^2 & 1 \\ 1 & 1 & k^2 \end{bmatrix} \begin{bmatrix} V_i^2 \\ V_j^2 \\ V_k^2 \end{bmatrix} \tag{3.11}$$

where V_i, V_j, V_k are the velocity components in the i, j, k wire orientations respectively. Adachi and Murakami (1979) rearranged Eqn. 3.11 (neglecting k^4 terms) to solve for the

[2] A wire angle of 54.7° when rotated three times by an angle of 120° creates an orthogonal co-ordinate system.

three wire velocities,

$$\begin{bmatrix} V_i^2 \\ V_j^2 \\ V_k^2 \end{bmatrix} = \frac{1}{2-k^2} \begin{bmatrix} k^2-1 & 1 & 1 \\ 1 & k^2-1 & 1 \\ 1 & 1 & k^2-1 \end{bmatrix} \begin{bmatrix} v_i^2 \\ v_j^2 \\ v_k^2 \end{bmatrix} \tag{3.12}$$

By assuming that V_i is negative and $V_{j,k}$ are positive (Whitfield et al., 1972) the velocity components, with respect to the rig coordinates can be determined from the direction cosines. The axial (V_a), whirl (V_t) and radial (V_r) velocity components in the rig coordinate system (Fig. 3.7) are given by,

$$\begin{bmatrix} V_a \\ V_t \\ V_r \end{bmatrix} = \begin{bmatrix} -\sin\varphi\cos\Omega_{pi} & \sin\varphi\cos\Omega_{pj} & \sin\varphi\cos\Omega_{pk} \\ -\sin\varphi\sin\Omega_{pi} & \sin\varphi\sin\Omega_{pj} & \sin\varphi\sin\Omega_{pk} \\ -\cos\varphi & \cos\varphi & \cos\varphi \end{bmatrix} \begin{bmatrix} V_i \\ V_j \\ V_k \end{bmatrix} \tag{3.13}$$

where φ, is the wire angle (54.7°) and $\Omega_{pi}, \Omega_{pj}, \Omega_{pk}$ are the three rotations of the the hotwire probe. In order not to exceed the acceptance cone of the hotwire sensor, it is necessary to position the probe in such a way that i-direction is within $\pm 20°$ of the mean flow direction. Thus the method requires prior knowledge of the approximate mean flow direction.

The flow sector covered by the hotwire probe was from 3% to 98% annulus height. The hotwire probe could not be traversed closer to the hub endwall due to the length of the hotwire prong. The circumferential extent of the traversed sector was 4.0299°, comprising 37 increments of 0.108916°. The resulting traverse matrix was 20x38. The traversed sector for the hotwire probe was different to that of the stationary cobra probe as the time at each measurement point was significantly longer for the hotwire probe.

3.3.1.2 Comparison Between Hotwire and Cobra Probe

The unsteady hotwire data was time-averaged and compared to the results from the cobra probe. The V_a/U_{mid} contours compare well (Figs. 3.8(a) and 3.8(b)). Good to reasonable agreement between the mean absolute yaw angle is achieved (not shown) between the two measurement techniques with the cobra probe showing large gradients in α which is probably caused by the large sensing area of the cobra probe compared to that of the hotwire probe. The cobra probe was traversed closer to the casing and had a finer traverse grid compared to the hotwire probe due to the complexity of the slanted hotwire mea-

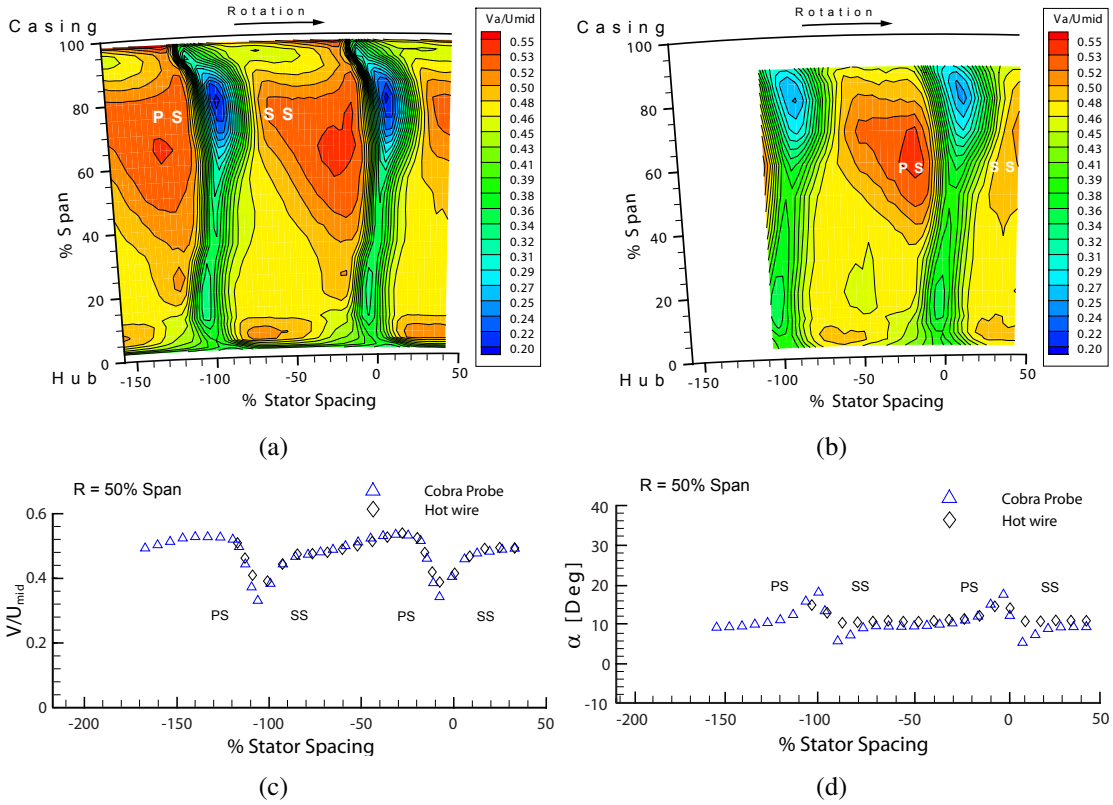

Figure 3.8: Comparison of measurement technique at exit of third-stage stator at peak efficiency: a) cobra probe, b) slanted hotwire probe, c) absolute velocity magnitude, d) absolute yaw angle.

surement technique. This causes slight differences in the mean contours between the two measurement techniques. A blade-to-blade comparison of the time-average V/U_{mid} and α measured by the slanted hotwire probe and cobra probe is shown in Figs. 3.8(c) and 3.8(d). This gives an added degree of confidence in the slanted hotwire measurement technique.

3.3.1.3 Boundary Layer Hotwire Measurements

Boundary layer traverses were performed using a Dantec 55P15 single wire boundary layer probe with a 5 μm diameter, 1 mm long tungsten element. The position of the first four axial traverse holes were situated at their optimum location on the cassette which produced a maximum non-normality of 5.5°. This gave rise to a bias error of less than 1% in both the measured displacement thickness, δ^* and momentum thickness, θ. Due to rotor four's leading edge, the fifth axial hole was not positioned in its optimal location. This resulted in an increase in the non-normality of the traverse to 14°. Due to the non-perpendicular movement of the probe the normal distance above the suction surface was calculated using the method of (Wheeler, 2007),

$$y = y' \cos \alpha \tag{3.14}$$

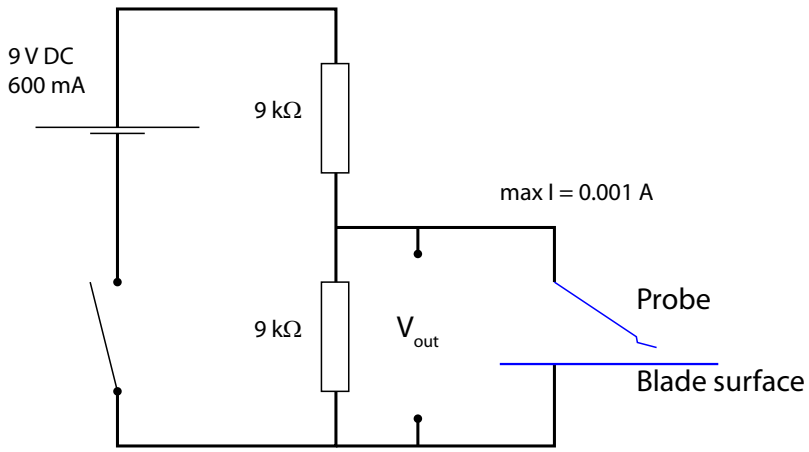

Figure 3.9: Circuit for setting the first point from the wall.

where α was the surface angle to the tangential direction at the measurement location and y' was the probe movement.

In the measurement region traversed at midspan and peak efficiency, the boundary layer thickness was typically between 0.5-3 mm, with a minimum of 10 points logged in the boundary layer. The location of the first measurement point above the surface was set during a run. A electrical circuit (Fig. 3.9) was constructed so that when the hotwire prongs came into contact with the blade surface the electrical connection was closed causing the stepper motor to stop. The distance of the wire from the wall was then estimated by to be half of the diameter of the hotwire prongs tip. In this way, the first point was estimated to be approximately 50 μm from the surface.

3.3.1.4 Calibration

Calibration of the hotwire probes described above were performed before and after each measurement run using a Dantec 55D90 calibration nozzle. Twenty calibration points encompassing the velocities to be measured, were used in the calibration. The pressure drop across the nozzle was evaluated using a Furness FS0510 micro-manometer connected to the data acquisition PC through a RS232 serial link. In addition the slanted hotwire was calibrated for yaw. A best-fit calibration for Kings law and k was then determined.

3.3.2 Cobra Probe

The rotating and stationary frame pressure measurements were not carried out be the author, but were made available through Dr. Herring. But the presentation of the data and the figures, as well as the interpretation of the results are due entirely to the author.

A three-hole cobra probe with 0.8 mm O.D. hypodermic was used to measure the two-

dimensional flow field. The cobra probes operate on the mechanism that an open ended tube facing into a flow will record a different pressure as its angle of incidence to the flow is varied. By calibrating the probe in a known flow over a specified yaw angle the differential pressures recorded can be related to the flow quantities. The probe was calibrated in a 8 inch low-speed wind tunnel for yaw angle ($\pm 40^\circ$), total pressure and static pressure. The probe coefficients were defined as,

$$\text{x ordinate} \qquad x = \frac{s_2 - s_1}{P_1 - 0.5(s_2 + s_3)} \tag{3.15}$$

$$\text{Total pressure coefficient} \qquad C_t = \frac{P_1 - P_0}{P_1 - 0.5(s_2 + s_3)} \tag{3.16}$$

$$\text{Static pressure coefficient} \qquad C_s = \frac{0.5(s_2 + s_3) - P}{P_1 - 0.5(s_2 + s_3)} \tag{3.17}$$

The probe was used to perform area traverses of the flow field at plane 8 and 9 (Tab. 3.3). Both the stationary and rotating traverses radial movement was from 2% to 98% annulus height and the circumferential extent was 5.3731° and 5.1817° respectively. The difference in the sector of the flow covered by the rotating traverses and stationary traverses were due to the relatively large backlash in the rotating traverse gear (2°). The stationary traverse matrix was 27x60 with clustering in the radial direction at the endwalls. The rotating traverses matrix was 27x38, again with clustering applied in the radial direction.

Radial profiles were derived by circumferentially area-averaging the measured quantities. The area traverse data was converted into static and total pressure coefficients given by,

$$C_{P_{0/s}} = \frac{P_{0/s} - P_{ref}}{0.5\rho U_{mid}^2} \tag{3.18}$$

where $P_{0/s}$ is either a total or static pressure, P_{ref} and ρ are the atmospheric pressure and density at inlet to the rig.

3.3.3 Surface Pressure Measurement

A line of static pressure tappings are located on the pressure and suction surface of three pairs of stator blades in the third-stage. A pair consisted of two adjacent blades so that the tappings on the pressure suction are located in the same passage. Conventional surface static tappings were used which consisted of 0.8 mm diameter holes drilled normal to the blade surface. The pressure tappings were connected to a Scani-valve and pressures were measured using a FS0510 Micro-manometer Furness with 20 kPa range. The Furness was connected to the data acquisition PC via an RS232 link.

The blades are instrumented at three heights 15, 50 and 95% annulus height. At each

Annulus height (%)	Tangential Chord (%)									No. of tappings
95	0.488	3.05	5.86	8.69	12.2	15.51	**19.29**	25.81	33.29	17
	41.68	50.88	60.79	69.53	76.77	84.2	89.85	95.56		
50	0.588	3.20	6.14	8.99	11.93	15.41	**19.41**	24.92	32.27	18
	40.53	50.97	60.90	69.93	77.77	84.25	89.21	92.55	95.93	
15	0.729	3.13	5.86	8.73	11.42	14.42	**17.73**	22.25	28.15	18
	35.57	45.82	60.41	71.85	82.27	87.52	91.48	94.12	96.76	

Table 3.4: Locations of stator suction surface static tappings.

Annulus height (%)	Tangential Chord (%)									No. of tappings
95	2.21	5.44	8.49	12.56	17.75	25.36	**34.49**	45.03	56.88	14
	67.62	76.73	83.82	88.62	93.49					
50	2.42	5.54	8.95	13.04	18.21	25.59	**34.41**	44.54	57.63	14
	70.32	81.99	88.06	91.85	94.82					
15	3.32	6.65	9.99	14.06	18.73	25.08	**35.81**	51.93	68.12	14
	79.11	85.52	89.76	92.78	95.78					

Table 3.5: Locations of stator pressure surface static tappings.

of these heights static pressure tappings are installed at the percentage tangential chord locations shown in Tabs. 3.4 and 3.5. Each of the instrumented stator blades has a single pressure tapping on the opposite surface to the measuring surface at the 7th tapping from the leading edge (shown in bold in Tabs 3.4 and 3.5). The isentropic Mach number was then calculated from the static pressure tappings using Eqn. 3.19.

$$M_{isen} = \sqrt{\left[\left(\frac{P_0}{P}\right)^{\frac{\gamma-1}{\gamma}} - 1\right]\left(\frac{2}{\gamma-1}\right)} \tag{3.19}$$

3.3.4 Flow Visualisation

Careful interpretation of patterns obtained from surface flow visualisation can give a reasonable description of the secondary flows generated by separation.

The principle of surface flow visualisation is to cover the surface of interest in a thin coat of oil-paint, the shear stress within the flow will carry the oil-paint with it and, in time, will establish a persistent pattern. Squire (1962) and then later Tobak and Peake (1979, 1982) concluded that the surface flow visualisation patterns should be interpreted as being representative of skin-friction lines.

In regions of separation, the streamwise pressure gradient strongly affects the oil-paint

flow be decelerating the flow, thickening the oil-paint film, and causing the oil-paint to accumulate. This flow pattern is characteristic of a two-dimensional separation line. If local reattachment occurs, the oil-paint accumulation will stop as the shear stress increases. Care must be taken interpreting the accumulation as a region of laminar separation and turbulent reattachment, since a similar pattern is formed through transition where the laminar skin-friction lines increase to the point where the turbulent shear stress removes the oil-paint film quicker. Finally regions of high shear stress can be identified as the oil-paint mixture is removed from the model surface altogether. The technique is described extensively in Squire (1962), Merzkirch (1974) and Barlow et al. (1999).

It is important in oil-paint work to ensure that a sufficient high velocity is obtained, otherwise gravity will cause the flow pattern on the blades to be meaningless. The following general procedure was used when performing the tests:

- First the surface was painted with a matt black finish. This increased the contrast between the models surface and the developed flow pattern.
- Oil-paint was mixed together in 5:1 by mass ratio (silicon:dye). The oil used was a silicon based solution (200/500 cs viscosity). Two different coloured dyes were used red and green. The dye had the useful property of fluorescing under ultraviolet (UV) light. The oil/dye was applied in a uniform manner using a paintbrush.
- The removable cassette was then inserted into the Cranfield rig, secured and the rig brought up to test conditions as rapidly as possible to the prevent the dye 'running'.
- The Cranfield rig was left at the chosen test point for approximately 80 minutes, to ensure the dye has dried.

The blade and endwall surface was painted in a different colour. This allowed information on fluid migration from the endwall up the blade surface to be captured. Interpretation of surface flow visualisation patterns can be very subjective, with a strong dependence on the quality of the patterns. In addition, surface flow visualisation methods have essentially zero-time response and thus give no information on the flow unsteadiness

3.3.5 Post-Processing of Unsteady Data

The ensemble average of a quantity x at a particular rotor phase or time t is given by

$$\tilde{x}(t) = \frac{1}{M}\sum_{i=1}^{M} = x_i(t) \tag{3.20}$$

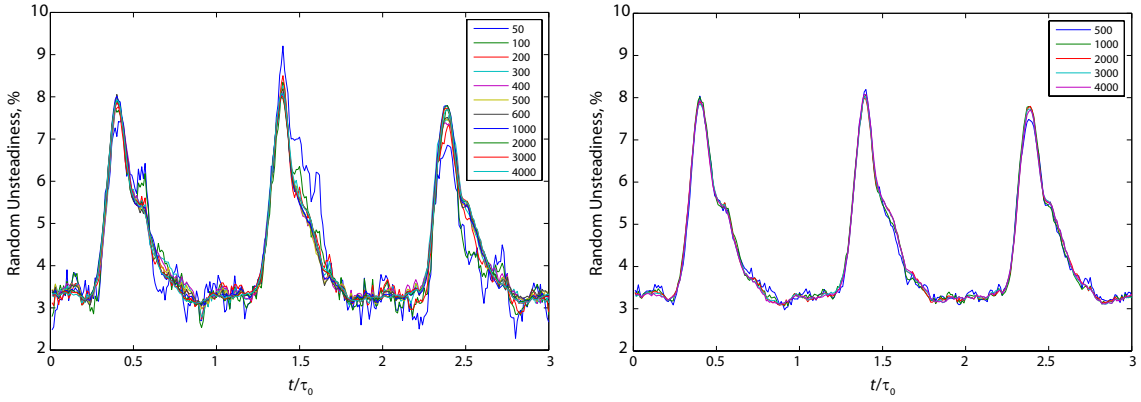

(a) (b)

Figure 3.10: Variation of free-stream random unsteadiness at rotor 3 exit plane, 50% span, $\phi = 0.450$: a) $M = 50 - 4000$, b) $M = 500 - 4000$.

where M is the number of ensembles. Initial analysis of the hotwire data showed significant variation of the time-average value with M. Values between 100-300 have been suggested in the literature. Gostelow (1977) stated that in practice the summation must take place over a significant number of ensembles. With the value of M depending on the signal-to-noise ratio of the raw data trace. In order to ensure that the sampled data was independent of ensemble size the hotwire was positioned downstream of rotor 3 (plane 8) at 50% span with the flow normal to the wire. Data was then sampled over three rotor blades for 4000 revolutions. Figure 3.10(a) illustrates the apparent variation of noise in the random unsteadiness with ensemble size. From this study the number of phase-locked time series acquired was chosen as 500. From Fig. 3.10(b) it is possible to see that the variation in the random unsteadiness for 500 ensembles has reached the critical value of $M \longrightarrow \infty$.

The ensemble standard-deviation or root-mean-square (rms) is given by

$$rms(t) = \sqrt{\frac{1}{M}\sum_{i=1}^{M}\left(x_i(t) - \tilde{x}(t)\right)^2} \tag{3.21}$$

The rms was used to provide the unsteady variation of the turbulence level.

The unsteady variation of the boundary layer parameters were calculated using the measured ensemble-average velocities from the boundary layer traverses discussed above. At each rotor phase the displacement thickness δ^* was,

$$\delta^* = \int_0^{\delta_{99}} \left(1 - \frac{V(y,t)}{V(\delta,t)}\right) dy \tag{3.22}$$

the momentum thickness θ was,

$$\theta = \int_0^{\delta_{99}} \frac{V(y,t)}{V(\delta,t)} \left(1 - \frac{V(y,t)}{V(\delta,t)}\right) dy \tag{3.23}$$

where δ_{99} is the boundary layer thickness at 0.99 of the boundary layer edge velocity.

The concept of intermittency, γ, is employed in order to describe the alternating characteristic of a transitional boundary layer. The method used for calculating the intermittency in this thesis is that by Walker and Wu (1991). Walker and Wu's method is based on a variable time averaging scheme with the RMS value of the longitudinal velocity fluctuations as the detector function.

$$S = \left(\frac{dV}{dt}\right)_{rms} \frac{\delta}{V_\infty^2} \tag{3.24}$$

Each flow record is divided into a number of short sub-intervals. The flow in a particular sub-interval is deemed turbulent when the detector function exceeds the threshold value. The intermittency is then obtained from the ratio of the number of turbulent sub-intervals to the total number of sub-intervals in the record.

The advantage of this method is that all signal processing, apart from the initial band-pass filtering of the raw data, is implemented by a PC. This allows a parametric study to be done on the parameters T, sub-interval time, and the level of the threshold.Following the results from Walker and Wu (1991) a value of $S = 0.15$ and $T = 0.002$ s was selected.

3.4 Numerical Methods

3.4.1 Computational Fluid Dynamics

The Navier-Stokes equations are a set of equations that completely describe the flow of Newtonian fluids. These equations establish that changes in momentum of the particles of a fluid are simply the product of changes in pressure and dissipative viscous forces (analogous to friction) acting inside the fluid.

The Navier-Stokes equations can only be solved analytically for the simplest of cases, i.e. pipe and parallel surfaces flows. Thus the task of obtaining good quality solutions to the governing equations of fluid mechanics, for practical engineering problems, represents one of the most challenging problems in engineering.

In general, the Navier-Stokes equations form a set of coupled, non-linear partial differential equations (Eqns. 3.25-3.29) which must be solved in an irregular domain subject to a set of initial and boundary conditions.

Computational Fluid Dynamics (CFD) is the analysis of systems of equations describing fluid flow and associated phenomena i.e. heat transfer, by means of a computer-based

simulation.

A key difficulty is that in reality fluid motion takes place in a continuum described by continuous differential equations. A computer can only handle a limited quantity of numbers (2 Mb stores 500,000 32 bit numbers, Dawes and Cant (2005)) and perform basic arithmetical operations. The function of CFD is therefore to construct an appropriate discrete representation of the continuum. This construction is governed by

- Physical behaviour of the continuum equations - conservation; the possible presence of real characteristics; whether the problem is initial value or boundary value
- Numerical behaviour of the discrete representation - accuracy; stability; false diffusion; false convection.

CFD codes are structured around the numerical algorithms that can tackle fluid flow problems. To enable the end users easy access to the solving power CFD software packages include user interfaces to input problem parameters and to examine results. A CFD code is made up of three main elements:

- a pre-processor
- a solver
- a post-processor

At the pre-processor stage the geometry is defined and the grid generated. Specification of the physical phenomena that need to be modelled, definition of fluid properties and specification of appropriate boundary conditions.

The solution to a flow problem, which consists in computing flow variables u, v, w, P and t being the typical combination, is defined at nodes inside each computational cell into which the flow domain is subdivided. The generation of the grid is a time consuming operation, over 50% of the time spent in industry on a CFD project is devoted to the definition of the domain geometry and grid generation (Versteeg and Malalasekera, 1995). In addition the assembly of computational meshes require care and knowledge from the part of the operator since the quality of the grid has a significant impact on the accuracy of the CFD solution.

Hirsch (1988) wrote that the accuracy of a numerical approximation is directly dependent on the size of the mesh, that is, the better the discretised space approaches the continuum, the better the approximation of the numerical scheme. In fact the accuracy of any CFD solution is governed by three kinds of systematic errors, (Ferziger and Peric, 2002):

- Modelling errors. These are the difference between the actual flow and the exact solution of the mathematical model.

- Discretisation errors. These are the difference between the exact solution of the algebraic system of equations obtained by discretising these equations.

- Iteration/convergence errors. These are the difference between the iterative and exact solution of the algebraic equations system.

There are three main methods of numerical solution techniques in terms of the discretisation approach employed: finite difference, finite elements and finite volume. Other methods like spectral schemes, boundary element methods, and cellular automata are used in CFD but their use is limited to special classes of problems, Ferziger and Peric (2002).

Independently of which one of these three numerical techniques is employed, the solution procedure involves the following steps

- selection of the appropriate mathematical model to characterise the flow (i.e. viscous versus inviscid).

- assembly of the computational grid subdividing the domain over which the solution is to be obtained.

- selection of the level of finite approximation to be used in the process of discretisation of the partial differential equations that describe the flow.

- solution of the algebraic equations that are the discrete counterpart of the continuous partial differential equations subject to previously specified convergence criteria.

The main differences between the three separate discretisation approaches are associated with the way in which the flow variables are approximated and with the processes employed in the discretisation of the flow domain.

Finite difference methods describe the unknowns, ϕ, of the flow problem by means of point samples at the node of a grid. Finite Element Methods use simple piecewise functions (e.g. linear or quadratic) valid on elements to describe the local variations of unknown flow variables. Finite Volume methods rely on the subdivision of the domain into a collection of adjoining control volumes over which the conservation equations are applied. Finite Volume methods are the most widely used of the discretisation approaches with most of the commercial CFD solvers employing this technique.

The numerical algorithms of a Finite Volume formulation consists of the following steps:

- Formal integration of the governing equations of fluid flow over each of the (finite) control volumes that fill the flow solution domain.
- The algebraic equations for each control volume are obtained through the approximation of surface and volume integrals. This step involves substitution of a variety of finite-difference-type approximations for the terms in the integrated equations representing flow processes such as convection, diffusion and sources. The process converts the integral equations into a system of algebraic equations.
- Solution of the algebraic equations by an iterative method.

The first step, the control volume integration, distinguishes the Finite Volume method from all other CFD techniques. The resulting statements express the (exact) conservation of relevant properties for each control volume. This clear relationship between the numerical algorithm and the underlying physical conservation principle forms one of the main attractions of the Finite Volume methods and makes its concepts simpler to understand by engineers than Finite Element. The conservation of a general flow variable ϕ with a Finite Control volume can be expressed as a balance between the various processes tending to increase or decrease it.

CFD codes make use of discretisation techniques suitable for the treatment of the key transport phenomena, convection (fluxes due to the flow of the fluid) and diffusion (fluxes due to molecular motion) as well as for the source terms (associated with the creation or destruction of the flow variable) and the rate of change with respect to time.

Since the analogous physical phenomena are complex and non-linear an iterative solution is required. Finally the solutions from the CFD codes can be examined qualitatively and quantitatively through the use of the post-processor software. In the post-processor stage the domain and grid can be displayed, vector plots and contour plots can be constructed and numerical data extracted for treatment by other numerical methods, i.e. acoustic codes etc.

3.4.2 The Governing Equations

The task of obtaining solutions to the governing equations of fluid mechanics represents one of the most challenging problems in engineering and science. In general, these equations form a set of coupled, non-linear partial differential equations which must be solved in an irregular domain subject to a set of initial and boundary conditions.

All computational fluid dynamics is based on the fundamental governing equations of fluid dynamics - the continuity, the momentum and the energy equations which are the mathematical statements of three fundamental physical principles upon which all of fluid dynamics is based:

- Conservation of mass
- Newton's second law
- Conservation of energy

The equations governing all fluid flows in turbomachinery are the unsteady Navier-Stokes and neglecting viscid effects the Euler equations. The exact derivations of these equations is beyond the scope of this PhD thesis and so only the Navier-Stokes equations are shown here in the conservative form for completeness.

$$\frac{\partial \rho}{\partial t} + div(\rho \mathbf{u}) = 0 \tag{3.25}$$

$$\frac{\partial \rho u}{\partial t} + div(\rho u \mathbf{u}) = -\frac{\partial P}{\partial x} + div(\mu \ grad \ u) + S_x \tag{3.26}$$

$$\frac{\partial \rho v}{\partial t} + div(\rho v \mathbf{u}) = -\frac{\partial P}{\partial y} + div(\mu \ grad \ v) + S_y \tag{3.27}$$

$$\frac{\partial \rho w}{\partial t} + div(\rho w \mathbf{u}) = -\frac{\partial P}{\partial z} + div(\mu \ grad \ w) + S_z \tag{3.28}$$

$$\frac{\partial (\rho i)}{\partial t} + div(\rho i \mathbf{u}) = -P \ div \ \mathbf{u} + div(k \ grad \ T) + \Phi + S_i \tag{3.29}$$

In addition to the above equations the Equation of state is also required. The continuity equation Eqn. 3.25 simply states that the rate of change of mass within a control volume equals the rate of mass influx. Equations 3.26, 3.27 and 3.26 are the momentum equations for three dimensional flows which state that the rate of change of momentum within the element is equal to the rate at which momentum is entering the element through its surface plus the sum of the forces along the element due to the normal and tangential stresses acting on its surface.

In order to obtain results which can be periodic in time but not random, the high frequency random fluctuations in all flow properties are usually removed by averaging the equations over a period of time which is large compared to the time scales of the turbulence but still short enough to leave the possibility of periodic flows due to phenomena such as blade passing. When this is done the 'Reynolds averaged Navier-Stokes equations are obtained. These conceptually are exactly the same as the Navier-Stokes equations but include extra viscous stresses and heat flux due to transfer of momentum and energy by the random turbulent motion. Note the average continuity equation does not contain any such additional terms.

3.4.2.1 Differential and Integral Forms of the General Transport Equations

It is clear from Eqns. 3.25-3.29 that there are significant commonalities between the various equations. By introducing a general variable ϕ the conservative form of all fluid flow equations can be written in the following form:

$$\frac{\partial(\rho\phi)}{\partial t} + div(\rho\phi\mathbf{u}) = div(\Gamma\ grad\ \phi) + S_\phi \tag{3.30}$$

Equation 3.30 is the so-called transport equation for property ϕ. It clearly highlights the various transport processes: the **rate of change** term and the **convective** term on the left hand side and the **diffusive** term (Γ = diffusion coefficient) and the **source** term respectively on the right hand side. In order to bring out the common terms that are not shared between the equations, they have been grouped in the source terms.

Equation 3.30 is used as the starting point for computational procedures in the finite volume method. By setting ϕ equal to 1, u, v, w and i and selecting appropriate values for the diffusion coefficient Γ and source terms we obtain special forms of Eqns. 3.25-3.29. The key step of the finite volume method is the integration of Eqn. 3.30 over a three-dimensional control volume CV yielding,

$$\int_{CV} \frac{\partial(\rho\phi)}{\partial t}\, dV + \int_{CV} div(\rho\phi\mathbf{u})\, dV = \int_{CV} div(\Gamma\ grad\ \phi)\, dV + \int_{CV} S_\phi\, dV \tag{3.31}$$

The volume integrals in the second term on the left hand side, the convective term, and in the first term on the right hand side, the diffusive term, are re-written as integrals over the entire bounding surface of the control volume by applying Gauss' divergence theorem. For a vector $\mathbf{a}$ this theorem states,

$$\int_{CV} div\,\mathbf{a}\, dV = \int_A \mathbf{n}\cdot\mathbf{a}\, dA \tag{3.32}$$

The physical interpretation of $\mathbf{n}\cdot\mathbf{a}$ is the component of vector $\mathbf{a}$ in the direction of the vector $\mathbf{n}$ normal to surface element dA. Thus the integral of the divergence of $\mathbf{a}$ over a volume is equal to the component of $\mathbf{a}$ in the direction normal to the surface which bounds the volume summed (integrated) over the entire bounding surface A. Applying Gauss' divergence theorem, Eqn. 3.31 can be written as follows:

$$\frac{\partial}{\partial t}\left(\int_{CV} \rho\phi\, dV\right) + \int_A \mathbf{n}\cdot(\rho\phi\mathbf{u})\, dA = \int_A \mathbf{n}\cdot(\Gamma\ grad\ \phi)\, dA + \int_{CV} S_\phi\, dV \tag{3.33}$$

The first term on the left hand side is the rate of change of the total amount of fluid property ϕ in the control volume. The second term on the left hand side , the convective term, is the

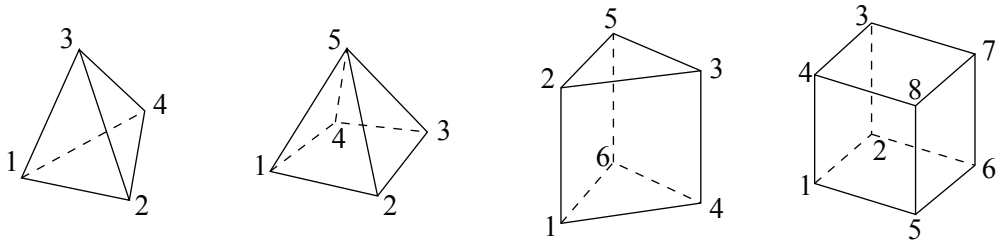

Figure 3.11: ANSYS-CFX element types.

net rate of decrease of fluid property ϕ of the fluid element due to convection across the faces of the volume. The first term on the right hand side, the diffusive term, represents the net rate of increase of fluid property ϕ of the fluid element due to diffusion. The final term on the right hand side of this equation gives the rate of increase of property ϕ as a result of sources inside the fluid element.

3.4.3 ANSYS-CFX

All the numerical computations in this thesis were performed using the commercial CFD code CFX. Several versions were employed starting with AEA CFX5.7 and concluding with ANSYS-CFX10. The CFX solver supports arbitrary mesh topologies, including hexahedral, tetrahedral, prism, and pyramid elements (Fig. 3.11) It uses a hybrid finite element/finite volume approach to discretise the Navier-Stokes equations. As a Finite Volume method, it satisfies strict global conservation by enforcing local conservation by enforcing local conservation over control volumes which are constructed around each mesh vertex or node. The finite element methodology is used to describe the solution variation (needed for various surface fluxes and source terms) with each element.

3.4.4 Discretisation

As mention earlier, numerical solutions require that the continuous equations are replaced by their discrete counterparts which are then evaluated at discrete locations in space and time

The formulation of the finite volume method by ANSYS-CFX involves the assembly of a control volume around each of the grid's nodes. The conservation principles derived for infinitely small volumes are expanded through integration to apply for finitely sized volumes (Patankar, 1980) which surround each grid node. Interpolation functions are then used to evaluate the gradients of variables between general convection and diffusion equation for a scalar ϕ, in the absence of sources, can be given as (Versteeg and Malalasekera,

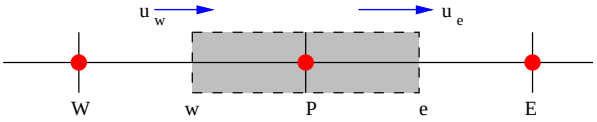

Figure 3.12: A control volume around node P (Versteeg and Malalasekera, 1995).

1995; Patankar, 1980):

$$\frac{d}{dx}(\rho u\phi) = \frac{d}{dx}\left(\Gamma\frac{d\phi}{dx}\right) \tag{3.34}$$

The flow must also satisfy continuity so,

$$\frac{d(\rho u)}{dx} = 0 \tag{3.35}$$

Figure 3.12 shows a one-dimensional control volume. Integration of the transport equation (Eqn. 3.34) over the control volume gives,

$$(\rho uA\phi)_e - (\rho uA\phi)_w = \left(\Gamma A\frac{\partial\phi}{\partial x}\right)_e - \left(\Gamma A\frac{\partial\phi}{\partial x}\right)_w \tag{3.36}$$

Integration of the continuity equation (3.35) yields,

$$(\rho uA\phi)_e - (\rho uA\phi)_w = 0 \tag{3.37}$$

The terms on the left hand side of Eqns. 3.36 and 3.37 are convection driven and the terms on the right of Eqn. 3.36 are diffusion driven. To obtain the discretised equations, evaluation of the scalar, ϕ, at the cell faces e, w are required, in addition to the calculation of the gradients of ϕ in the diffusion terms are required.

ANSYS-CFX evaluates the derivatives for all the diffusion terms using a standard finite element approach of shape functions. The solution fields are stored at the mesh nodes, but, various terms in the discretised equations require solution gradients to be evaluated at integration points on face boundaries. This is achieved with finite element shape functions (Eqn. 3.38).

$$\left.\frac{\partial\phi}{\partial x}\right|_e = \sum_n \left.\frac{\partial N_n}{\partial x}\right|_e \phi_n \tag{3.38}$$

The summation is over all the shape functions for the element. For the convection terms, the variable ϕ_e must be related to the nodal values of ϕ. The convection schemes implemented in ANSYS-CFX can be cast in the form

$$\phi_e = \phi_p + \beta\nabla\phi\cdot\Delta\vec{r} \tag{3.39}$$

where $\vec{r}$ is the vector from the upwind node to the integration point. When using the

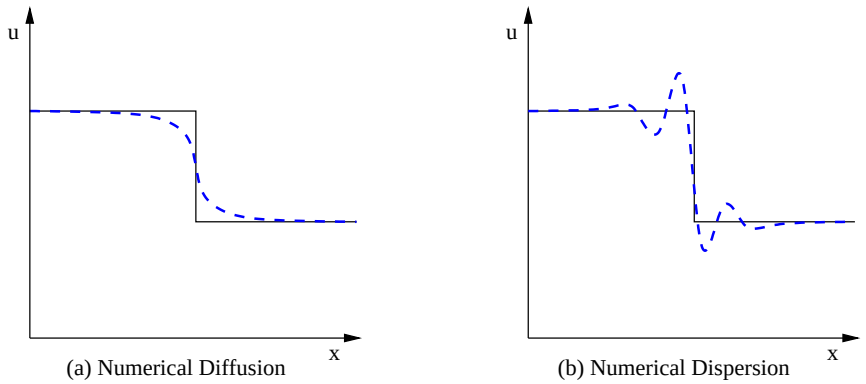

(a) Numerical Diffusion (b) Numerical Dispersion

Figure 3.13: Effect of numerical errors. Solid line - initial wave at time $t = 0$. Dashed line - shape of the wave at some time $t > 0$ from the numerical solution as affected by numerical dissipation (a) or dispersion (b).

specified blend, $\nabla\phi$ is the average of the adjacent nodal gradients and when using high resolution scheme $\nabla\phi$ is the nodal gradient of the upwind node (ANSYS, 2005). Particular choices for β give rise to different schemes of various robustness and accuracy. The available schemes in ANSYS-CFX are:

- Upwind differencing
- Numerical advection correction (specify blend)
- High resolution
- Central Difference

The upwind difference scheme (UDS), resulting from β=0, calculates ϕ_e=ϕ_p for positive flow direction and ϕ_w=ϕ_p for reverse direction. UDS is robust (numerically stable) and does not introduce non-physical overshoots and undershoots. However, first order UDS are very inaccurate; their truncation error has the effect of a false diffusion (Ferziger and Peric (2002) Fig. 3.13(a)).

By choosing a value for β between 0 and 1, the diffusive properties of UDS are reduced. The quantity $\beta\nabla\phi\cdot\Delta\vec{r}$, called the Numerical Advection Correction, may be viewed as an anti-diffusive flux added to the upwind scheme. The choice β=1 is formally second order accurate. The disadvantages of these schemes are that they may be less robust than UDS and they may display non-physical overshoots and undershoots in the solution (Fig. 3.13(b)).

The High Resolution Scheme computes β locally to be as close to 1 as possible without violating boundedness principles. The recipe for β is based on that of Barth and Jesperson (1989). The high resolution scheme is therefore both accurate (reducing to first order near discontinuities and in the free stream where the solution has little variation) and bounded.

The central difference scheme in ANSYS-CFX evaluates ϕ_p using a trilinear shape functions. Although the central difference scheme is second-order accurate, it may suffer from serious decoupling issues, and is appropriate only for Large Eddy Simulations (LES) (ANSYS, 2005).

3.4.5 Pressure velocity coupling

The non-linear and inter-linked nature of the fluid flow equations means that an iterative solution method is used. The main difficulty in the calculation of the velocity field lies in the unknown pressure field. The pressure gradient forms a part of the source term for a momentum equation, but there is no obvious equation for obtaining pressure. In addition the pressure field is indirectly specified via the continuity equation.

If the flow is compressible the continuity equation may be used as a transport equation for density and, in addition to the momentum equations, the energy equation is a transport for temperature. The equation of state, p=$p(\rho, T)$, may then be used to obtain the pressure. Here a time marching approach is usually adopted. But for incompressible flow the density is constant and as such is not linked to pressure. In this case coupling between pressure and velocity introduces a constraint on the solution of the flow field. If the correct pressure field is applied in the momentum equations the resulting velocity field should satisfy continuity.

For incompressible flows the pressure correction technique has found widespread application (Anderson, 1995) and is described in detail in most text books on CFD (Patankar, 1980; Anderson, 1995; Versteeg and Malalasekera, 1995).

If the velocities and scalar variables such as pressure, temperature, etc. are both defined at the nodes of an ordinary control volume a highly non-uniform pressure field can act like a uniform field in the discretised momentum equations. This problem does not occur for UDS and compressible flows. In compressible flows the inclusion of the density variation in the continuity equation would generally wipe out the checkerboard pattern after the first time step (Anderson, 1995). A staggard grid approach, Fig. 3.14 can be used to overcome this problem, where scalar variables are evaluated at ordinary nodal points and velocity components are calculated on staggard grids centred around the cells faces.

This staggering of the velocity components is of huge benefit on structured meshes but the method does not extend easily to unstructured meshes. As a consequence a method is required which uses collocated grids to calculate values of the velocity components, on a face, which do not suffer from the checkerboard effects. The Rhie - Chow interpolation method (Rhie and Chow, 1982) offers one approach which satisfies these requirements. ANSYS-CFX uses a method similar to that of Rhie - Chow (ANSYS, 2005) to overcome the problem when variables are collocated.

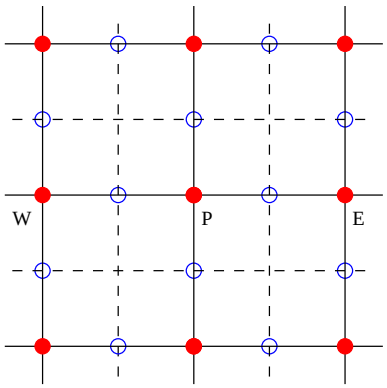

Figure 3.14: Staggard computational grid. P points, solid circles; u, v open circles.

3.4.6 The Coupled System of Equations

The linear set of equations that arise by applying the finite volume method to all elements in the domain are discrete conservation equations. The system of equations can be written in the form,

$$A_P \phi_P + \sum_l A_l \phi_l = Q_P \tag{3.40}$$

where P denotes the node at which the partial differential equation is approximated and index l runs over the neighbour nodes involved. A_l is the coefficients of the equation and Q_P contains all the terms which do no contain unknown variables. The node may have any number of such neighbours, so that the method is equally applicable to both structured and unstructured meshes. The set of these for all finite volumes constitutes the whole linear equation system.

It is at the equation level that coupling in question is returned and at no point are any of the rows of the matrix treated any differently (e.g. different solution algorithms for momentum versus mass). The advantage of such a coupled treatment over a non-coupled or segregated approach are several; robustness, efficiency, generality and simplicity.

3.4.6.1 Solution Strategy - The Coupled Solver

Segregated solvers employ a solution strategy where the momentum equations are first solved, using a guessed pressure, and an equation for a pressure correction is obtained. Because of the 'guess-and-correct' nature of the linear system, a large number of iterations are typically required in addition to the need for selecting relaxation parameters for the variables.

ANSYS-CFX uses a coupled solver, which solves the hydrodynamic equations (for u, v, w, P) as a single system. This solution approach uses a fully implicit discretisation of the equations at any given time step. For steady state problems the time step behaves like an

'acceleration parameter', to guide the approximate solutions in a physically based manner to a steady state solution. This reduces the number of iterations required for convergence to a steady state, or to calculate the solutions for each time step in a time dependent analysis.

3.4.6.2 Linear Equation Solution

ANSYS-CFX uses a Multigrid (MG) accelerated Incomplete Lower Upper (ILU) factorisation technique for solving the discrete system of linearised equations (ANSYS, 2005). It is an iterative solver whereby the exact solution of the equations is approached during the course of several iterations. The linearised system of discrete equations described above can be written in the general matrix form

$$A\phi = \mathbf{Q} \tag{3.41}$$

where A is the coefficient matrix, ϕ is a vector (or column matrix) containing the variable values at the grid nodes, and $\mathbf{Q}$ is the vector containing the terms on the right-hand side of Eqn. 3.40. The above equations are solved by an iterative technique that involves guessing a solution. After n iterations we have an approximate solution ϕ^n which does not satisfy these equations exactly. Instead, there is a non-zero residual r^n:

$$A\phi^n = \mathbf{Q} - r^n.$$

A relation between the iteration error can be defined by:

$$\varepsilon^n = \phi - \phi^n,$$

where ϕ is the converged solution, and the residual:

$$A\varepsilon^n = r^n.$$

The above process is repeated until a converged result is obtained. Iterative solvers such as ILU tend to rapidly decrease in performance as the number of computational mesh element increases (ANSYS, 2005). Performance also tends to rapidly decrease if there are large element aspect ratios present. The performance of the solver can be greatly improved by employing a technique called 'multigrid'.

3.4.7 Algebraic Multigrid

Most iterative solvers converge more slowly on finer grids. This behaviour is related to the fact that information travels only one grid per iteration. For a converged solution,

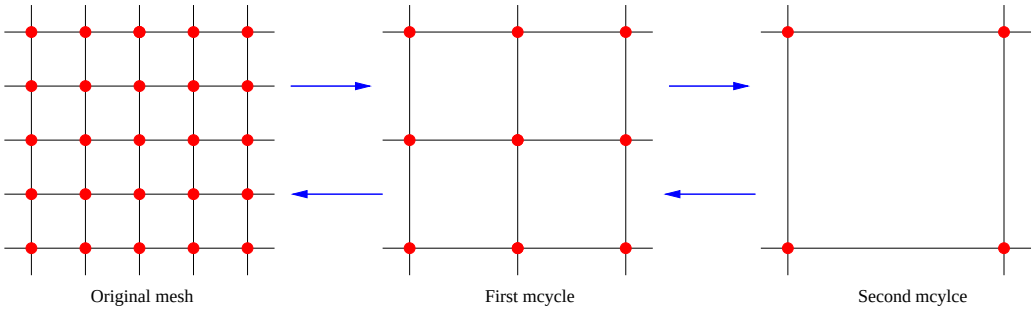

Figure 3.15: Three level multigrid.

information needs to travel back and forth through the domain many times (Ferziger and Peric, 2002). The convergence of these solvers can be enhanced by the use of a multigrid method. The use of a multigrid scheme bypasses this problem by using a series of coarse meshes such that the longer wavelength errors appear as shorter wavelength errors relative to the mesh spacing (Fig. 3.15). To prevent the need to mesh the geometry using a series of different mesh spacing, ANSYS-CFX uses an algebraic multigrid scheme. Algebraic multigrids form a system of discrete equation for a coarse mesh by summing the fine mesh equations. This results in the virtual coarsening of the mesh spacing during the course of the iterations, followed by refining of the mesh to obtain an accurate solution (ANSYS, 2005).

3.4.8 Turbulence Modelling

Most flows of engineering significance are turbulent. Turbulence consists of chaotic fluctuations in the flow field in time and space. It is a complex, three dimensional, unsteady process and can have a significant effect on the characteristics of the flow. Turbulence occurs when the inertia forces in the fluid become significant compared to viscous forces, and this situation is characterised by a high Reynolds number.

A typical flow domain of 0.1 m by 0.1 m with a high Reynolds number can contain eddies down to 10-100 μm size. To describe spatially processes at all length scales would require computing meshes of 10^9 up to 10^{12} points. The fastest events take place with a frequency on the order of 10 kHz. This would need to be discretised in time, in steps of about 100 μs (Versteeg and Malalasekera, 1995). The exact computation of these flows, as is done by the Direct Numerical Simulations (DNS) approach, would require computing power which is many orders of magnitude higher than available in foreseeable future (Speziale, 1991).

Engineers need computational procedures which can supply information about the turbulent processes, but which avoid the need to predict the effects of each and every eddy in the flow. Looking at time scales much larger than the time scales of turbulent eddies, tur-

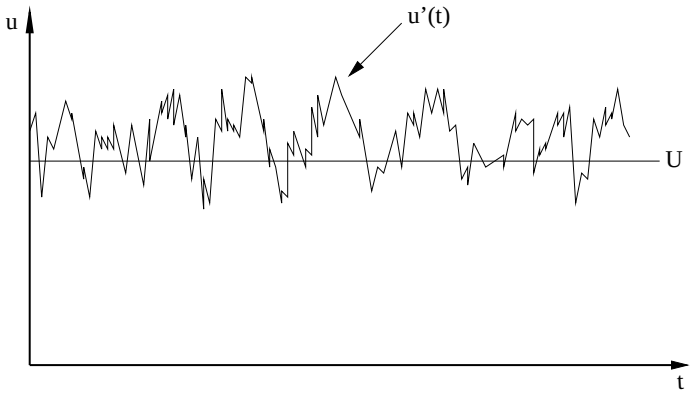

Figure 3.16: Typical point velocity measurement in turbulent flow.

bulent flow can be said to exhibit average characteristics, with an additional time-varying, fluctuating component (Fig. 3.16). The small scale turbulent fluctuations can be removed through time-averaging of the governing flow equations so that the bulk flow equations are solved and the effects of the turbulent fluctuations are modelled. This results in the Reynolds Averaged Navier-Stokes equations, RANS:

$$\frac{\partial u}{\partial t} + div(u\mathbf{u}) = -\frac{1}{\rho}\frac{\partial P}{\partial x} + \mu\, div\ grad\ u + \left[-\frac{\partial \overline{u'^2}}{\partial x} - \frac{\partial \overline{u'v'}}{\partial y} - \frac{\partial \overline{u'w'}}{\partial z}\right] \tag{3.42}$$

$$\frac{\partial v}{\partial t} + div(v\mathbf{u}) = -\frac{1}{\rho}\frac{\partial P}{\partial y} + \mu\, div\ grad\ v + \left[-\frac{\partial \overline{u'v'}}{\partial x} - \frac{\partial \overline{v'^2}}{\partial y} - \frac{\partial \overline{v'w'}}{\partial z}\right] \tag{3.43}$$

$$\frac{\partial w}{\partial t} + div(w\mathbf{u}) = -\frac{1}{\rho}\frac{\partial P}{\partial z} + \mu\, div\ grad\ w + \left[-\frac{\partial \overline{u'w'}}{\partial x} - \frac{\partial \overline{v'w'}}{\partial y} - \frac{\partial \overline{w'^2}}{\partial z}\right] \tag{3.44}$$

The Reynolds Averaged form of the Navier-Stokes equations contain new terms which have the form of stresses and are known as Reynolds stresses. They can be viewed as stresses that result from the small scale turbulent fluctuations which are responsible for the dissipation of the energy of the flow (Coldrick, 2003).

The complexity of turbulence precludes simple formulae for the extra stresses and turbulent scalar transport terms. To enable the effects of turbulence to be predicted, a large amount of CFD research has been concentrated on methods which make use of turbulence models. Turbulence models have been specifically developed to account for the effects of turbulence without recourse to a prohibitively fine mesh and DNS.

The Reynolds stresses need to be modelled by additional equations of known quantities in order to achieve 'closure'. Closure implies that there are a sufficient number of equations for all unknowns, including the Reynolds-Stress tensor resulting from averaging procedure.

Classical models	Based on (time-averaged) Reynolds equations
	1) zero equation model - mixing length model
	2) two equation model - k-ε
	3) Reynolds stress model
	4) algebraic stress model
LES	Based on space filtered equations

Table 3.6: Types of turbulence models (Versteeg and Malalasekera, 1995).

The equations used to close the system define the type of turbulence model (ANSYS, 2005). The most common turbulence models are classified in Tab. 3.6.

The classical models use the time-averaged Reynolds equation. The large eddy simulations are turbulence models where the time-dependent flow equations are solved for the mean flow and the largest eddies and where the effects of the smaller eddies are modelled.

3.4.8.1 Eddy Viscosity Model

One method to calculate the values of Reynolds stress is based on the premise that turbulence consists of small eddies which are continuously forming and dissipating and that the Reynolds stresses are proportional to mean velocity gradient. This is known as the Bousinessq eddy-viscosity model (Bradshaw, 1978). Eddy-viscosity models are based on the assumption that there exists an analogy between the action of viscous stresses and Reynolds stresses on the mean flow. In this sense, the extra stress terms are treated as extra viscous stresses (Shaw, 1992), the viscosity is then enhanced by an additional viscosity; $\mu_{eff} = \mu + \mu_t$.

The underlying assumption for the Boussinesq models is that the turbulent viscosity μ_t is isotropic, in other words that the ratio between Reynolds stress and mean rate of deformation is the same in all directions. This has the advantage that the numerical effort required for the solution of the model is moderate. In addition, eddy-viscosity models are numerically robust (Menter et al., 2004a).

All turbulence models that use the eddy-viscosity assumption have the same basis, the difference lies in the way that the turbulent viscosity is calculated. Mixing length models attempt to describe the Reynolds stresses by means of simple algebraic formulae for μ_t as a function of position.

The two equation models are more sophisticated and general, but also more costly than the zero equation models, and include a description of turbulence which allows for the effects of transport of turbulence properties by mean flow and diffusion and for the

production and destruction of turbulence. In two equation turbulence models, such as the k-ε and k-ω models, a transport equation is solved for each of the two properties, in order to compute the turbulent velocity and turbulent length scale. The turbulence velocity is extracted from the solution of the turbulent kinetic energy transport equation. The turbulent length scale is computed from two properties of the fluid, usually the turbulent kinetic energy, k, and the dissipation rate, ε or the specific dissipation, ω. The turbulent viscosity scale is modelled as the product of a turbulent velocity and turbulent length scale.

The k-ε model has become the industry standard two-equation turbulence model essentially due to the capability of the model of predicting, for a reasonable computational cost, a wide range of flows with minimal adjustment of its empirical coefficients. Nevertheless models based on the k-ε formulation present a number of well documented limitations, Mohammadi and Pironneau (1994):

- failure to account for rotational strain or shear
- under adverse pressure gradients the model significantly over predicts the shear stress levels and delays, or even completely prevents, separation
- excessively dissipative nature of the model with over prediction of the turbulent viscosity in recirculating flows leading to undue damping out of vortices
- under prediction of flow separation past steps and obstacles
- standard model applicable only for high turbulent Reynolds numbers

The main advantage of the k-ω formulation is the near wall treatment for low-Reynolds number computations. The low-Reynolds formulation of k-ε model requires complex non-linear damping functions and requires a near wall resolution of $y^+ < 0.2$. The k-ω model does not require these damping functions and requires a near wall resolution of $y^+ < 2$ (ANSYS, 2005) which makes the model more accurate and robust.

The k-ω model of Wilcox (1988) relates the turbulent viscosity to the turbulent kinetic energy and turbulent frequency via:

$$\mu_t = \rho \frac{k}{\omega} \tag{3.45}$$

The original form of Wilcox's k-ω model suffered from a strong sensitivity to free-stream conditions (Menter, 1992). The value of ω specified at the inlet, had a significant influence on the result. This is obviously an undesirable behaviour of the turbulence. Menter (1994) developed a blending function between the k-ω model near solid surfaces and the k-ε model in the free-stream. The Wilcox model is thereby multiplied by a blending function F_1 and the k-ε model by the function $1-\mathrm{F}_1$. F_1 is equal to one near the surface

and switches to zero outside the boundary layer (i.e. a function of the wall distance). The result of this limiter is the k-ω Baseline (BSL) model.

The BSL model combines the advantages of the Wilcox and the k-ε model, but still fails to properly predict the onset and amount of flow separation from smooth surfaces (ANSYS, 2005). It is known that two-equation models will not provide the correct response to adverse pressure gradients unless the transport of the principal turbulent shear-stress is taken into account. This results in an over-prediction of the eddy-viscosity (Menter, 1994).

The aim of the k-ω Shear Stress Transport (SST) model of Menter (1994) is to overcome the failure to properly predict separation by accounting for the transport of turbulent shear-stress. The SST model modifies the eddy-viscosity to account for transport of the principal turbulent shear-stress through the use of a limiter on the eddy-viscosity:

$$\nu_t = \frac{a_1, k}{\max(a_1, \omega, S\mathrm{F}_2)} \tag{3.46}$$

where

$$\nu_t = \mu_t / \rho \tag{3.47}$$

F_2 is a blending function similar to F_1, which restricts the limiter to the wall boundary layer, as the underlying assumptions are not correct for free shear flows. S is an invariant measure of the strain rate.

The k-ω SST model in ANSYS-CFX has automatic wall treatment. A low-Reynolds number model that treats the viscous sublayer is used if the grid near the wall is fine, and a wall function is used beyond it (Grotjans and Menter, 1998).

3.4.8.2 Transition Modelling

It should be noted that although a great deal has been learnt from simple flows there is no comprehensive theory of transition (Chapter 2). Recent advances in supercomputer technology have made it possible to simulate the events leading up to transition, including turbulent spot formation, by solving the complete, time-dependent Navier-Stokes equations at modest Reynolds numbers for a number of very simple geometries.

At low Reynolds numbers, transition can play a dominant role. Low-Reynolds number turbulence models, where the wall damping functions of the underlying turbulence model trigger transition onset, can produce transition like-phenomena. However, the predictive capability of such formulations is low (Savill, 1993b,a; Suzen et al., 2003) and industrial designers do not typically rely on this option, instead preferring to use correlation-based formulations (Menter et al., 2004b). This is not surprising, as the ability of a low-Reynolds model to predict transition seems coincidental. There is no reason, why damping functions, which were optimised to damp the turbulence in the viscous sublayer, should predict an

entirely different physical process.

The location of the onset and extent of transition are of major importance in turbomachinery design applications, where the wall shear-stress or wall heat transfer are of interest. In addition, blockage and loss, which are important criteria for assessing turbomachinery performance, are strongly affected by transition. Matters are further complicated by the fact that a number of fundamentally different transition mechanisms can be found in turbomachinery flows, including bypass transition, separation-induced transition, wake-induced transition and shock-induced transition (Menter et al., 2004a).

The implementation of a transition model in ANSYS-CFX is based on experimental correlations which relate the turbulence intensity to the free-stream to the momentum thickness Reynolds number at transition onset. The model uses a locally formulated transport equation for intermittency, γ, which is used to turn on the production of the turbulent kinetic energy downstream of transition point. In addition to the transport equation for intermittency a second transport equation is solved for the transition onset momentum thickness Reynolds number, $\widetilde{\mathrm{Re}}_{\theta t}$. Solving the transport equation for $\widetilde{\mathrm{Re}}_{\theta t}$ captures the non-local influence of the free-stream turbulence intensity which changes due to decay of the turbulent kinetic energy in the free-stream and pressure gradient influence at the boundary layer edge (Menter et al., 2004b; Langtry et al., 2004; Langtry and Menter, 2005).

The transport equation for intermittency is defined as

$$\frac{\partial \rho \gamma}{\partial t} + div\left(\rho \gamma \mathbf{u}\right) = div\left[\left(\mu + \frac{\mu_t}{\sigma_f}\right) \; grad\; \gamma\right] + P_{\gamma 1} - E_{\gamma 1} + P_{\gamma 2} - E_{\gamma 2} \tag{3.48}$$

where $P_{\gamma 1}$ and $E_{\gamma 1}$ are the transition source terms and $P_{\gamma 2}$ and $E_{\gamma 2}$ are the destruction / relaminarisation source terms. The transition onset term that appears in $P_{\gamma 1}$ is formulated as a function of vorticity Reynolds number, which is related to the critical momentum thickness Reynolds number by

$$F_{onset_1} = \frac{\mathrm{Re}_v}{2.193 \mathrm{Re}_{\theta_{\mathrm{crit}}}} \tag{3.49}$$

The critical Reynolds number initiates the growth of intermittency in the boundary layer. The critical Reynolds occurs upstream of the transition Reynolds number. The correlation between critical Reynolds number and the transported onset transition momentum thickness Reynolds number was determined based on a series of numerical experiments on a flat plate (Menter et al., 2004b). The parameter F_{length} is an empirical correlation that controls the length of the transition region. It is based on numerical experimentation whereby a series of flat plate experiments where reproduced and curve fitted to provide a correlation for the transition length.

The second transport equation, transition onset Reynolds number, is defined as

$$\frac{\partial \rho \widetilde{\mathrm{Re}}_{\theta t}}{\partial t} + div\left(\rho \widetilde{\mathrm{Re}}_{\theta t}\mathbf{u}\right) = div\left[\sigma_{\theta t}\left(\mu + \mu_t\right)\ grad\ \widetilde{\mathrm{Re}}_{\theta t}\right] + P_{\theta t} \tag{3.50}$$

The source term $P_{\theta t}$ is designed to force the transport scalar $\widetilde{\mathrm{Re}}_{\theta t}$ to match the local value of $\mathrm{Re}_{\theta t}$ calculated from empirical correlation outside the boundary layer and then allow the free-stream value to diffuse into the boundary layer. The empirical correlation is a function of turbulence intensity, pressure gradient and acceleration (Langtry et al., 2004).

$$\mathrm{Re}_{\theta t} = 803.73\left(Tu + 0.6067\right)^{-1.027} F(\lambda_\theta, K) \tag{3.51}$$

for adverse pressure gradients $F(\lambda_\theta, K)$ is given by

$$F(\lambda_\theta, K) = 1 - \left(-10.32\lambda_\theta - 89.47\lambda_\theta^2 - 265.51\lambda_\theta^3\right) e^{\left[\frac{-Tu}{3.0}\right]} \tag{3.52}$$

and for favourable pressure gradients

$$\begin{aligned} F(\lambda_\theta, K) =& 1 + \left(0.0962\left[K10^6\right] + 0.148\left[K10^6\right]^2 + 0.0141\left[K10^6\right]^3\right) \\ & \left(1 - e^{\left[\frac{-Tu}{1.5}\right]}\right) + 0.556\left(1 - e^{[-23.9\lambda_\theta]}\right) e^{\left[\frac{-Tu}{1.5}\right]} \end{aligned} \tag{3.53}$$

At low turbulence intensity ($Tu < 1.0$) the correlation was curved fitted to agree with the zero pressure gradient results from e^n type models. In adverse pressure gradient the correlation was curved fitted to match the correlation of Abu-Ghannam and Shaw. Unsurprisingly then little improvement over Abu-Ghannam and Shaws model is seen at moderate free-stream turbulence intensities and adverse pressure gradients. At high free-stream turbulence intensities it behaves similar to Mayle's correlation.

The transition model can be used with the BSL, SST and SST-SAS turbulence models. The following three transition models are available in ANSYS-CFX,

- zero equation model.
- one equation model.
- two equation model.

For the computational studies in this investigation, the primary turbulence model used was the k-ω SST model. The reason for this choice was it suitability for detection of separation in adverse pressure gradients and its transition modelling add-on.

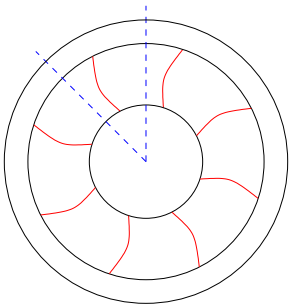

Figure 3.17: Rotational periodic geometry.

3.4.9 Grid Generation

ANSYS-CFX supports the use of arbitrary mesh topologies (structured, unstructured). ANSYS-CFX has a purpose built grid generation package, CFX-TurboGrid 10 for generation of meshes suitable for turbomachinery application. The user supplies the curves describing the hub and casing and the blade profiles. The remainder of the mesh is automatically built around existing blade topology allowing the process to be easily integrated into an optimisation strategy. The user is able to interactively modify the grid and see the results in realtime. CFX-TurboGrid is built around ICEMCFD using standard blocking structures. It is capable of producing both structured and unstructured meshes.

The solver of ANSYS-CFX puts certain requirements on the quality of the grid that have to be met as well as the restrictions put on it by the turbulence model, these are:

- Skew angle - ideally, the elements are orthogonal, in practice there is some skew angle between adjacent elements. Excessively skewed elements can degrade the accuracy of the computation due to the conversion between physical and computational space (recommended minimum skew is 20°).
- Aspect ratio - the aspect ratio of individual elements is not recommended to fall below 100:1.
- Volume size - negative volumes can occur if an element is collapsed in on itself, with the result that the solver will not run.

3.4.10 Boundary Conditions

The solution of the governing equations requires the specification of boundary conditions. A CFD solution can be visualised as the extrapolation of the boundary conditions into the interior of the domain (Versteeg and Malalasekera, 1995). The following boundary conditions were used in this thesis:

- Inflow

- Outflow
- Wall
- Grid interface (GGI)
- Periodicity

An inflow or outflow requires the specification of mass flow, velocity, total pressure or static pressure. Wall boundaries describe solid surfaces through which the fluid does not pass, effectively the velocity zero. ANSYS-CFX also allows rotating walls, which can be used to specify the rotating hub of a compressor.

The grid interface is a way to connect surfaces of grids with others. The grid interface is used to join grids together to make multi-block grids. In this project, the GGI or General Grid Interface (ANSYS, 2005) was used, which means that the nodes on adjoining grid surfaces do not need to be coincident or even be topologically similar i.e. structured connected to unstructured.

The periodic boundary condition allows the computational problem to be greatly simplified by dividing the problem into sectors. For a compressor blade row problem the use of periodic boundary conditions can reduce the problem from having to model the complete blade row to just a single passage (Fig. 3.17). To apply a periodic boundary condition the flux needs to be set for all the flow variables leaving one periodic boundary face equal to the flux entering the other periodic boundary face.

Both two equation turbulence models, as with the mean flow equations, require the specification of appropriate boundary conditions in order to obtain a solution. This is usually values of k and ω at the inlet to the domain. If values of these are unknown then they can be estimated, or calculated from estimations of related quantities, for example turbulence intensity or length scale.

$$k = \frac{3}{2}(VTu)^2 \tag{3.54}$$

$$\varepsilon = \frac{k^{3/2}}{l} \quad \text{and} \quad \omega = \frac{\varepsilon}{k} \tag{3.55}$$

An issue arises when viewing velocity data on solid walls with the no-slip boundary condition in ANSYS-CFX . The solver in ANSYS-CFX calculates the solution to flow problems using Finite Volume elements, which are not the same as mesh elements. Each node in the mesh is at the centre of a finite volume element. The result of this is that the values of some variables on the boundary nodes (i.e. on the geometry) are not precisely equal to the specified boundary conditions (e.g. the value of velocity on a node on the wall will not be exactly zero).

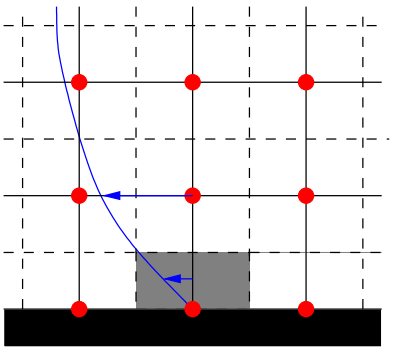

Figure 3.18: Wall boundary condition.

This is illustrated in Fig. 3.18, using a velocity profile as an example. The velocity value calculated at a mesh node is based upon the 'average' in the control volume surrounding that node. For calculation purposes, the entire control volume is assumed to posses that velocity. At a boundary node, the surrounding control volume includes an area in the bulk flow of the fluid (shaded area in Fig. 3.18). Hence, the velocity calculated at the wall is not zero, but an average over the control volume. This works for calculation purposes since quantities such as mass flow are calculated correctly. A velocity of zero would produce zero mass flow through the control volume which is clearly incorrect. ANSYS-CFX overcomes this through the use of Hybrid values, which correct the wall node velocity to its true value of zero and this value is used to produce plots.

3.5 Numerical Model of Third-Stage Stator

3.5.1 Geometry and Grid Generation

Geometrical details of the stator were obtained from Mr Timmis in two halves in the form of x, y, z co-ordinates with additional information given in the tail of the file required for machining. A short matlab routine was written to extract the pressure and suction surface co-ordinates and output a text file in the required format for ANSYS-TurboGrid . ANSYS-TurboGrid was then used to build the grids around the blade using a H-O-H mesh topology (Fig. 3.19)

The hub clearance was meshed by adding an additional H-mesh on top of the blade (Fig. 3.19). Alignment of the topology over the hub gap was enforced. ANSYS-TurboGrid allows a topology mismatch over the tip gap if desired. A General Grid Interface (GGI) is used here to join the two sides. The number of nodes in the clearance was calculated automatically based on the casing-to-tip expansion.

In order to ensure that the results from the numerical simulations were independent

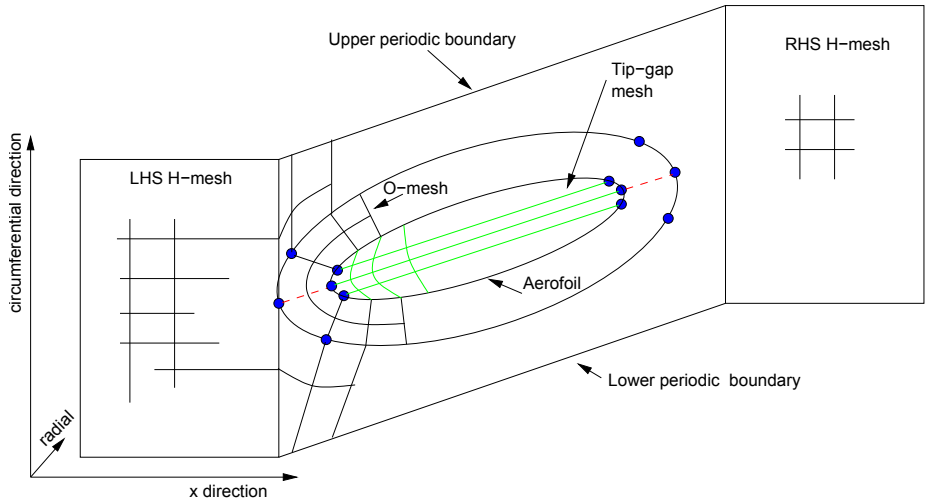

Figure 3.19: Mesh topology.

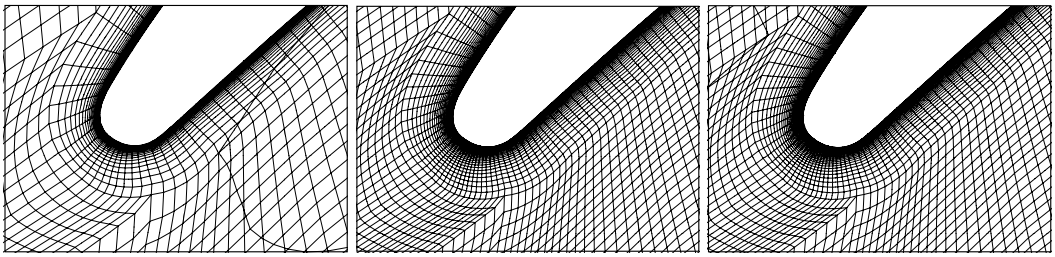

(a) 1.5 million nodes (b) 5.5 million nodes (c) 8.0 million nodes

Figure 3.20: Computational mesh; Leading edge for different mesh densities.

of mesh size a grid independence study was performed. Three individual stator meshes were generated all based on the standard topology, but had three different node densities; 1,500,000, 5,500,000 and 8,000,000. Details of the leading edge region of the three meshes are shown in Fig. 3.20 The approximate size of the individual blocks are shown in Tab. 3.7[3], along with the number of nodes in the hub clearance and the y^+ that was aimed for.

Because the transition model requires the solution of two extra transport equations, there is an additional overhead in terms of CPU. According to ANSYS (2005) this can be estimated as 18% additional CPU time compared to a fully turbulent solution using the same grid. The transition model cannot be used with wall functions (as they cannot properly resolve laminar boundary layer) and as such requires a y^+ of approximately 1 and sufficient grid points in the streamwise direction are needed to resolve the transition region. For these reasons a method of estimating the relative percentage of laminar flow on a device can be estimated using a formula which is based on the empirical correlation

[3]Grid size specified in i, j and k. Where i is in the streamwise, j is in the pitchwise and k is in the spanwise direction

	1,500,000	5,500,000	8,000,000
LHS H-mesh	30x54x120	50x90x170	50x90x225
O-mesh	96x90x120	160x140x170	160x160x225
RHS H-mesh	36x54x120	60x90x170	60x90x225
hub clearance	26	36	42
y^+	0.8	0.5	0.5

Table 3.7: Comparison of mesh size for different grid densities.

for transition onset, (Mayle, 1991):

$$\frac{\mathrm{Re}_{xt}}{\mathrm{Re}_x} = 380000\,(100Tu)^{-5/4}(\rho/\mu)\,V_l l \tag{3.56}$$

Using Eqn. 3.56 for the ANT2 stator operating at peak efficiency with an assumed inlet turbulence level of 5% results in a transitional length of approximately 30%.

ANSYS-CFX recommends the following mesh guidelines for use with the transition model:

- a max y^+ of 1.
- 75-100 grid nodes in the streamwise direction. In fact the model proved to be surprisingly insensitive to this.
- a wall normal expansion ratio of 1.1.

3.5.2 Boundary Conditions

Density variation in the flow through the single blade row was assumed to be negligible enough to solve the flow field incompressibly. This is a valid assumption for Mach numbers lower than 0.2 (Schlichting, 1967), which was larger than expected. All subsequent computations were therefore treated as incompressible.

At the inlet boundary, cylindrical velocity components were specified as a function of R and θ. This information came from the time-averaged data taken downstream of rotor 3 using the slanted hotwire. The outlet boundary was set as a area averaged static pressure boundary taken from a casing static. Periodic boundaries were assigned to the passage sides of the grids to simulate repeating blade rows. Wall boundaries were applied to the solid surfaces, and the wall boundary for the hub section was specified as rotating. The computational domain is shown in Fig. 3.21.

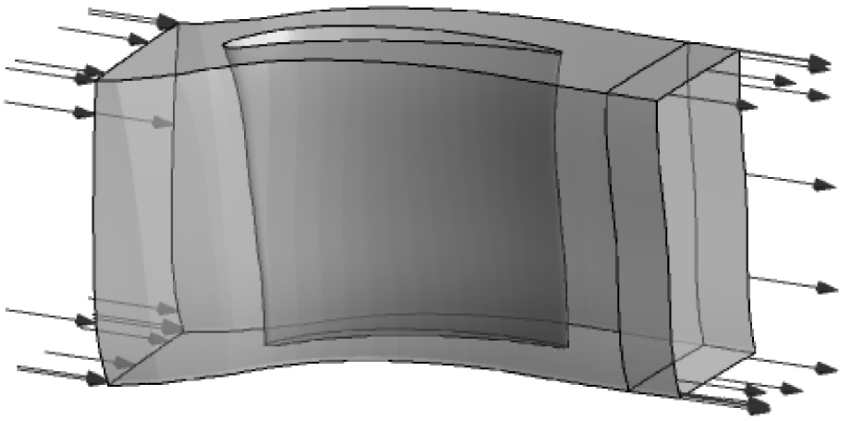

Figure 3.21: ANT2 stator computational domain.

The inlet turbulence kinetic energy was derived from the hotwire data at exit of the rotor. The turbulent kinetic dissipation rate was evaluated based on the following formula (ANSYS, 2005):

$$\varepsilon = \frac{k^{3/2}}{L_e} \tag{3.57}$$

where L_e is the inlet length scale and was assumed to be 10 % of the inlet annulus height. ANSYS (2005) recommends that when using the transition model that the high resolution advection scheme should be used for all equations including the turbulent and transition equations, which is automatically set when the high resolution scheme is selected for the hydrodynamic equations.

3.5.3 Grid Dependance

All three grids were run at the peak efficiency point, with the aim to determine the minimum grid density that could be used in subsequent computations.

The stator exit profiles were calculated using the turbo-post-processing module in ANSYS-CFX . The span is divided into a number of sections, at which the values were area-averaged in the pitchwise direction. Figure 3.22 shows the comparison of the stator yaw angle for peak efficiency. There is very little difference between the three levels of grid density. Figure 3.23 shows the pitchwise variation of velocity normalised by the mid-height blade speed at midspan at the exit of the stator. This points to the ability of the grids to capture the thickness of the boundary layer at the trailing edge of the stator and its subsequent convection downstream. There is very little difference between the three levels of grid density which is to be expected due to large size of the coarse grid.

Figure 3.24 shows the variation of shape factor over the suction surface at midspan. The lower density grid shows a reduction in shape factor from 0-0.4 s/S_0. After flow

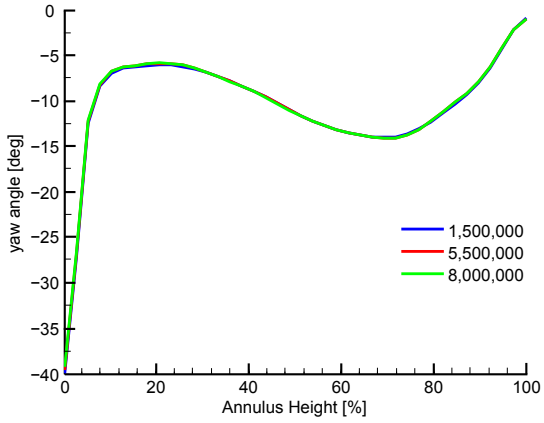

Figure 3.22: Area-averaged yaw angle from mesh sensitivity study.

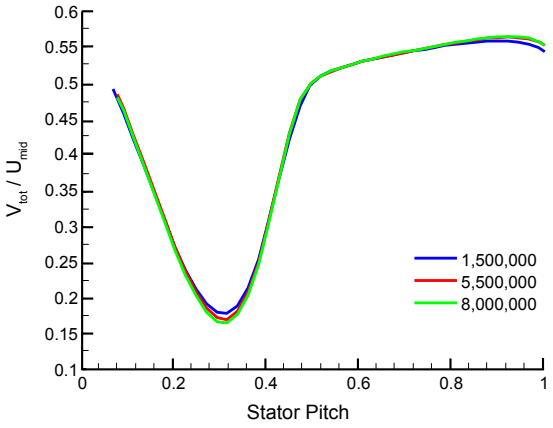

Figure 3.23: Midspan stator wake profile from mesh sensitivity study.

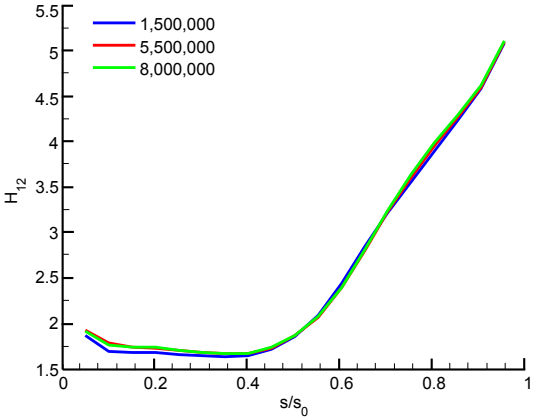

Figure 3.24: Comparison of shape factor for different grid densities.

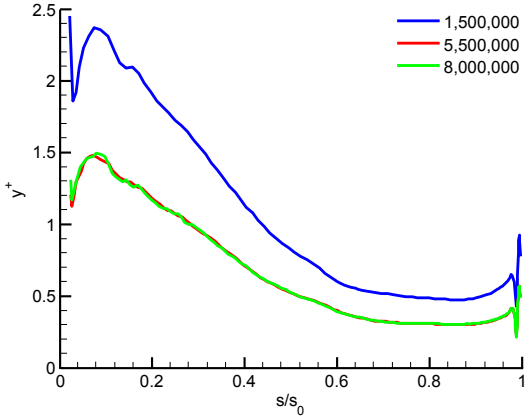

Figure 3.25: Comparison of y^+ for different grid densities.

separation the three grids converge to similar values of shape factor. Although the y^+ for all three grids were designed for a value below 1, (Tab. 3.7) the actual y^+ distribution is shown in Fig. 3.25. It can be observed that the lower grid density is near the upper limit of acceptable performance in the transition model (ANSYS, 2005). Based on this study the middle grid size (5,500,000 nodes) was selected for the computational modelling of the third-stage stator.

3.5.4 Unsteady Computation

In order to aid the analysis of the experimentally measured data, a thin-slice (4 nodes in the radial direction) unsteady calculation of $1\frac{1}{2}$ stages of the Cranfield Rig was modelled (Fig. 3.26). Both the rotor and stator blades were meshed using ICEM-HEXA. Each rotor passage was meshed using approximately 65,000 nodes. The stator mesh was representa-

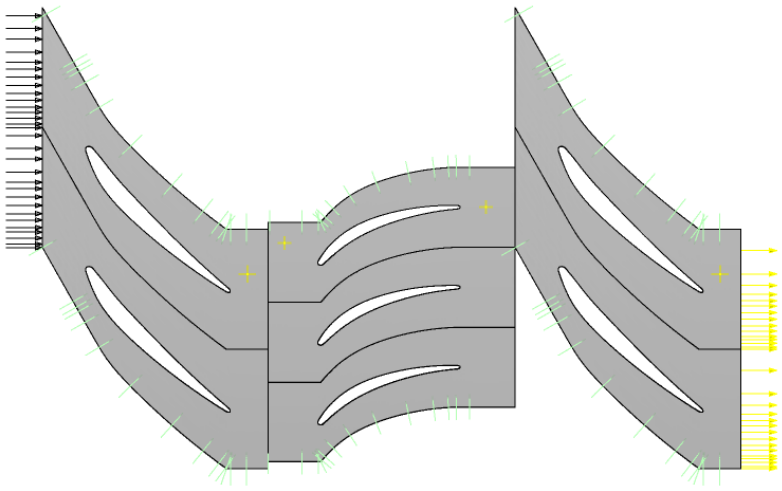

Figure 3.26: Unsteady calculation of $1\frac{1}{2}$ stages of the Cranfield Rig; 50% span.

tive of the mesh used in the three-dimensional steady calculations and contained approximately 100,000 nodes per passage. The increased node count for the stator blade row is due to the enhanced resolution of the boundary layer required for the transition model.

The rotor/stator/rotor blade count ratio was adjusted from the actual value of 88:134:88 to 88:132:88, so that only two rotors and 3 stators passages were modelled for the calculation. The effect of this adjustment was checked by comparing the predicted loading distribution from a steady state calculation with 132 and 134 stator blades. The influence of the reduced blade count on the predicted loading was found to be negligible. The inlet boundary condition was taken from the experimentally measured value at 50% span at rotor 3 inlet and comprised axial velocity and tangential velocity. The exit static pressure was held constant, and was set to achieve the midspan flow coefficient for peak efficiency.

ANSYS-CFX advances through time using the dual time-stepping approach where, the rotor is clocked relative to the stator on every outer iteration. Inner interactions are used to achieve convergence at that outer interaction. The advection scheme used was the High Resolution scheme and time was discretised using the 2^{nd} order Backward Euler scheme. The unsteady calculation presented in this thesis initially used 128 time steps per period (a period covered two rotor passes) for 8 periods. This gave an initial periodic solution which was used to restart the calculation using 512 time steps per period, which was run for 2 periods. Both runs used 8 inner time steps per outer time step.

3.6 Chapter Closure

This Chapter has provided detailed descriptions of the experimental and numerical techniques that were used in the proceeding Chapters. The Cranfield four-stage low-speed research compressor was introduced and the experimental techniques that were used to acquire the data presented in this thesis, were described. The commercial CFD package, ANSYS-CFX , was described along with the principles of finite volume discretisation and the problem of closure of the Navier-Stokes equations. Finally details of the numerical set-up for the predictions of the third-stage stator were described.

Chapter 4

Time Mean Measurements

4.1 Introduction

This chapter describes the measurements of the time-average flow field within the Cranfield four-stage rig. The cobra probe measurements were not performed by the author and were made available by Dr. Herring. The presentation of the data and all figures, as well as the interpretation of the cobra probe data are due entirely to the author.

The aim of this chapter was to investigate the time-average flow field of the third-stage and how this changed when the rig was throttled. In addition to this aim, quantification of the rotor wake parameters with flow coefficient, were required in order to understand the unsteady boundary layer development. For this reason measurements were performed in the stationary frame using three-hole cobra probes, a slanted hotwire and in the rotating frame using a cobra probe.

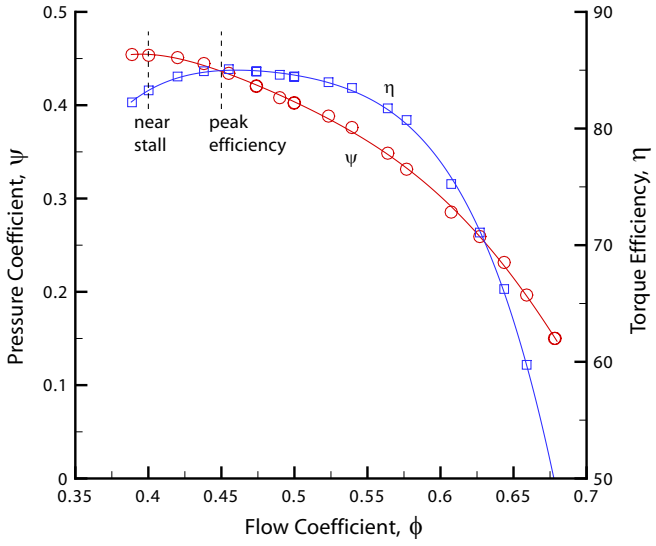

Figure 4.1: The Cranfield four-stage rig performance characteristic.

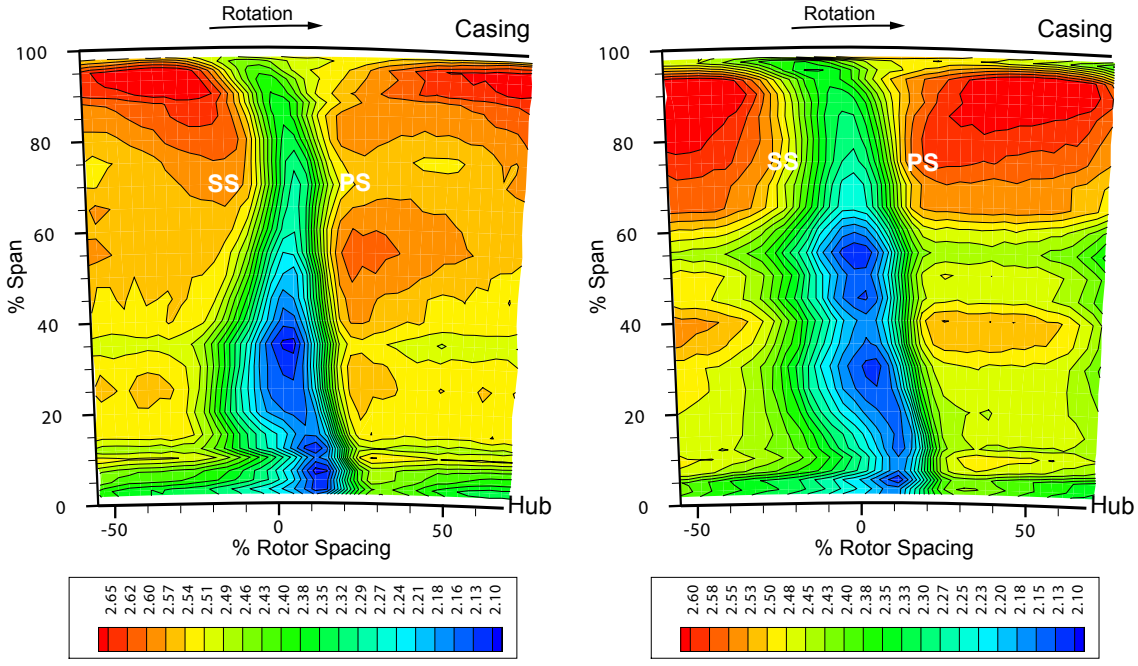

(a) (b)

Figure 4.2: Relative total pressure coefficient, $C_{P_{0\,rel}}$, at Rotor 3 exit plane: a) peak efficiency, b) near stall.

4.2 Rig Characteristic

Overall performance of the Cranfield rig is shown as a four-stage average in Fig. 4.1, based on measured massflow, measured work-input (torque and speed) and measured pressure rise. The torque efficiency and pressure coefficient are defined by Eqns. 3.3 and 3.5. All the experimental and numerical work presented in this thesis were conducted at the two loading levels shown Fig. 4.1. For the peak efficiency point, the flow coefficient, ϕ, was 0.450, the pressure coefficient, ψ, was 0.437, and the efficiency, η, was 85.0%. At increased loading the Cranfield rig was operating near its stall point (near stall) and these values were 0.400, 0.453 and 83.3%, respectively. The design point of the rig occurred at a flow coefficient of 0.477, but no data was acquired at this point. The efficiency characteristic is very flat at low flow coefficients with only a 0.2% efficiency change occurring between design point and peak efficiency.

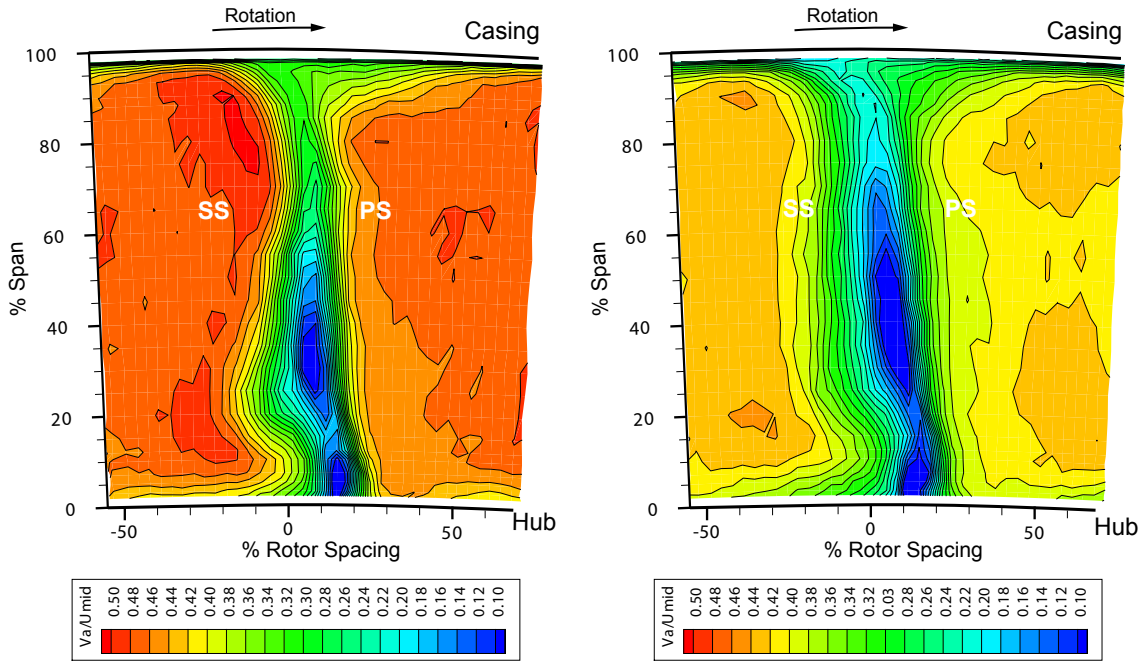

(a) (b)

Figure 4.3: Axial velocity, V_a/U_{mid}, at Rotor 3 exit plane: a) peak efficiency, b) near stall.

4.3 Rotor Exit Flow Field

4.3.1 Area Distribution

Detailed area traverse measurements of the total and static pressures and flow direction were made at exit of the third-stage rotor (35% of rotor axial chord downstream of the rotor trailing edge) in the rotating frame of reference using a conventional 3-hole cobra probe.

Contours of relative total pressure coefficient, $C_{P_{0\,rel}}$, are shown in Fig. 4.2 and for the peak efficiency ($\phi = 0.450$) and near stall ($\phi = 0.400$) operating points respectively. Marked in Fig. 4.2 is the location of the hub and casing, direction of rotation and the pressure (PS) and suction (SS) side of the wake.

Low total pressure regions are confined to the wake and the hub region adjacent to the suction surface (see Fig. 4.2). This low total pressure region in the rotor wake near the hub is the result of a rotor-hub corner separation. Dring et al. (1983) and Joslyn and Dring (1985) observed that as ϕ was reduced the rotor-hub corner separation grow in spanwise and pitchwise extent. Reducing ϕ from 0.450 to 0.400 resulted in a spanwise growth of the low total pressure region to approximately 70% of span, but no pitchwise growth was observed. The relative flow in the rotor wake will be restricted by interposition of the downstream stator causing accumulation of rotor wake fluid on the stator vane pressure

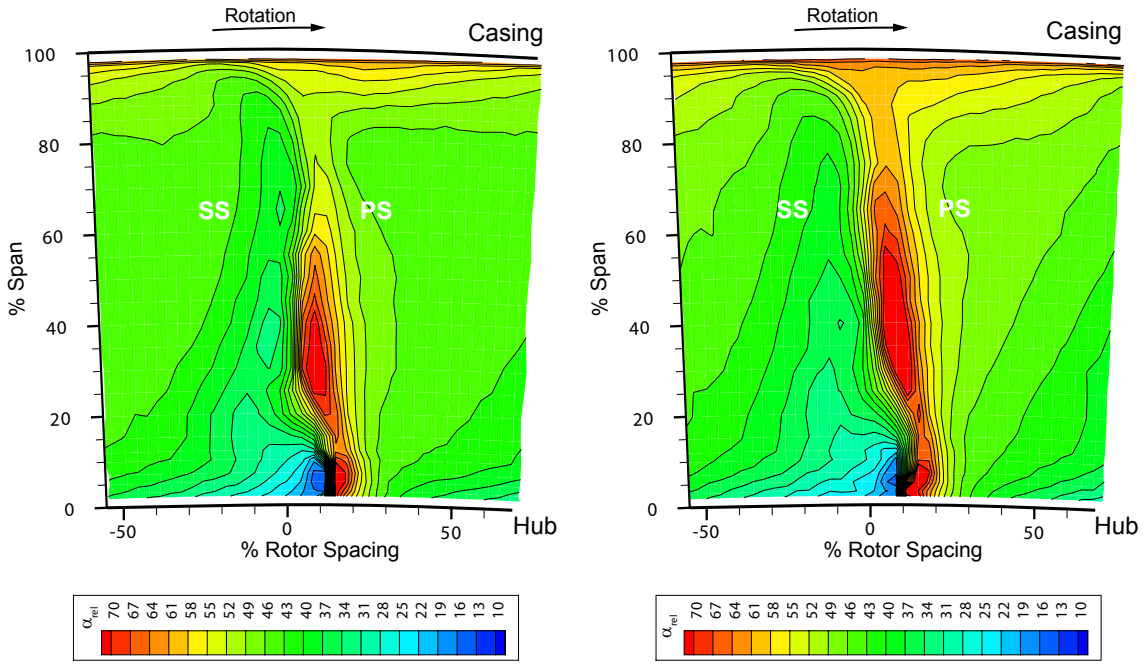

(a) (b)

Figure 4.4: Relative yaw angle, α_{rel}, at Rotor 3 exit plane: a) peak efficiency, b) near stall.

surface, the negative jet effect (Kerrebrock and Mikolajczak, 1970). The large region of low momentum fluid will increase locally the incidence onto the downstream stator blade row and thus the loading. Wheeler et al. (2006) observed that an increase in incidence caused by a propagating wake resulted in a local increase in the momentum thickness, and an upstream movement of the transition location.

The interaction of the tip clearance vortex and the mainstream flow is not visible in the contour plots of $C_{P_{0\,rel}}$. But the interaction of the tip clearance vortex with the mainstream flow, is visible in the distribution of normalised axial velocity, V_a/U_{mid}, at rotor 3 exit plane (see Fig. 4.3). The mixing of the tip clearance vortex can be observed as a region of reduced axial velocity at the interface of the pressure side leg of the wake and the casing, extending inboard to approximately 80% span. The clearance vortex has propagated right across the passage by the time it has reached the measurement location. As ϕ is reduced to 0.400 the impact of the tip clearance flow on V_a is reduced, due to the enhanced mixing (see §4.3.2).

The distributions of the relative yaw angle downstream of the third-stage rotor are presented in Fig. 4.4. Extremely high flow angles are recorded in the regions associated with the rotor-hub separation. An increase in flow angle would be expected in this region due to the reduced turning caused by the separated flow. But this cannot account for a deviation of approximately 30°. This is mostly likely caused by the ports on the cobra probe being located in a shear layer, causing biasing on one of the ports and therefore

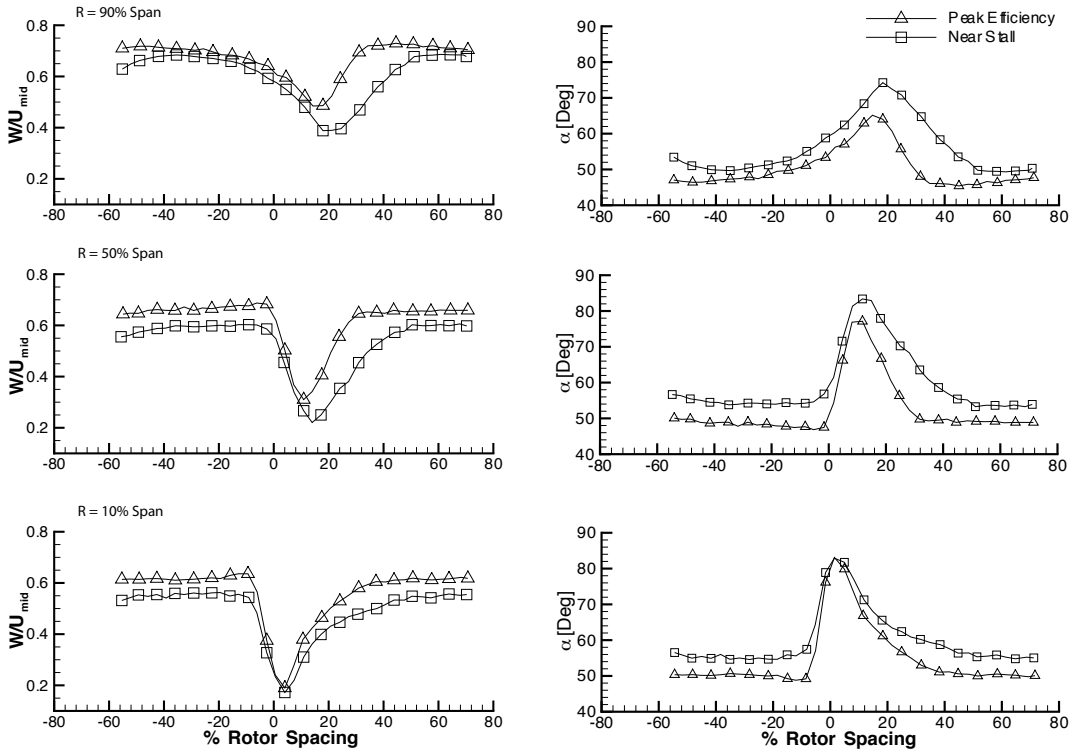

(a) relative velocity, W (b) absolute yaw angle, α

Figure 4.5: Rotor 3 blade-to-blade variation of relative velocity, W, and absolute yaw angle, α, at peak efficiency near stall.

invalidating the calibration coefficients. As the rig is throttled towards stall, the region of reduced turning which was confined to the rotor-hub corner separation region grows radially outwards towards the casing. The reduced turning caused by the tip clearance can also be observed in Fig. 4.4.

4.3.2 Blade-to-Blade Distribution

To understand the mechanics of wake boundary layer interaction it was necessary to understand the variations in the rotor wake parameters at inlet to the third-stage stator blade row. Figures 4.5(a) and 4.5(b) shows the blade-to-blade distribution of the incoming rotor wake profiles of rotor relative velocity (W) and absolute yaw angle (α) for peak efficiency and near stall. Looking at midspan initially, the rotor wake deficit ($W_{max} - W_{min}$) increases from 55% W_{max} at $\phi = 0.450$ to 65% W_{max} at $\phi = 0.400$. The width of the wakes also increases from 36% rotor pitch to 53% rotor pitch as the compressor is throttled. The level of absolute yaw outside of the wake rises from 48° to 54° as ϕ is reduced from peak efficiency to near stall. Within the wake at midspan, the yaw angle rises by 28° at peak efficiency and rises by 30° at near stall. At 10% span, the rotor velocity deficit at $\phi = 0.450$ has increased

from 55% W_{max} at midspan to 70% W_{max}. A similar increase in rotor velocity deficit is observed at near stall. The rotor wake profile at 10% span is dominated by the rotor-hub corner separation. The wake width at this location occupies 50% rotor pitch at $\phi = 0.450$ increasing to 63% at $\phi = 0.400$. The blockage generated by the separation causes the flow to under-turn increasing the incidence onto the downstream stator. A peak yaw angle of $> 80^\circ$ is observed which is an increase of 33° and 27° above the free-stream value for peak efficiency and near stall respectively. At 90% span the rotor wake deficit has reduced at peak efficiency and near stall to the values at midspan. The reduction in rotor relative velocity deficit is caused by the enhanced mixing generated by the rotor tip clearance vortex. The variation in α was also reduced. The fluctuations in α over the span are a factor of 3 larger than the change in the time-average α over the range of ϕ tested (see §4.3.3). Therefore, the wake incidence is expected to have a significant effect on the leading edge boundary layer especially close to stall. Valkov and Tan (1995) showed through the use of an incompressible two-dimensional Navier-Stokes analysis that the wake strength is directly related to the excess of tangential velocity in the wake stationary frame. The wake strength is thus proportional to the wake velocity deficit in the rotor frame and the rotor blade tangential velocity. As the rotor wake convects through the stator passage, the wakes will migrate toward the pressure surface of the stator blades, due to the excess of tangential velocity, where they evolve into pairs of counter-rotating vortices (see §5.4). The strength of the pair of vortices are directly related to the strength of the wake.

4.3.3 Radial Profiles

Radial distributions of mass-average quantities are reported in this section for both operating points. The definition of any passage mass-average quantity $\hat{f}$ is given below

$$\hat{f} = \frac{\int_{ss}^{ps} \rho V_a f \, d\theta}{\int_{ss}^{ps} \rho V_a \, d\theta} \tag{4.1}$$

Mass-averaging reduces the influence of separated flow and the low speed, nearly axial flow that results from separated flow regions.

Figure 4.6 shows the circumferentially mass-averaged radial profiles of relative yaw angle, α_{rel}, absolute yaw angle, α and pitch angle β. The yaw angles were measured with the cobra probe and the pitch angle with the slanted hotwire. A positive yaw angle is in the direction of rotor rotation and a positive pitch angle is towards the casing. Included in Fig. 4.6 are the rotor exit metal angle, χ_2 and the stator inlet metal angle, χ_3

The low total pressure region in the rotor wake was observed to increase in radial extent from 40% span at $\phi = 0.450$ to 80% span at $\phi = 0.400$ (see Fig. 4.2). This corresponds to the region of reduced turning (increased α_{rel}) seen in the $\phi = 0.400$ radial profiles of

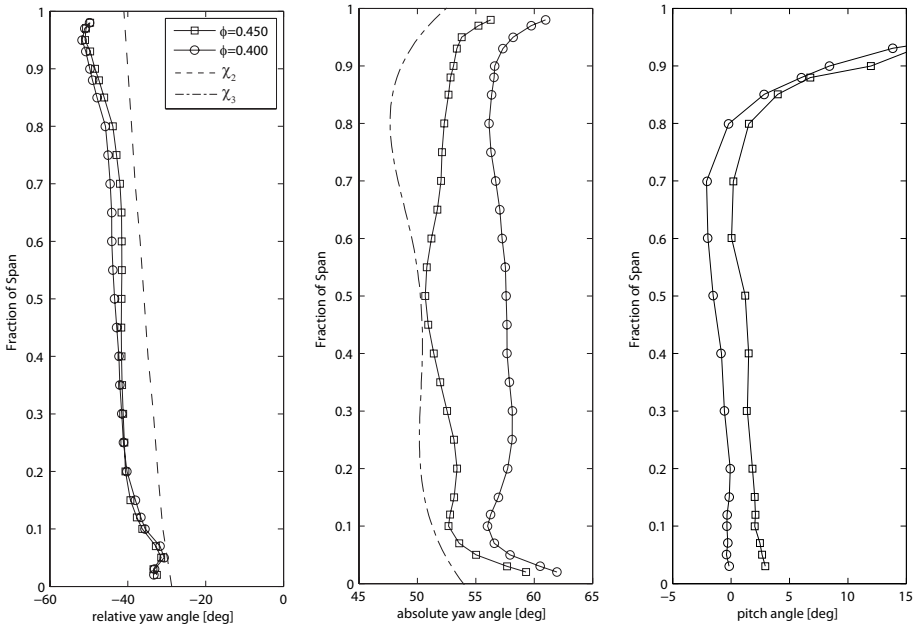

Figure 4.6: Mass-averaged radial profiles at rotor exit (plane 8).

mass-averaged yaw angle in Fig. 4.6. Below 40% span the blockage due to rotor corner separation is comparable at both flow coefficients, hence similar values of α_{rel} with reduction of ϕ. From 80% span, a region of increased deviation can be observed. This large deviation is caused by the rotor tip clearance flow. Close to the hub, below 10% span a reduction in the deviation is observed. This reduction is due to the endwall fluid being over-turned by the circumferential pressure gradient. The radial distribution of α indicates that the stator is operating at positive incidence at all spanwise locations and at both operating points. Only at a small region close to midspan at peak efficiency can the stator be seen to be operating close to zero incidence. As ϕ is reduced to 0.400, the inlet flow angle increases over the entire span. An increase of nearly 8° is seen at midspan. This increase in stator inlet angle in turns increases the stator loading and triggers rapid growth of the stator boundary layer as observed in the flow visualisation (see §6.2.2). The increases in stator inlet angle away from the endwalls is due to the opposing influences of the reduced flow coefficient and the increased rotor deviation, the former being dominant. A region of increased incidence can be seen between 10% and 30% span which is caused by the large loss core seen in the rotor exit traverses. Between 90% of span and the casing, the stator inlet angle increases rapidly with span, due to the rapid drop in V_a in the rotor tip region. The pitch angle at rotor exit is relatively low over must of the span ($< 5^\circ$). Above 80% span a significant increase in pitch angle can be observed. This increase in pitch angle is due to leakage through the traverse hole. As the traverse hole was designed for accepting cobra probes the I.D. diameter is larger then the O.D. diameter of the traverse shaft. The

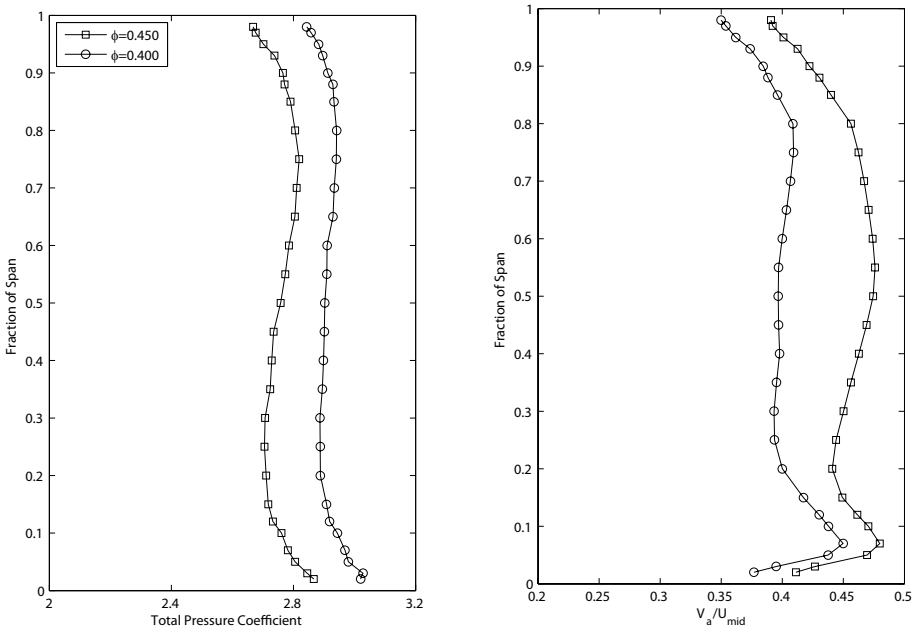

Figure 4.7: Mass-averaged radial profiles at rotor exit (plane 8).

accuracy of the measurements taken near the casing will therefore be reduced, especially those relating to the component of velocity in the radial direction.

Figure 4.7 shows the circumferentially mass-average profiles of absolute total pressure coefficient, C_{P_0} and normalised axial velocity, V_a/U_{mid}. The rotor-hub corner separation results in low axial velocity in the hub region (10-30% of span) at the stator inlet. As ϕ is reduced the minima in the dip has moved to a higher fraction of the span, due to centrifugal effects which tend to transport lower momentum fluid radially outwards. At the casing a corresponding drop in axial velocity and total pressure occurs. This reduction in total pressure is caused by the tip clearance. There are two mechanisms at work. The first is the reduced flow turning caused by the leakage vortex and hence lower work input in the tip region. The second is the increased losses due to the interaction and mixing of the leakage jet with the mainstream.

4.3.4 Secondary Flow

Contours of secondary flow vectors downstream of the third-stage rotor at peak efficiency and near stall operating points are presented and discussed in this section. Since the Cranfield rig has a parallel annulus, any component of radial velocity is undesirable. The secondary flow vectors are, therefore, defined as the vector sum of any radial component of velocity and the difference between the measured tangential velocity and desired tangential velocity. Thus, the secondary flow vectors are given by:

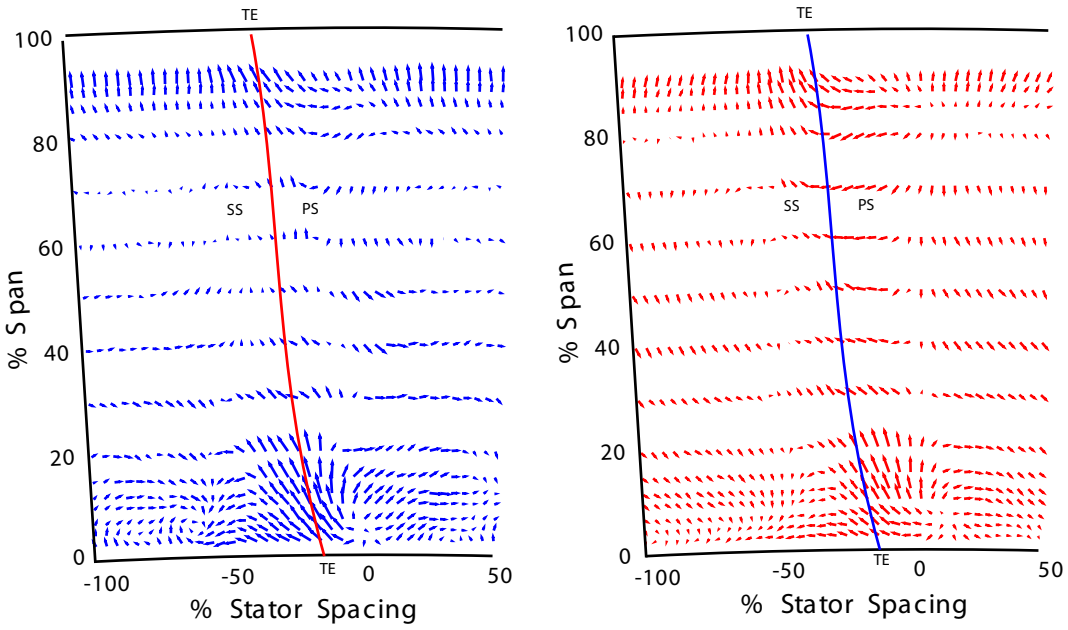

(a) (b)

Figure 4.8: Measured secondary flow vectors at exit of third-stage rotor; (a) peak efficiency, (b) near stall.

$$V_{t_{sec}} = V_{t_m} - V_{t_{desired}}$$
$$V_{r_{sec}} = V_r \tag{4.2}$$

A snap shot of the distribution of secondary flow vectors at exit of the third-stage rotor at $t/\tau_0 = 0.66$ for peak efficiency and near stall are shown in Fig. 4.8. This position in time corresponds to a rotor position that ties with the rotating cobra probe plots. Marked in the figures are the location of the rotor trailing edge and the suction and pressure side of the wake. The secondary flow vectors above 80% span are believed to be corrupted due to the leakage through the casing. The wake is characterised by radially outward flow, due to centrifugal effects, that will tend to transport the lower momentum fluid radially outwards. Large secondary flow vectors can be seen at the root of the rotor at both operating point, caused by the lower momentum fluid being centrifuged radially outwards.

4.4 Stator Exit Flow Field

4.4.1 Area Distribution

Detailed area measurements of the total and static pressures and the flow direction were made at the stator exit plane (49% of stator axial chord downstream of the stator trailing

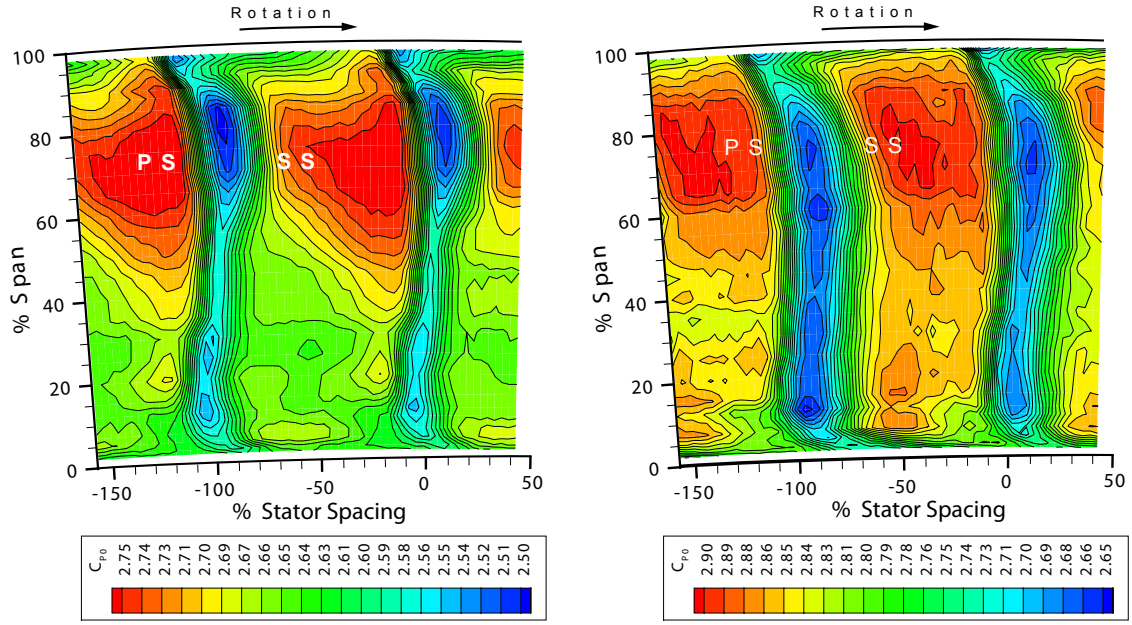

(a) (b)

Figure 4.9: Total pressure coefficient, C_{P_0}, at Stator 3 exit plane: a) peak efficiency, b) near stall.

edge) using a conventional 3-hole cobra probe.

The contours of total pressure coefficient, C_{P_0}, are shown in Fig. 4.9 for the peak efficiency and near stall operating point, respectively. The presence of stator wakes, the effect of secondary flow and the thickening of the boundary layer near the suction surface corner in the endwall are clearly visible. At $\phi = 0.450$, the core region extends from approximately 30% to 90% span. The wakes width and strength are at a minimum at 50% span covering approximately 10% of the blade pitch. This value increases to a maximum value of 30% of the blade pitch at 80% span.

The total pressure coefficient contours at $\phi = 0.400$ indicate that the core region has substantially altered in shape and position in the passage, from that observed at $\phi = 0.450$. This is caused by a significant increase in the wake width across the whole span. The wake width has increased from approximately 10% of blade pitch at midspan to 30%. The wake width varies very little over the span and on the whole the flow exhibits a more two-dimensional pattern than compared to peak efficiency.

The total pressure contours near the hub indicate a low energy core located on the pressure side of the wake. This low energy core extends to nearly 10% of the span and is better seen at the near stall operating points where the influence of the tip clearance is more pronounced (-130% and -110% stator spacing, 2-15% span). No measurements were taken closer than 2 percent of span from the rotating hub, hence no definitive conclusions can be drawn with regard to the presence of leakage. The endwall boundary layer in this

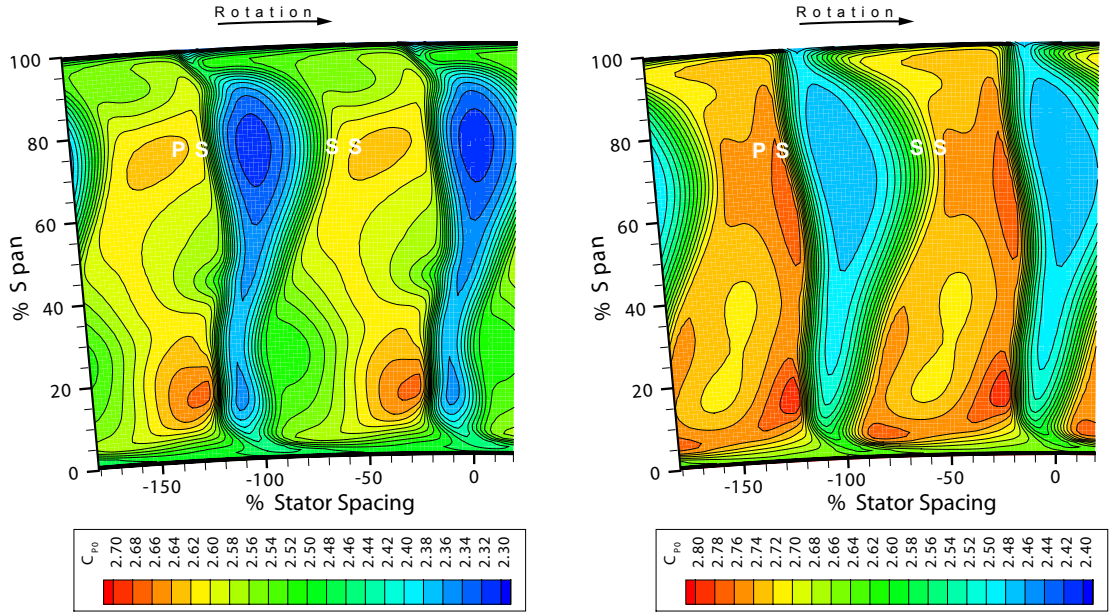

(a) (b)

Figure 4.10: Predicted total pressure coefficient, C_{P_0}, at Stator 3 exit plane: a) peak efficiency, b) near stall.

region is 6% and 8% of span respectively for $\phi = 0.450$ and $\phi = 0.400$ which is larger than the tip gap (1.1% of span), hence the presence of a scraping vortex is expected.

The predicted flow field at exit of the stator from the numerical calculations are shown in Fig. 4.10. The numerical calculations have massively over-predicted the size of the boundary layer separation at 80% span. The blockage caused by the over-predicted separation has resulted in a complete redistribution of the flow field. The over-prediction of the boundary layer separation is not believed to be a result of the turbulence model used, but rather the lack of an upstream and downstream rotor in the calculation. Aurifeille (2003) observed that for a single stage simulation the distribution of C_{P_0} at exit of the stator showed that the width of the low total pressure region due to the casing corner separation was over-predicted. When the compressor was re-run as a multistage calculation, with mixing planes, good agreement between the measurements and CFD was achieved. Due to the large mesh size used for the stator in these calculations (5.5 million nodes) it was decided against calculating an upstream and downstream rotor which would have produced a resulting mesh of 16.5 million nodes.

Figure 4.11 shows the time-average random unsteadiness, Tu, at exit of the third-stage stator as measured by the slanted hotwire probe for $\phi = 0.450$ and $\phi = 0.400$ respectively. The levels are based on the percentage of the time-average stator velocity magnitude ($\overline{V}$) at a given point. At peak efficiency (see Fig. 4.11(a)) between 60% and 80% span located between the wakes a region of relative low Tu ($\approx 4\%$) can be observed. This region

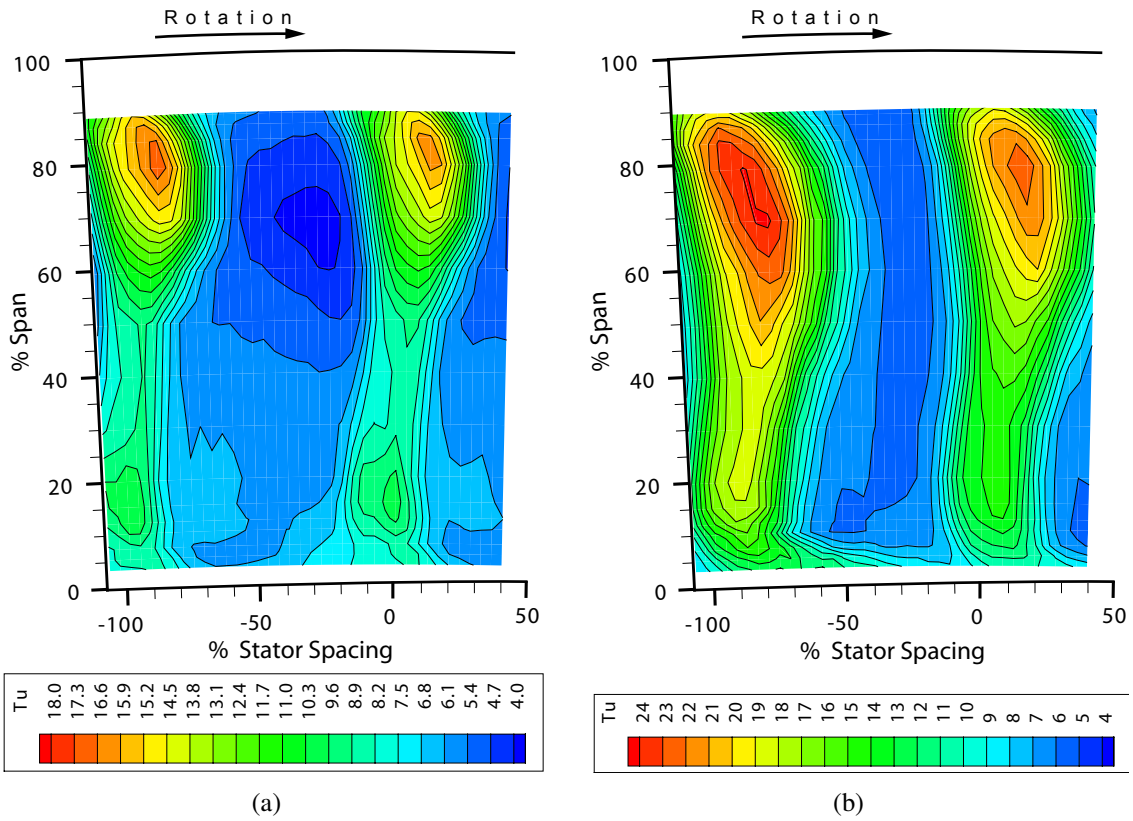

(a) (b)

Figure 4.11: Random unsteadiness, Tu, at Stator 3 exit plane: a) peak efficiency, b) near stall.

corresponds to the high C_{P_0} region seen in Fig. 4.9(a). Below 60% span the free-stream unsteadiness increases to a level between 6 and 7%. Regions of high random unsteadiness are confined to the hub endwall and the wakes shed from the stator. The stator vane wakes are characterised by two peaks in Tu one at approximately 15% span of 10% Tu and the other at 80% span of 17% Tu. This second peak of high unsteadiness corresponds to the region of low C_{P_0} caused by the boundary layer fluid separating of the stator blade. At midspan the unsteadiness in the wake has dropped to 10% Tu. The time-average distribution of random unsteadiness in the wake show a slight asymmetry between the two adjacent stator blades. The asymmetry between the two blades is more noticeable at $\phi = 0.400$ (see Fig. 4.11(b)).

At near stall the overall level of random unsteadiness has increased. The free-stream level has increased from 4% to 6% Tu and the peak unsteadiness at approximately 80% span has increased to 24% Tu. The unsteadiness created by the wakes now occupies approximately 50% of the stator pitch, peaking to 75% of pitch between 60% and 80% span. The high level of unsteadiness seen towards the hub, that stretches from the suction side of the stator towards midpitch is created by the tip clearance flow. This region of raised unsteadiness was also evident to a lesser extent at $\phi = 0.450$. The level of free-stream

random unsteadiness observed at the exit of stator 3 agree with those found by Camp and Shin (1995) and Wisler (1985). Wisler (1985) measured free-stream unsteadiness levels of approximately 5% at design which is comparable to to that measured in the Cranfield rig (between 4-6% at peak efficiency). Similar levels of unsteadiness were also measured at increased levels of loading towards the endwalls and the stator wakes.

4.4.2 Blade-to-Blade Distribution

The blade-to-blade profiles of total pressure and yaw angle acquired at peak efficiency and near stall are presented for three representative radii 7%, 50% and 80% span and are compared to the numerical calculations. The hub rotation is from left to right in the blade-to-blade profiles presented.

Figure 4.12(a) shows the blade-to-blade distribution of the total pressure coefficient at peak efficiency and near stall. The near stall operating point typically increases the total pressure coefficient by 7% outside of the stator wakes. This is also evident in the numerical calculations with on the whole good agreement between the two in the free-stream. The increased loading is evident across the entire blade passage. The wakes associated with near stall have larger total pressure deficits and wake widths.

Good agreement is achieved between the measured total pressure and that predicted at 7% span. At near stall the agreement is worse but at both operating points the numerical calculations have predicted the correct minimum in the wake. The solutions failed to predict the slight drop in total pressure caused by the tip clearance vortex as seen in the experimental data. This is due to the vortex in the numerical calculations hitting the pressure surface of the adjacent blade and being transported radially outwards. The drop in total pressure in the blade passage seen in the experimental data is due to the low momentum fluid from the stator blade clearance flow. The rotation of the hub is from left to right. The low pressure region associated with the clearance flow is transported from the suction to the pressure side by the rotating hub. The deficit in total pressure in this region increases slightly, with loading as the loss core is expected to increase in magnitude due to the increased blade loading at the stator blade tip.

At 50% span, good agreement between the experimental data and the numerical calculation is achieved for near stall. The numerical calculations show a slightly lower total pressure coefficient at the wake centre. Agreement with peak efficiency at this span is poor. The numerical calculations fail to capture the correct distribution of total pressure in the passage, locating the high total pressure near to the suction side of the wake and has over-estimated the strength of the wake. The distribution of total pressure seen in the experiment is due to rotor wake interspersion which is not modelled in the steady CFD calculation. Finally at 80% span it is clear that the numerical calculations have over predicted

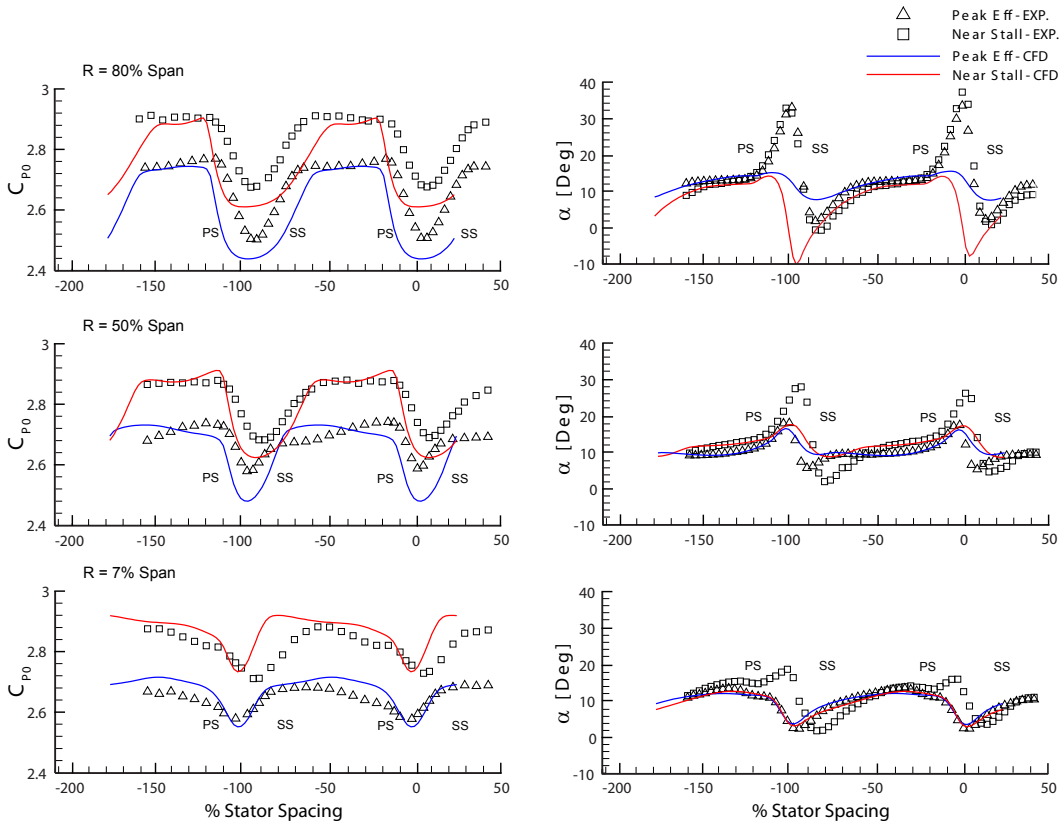

(a) total pressure coefficient (b) Yaw angle

Figure 4.12: Stator 3 blade-to-blade distribution of total pressure coefficient and yaw angle at peak efficiency and near stall.

the size of the separation on the stator vane surface, with agreement only be achieved in the free stream.

Figure 4.12(b) shows the distribution of the blade-to-blade yaw angle at the two operation conditions. At all radii, the difference in the yaw angle outside of the wake regions is nearly invariant between the two operation points. The numerical calculations have predicted the distribution outside of the wake well. The experimental data shows very large yaw angle value in regions close to the edge of the wake. This is the result of the spatial resolution of the cobra probe and biassing of the ports. At 50% and 80% span the flow is overturned on the suction side and under-turned on the pressure side of the wake compared to the flow angle near mid-pitch. At 7% span only the experimental data at near stall shows any evidence of the flow being under-turned on the pressure side. The over- and under-turning is caused by the secondary flow which induces over-turning in the entire passage near the casing. The dominant effect is near the suction surface at the casing. Hence, the wake flow and classical secondary flow have a cumulative effect in over-turning the the flow near the suction surface and the opposite effect near the pressure surface.

Figure 4.13(a) shows the blade-to-blade distributions of the static pressure coefficient

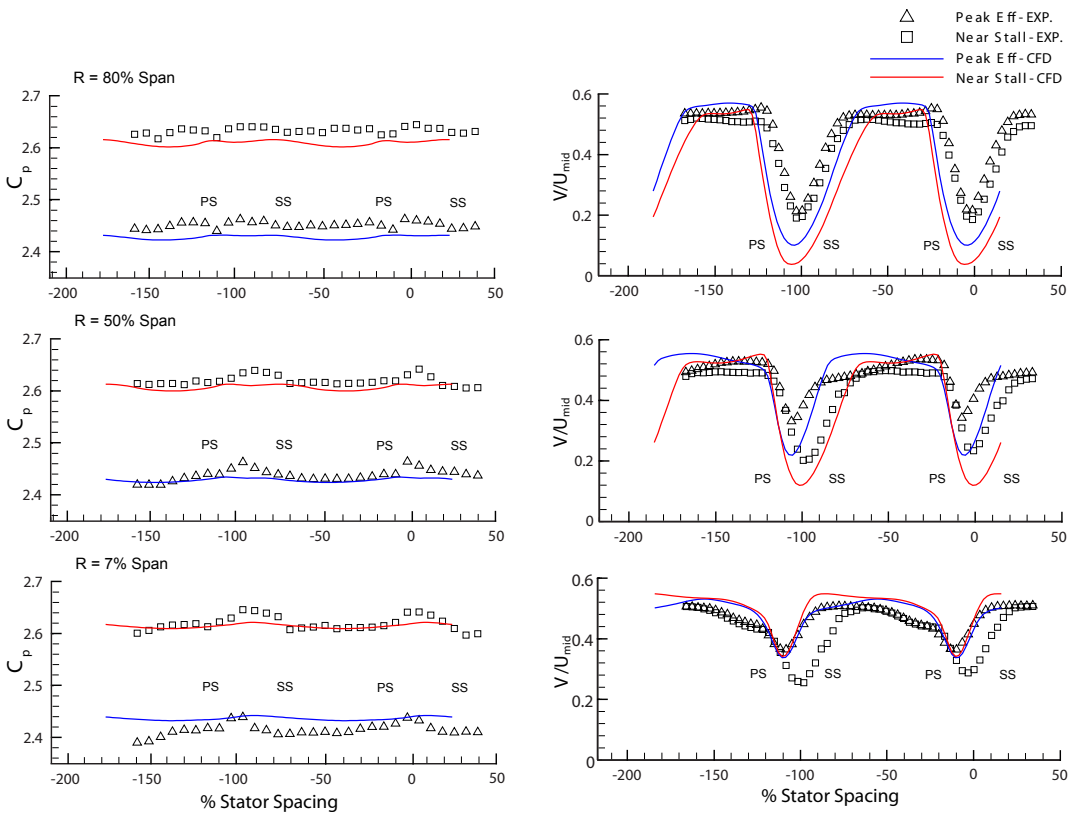

(a) Pressure coefficient

(b) Velocity magnitude

Figure 4.13: Stator 3 blade-to-blade distribution of pressure coefficient and velocity magnitude at peak efficiency and near stall.

at peak efficiency and near stall. At all radii, the difference in the static pressure coefficient between the two operating points is nearly constant across the entire blade passage. The blade-to-blade variation in static pressure is nearly invariant with small changes occurring across the stator wakes. The static pressure is expected to remain constant across the stator wakes, as predicted by the numerical calculations, and as such variations in total velocity are attributed mainly to variations in total pressure.

Figure 4.13(b) shows the blade-to-blade distribution of the total velocity at both operating points. At all locations, the wakes associated with near stall have larger velocity deficits and wake width. At 7% span, the experimental data shows a low velocity region extending from -50% to -20% stator spacing which is due to the clearance flow and the entrainment of the fluid across the blade passage by the rotating hub. The numerical calculations do not show this phenomena and is due to the vortex moving radially outwards. As already noted, the static pressure was found to be very nearly constant in this and all regions at the exit of the stator blade row. Thus, the decrease in total velocity in this region is due primarily to a drop in total pressure, which is due to the stator hub clearance flow. The deficit in total pressure in this region increases slightly, with increased loading, as the

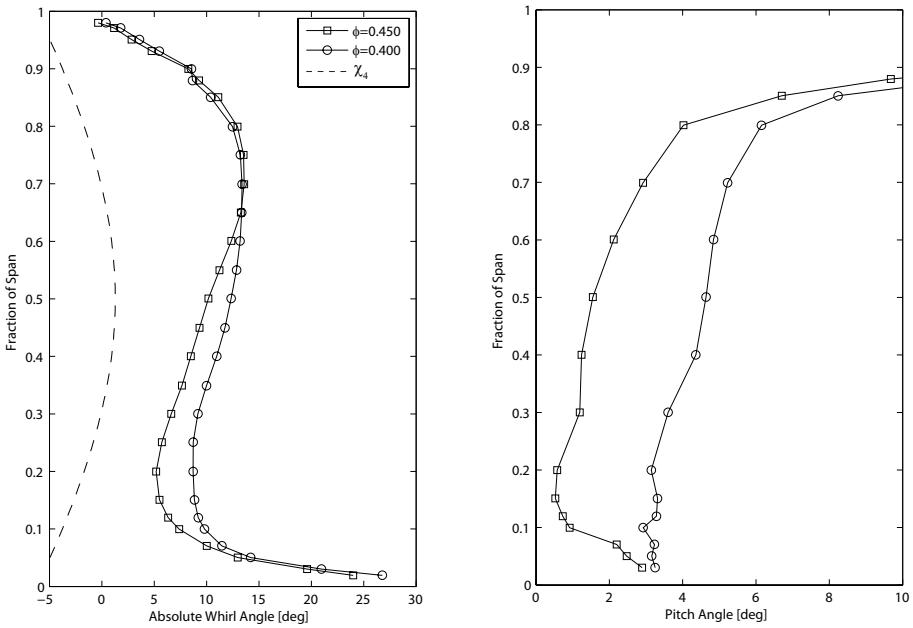

Figure 4.14: Mass-averaged radial profiles at stator exit (plane 9)

loss core is expected to increase in magnitude. At 80% span the experimental data shows that the wake width and deficit are in close agreement for the two operating points. The numerical calculations also show a similar trend between operating points.

4.4.3 Radial Distribution

Figure 4.14 presents the circumferentially mass-average values of yaw and pitch angle at exit of the third-stage stator. Also marked in the fig. 4.14 is the stator exit metal angle χ_4. Positive yaw angle is taken to be in the direction of rotation and positive pitch angle is towards the casing.

The stator is operating with positive deviation at all spanwise locations, between $5-30^\circ$. Reducing the flow coefficient increases the deviation and the exit flow angle over most of the span. A maximum of 5° occurring at 20% span. Above 70% span the exit flow angle shows little variation with flow coefficient. This is evident in the the distribution of total pressure at the measurement location (see Fig. 4.9) where depth or the pitchwise extent of the low total pressure region can be observed not to vary with ϕ. The increased deviation below 60% of span is due primarily to the increased incidence (Fig. 4.6) and hence loading caused by the rotor-hub corner separation. At the casing a reduction in deviation is seen, caused by over-turning of the flow by the cross-passage pressure gradient. Near the hub a region of increased deviation is caused by the stator tip clearance flow.

The influence of the leakage around the probe support is evident in the radial profile of pitch angle. Above 80% span a rapid increase can be observed. Below 80% span the

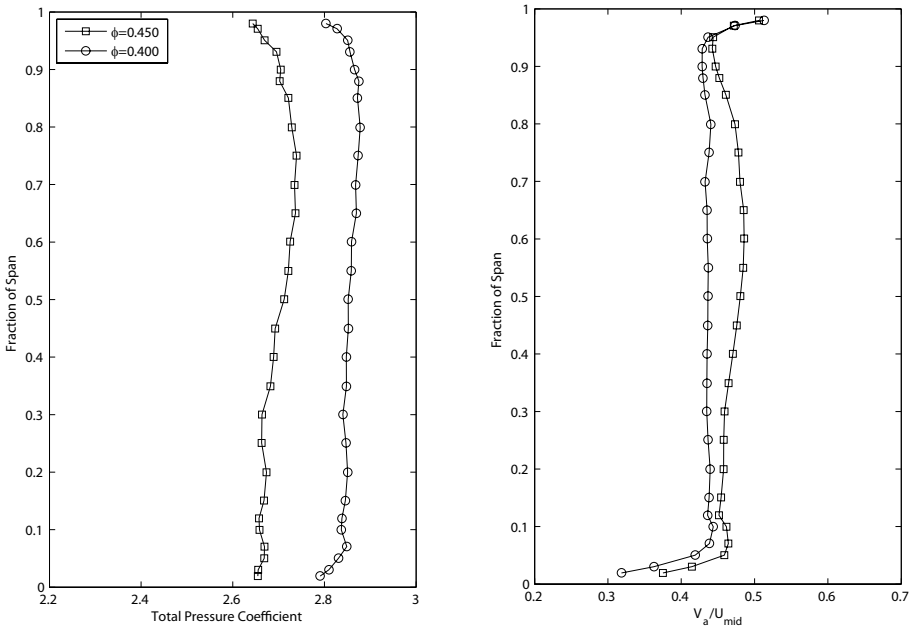

Figure 4.15: Mass-averaged radial profiles at stator exit (plane 9)

measure pitch angle is below 6°. As the flow coefficient is reduced towards stall the pitch angle can be seen to increase by approximately 2°, suggesting that the three-dimensional effects increase towards off-design. Below 10% span an increase in pitch angle can be seen as the hub is approached. This is due to the tip clearance flow.

Figure 4.15 presents the circumferentially mass-averaged total pressure coefficient, C_{P_0} and normalised axial velocity, V_a/U_{mid}. The total pressure coefficient shows little variation over the span. A dip in total pressure is seen at both endwalls, due to losses generated in the endwall boundary layers. Reducing the flow coefficient results in an increase in the magnitude and radial extent of the hub endwall loss region. Between 80% and 95% a dip can be observed in V_a/U_{mid} caused by the loss core seen in the area traverse data (see §4.4.1). From 95% of span a sharp rise in the axial velocity distribution can be seen. This is caused by a sharp fall in the static pressure (not shown) measured by the cobra probe. The fall in static pressure is caused by two factors. First, the interaction of the cobra probe with the outer casing (Livesey, 1956). This causes the fluid to accelerate around the probe head. Second, leakage between the traverse shaft and the probe hole. Both of these factors will reduce the static pressure and cause the observed increase in V_a/U_{mid}.

4.4.4 Secondary Flow

Figure 4.16 show the secondary flow vectors at the exit of the third-stage stator at peak efficiency and near stall operating points as measured by the slanted hotwire. The location of the stator is at approximately -100% and 0% stator spacing in Fig. 4.16.

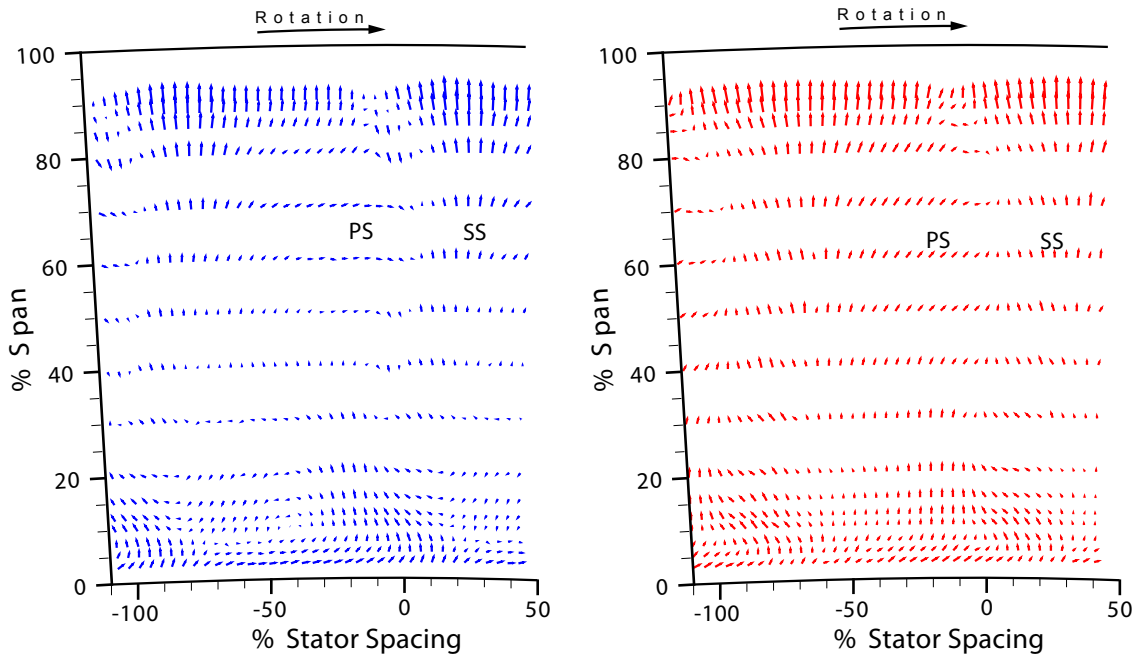

Figure 4.16: Measured secondary flow vectors at exit of third-stage stator: (a) peak efficiency, (b) near stall.

At peak efficiency in Fig. 4.16(a) cross-passage velocities toward the pressure surface (PS) and radial velocities toward the casing were observed from 60% span. At 80% span and 0% stator pitch, the secondary flow vectors indicate radially inward flow. The stator wake is characterised by radially inward velocities from approximately 30% of span.

The level of cross-passage flow reduces towards midspan. At 50% stator pitch and 40% span the secondary flow vectors are at a minimum with a small amount of radially outward flow. At the hub the flow is primarily from the suction side towards the pressure side. At the pressure side the flow is driven radially outwards until approximately 30% of span where it is over-turned and migrates towards the suction surface. The radially outward velocities are confirmed by the flow visualisation (see §6.2.2) where in the first 30% of span the streak lines indicate radially outward migration of boundary layer fluid. Close to the hub in Fig. 4.16(a) and shown schematically in Fig. 4.17 the presence of the clearance vortex can be seen.

At near stall (see Fig. 4.16(b) the secondary flow velocities are observed to increase, with higher cross-passage and radially outward velocities. Between the hub and 20% span increased under-turning can be seen, due to the blockage caused by the boundary layer flow separating (see §6.2.2).

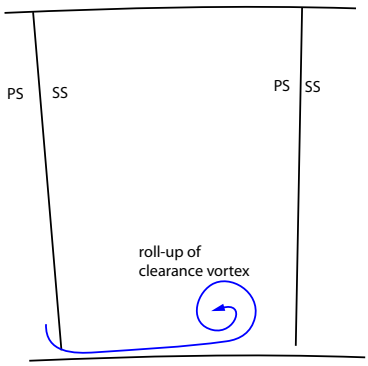

Figure 4.17: Schematic of tip leakage vortex roll-up

4.5 Chapter Closure

This chapter has described the time-average flow field of the third-stage of the Cranfield four-stage compressor at two flow coefficients. A cobra probe was used for the measurements of yaw angle and pressures. The three-dimensionality of the flow was assessed using the time-average pitch angle from the slanted hotwire. The results showed that from 85% span the flow contained a large component of positive radial velocity, due to leakage between the traverse shaft and the traverse hole.

In summary, rotor-hub corner separation has a major impact on the stator inlet angle profile due to its effects on the rotor exit axial velocity. As the rig was throttled the rotor loss core was observed to grow in the radial direction. This had the effect of increasing the incidence onto the downstream stator and hence loading. The deviation was observed to increase by 10° compared to the peak efficiency point in this region. In a multistage environment this would have a significant consequence on the performance of the downstream rotor blade row. Rotor tip leakage results in a region of low axial velocity and thus governs the stator inlet angle profile in the tip region. The secondary flow field showed considerable cross-passage and spanwise fluid motion. Radially inward velocities were observed along the stator trailing edge which would transport the low momentum fluid near the casing towards midspan. Radially outward velocities were found in the rotor wakes, indicating wake centrifugation.

These measurements provide a time-averaged picture of the flow in the third-stage of the rig. The following chapters will now involve a discussion of the unsteady flow in the stage.

Chapter 5

Time Resolved Flow Field

5.1 Introduction

The flow in a multistage compressor is highly unsteady. This unsteadiness is caused by the aerodynamic interaction of rotor and stator flow fields. The rotor-stator interactions can effect the aerodynamic and mechanical performance of a compressor. However up to now, virtually all compressor designs are based on an assumption that the flow is steady in time. Therefore, a better understanding of the unsteady flow interactions can lead to an improvement in the ability to predict the performance of a compressor.

From the view point of understanding boundary layer development in axial compressors, it becomes apparent that this highly unsteady turbulent flow will have a strong effect on the behaviour of blading upon which the turbulence impinges. Higher turbulence levels can suppress separation, through movement of the transition point. This becomes an important consideration at flow conditions where blades are highly loaded.

This chapter describes in detail the unsteady flow field that exists at inlet and exit of the the third-stage stator of the Cranfield four-stage rig at two loading levels. This is achieved through hotwire traverses and two-dimensional unsteady non-linear CFD. The numerical methods allow for a greater insight into the complex flow structures and vortex motions that exist in the blade row. Analysis of the results will be described here, details of the numerical and experimental methods can be found in Chapter 3.

5.2 Rotor Exit

Description of the steady rotor wake parameters were described in the rotating frame of reference in §4.3.2. The unsteady rotor wake parameters are presented in this section in terms of space-time (S-T) diagrams for peak efficiency and near stall at 50% and 80% span. All such diagrams present 3 periods of ensemble-average data. The S-T diagram allows

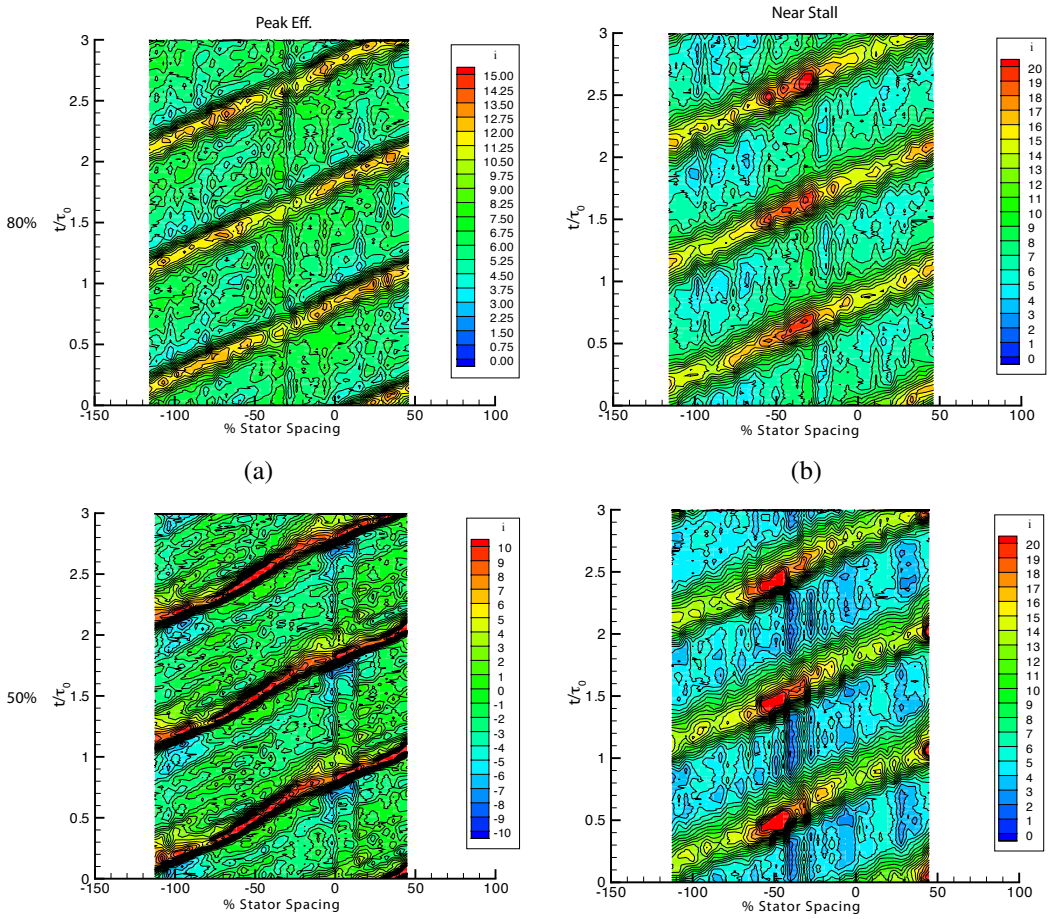

Figure 5.1: S-T diagram of incidence, i, onto third-stage stator: a) 80% span peak efficiency, b) 80% span near stall, c) 50% span peak efficiency, d) 50% span near stall

a description of a parameter as a function of both time and space. Lines of constant time drawn parallel to the s-axis provide the instantaneous state of the flow in space. Vertical lines parallel to the t-axis provide the unsteady behaviour of the flow at a given location in space. For a constant velocity, the boundaries are straight lines in S-T space, otherwise they are curved. In the following figures the s-axis has been non-dimensionalised by the stator pitch and the t-axis has been non-dimensionalised by rotor passing period τ_0. Stator 3 leading edge is at approximately -40% stator spacing.

In Fig. 5.1 the incidence angle, i, at inlet to stator 3 as measured by the slanted hotwire is presented. The propagation of three rotor wakes passing the measurement location are clearly visible as diagonal lines traveling at U. Rotor wakes tend to increase the incidence onto the downstream blade row which has the effect of increasing the momentum thickness. At 80% span for $\phi = 0.450$ and $\phi = 0.400$ the stator blade is continuously operating at positive incidence. A maximum incidence of 15° and 20° occurs in the wake for peak efficiency and near stall respectively. A hot spot of positive incidence which has a period

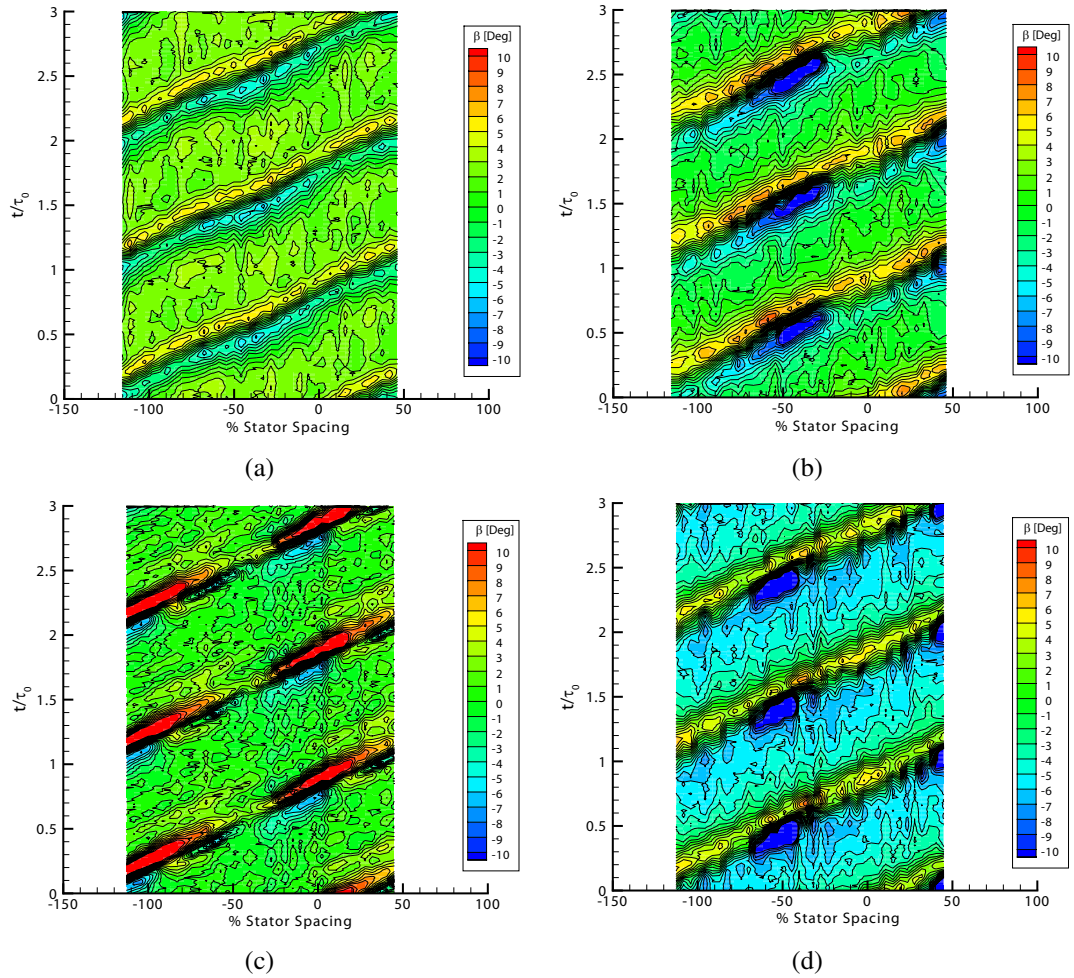

Figure 5.2: S-T diagram of pitch angle, β, at Rotor 3 exit plane: a) 80% span peak efficiency, b) 80% span near stall, c) 50% span peak efficiency, d) 50% span near stall

of the order of the stator pitch can be observed to occur at $\phi = 0.400$ and approximately -50% stator spacing (Fig. 5.1(b) and 5.1(d)). This region corresponds to the wake street from the upstream stator blade row (second-stage). This becomes apparent when viewing the distribution of random unsteadiness, Tu at $\phi = 0.400$ (Fig. 5.3) where the higher fluctuations of the wake street can be seen above those of the surrounding free-stream. At 50% span and $\phi = 0.450$, the free-stream flow can be seen to operate close to zero incidence. The wake path is no longer straight, but appears to 'wobble'. As the rig is throttled the free-stream incidence increases to 5° at $\phi = 0.400$. The variation of incidence with time are approximately 3 times greater than that observed with change of flow coefficient. Therefore, the periodic passing of a wake is expected to have a dominate effect on a developing boundary layer.

The distribution of radial flow angle, β as a function of space and time at rotor 3 exit plane is shown in Fig. 5.2. At midspan and $\phi = 0.450$ (see Fig. 5.2(c)) the free-stream is

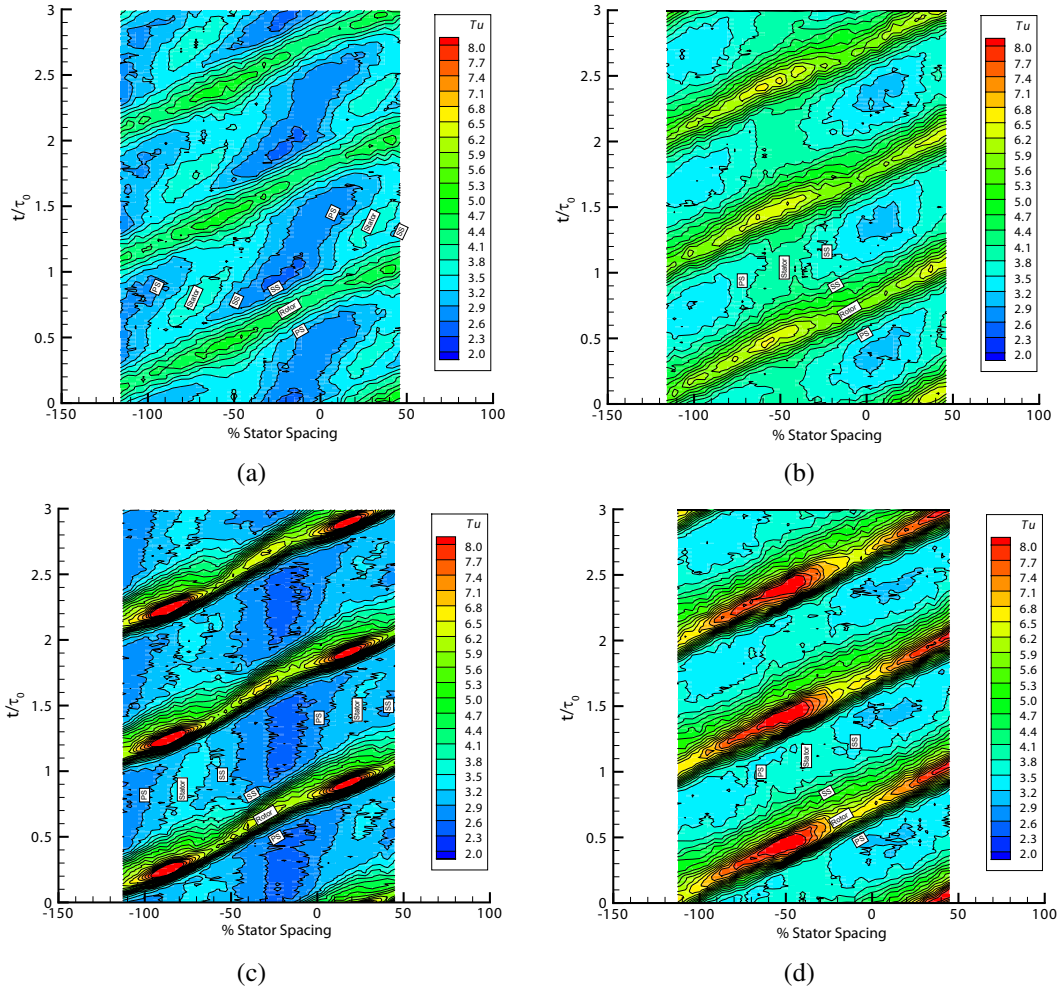

Figure 5.3: S-T diagram of random unsteadiness, Tu, at Rotor 3 exit plane: a) 80% span peak efficiency, b) 80% span near stall, c) 50% span peak efficiency, d) 50% span near stall

characterised by low radial flow angle ($0^\circ < \beta < 3^\circ$). The rotor wake is characterised by a radial flow angle above that in the free-stream. This is caused by the centrifugal force tending to transport the lower momentum fluid in the wake radially outwards. The large radial flow angle ($\beta > 10^\circ$) is due to a combination of the rotor-hub corner separation and the interaction of stator 2 and rotor 3 wake street. Large radial velocities will transport the low momentum fluid towards the casing, thereby redistributing the loss into the downstream blade row. The rotor wake can be observed to be discontinuous between -50% and -30% stator spacing, caused by the potential interaction from stator 3. At 80% span and $\phi = 0.450$ (see Fig. 5.2(a)) the rotor wake is characterised by a band of negative followed by positive radial flow angle. The peak radial flow angle in the rotor wake has decreased from 10° to 5° compared to that at midspan.

As the rig is throttled to $\phi = 0.400$ the fluctuations in the radial flow angle increase. Again at 80% span the wake is characterised by a band of negative followed by positive ra-

dial flow angle (see Fig. 5.2(b)). In addition a region of negative flow angle ($\beta < -6^\circ$) has developed at both 50% and 80% span between -50% and -30% stator spacing. This region corresponds to the location of stator 3 leading edge and stator 2 wake street. Between the rotor wakes at 50% span and $\phi = 0.400$ the radial flow angle has reduced to approximately -3°.

The exit random unsteadiness, Tu is shown in Fig. 5.3 for 50% and 80% span at $\phi = 0.450$ and $\phi = 0.400$. The levels are based on the percentage of the average rotor relative velocity ($\overline{W}$) at a given point. The location of the rotor and stator wakes are labelled in the figure, along with the suction and pressure side of the wake. At $\phi = 0.450$ the free-stream Tu is approximately 3% increasing to 4% at $\phi = 0.400$. Stator 2 wake street is visible, as vertical lines of elevated Tu. The upstream stator wake street is no longer continuous and is terminated by the rotor wakes. The rotation of the wake street through the rotor passage is governed by the lift (circulation) of the blade row. The presence of stator 2 wake street adjacent to the rotor wake leads to an interaction which can significantly increase the level of Tu. Due to the mixing of the upstream stator wakes which acts to restrict the relative flow within the rotor wake. Therefore, the avenue of chopped stator wake segments effectively form barriers against which the low momentum rotor wake fluid accumulates. At the reduced ϕ, the second-stage stator wake segments are hardly visible against the background Tu, due to the accelerated mixing experienced. A detailed look at Tu of the incoming flow at midspan is presented in Fig. 5.4(a). Here the levels of Tu are examined when the measurement location is in the centre of stator 2 wake street, -75% and -50% stator spacing for peak efficiency and near stall respectively and when the measurement location is outside the upstream stator wake street -25% and 0% stator spacing. At $\phi = 0.450$ and 50% span the level of Tu outside of the upstream stator wake remains constant at approximately 3%. The free-stream Tu distribution aligned with the upstream stator wake is characterised by slightly higher levels of Tu with a non-constant value between successive wakes. At $\phi = 0.400$ the enhanced mixing results in a faster rate of decay of the upstream stator street and thus a higher average Tu than at $\phi = 0.450$ but less variation in the free-stream with circumferential position. The higher free-stream Tu results in a faster rate of decay of the rotor wake as well. This is evident in the top half of Fig. 5.4(a) where the maximum Tu in the wake has decreased slightly from that at $\phi = 0.450$, coupled to a significant broadening of the wake.

Plotted in Fig. 5.4(b) are the measured axial velocity distributions at exit of the third-stage rotor at the same two clocking positions in Fig. 5.4(a). At $\phi = 0.450$, the characteristics of the rotor wake velocity disturbance vary continuously with position relative to the stator wake street. Within the stator wake street the rotor wake width and velocity deficit are both appreciably smaller, being reduced by a factor of approximately 2 from their max-

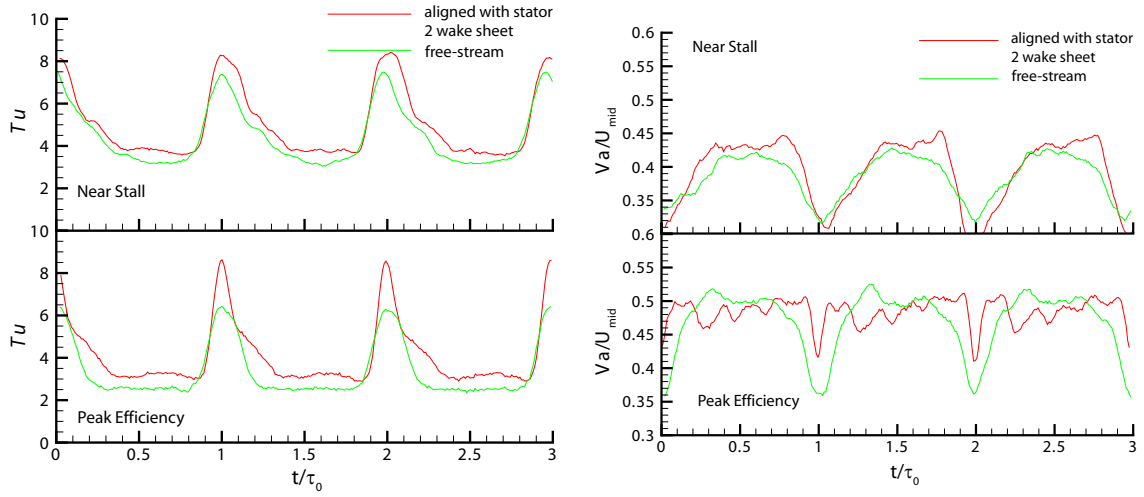

(a) (b)

Figure 5.4: Temporal variation of ensemble-average random unsteadiness, Tu, and axial velocity, V_a/U_{mid}, at Rotor 3 exit plane; variation with ϕ and clocking.

imum values outside of the street. As explained earlier the stator wake segments are no longer aligned due to the rotor's circulation. Therefore the clocking position at -75% stator pitch is intermittently within the stator wake segment. Therefore, the increased Tu is only observed for a fraction of the rotor passing. This results in a non-constant free-stream velocity distribution, compared to when the probe is outside of the influence of the wake street. Similar observations were made by Lockhart and Walker (1974) in a 1.5 stage low-speed compressor. The distribution of V_a/U_{mid} at $\phi = 0.400$ does not show any significant variation with clocking position. This is due to the enhanced mixing of the upstream stator wake resulting in a more uniform free-stream distribution of Tu (Fig. 5.4(a)).

The level of free-stream Tu has a significant effect on wake dispersion and thus ultimately boundary layer transition processes. High free-stream Tu enhances the dispersion of wake street. This modifies the interaction of a stationary frame blade row wake with one in the rotating frame of reference, leading to a significant decrease in periodic unsteadiness experienced by a downstream stator. These observations have important implications for multistage compressors where the number of blades in a blade row are likely to be different throughout the machine. This will inevitability result in blades operating continuously in the wake street from two blade rows upstream. A number of authors have investigated clocking effects in compressors such as Walker et al. (1999); Mailach and Vogeler (2004); Henderson et al. (2006).

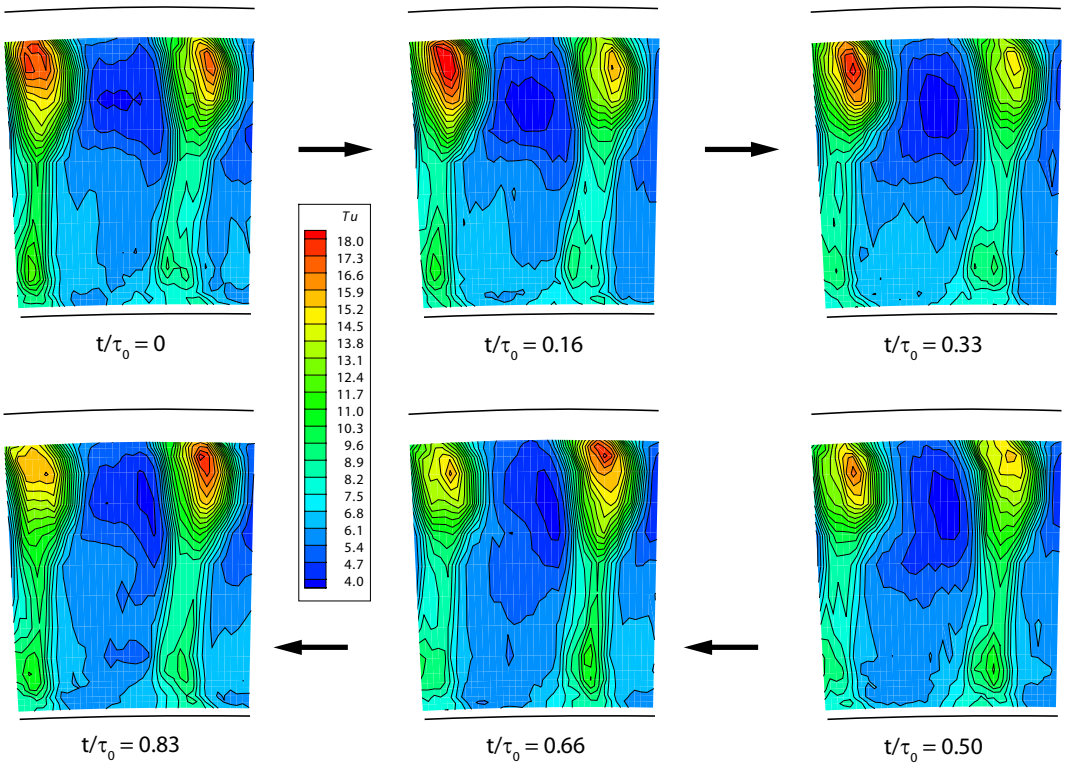

Figure 5.5: Unsteady snap shots of Tu at Stator 3 exit plane, peak efficiency

5.3 Stator Exit

In the previous section the time varying exit conditions from the third-stage rotor was described at two radial heights, 50% and 80% span. In this section, the time varying conditions at the stator exit flow will be discussed.

Unsteadiness at the exit of the stator arises due to interaction of at least three different mechanisms: I) the presence of rotor exit flow including wakes, secondary flow and tip clearance flow being convected through the stator passage which have not fully mixed out, II) the shedding of vorticity from the stator trailing edge due to time varying stator circulation caused by the passage of the rotor flow over the stator surface, and III) the presence of a potential field due to upstream and downstream rotors.

5.3.1 Unsteady Flow Field at Stator Exit

In this section, the time-resolved evolution of the flow field at stator 3 exit plane will be discussed. Figures 5.5–5.8 show several perspectives of the stator exit flow frozen at the same instant in time within a rotor passing period. Six frames from the passage of the rotor blade across the stator passage is shown. The interpretation is based on the analysis of 300 frames over 3 rotor blade passings. These times are arbitrary as the location of the rotor

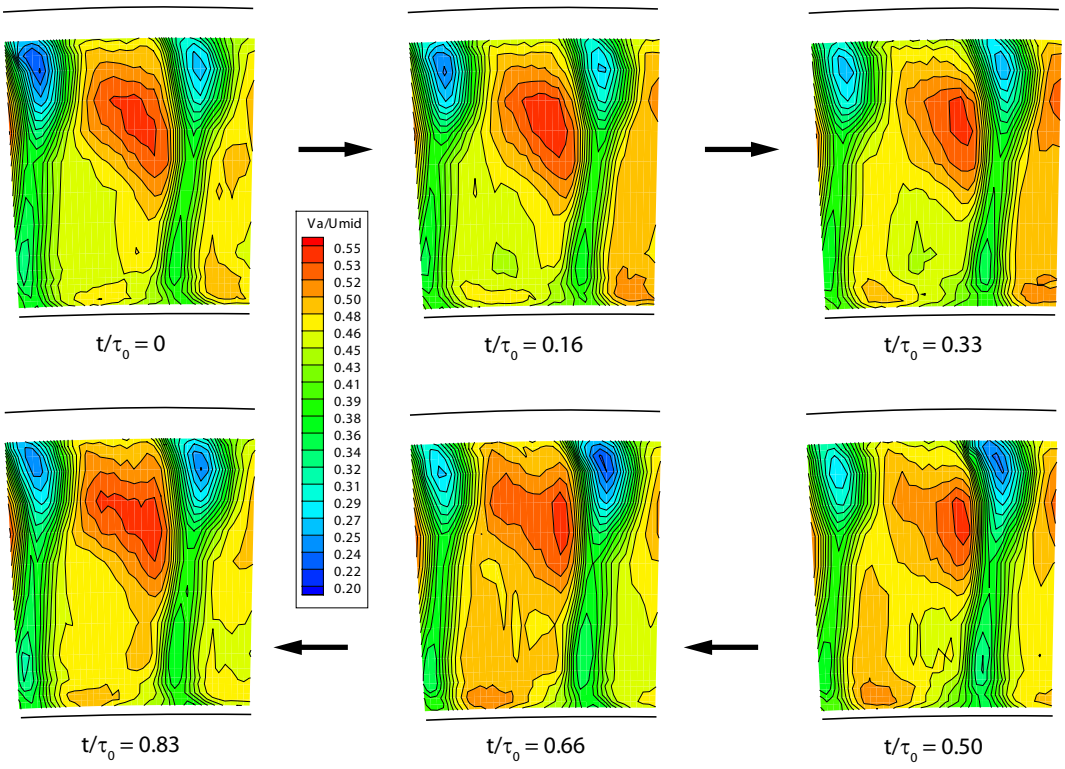

Figure 5.6: Unsteady snap shots of V_a/U_{mid} at Stator 3 exit plane, peak efficiency

blade with respect to the stator is not known. The discussion is focused on the influence of the rotor passing on the stator behaviour.

The distribution of random unsteadiness and axial velocity at peak efficiency are shown in Figs. 5.5 and 5.6 which give a complete perspective on how the flow field downstream of the stator is changing with passage of the rotor. The levels of Tu are based on the percentage of the average velocity ($\overline{V}$) at a given point. It can be seen that the stator wake behaves differently across the span with passing of the rotor.

At $t/\tau_0 = 0.00$ a small asymmetry is observed in the stator wake between 70% and 90% span. The left most stator wake is characterised by increased Tu and velocity deficit compared to the right most stator wake. The asymmetry between the two wakes peaks at $t/\tau_0 = 0.16$. Between $t/\tau_0 = 0.16 - 0.33$ the region of high Tu is significantly reduced in the left most stator wake. At the same time a corresponding increase in V_a/U_{mid} is observed to occur. Between $t/\tau_0 = 0.50 - 0.66$ the random unsteadiness at 80% span continues to decrease, but now the distribution of random unsteadiness in the right most stator wake starts to increase. This is coupled with a decrease in axial velocity in the same wake. Between $t/\tau_0 = 0.66 - 0.83$ the random unsteadiness can be observed to continue to increase in the right stator wake, but now the left stator wake unsteadiness also starts to increase. The velocity deficit has already started to decrease for the right wake, with a

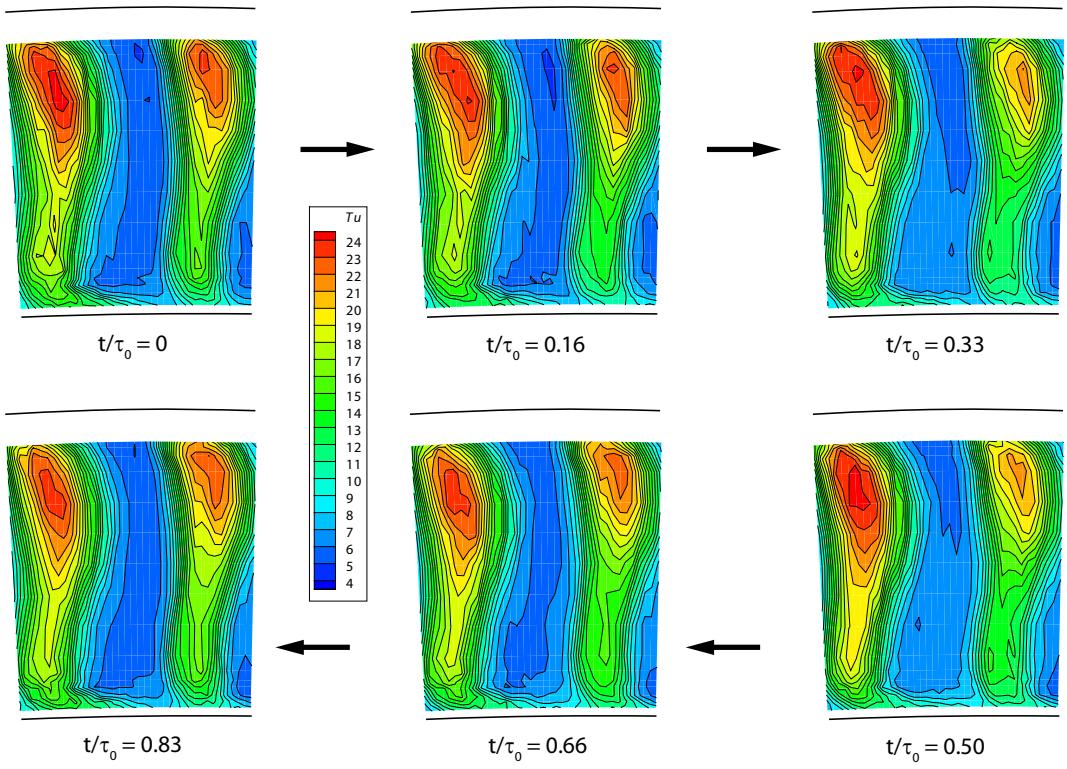

Figure 5.7: Unsteady snap shots of Tu at Stator 3 exit plane, near stall

increase in the left wake observed.

The free-stream distribution of Tu and V_a/U_{mid} shows variation with rotor passing period. At $t/\tau_0 = 0.00$ the region of low random unsteadiness and high axial velocity is confined to the upper most 50% of span. As the rotor passing period advances from $t/\tau_0 = 0.00 - 0.66$ the region of low random unsteadiness and high axial velocity is observed to migrate towards the hub. At $t/\tau_0 = 0.66$ free-stream random unsteadiness has reduced by 1% of Tu and the axial velocity has increased by 0.05 of V_a/U_{mid}. After $t/\tau_0 = 0.66$ the high momentum and low unsteadiness fluid begins to retreat again.

The distribution of random unsteadiness and axial velocity at near stall is presented in Figs. 5.7 and 5.8 respectively. At the reduced flow coefficient a greater variation in the stator wake can be observed with passing of the rotor. As at $\phi = 0.450$ this variation is brought about by the time varying influence of the stator loss core located near the casing.

At $t/\tau_0 = 0.00$ the blockage generated by the loss core of the left stator wake is at a maximum. The left stator wake is characterised by increased random unsteadiness and velocity deficit over the whole span compared to the right stator wake. As the time advances from $t/\tau_0 = 0.00 - 0.50$ the velocity deficit in the left wake below 50% span starts to decrease, although the circumferential extent remains approximately the same. At the same time the velocity deficit of the right side wake can be observed to increase. The low

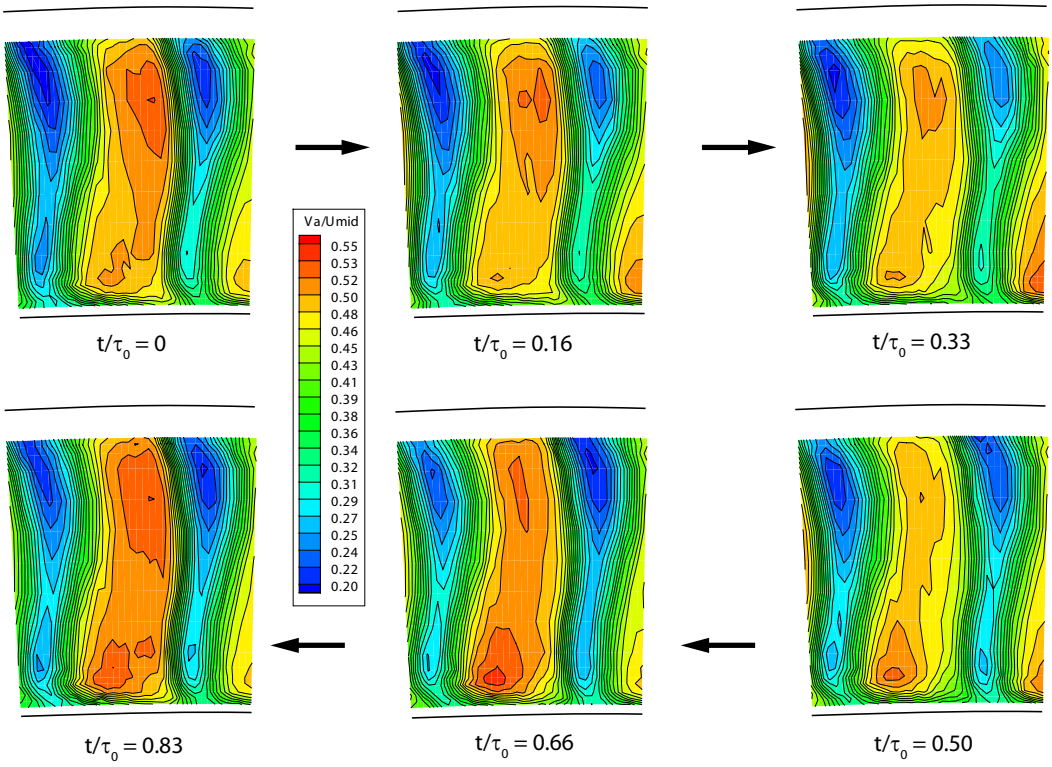

Figure 5.8: Unsteady snap shots of V_a/U_{mid} at Stator 3 exit plane, near stall

momentum fluid at approximately 80% span starts to migrate towards the hub. This is coupled to a small low momentum region at approximately 15% span that starts to migrate radially outwards. By $t/\tau_0 = 0.66$ these two low momentum regions in the right stator wake coalesce. At this time the left stator wake velocity deficit across the whole span is at a minimum. This is evident in the random unsteadiness with the distribution in the left wake at a minimum and that in the right wake at a maximum. From $t/\tau_0 = 0.66$ the velocity deficit in the right wake starts to reduce with the velocity deficit in the left wake beginning to increase to its maximum at $t/\tau_0 = 0.00$.

A small variation of random unsteadiness and axial velocity is also observed in the free-stream with rotor passing. At $t/\tau_0 = 0.50$ and $t/\tau_0 = 0.83$ the distribution of V_a/U_{mid} in the free-stream is at a minimum and maximum respectively. A max variation of 0.07 V_a/U_{mid} between these two time instances can be seen to occur.

From the above description of the flow field it can be concluded that the stator flow field is adversely affected by the propagation of the rotor wake. The velocity distribution of the stator wake almost appears to breathe, brought about by the upstream rotor wake passing. However, this breathing occurs at different times at various radial heights. This is most certainly due to differential wake decay and shearing of the rotor wake as it passes through the stator passage. The largest variation was observed to occur at approximately 80% span

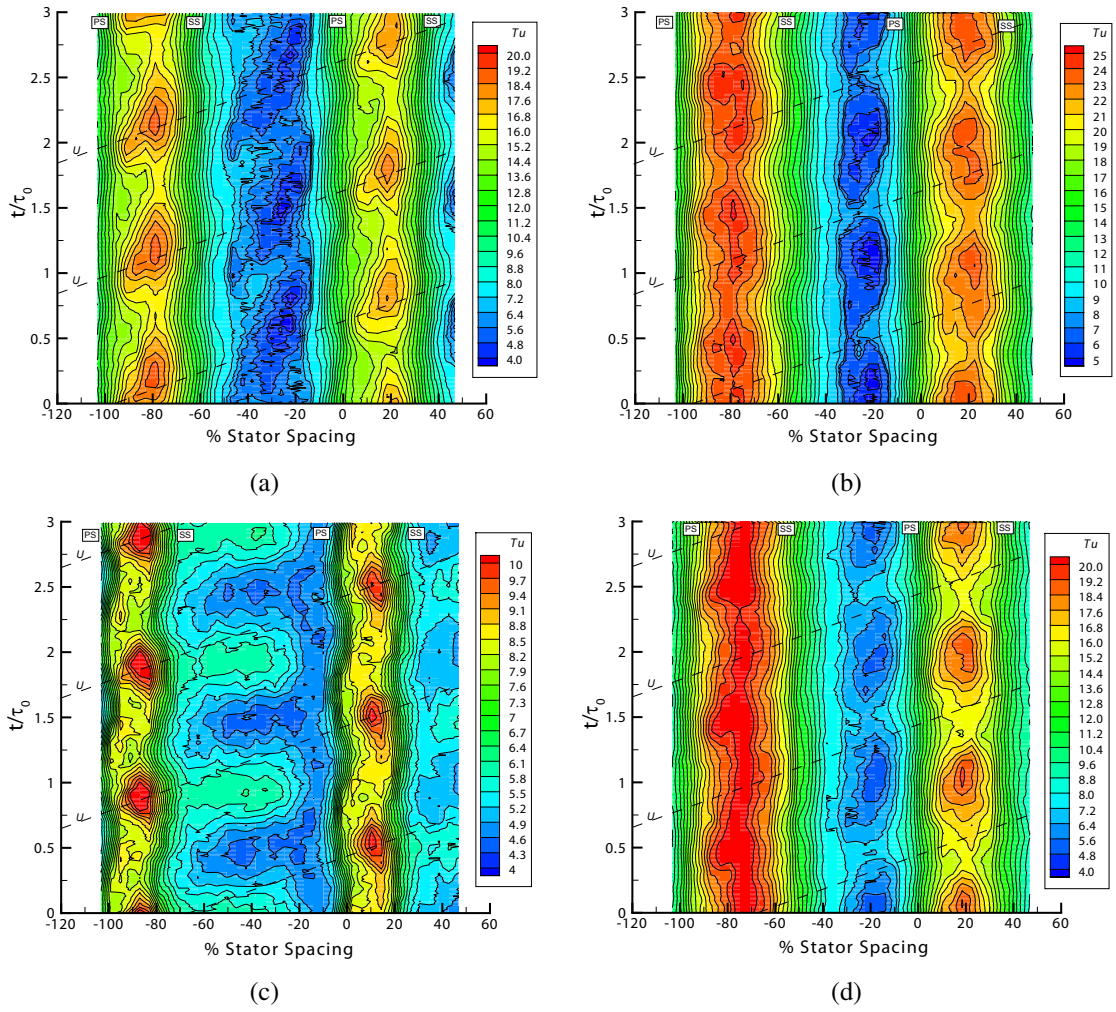

Figure 5.9: S-T diagram of random unsteadiness, *Tu*, at Stator 3 exit plane: a) 80% span peak efficiency, b) 80% span near stall, c) 50% span peak efficiency, d) 50% span near stall.

in the suction surface and the lowest at 50% span for both flow coefficients. There is certainly an influence of rotor 4 which will affect the stator wake behaviour through the potential influence, but it is difficult to separate from the viscous interaction caused by rotor 3.

5.3.2 Blade-to-Blade Distribution

5.3.2.1 Measurement

The blade-to-blade profiles of random unsteadiness, axial velocity and yaw angle at peak efficiency and near stall are presented for two representative radii, 50% and 80% span. The data is presented in the form of S-T diagrams. The dashed lines marked in the Figs. 5.9-5.10 are used to represent the passing of three rotor blades drawn at the rotor wheel speed.

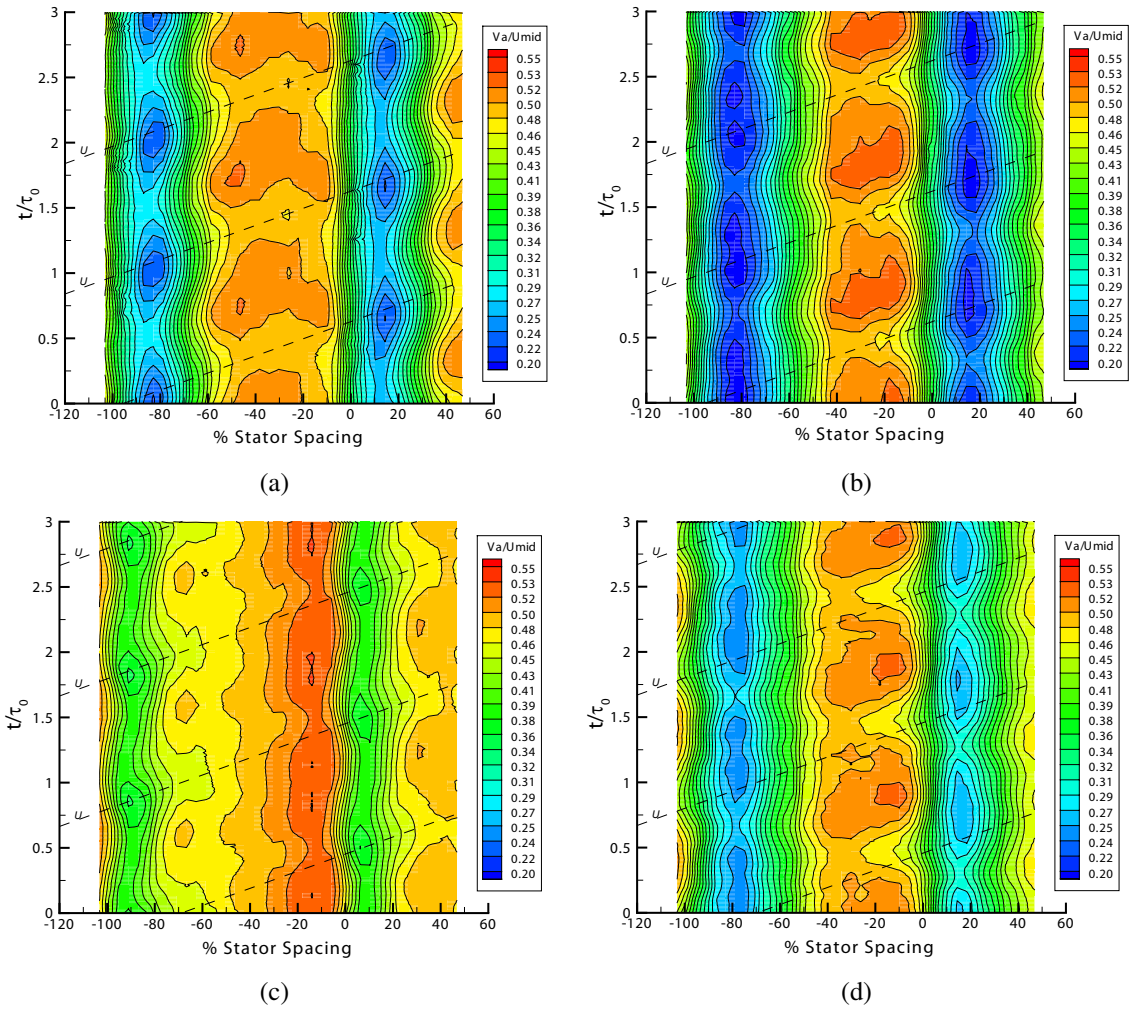

Figure 5.10: S-T diagram of axial velocity, V_a/U_{mid}, at Stator 3 exit plane: a) 80% span peak efficiency, b) 80% span near stall, c) 50% span peak efficiency, d) 50% span near stall.

Again the location of these dashed lines are arbitrary as the location of the rotor blade with respect to the stator is not known.

The distribution of random unsteadiness as a function of space and time at stator 3 exit is shown in Fig. 5.9. Labelled in the figure are the suction and pressure side of the stator wake. The stator blade wakes are seen as the two vertical regions of elevated Tu. At peak efficiency and 50% span (see, Fig. 5.9(c)) the random unsteadiness in the stator wake is modulated with the rotor passing period. As the rotor wake propagates through the stator passage the unsteadiness in the stator wake increases by approximately 2% of Tu. A region of elevated random unsteadiness (approximately 2% higher than the surrounding free-stream) that is in phase with the rotor blade passing frequency occurs between the stator wakes. This region does not extend right across the passage and is approximately parallel to the s-axis indicating that it occurs almost instantaneously. As this region does

not convect across the passage it is unlikely to be the remains of rotor 3 wake street. It is possible that this region is associated with stator 2 wake. Stator 2 wake street would not appear continuous at stator 3 exit plane. The discontinuous stator wake is caused by rotor 3 chopping the wake street into segments. Although the levels of unsteadiness present in this region are higher than that which would be expected from stator 2 wake alone (see, Fig. 5.3(c)).

At 80% span (see, Fig. 5.9(a)) the increased blockage caused by the stator wake is evident. Again the peak unsteadiness in the stator wake is in phase with the rotor passing. The peak unsteadiness measured is 20% of Tu compared to 10% of Tu at 50% span. The asymmetry in the wake is also evident with the peak unsteadiness in the left stator approximately 2-3% higher than the right wake. In the free-stream a region of elevated unsteadiness (approximately 3% higher) which occurs once every blade passing period can be observed. Unlike the increased unsteadiness present in the free-stream at 50% span (see, Fig. 5.9(c)), this region does not occur instantaneously and is convected at approximately 0.4 of the rotor blade speed, U. This region is therefore likely to be caused by rotor 3 wake street convecting through the stator passage.

At the near stall operating point the increase in wake width and random unsteadiness is immediately evident at both radii. The variation in the distribution of unsteadiness at 50% span (Fig. 5.9(b)) and 80% span (Fig. 5.9(d)) is very similar. This is caused by the increase in the spanwise extent of the loss core from peak efficiency towards near stall. At near stall the asymmetry between the two stator wakes has increased. The left stator wake shows an increased level of unsteadiness compared to the right stator wake. At 50% span the peak unsteadiness in the stator wake has increased by 10% of Tu from that at $\phi = 0.450$ and at 80% span the peak unsteadiness has increased by 5% of Tu. The free-stream unsteadiness is also modulated at both radii in a similar manner to that at 80% span and peak efficiency.

The blade-to-blade distribution of axial velocity as a function of space and time at stator 3 exit plane is presented in Fig. 5.10. At both operating points and radii the influence of the periodic passing of the rotor wake is evident. The stator wake is seen to pulse (increase and decrease in size) as the rotor passes. This pulsing is caused by the time varying inlet angle (see, Fig. 5.1) and hence loading. The periodic fluctuation of the stator wake deficit and width occurs at different rotor blade passing periods between the two stator wakes shown. A region of reduced axial velocity can be observed to link the minima in the stator wakes. The reduction in axial velocity in the free-stream is caused by the periodic passing of rotor 3 wake street.

At 50% span and peak efficiency (see, Fig. 5.10(c)) the maximum velocity deficit in in the stator wake occupies approximately 0.3 of t/τ_0. This increases to 0.8 of t/τ_0 at 80% span (see, Fig. 5.10(a)). As the flow coefficient is reduced to $\phi = 0.400$ the maximum

velocity deficit increasingly occupies more of the rotor passing period. At 80% span (see, Fig. 5.10(b)) the maximum velocity deficit occurs over the complete rotor passing period for both stator wakes.

It is well known that the low momentum fluid in the rotor wake in a compressor migrates towards the pressure side of the downstream stator (Kerrebrock and Mikolajczak, 1970), but the time-resolved velocity distribution in Fig. 5.10(c) and the time-average data (see, Figs. 4.12(a) and 4.13(b)) suggests that a different phenomenon is taking place as the high momentum fluid has accumulated on the pressure side of the stator wake. The free-stream velocity distributions shown in Chapter 3 and in Fig. 5.10 for 80% span peak efficiency and near stall at 50% and 80% span show a more circumferentially uniform free-stream distribution. The gradient in axial velocity is due to a region of low axial momentum fluid (0.035 of V_a/U_{mid} lower than the surrounding free-stream) located between -80% and -60% stator spacing, that occurs intermittently with rotor passing. This low momentum fluid is orientated parallel to the s-axis suggesting that it is not convected across the pitch, but is switched on/off by the rotor passing. It is located in time just after the maximum velocity deficit and the region of elevated random unsteadiness observed in the free-stream in Fig. 5.9(c). The location of stator 2 wake street at inlet to stator 3 blade row at 50% span and $\phi = 0.450$ is approximately mid-pitch (see, Fig. 5.3(c)), whereas at the other conditions stator 2 wake street is aligned with stator 3 leading edge. Stator 2 wake street for peak efficiency and 50% span would therefore be able to convect between the stator blades and assuming that it did not mix-out completely by the time it reached stator 3 exit would be visible. Whereas at the other conditions stator 2 wake street would coalesce with stator 3 boundary layer fluid.

5.3.2.2 Peak Efficiency Prediction

The predicted time-resolved blade-to-blade variation of random unsteadiness and axial velocity at the stator exit plane is presented in S-T diagram format in Fig. 5.11 for peak efficiency. The s-axis is the non-dimensional stator spacing covering three stator pitches and the t-axis is the non-dimensional blade passing period covering two rotor periods. The dashed lines marked in Fig. 5.11 represent the passing of three rotor blades drawn at the rotor wheel speed U. Details of the computational domain, boundary condition and turbulence model are given in §3.5.4.

Figure 5.11(a) presents the predicted turbulence, Tu, calculated from the turbulent kinetic energy from the CFD solution and the time-average velocity, $\overline{V}$ at a given point using Eqn. 3.54. Marked in the figure is the location of the pressure and suction side of the stator wake and rotor wake. Good agreement is seen between the measured and predicted unsteadiness especially in the free-stream. The CFD does not correctly predict the rate of

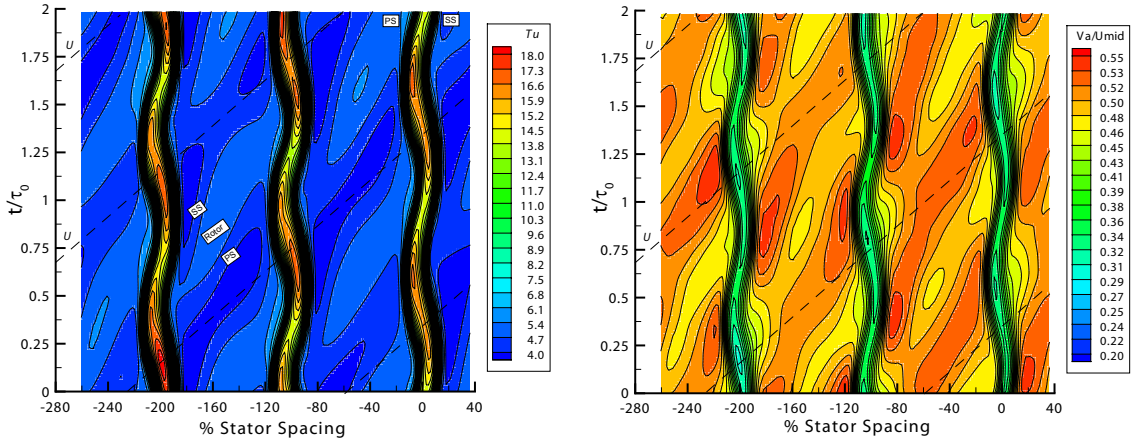

(a) (b)

Figure 5.11: Predicted S-T diagram taken downstream of stator in 2D numerical calculation: a) random unsteadiness, b) axial velocity.

mixing in the stator wake (see, Figs. 5.10(c) and 5.11(b)). This causes the turbulence in the stator wake to be over-predicted by approximately 6-8% of Tu. The predicted locations of maximum turbulence correlates with rotor passing as in the measurements. The influence of the rotor is also observed at stator exit. The effect of differential convective velocity between the pressure and suction surface is clearly evident in Fig. 5.11(a), with the rotor wake on the suction side of the stator wake arriving at the stator exit plane before the pressure side. A differential rotor wake width can also be observed. The pressure side leg is substantial wider than the suction side leg. This is caused by the negative jet, where the low momentum fluid in the rotor wake is transported and accumulates on the stator pressure side.

The predicted axial velocity distribution is shown in Fig. 5.11(b). As already noted the velocity deficit in the predicted stator wake is higher than the experiment by approximately 0.04 V_a/U_{mid}. The slower rate of mixing in the CFD results in a more pronounced rotor wake. The experimental data showed a blade-to-blade gradient in axial velocity, with the higher momentum fluid located on the pressure side of the stator wake and a region of evaluated free-stream Tu orientated approximately parallel to the s-axis. The predicted distribution does not show either of these trends. If this phenomenon was linked to stator 2 wake street then this would explain why these trends are missing in the predicted data.

5.4 Wake Convection Through a Stator Blade Row

The unsteady flow field in a compressor is governed by a combination of potential and convective interactions. Of these, the convected wakes from upstream blade rows play the

most significant role due to their effect upon the blade boundary layers. The primary effect of the wake convection is to dictate boundary layer transition and so it is the turbulence of the wake and the convection of the turbulent quantities through the blade row that is of prime importance. In this section the prediction of the wake convection through the stator blade row at 50% span and $\phi = 0.450$ is presented and described.

5.4.1 Velocity Field

The unsteady velocity field at six different instants during one period are presented in Figs. 5.12(a)-(f) to demonstrate the transport of upstream rotor wakes through the stator passage and the resulting disturbance to the stator flow field. The location of the rotor wake in the passage is more easily observed by the perturbation velocity vectors of Fig. 5.13 or unsteadiness field of Fig. 5.14, the position of the rotor wake may be located in Fig. 5.12 by the deficit in the velocity.

The influence of the rotor on the stator passage can be determined from Fig. 5.12. The location of maximum velocity (labelled A) on the suction surface is directly affected by the convection of the rotor wake through the blade row. The peak velocity slowly decreases through Fig. 5.12(a)-(c), while remaining in approximately the same position on the suction surface. This is caused by a reduction in the induced perturbation as the trailing boundary of the wake convect further downstream. Between Fig. 5.12(b) and (c) a velocity overshoot starts to emerge and grow at the blend point between the leading edge circle and the suction surface. This is caused by the interaction of the rotor wake and the stator's leading edge (see, Fig. 5.15). By the time of Fig. 5.12(d), the wake centre has passed the stator's leading edge. The magnitude of the perturbation velocity at location A has reversed in direction and is directed towards the wake centreline which lies upstream of location A. The perturbation velocity at the trailing boundary of the wake is in the direction of the mean flow and as a result, peak velocity moves upstream to location B and then C in Fig. 5.12(d) and (e) as the wake convects downstream. By Fig. 5.12(f) the location of peak velocity has returned to its original location, A, due to the convection of the wake and the induced perturbation velocity.

It is apparent that the convection of the rotor wake through the stator passage does not just simply raise or lower the peak velocity, but rather the velocity distribution is altered. This will in turn influence the unsteady boundary layer development.

5.4.2 Perturbation Field

The unsteady flow field can be visualised by the perturbation velocity. The perturbation velocity is defined as the difference between the instantaneous and the time-average veloc-

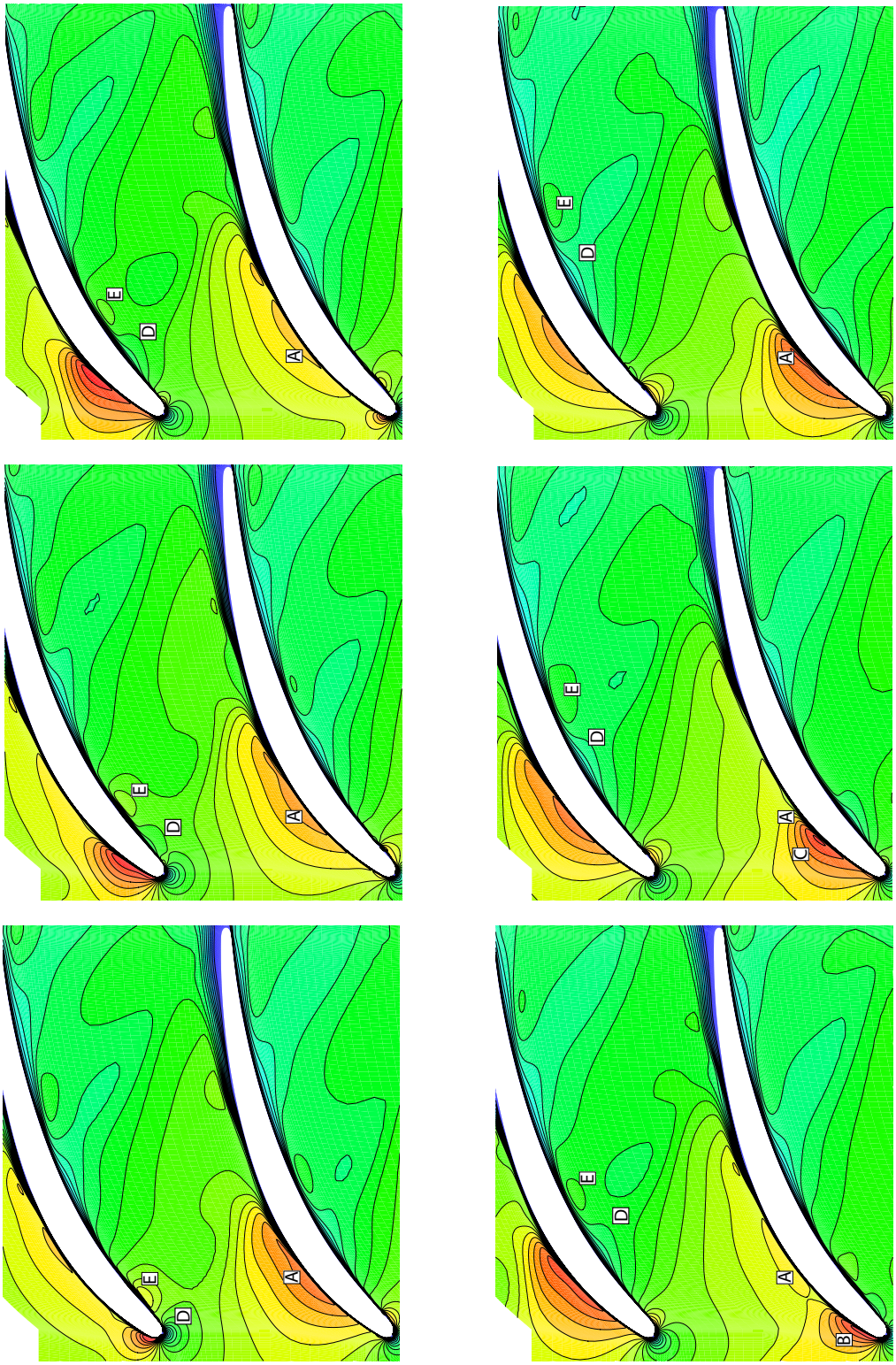

Figure 5.12: Predicted non-dimensional velocity magnitude, V/U, at six equal time intervals through the rotor passing period. Stator 3, 50% span, $\phi = 0.450$.

ities is given by

$$V_{a_p} = V'_a - \overline{V_a} \tag{5.1}$$

$$V_{t_p} = V'_t - \overline{V_t} \tag{5.2}$$

The perturbation velocity vectors are shown at the same six time instants in Fig. 5.13. The location (dashed line, in Fig. 5.13) and shape of the rotor wake is easily identified. The convection of the rotor wake through a blade row is characterised by bowing, re-orientation, elongation and stretching as described by Hodson (1998), although this was for a wake convecting through a turbine, the effect of re-orientation, elongation and stretching can be observed in compressors.

The re-orientation of the wake segment occurs due to the circulation of the stator blade. The velocities near the suction surface are higher than near the pressure surface (see, Fig. 5.12) and so fluid near the suction surface convects through the passage at a higher rate than the fluid near the pressure surface resulting in a re-orientation of the wake segment. Re-orientation of the wake segment is most evident by comparing the angles of the three wake segments seen in Fig. 5.13(c).

The rotor wake is perceived by the stator as a negative jet, pointing towards the source of the wake. The wake and low momentum fluid in the free-stream is convected towards the pressure surface. This is most clearly seen in Figs. 5.13(e)-(a). The high momentum fluid in the free-stream moves in an opposite direction to replace the transported fluid. The negative jet induces two contrarotating vortices appearing on each side of the wake (labelled D and E). The induced vortices have also been reported by Ho and Lakshminarayana (1995) and Valkov and Tan (1995). The influence of the contrarotating vortices are evident in Fig. 5.12, where an increase followed by a decrease in flow velocity can be observed on the pressure side of the passage, due to regions E and D respectively.

As the rotor wake approaches the stator leading edge, the perturbation velocity increases significant. The rotor wake induced incidence changes near the leading edge, which can be seen by the change in the stagnation point in Fig. 5.15. As the rotor wake is transported through the stator passage, the wake is diffused by fluid viscosity and turbulence and as such the fluctuating velocity becomes smaller. As the rotor wake convects further downstream the levels of perturbation velocity decrease, reaching significantly lower values at the trailing edge.

5.4.3 Turbulence Field

The predicted turbulence field, computed from Eqn. 3.54, where the velocity was based on the pitchwise mass-averaged inlet velocity, $\hat{V}$, are presented for the same six instances in Fig. 5.14. By using the mean-velocity at the inlet the interaction of the rotor wakes and

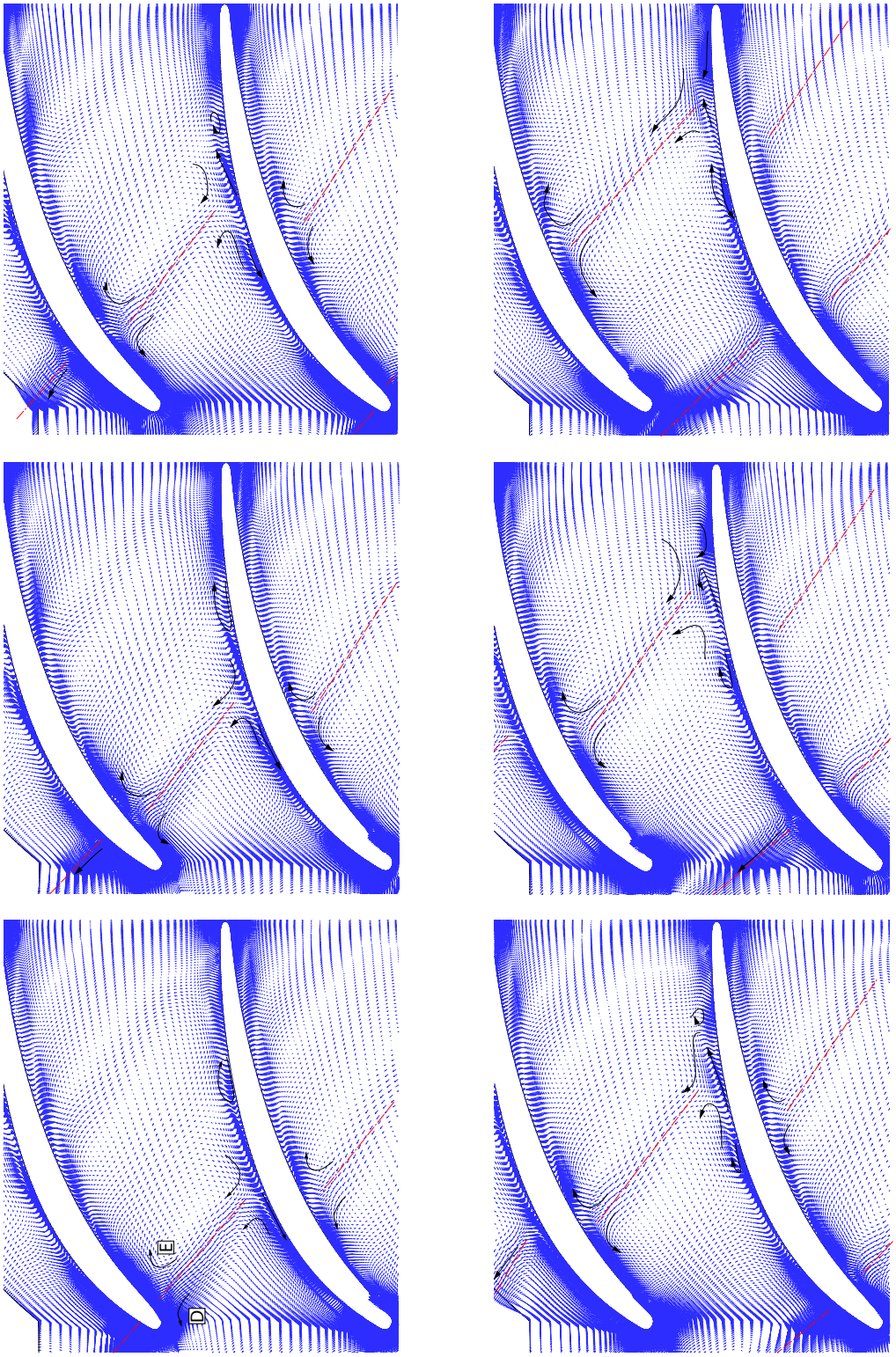

Figure 5.13: Predicted perturbation velocity vectors, at six equal time intervals through the rotor passing period. Stator 3, 50% span, $\phi = 0.450$.

the boundary layer are preserved. If the local time-average value was used, then as the velocity close to the wall is low (zero at the wall) these interactions would be swamped by the turbulence in the boundary layer.

The response of the boundary layer to the wake passing can be seen in Fig. 5.14. Very high levels of turbulence are generated in the boundary layer as the rotor wake impinges on the surface. The boundary layer response to the rotor wake is discussed in Chapter 6.

In Fig. 5.14(a) a region of elevated turbulence ($> 9\%$), region F, can be observed to propagate behind the wake centreline. At G another region of high turbulence from the previous rotor wake can be seen. It is evident from Fig. 5.14(a) that region G is significantly further behind the wake centreline than region F, suggesting that these regions of increased turbulence activity convect at a lower velocity than the wakes. The offset between region G and the wake centerline slowly increases through Figs. 5.14(b)-(d). By Fig. 5.14(e) the centreline of the previous wake is situated over region G and by Fig. 5.14(f) the two regions of increased turbulence start to interact and coalesce. Looking in detail at the propagation of the first region of increased turbulence (region F) through Figs. 5.14(a)-(f), it is evident that the leading and trailing boundaries convect at differing speeds. The trailing boundary convects at a lower velocity than the leading boundary which causes these regions to grow in the flow direction and eventually for the leading boundary of the proceeding region to catch-up and merge. Regions F and G are characteristic of the region of thickened boundary layer experimentally observed by Wheeler et al. (2006). Wheeler et al. (2006) states that these regions provide a favourable environment for the formation of turbulent spots, the front of which propagates at 70% of the wake speed. The trailing edge was found to travel at a reduced wake speed of 60%. The effect of this region on the unsteady boundary layer development is discussed in Chapter 6.

When the rotor wake impinges on the leading edge of the stator an intense region of turbulence is generated (Fig. 5.14(c)). It is from this interaction that regions F/G are generated. As the centreline of the wake moves over the leading edge a region of turbulence associated with regions F/G is lifted off from the surface due to the passing wake (region H, see Fig. 5.14). As region H is convected downstream (Figs. 5.14(e)-(c)), it decays due to the fluid viscosity and is transported along the wake centreline by the negative jet effect. Valkov and Tan (1995) observed a similar phenomena in their two-dimensional unsteady non-linear calculations and described this region as a moving row of B-vortices.

5.4.4 Unsteady Flow Near the Leading Edge

From Figs. 5.12-5.14 it is apparent that the passage of the rotor wake through the stator blade row has a significant influence on the leading edge. Figure 5.15 shows the velocity field, with lines of turbulence superimposed around the leading edge for the six time

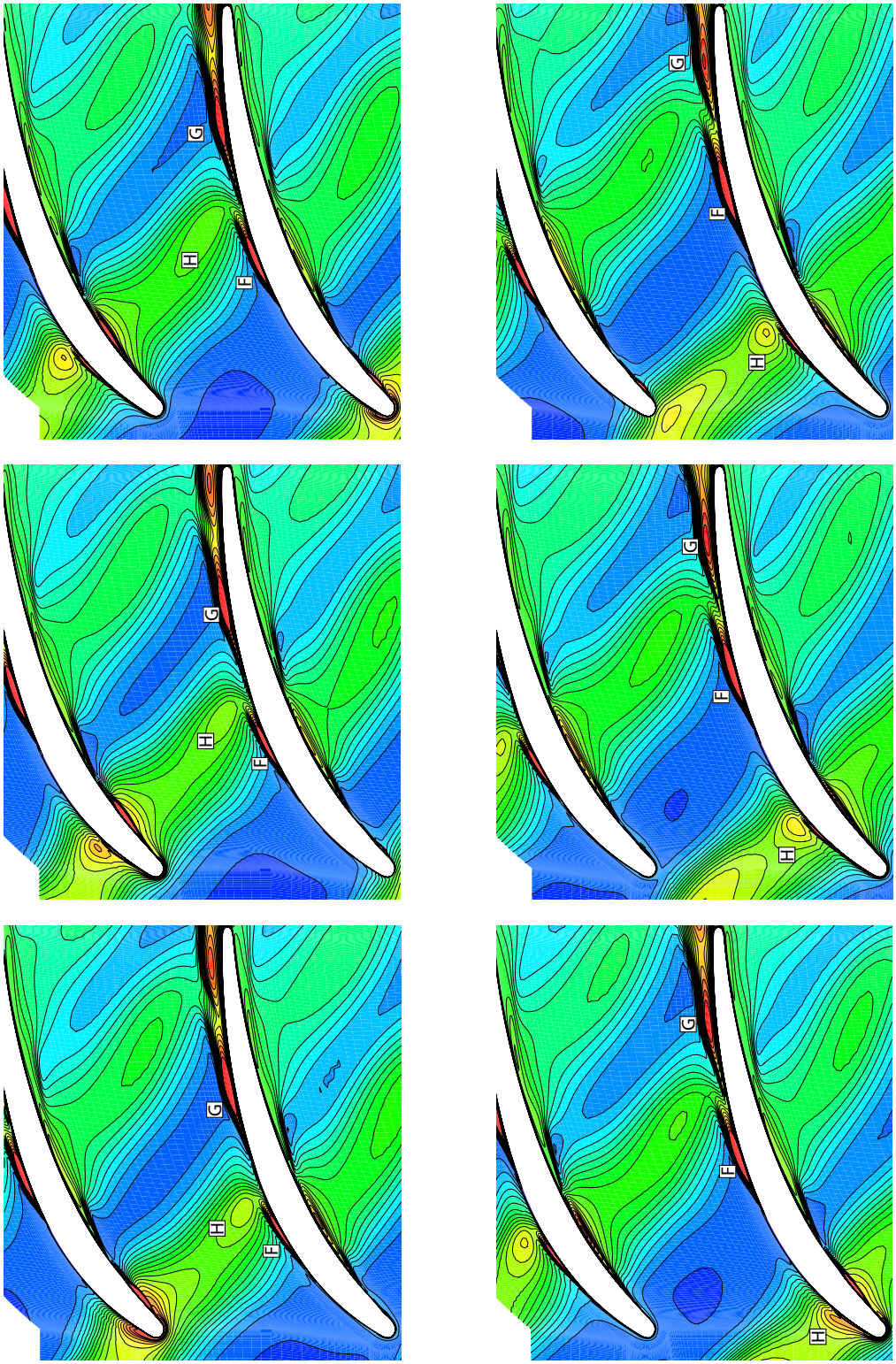

Figure 5.14: Predicted random unsteadiness, Tu, based on the time-average inlet velocity magnitude, $\overline{V}$, at six equal time intervals through the rotor passing period. Stator 3, 50% span, $\phi = 0.450$.

instants.

In Fig. 5.15(a) the rotor wake is just upstream of the stator leading edge and the stator is operating close to zero incidence. By Fig. 5.15(b) the leading boundary of the rotor wake approaches the stator's leading edge. There is a small shift in the stagnation point, resulting in an increase incidence. In addition to the increase in incidence, a separation bubble can be seen on the pressure side blend point. The wake centreline is located at the stator's leading edge in Fig. 5.15(c). This has resulted in a further increase in incidence, which results in an overspeed on the suction surface. The separation bubble seen in Fig. 5.15(b) has increased in height and length. As the wake convects over the suction surface, Figs. 5.15(d)-(f), a region of low momentum fluid can be observed underneath the wake's footprint. This region corresponds to the increased levels of turbulence seen in Fig. 5.14 and is characterised by reduced velocity (negative perturbation velocity, see Fig. 5.13) and increased boundary layer thickness. It can be seen to grow in height whilst it convects downstream. This is caused by the influence of the adverse pressure gradient downstream of peak suction, Figs. 5.13(f)-(b). The development of region H is also evident in Figs. 5.14(d) and (e). The pressure side leg of the convecting rotor wake interacts with the leading edge separation bubble. The increased turbulence in the wake suppresses the formation of the bubble at Figs. 5.15(e) and (f). By Fig. 5.15 the wake has convected downstream. The stator is again operating close to zero incidence. With the passing of the rotor wake the bubble is able to reestablish (see, Fig. 5.15).

5.5 Chapter Closure

Time-resolved measurements downstream of the third-stage rotor and stator in the Cranfield four-stage rig have been presented. In addition a numerical calculation of the rotor wake convecting through the stator blade row at 50% span and $\phi = 0.450$ has been described.

The measurements at the exit plane of the rotor showed that the rotor wake was characterised by high levels of random unsteadiness and increased incidence. The increase in incidence across the wake was 2-3 times that experienced with change in flow coefficient. Therefore the increased incidence and turbulence in a rotor wake will have a significant influence on the unsteady development of a downstream stator's boundary layer. The properties of the rotor wake were found not to be constant, but with local intense regions of elevated unsteadiness that form at the intersection of the third-stage rotor and second-stage stator wakes.

The influence of stator 2 wake street was also measured at the rotor exit plane. The circumferential position of stator 2 wake street varied with span and loading. At 80%

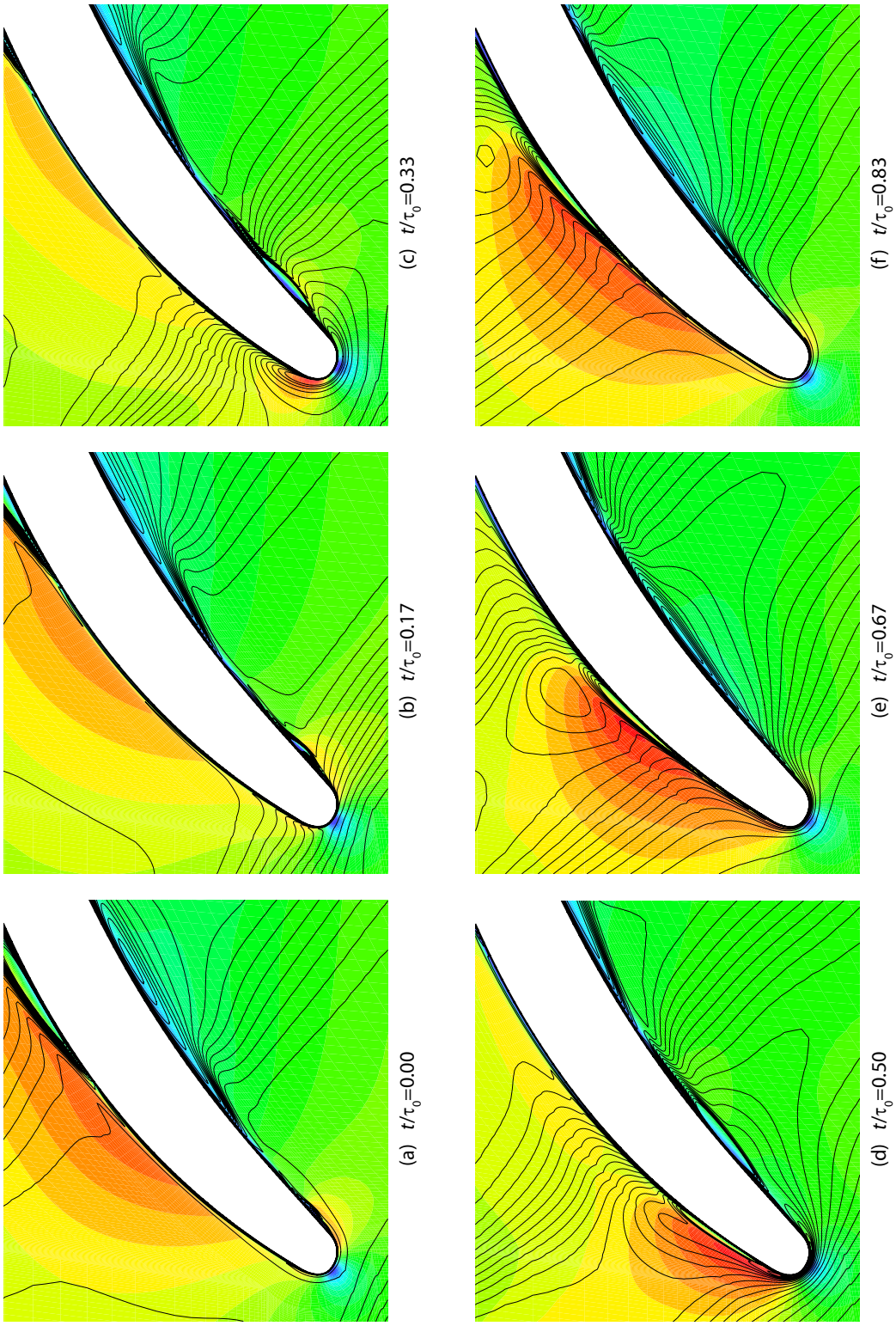

Figure 5.15: Predicted V/U with lines of Tu superimposed, at six equal time intervals through the rotor passing period. Stator 3 leading edge region, 50% span, $\phi = 0.450$.

span, peak efficiency and 50% and 80% span at near stall, stator 2 wake street was aligned with stator 3 leading edge. This will have the effect of elevating the free-stream turbulence experienced by the boundary layers at these radial heights and loading. The level of free-stream turbulence will have a significant affect on wake dispersion and ultimately boundary layer transition. At the reduced flow coefficient operating point the free-stream unsteadiness had increased by approximately 2%. This will enhance the rate of mixing of upstream wakes.

Significant changes occur to the stator exit flow features with passage of the upstream rotor. The separated zones in the stator flow were forced into unsteady periodic motion due to incoming wakes. This effect, in turn, amplifies the wake information, which will be transported further downstream. Increased random unsteadiness was measured at all spanwise locations and at both loading levels in the stator wakes. This increase in unsteadiness appeared at the blade passing frequency. The increase in turbulence and variation in wake width suggests that the boundary layer development is affected by the periodic passing of the rotor.

The numerical predictions of the wake convection confirm that the the wake fluid is, re-orientated, elongated and stretched in the stator blade row. The convection of the rotor wake through the blade row did not just simple raise or lower peak suction, but rather the velocity distribution was altered. By the trailing edge the levels of unsteadiness in the free-stream were significantly reduced due to viscous dissipation and turbulence. The numerical calculations predicted the thickened boundary layer that lags the rotor wake, as experimentally observed by Wheeler et al. (2006). This region is characterised by increased boundary layer thickness, turbulence and negative perturbation velocity.

Chapter 6

Unsteady Boundary Layer Development in a Multistage Environment

6.1 Introduction

In this chapter the unsteady nature of the boundary layer development on the suction surface of the third-stage stator will be described. The aim was to understand the physical picture of boundary layer development in a truly multistage environment, and how this picture changes with flow coefficient. Coupled to this the boundary layer development at 50% span was compared to that developing close to the endwalls. Answers were sought for the following key questions; is transition present, what is its extent and how well does a commercial CFD code predict this? The incoming flow field for Stator 3 was described in Chapters 4 and 5, along with a description of the flow field at the exit of Stator 3.

In this chapter, experiments were performed of the stator suction surface boundary layer. The development of the boundary layer along the middle half of the chord was investigated using traverses of the boundary layer using a hotwire probe. Details of the traverse gear can be found in Chapter 3. As well as the experimental data presented in this chapter, a series of steady and unsteady CFD calculations were performed to aid interpretation of the experimental data.

6.2 The Time Mean Picture

6.2.1 Velocity Distributions

Normalised velocity distributions for the third-stage stator derived from measured static pressures tappings, Eqn. 3.19, are shown in Fig. 6.1. The velocity is normalised by the exit velocity, V_{ex}. At both $\phi = 0.450$ and $\phi = 0.400$ all spanwise heights a clear over-

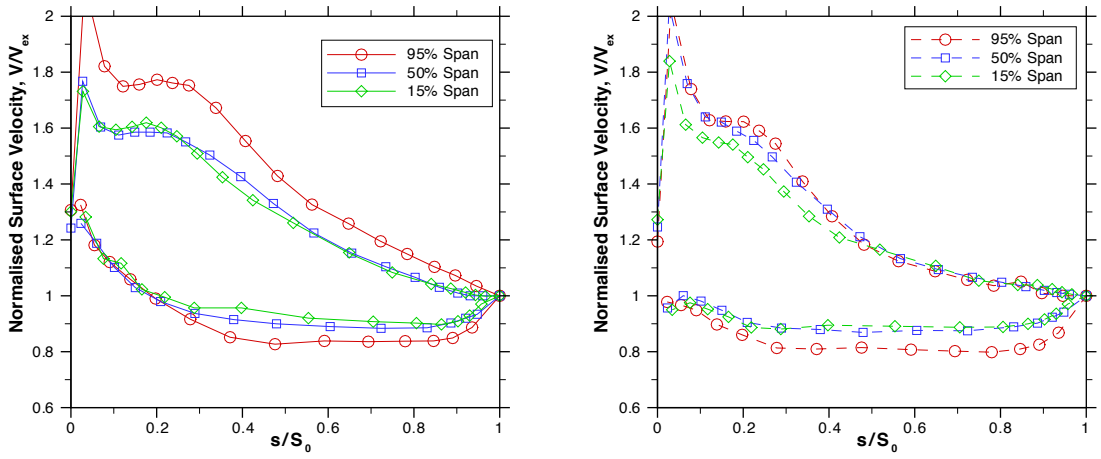

Figure 6.1: Normalised surface velocity for Stator 3 at 15, 50 and 95% span: a) $\phi = 0.450$, b) $\phi = 0.400$.

speed is seen in the velocity distribution. At $\phi = 0.450$ a small amount of acceleration is observed following the over-speed to approximately 0.3 s/S_0. After 0.3 s/S_0 the flow is slowly decelerated to the trailing edge. At $\phi = 0.400$ the strength of the over-speed has increased due to the increased incidence onto the stator. Deceleration of the flow has shifted forward and now occurs at approximately 0.2 s/S_0. The flow is observed to undergo a rapid diffusion between 0.2 s/S_0 and 0.5 s/S_0. This is followed by a plateau in the velocity distribution from 0.5 s/S_0 to the trailing edge for all three spanwise heights. This is indicative of boundary layer separation and is supported by surface flow visualisation (see Fig. 6.2). At $\phi = 0.450$ there is no sign of a separation bubble located after peak suction that is typical of controlled diffusion designs.

6.2.2 Flow Visualisation

Figures 6.2 and 6.3 show the results from surface flow visualisation done on the third-stage stator at $\phi = 0.450$ and $\phi = 0.400$. Next to each figure is a schematic highlighting the important phenomena seen in the flow visualisation. In Fig. 6.2 the flow direction is from right to left whilst in Fig. 6.3 the flow direction is from left to right.

Figure 6.2(b) indicates the main features of the flow at $\phi = 0.450$. Region **A** is the location where the paint has thinned down. This occurs due to the high shear stress present in this region and as such this is the location of maximum surface velocity (excluding the over-speed at the leading edge blend point). The flow direction, indicated by arrow **B**, shows that the flow at mid-span can be regarded as two-dimensional, with the flow separating just fore of the trailing edge. The foot print of the horseshoe vortex is highlighted

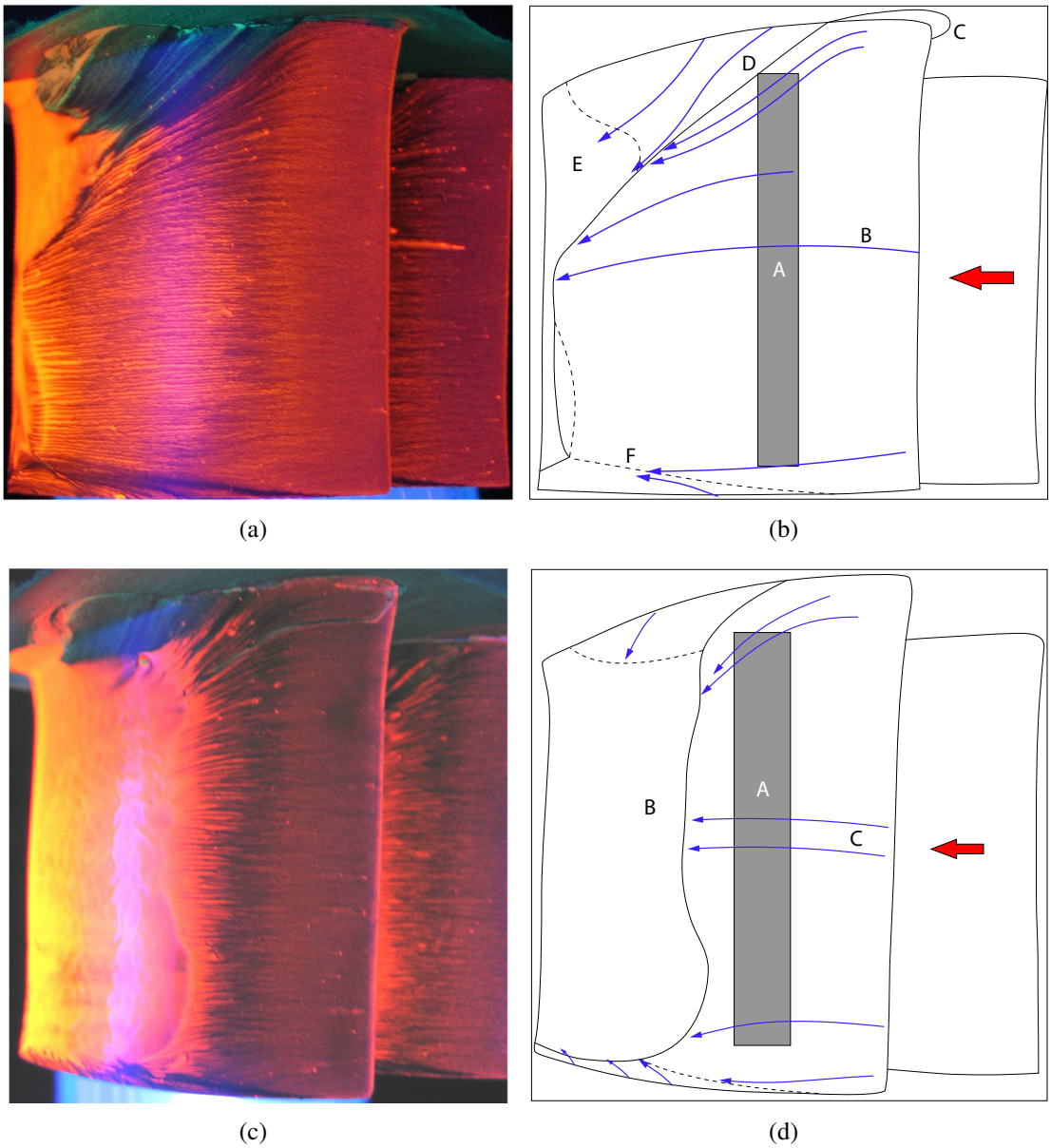

Figure 6.2: Flow visualisation on the suction surface of the third stage stator in the Cranfield LSRC: a) $\phi = 0.450$, b) $\phi = 0.450$ schematic, c) $\phi = 0.400$, d) $\phi = 0.400$ schematic. Flow direction is from right to left.

in region **C**. The suction surface leg of the horseshoe vortex is over-turned and breaches the blade at approximately 0.2 s/S_0. This is indicated in Fig. 6.2(b) by line **D**. This forms the limiting streamline (seen by the convergence of streamlines) that divides the boundary layer flow originating from the casing (green paint) with that on the blade (red paint). Region **E** indicates a region of still wet paint. This occurs in areas of stagnate fluid which are characterised by low shear stress and as such the paint is not removed from the surface. In regions like these paint can actually accumulate. This is characteristic of a corner separation. A second but smaller region of wet paint is seen between 10% and 40% span. Line **F** is formed from flow traveling through the tip clearance and rolling up on the suction surface.

At $\phi = 0.400$ the picture changes completely. The region of reduced paint accumulation, **A** in Fig. 6.2(d), is still present in the same location as seen at $\phi = 0.450$, but a significant area of the suction surface is covered with wet paint, region **B**. The two isolated regions of separated flow at $\phi = 0.450$ coalesce and form a significant region of separated flow that extends from approximately 0.5 s/S_0 to the trailing at all spanwise heights. Before the flow separates at line **B** the flow away from the endwalls is seen to exhibit two-dimensional behaviour, **C**.

Figure 6.3 presents the flow structures on the pressure surface. Although no hot-wire measurements were performed on the pressure surface a qualitative analysis of the boundary layer state can be formed. Looking at $\phi = 0.450$ and $\phi = 0.400$ it is clear that the flow at both operating points are very similar. Therefore only the flow features at $\phi = 0.450$ will be discussed.

A sharp contrast in the flow pattern can be observed in region **A** and that after the dashed-line in Fig. 6.3(b). The change in flow pattern can be associated with the boundary layer flow on the pressure surface undergoing transition. The fact that the line is so distinct would suggest that this process was steady in time. Flow visualisation can only provide qualitative information for processes that occur steady in time. A number of paint filaments can be seen in region **A**. They can be observed to act like turbulators. The flow over most of the surface can be seen to travel in a direction approximately parallel to the annulus. Only in regions close to the endwalls does the flow show signs of secondary flow. Region **B** is a good example of this, where streamlines can be observed to merge together. This is typical of a lift-off line. Below the dashed-line, towards the trailing edge, significant radially outward flow can be observed.

6.2.3 Measured Intermittency

Figure 6.4 presents the time-average peak intermittency, γ_{pk} as measured on Stator 3 suction surface at 50% span and 80% span for $\phi = 0.450$ only. The time-average data for

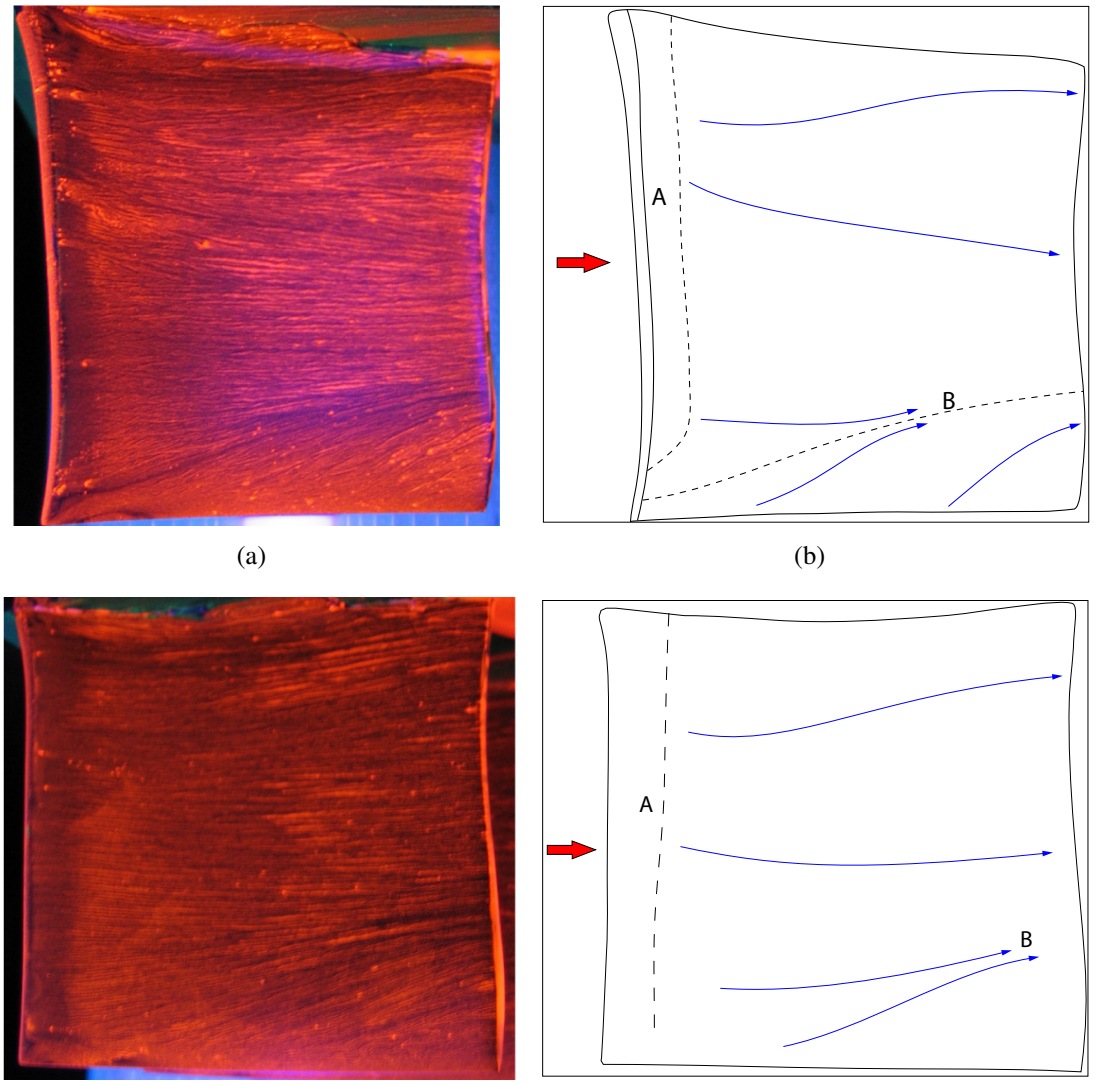

(a) (b)

(c) (d)

Figure 6.3: Flow visualisation on the pressure surface of the third stage stator in the Cranfield LSRC: a) $\phi = 0.450$, b) $\phi = 0.450$ schematic, c) $\phi = 0.400$, d) $\phi = 0.400$ schematic. Flow direction is from left to right.

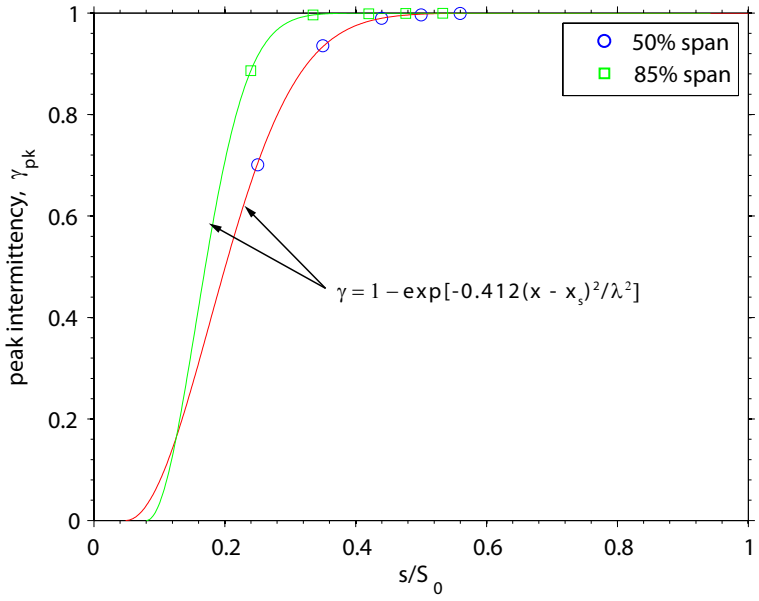

Figure 6.4: Time average peak intermittency, γ_{pk} as measured on Stator 3 suction surface for $\phi = 0.450$: variation with span

$\phi = 0.400$ showed that the boundary layer was fully turbulent, even at the upmost measurement location. The time-average experimental data is fitted to Narasimha's universal intermittency distribution, Eqn. 6.1

$$\gamma = 1 - \exp[-0.412(x - x_s)^2/\lambda^2] \qquad x \geq x_s \tag{6.1}$$

where $\lambda = x_{0.75} - x_{0.25}$. The value of intermittency plotted in Fig. 6.4 is the peak value measured above Stator 3 suction surface at the respective streamwise location. Narasimha's universal intermittency law agrees well with the measured time-average γ_{pk}. Using the fitted universal intermittency law, the location of transition start, x_s, can be extrapolated. This shows that $x_s = 0.04\ s/S_0$ for 50% span and $x_s = 0.08\ s/S_0$ for 85% span. Transition[1] is completed at $0.48\ s/S_0$ and $0.35\ s/S_0$ respectively for 50% and 85% span. From this it can be observed that transition starts close to the leading edge. Comparing the measured intermittency for the two spanwise height it is clear that the transition process occurs closer to the leading edge at 50% span but the length of the transition is shorter for 85% span. It can be seen from the measured surface velocity distribution shown in Fig. 6.1(a), that the loading increases towards the casing. The higher loading levels present would decrease the length of transition, due to the higher diffusion at 85% span, thereby, increasing the spreading rate of a turbulent spot.

[1]Completion of transition is taken to be when $\gamma_{pk} = 0.99$

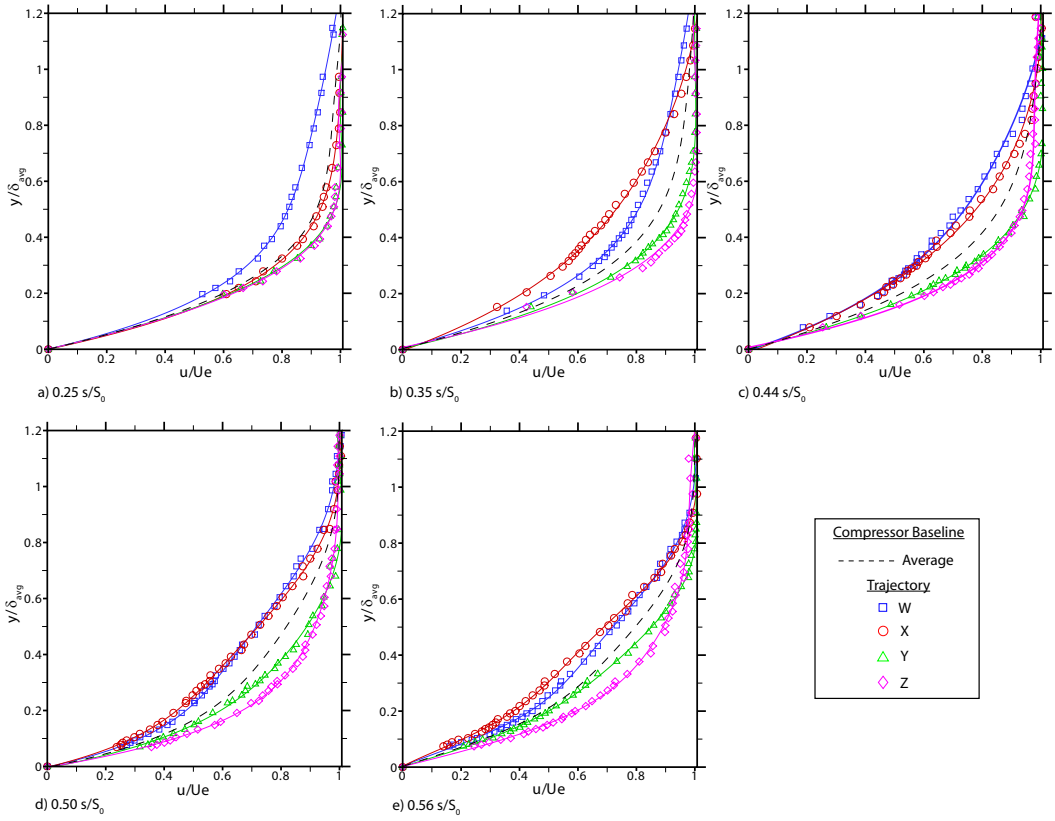

Figure 6.5: Boundary layer profiles for Stator 3 suction surface at 50% span. Trajectories W, X, Y and Z shown. Profiles normalised by time-average boundary layer thickness; $\phi = 0.450$.

6.3 Wake Boundary Layer Interaction

In this section the results from the boundary layer traverses across Stator 3 boundary layer at 50% span and 85% span for both peak efficiency, $\phi = 0.450$ and off design, $\phi = 0.400$ are described and discussed.

6.3.1 Response of Boundary Layer at 50% Span

6.3.1.1 Peak Efficiency

Ensemble-averaged velocity profiles measured at 0.25, 0.35, 0.44, 0.50 and 0.56 s/S_0 are shown in Fig. 6.5 and the boundary layer integral parameters calculated from the measured ensemble-average profiles through one wake passing cycle are presented in Fig. 6.6. Four profiles W, X, Y and Z are shown across a wake passing period. The time-average profile is shown as a dashed line. Trajectory W is located through the wake-induced transitional/turbulent strips. The wake-induced strip was determined through inspection of the integral properties of the boundary layer at the first measurement station. It is well known

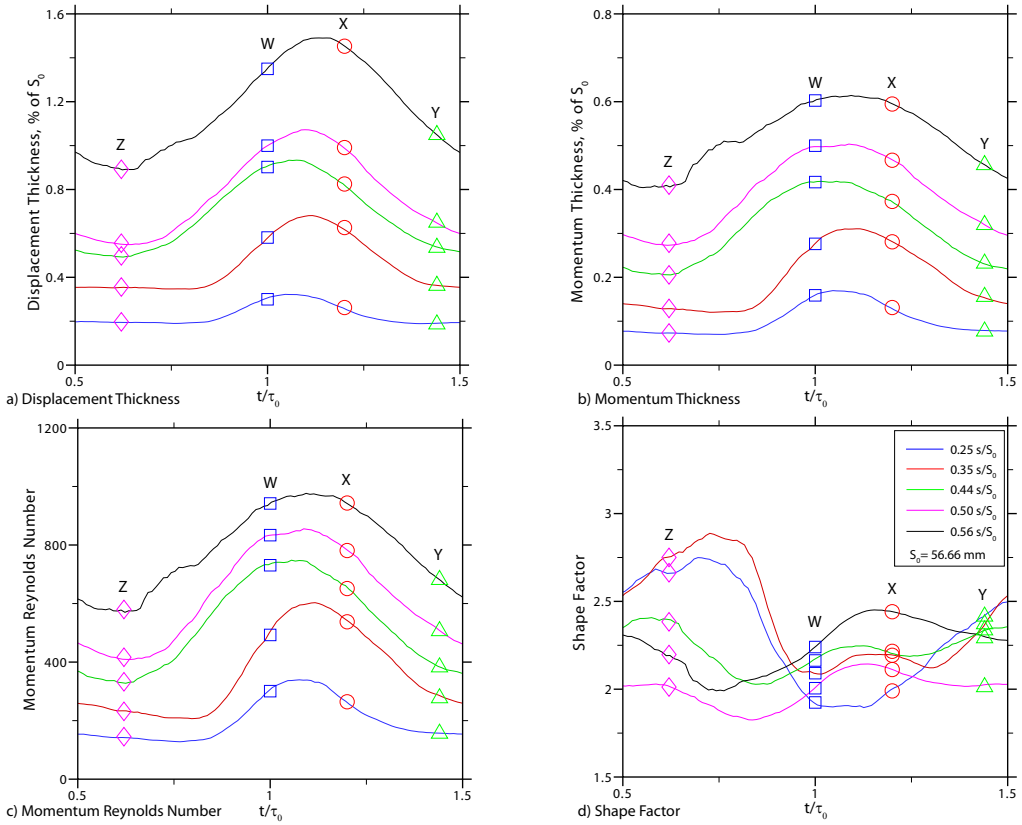

Figure 6.6: Variation of integral boundary layer parameters across wake passing period for Stator 3 suction surface at 50% span. Trajectories W, X, Y and Z are highlighted; $\phi = 0.450$.

that the propagation of a wake through the blade passage is known to increase the incidence onto the blade row and hence the loading. In addition Wheeler et al. (2006) showed that a thickened turbulent boundary layer was generated through the wake leading edge interaction. Therefore, an increase in momentum thickness at the first measurement station was deemed to be evidence of the wake-induced strip. Trajectories X, Y and Z were located in time at 0.20, 0.44 and 0.72 of the wake passing period, τ_0, behind trajectory W. The propagation of the trajectories were based on a velocity of $0.7V_\infty$ which is an average of quoted leading and trailing celerities of a turbulent spot (Halstead et al., 1997a).

The y-axis in Fig. 6.5 provides the height above the surface normalised by the time average boundary layer thickness. The instantaneous boundary layer thickness associated with that trajectory was not used as this would not allow the thickness of the various boundary layers to be distinguished. The x-axis has been normalised by the local free-stream value of each individual profile. Curve fits of the data were done using a cubic spline with zero velocity imposed at the wall. Displacement and momentum thicknesses in Fig. 6.6 have been normalised by stator suction surface length, S_0.

Both laminar, transitional and turbulent profiles occur across a wake-passing period at

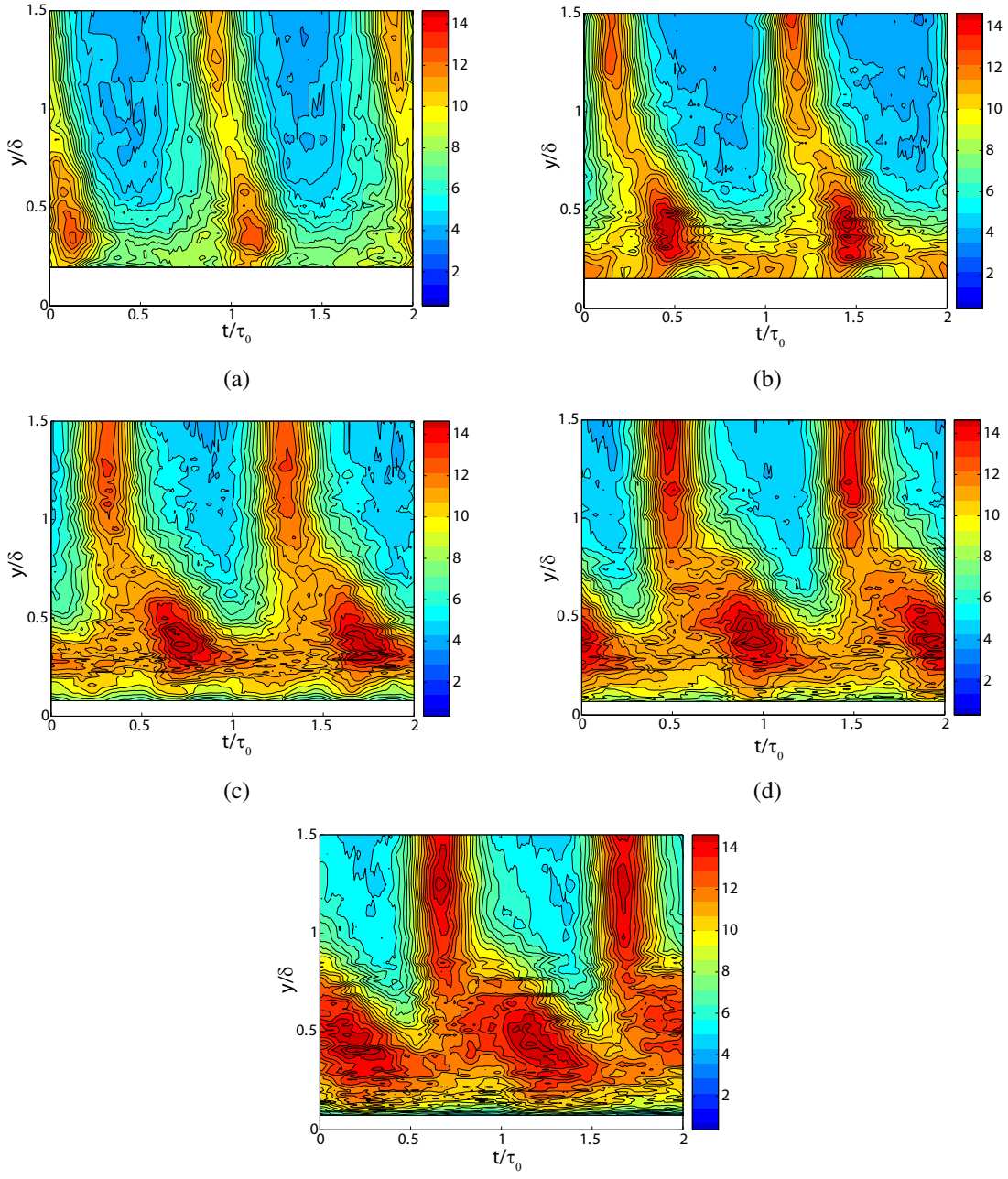

Figure 6.7: Random unsteadiness, Tu, through the boundary layer at 50% span and $\phi = 0.450$: a) 0.25 s/S_0, b) 0.35 s/S_0, c) 0.44 s/S_0, d) 0.50 s/S_0, e) 0.56 s/S_0

0.25 s/S_0 in Fig. 6.5(a). Profiles Y and Z are laminar, Profile W, within the wake-induced strip, is turbulent and Profile X is transitional being between the previous two states. Profile W in Fig. 6.5(a) and Fig. 6.6(a)(b) is thicker than the others and is clearly distinguishable from them. Being turbulent, it has a lower shape factor than the other trajectories, 1.9 compared to 2.5-2.75 for trajectories Y and Z.

For trajectory Y, the profile shape and the shape factor of 2.5 are consistent with those of a Blasius laminar boundary layer in spite of the adverse pressure gradient. The transitional nature of trajectory X is evident from its shape factor being between that of trajectory W and those of trajectories Y, Z. Momentum thickness Reynolds number of profiles X, Y, and Z are all below 200, which are below that at which transition onset would be expected for the background level of free-stream turbulence (Abu-Ghannam and Shaw, 1980).

For Profiles 0.35 and 0.44 s/S_0 the wake-induced profiles W remain clearly distinguishable from the others in Figs. 6.5(b)(c). These profiles are filling with lower momentum fluid and are seen in Figs. 6.6(a)(b) to occupy a larger percentage of the wake passing period. Their shape factors in Fig. 6.6(d) have only slightly increased from those at 0.25 s/S_0. Along the wake-induced strip, the tendency of shape factor to decrease as transition progresses is offset by the effects of the adverse pressure gradient, which maintains high shape factor (Halstead et al., 1997b). Profiles Y and Z remains laminar-like in appearance, with an increasing shape factor. The level of shape factor increases from Y to Z as the calming effect diminishes. The shape factor for Z has increased to a value of 3 at 0.35 s/S_0. This suggests that on average, the associated boundary layer is on the verge of separation. By 0.44 s/S_0, the shape factor are decreasing and the Z profile is much less inflectional.

For profiles at 0.50 and 0.56 s/S_0 along the wake-induced path, trajectory W and X in Fig. 6.5(d)(e) continue to fill with lower momentum fluid as they respond to the adverse pressure gradient. By 0.56 s/S_0 profile W and X have the highest value of shape factor in Fig. 6.6(d). This boundary layer, contained in wake-induced turbulent strip, will have completed transition earliest and will be the first to separate under continued conditions of adverse pressure gradient. Even at this early streamwise location the velocity profiles for trajectory W and X show signs of becoming inflectional.

For trajectory Z at 0.50 s/S_0, the shape factor has reached a minimum value suggesting completion of transition. By 0.56 s/S_0, its value has increased in a manner consistent with a diffusing turbulent boundary layer. At 0.56 s/S_0 trajectories Y and Z start to show signs of inflection, suggesting that on average the boundary layer is close to separation. Consequently, all layers are fully turbulent by 0.56 s/S_0.

Figure 6.7 presents the ensemble-average random unsteadiness, Tu, at the boundary layer traverse locations presented in Figs. 6.5 and 6.6. The x-axis shows time normalised by

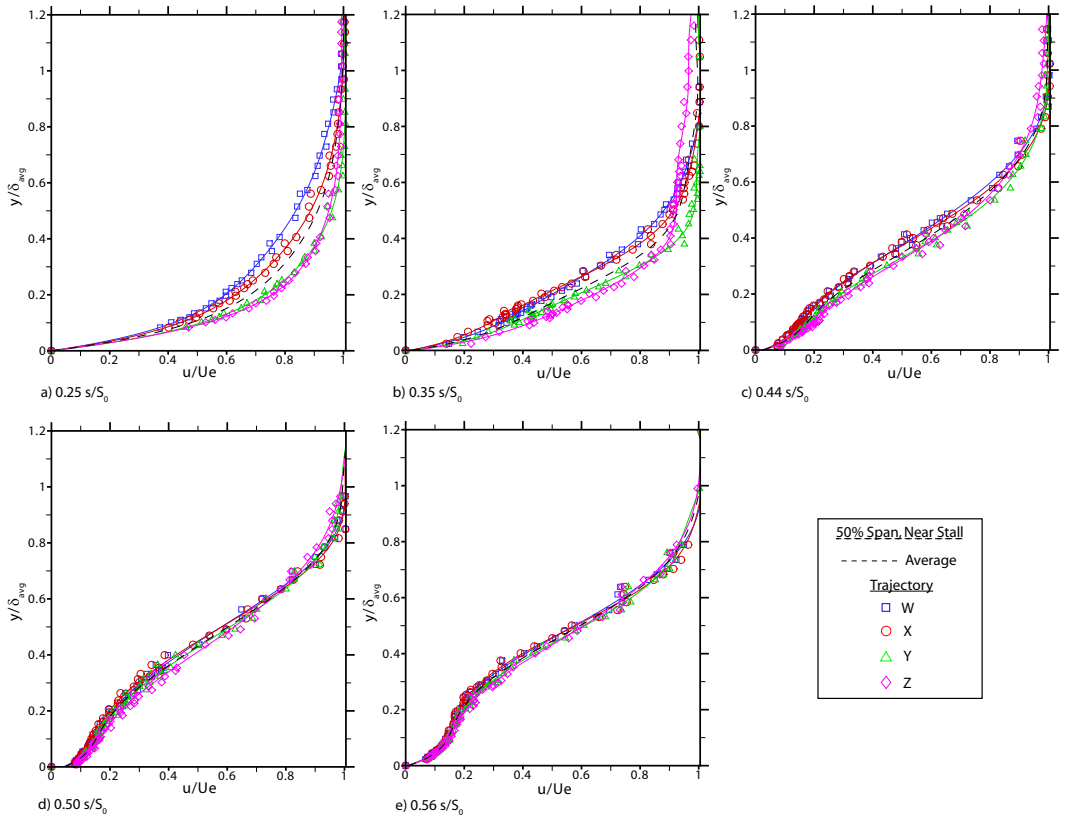

Figure 6.8: Boundary layer profiles for Stator 3 suction surface at 50% span. Trajectories W, X, Y and Z shown. Profiles normalised by time-average boundary layer thickness; $\phi = 0.400$.

the blade passing period and the y-axis is the distance above the blade surface normalised by the time-average boundary layer thickness. The impingement of the rotor wake onto the stator suction surface is clearly visible in the series of figures, as the regions of increased Tu. At 0.25 s/S_0 (Fig. 6.7(a)) the wake appears as a narrow band, 0.20 t/τ_0, and is very much distinct from the background and boundary layer Tu. Peak Tu in the wake occurs at approximately 0.4 y/δ. At 0.35 s/S_0 (Fig. 6.7(b)) the level of Tu in the boundary layer between the successive wakes has increased from approximately 7% to 10/11%. Along with the increase in the Tu between wakes the location of the peak Tu in the wake has moved away from the suction surface to nearly 0.5 y/δ and has increased to more than 15%. The increase in Tu between wakes is indicative of the boundary layer undergoing transition. Moving from Fig. 6.7(a)-(e) it can be observed that the level of Tu in the wake and the boundary layer between wake slowly merge. Inspecting these figures it is possible to see that the peak Tu in the wake propagates at a much lower convection speed than the wake in the free-stream, resulting in a kink in the wake just below the edge of the boundary layer. The momentum thickness Reynolds number and shape factor for trajectories Y and Z at 0.25 s/S_0 are typical of those of a laminar boundary layer. The reduced level of Tu

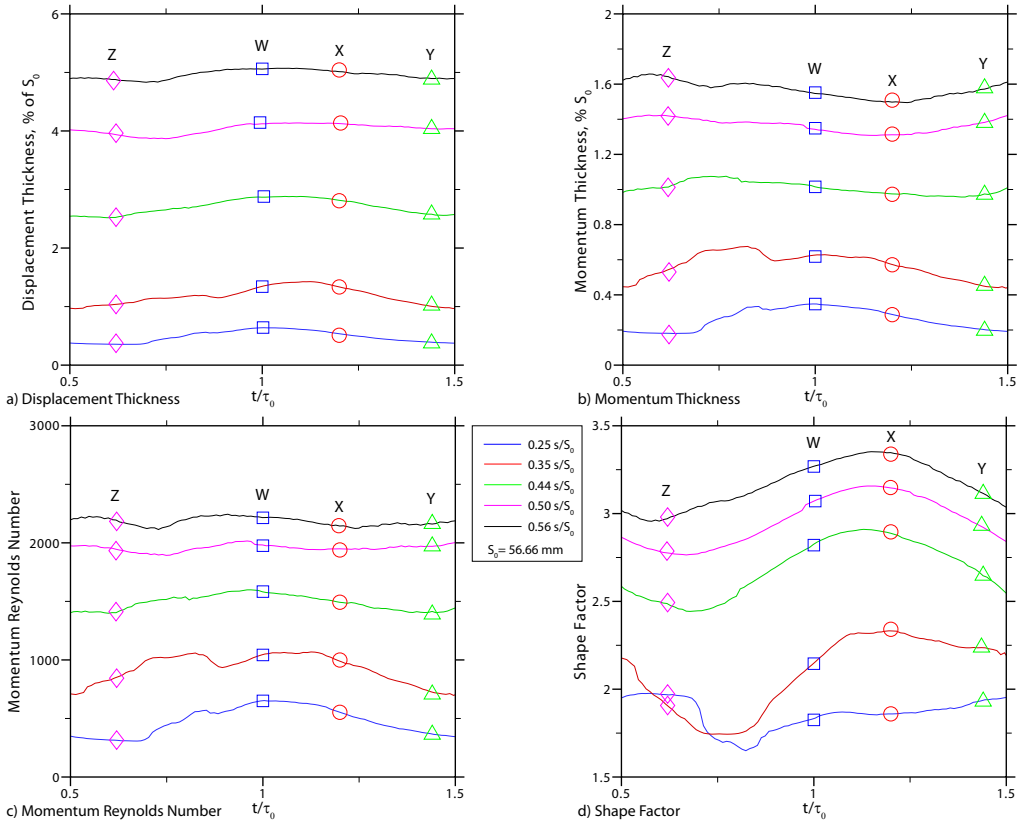

Figure 6.9: Variation of integral boundary layer parameters across wake passing period for Stator 3 suction surface at 50% span. Trajectories W, X, Y and Z are highlighted, $\phi = 0.400$.

seen between wakes in Fig. 6.7(a) correspond to trajectories Y and Z and as such help to validate the laminar nature of the boundary layer at that time.

The peak values of displacement and momentum thickness and momentum Reynolds number, in Figs. 6.6(a)-(c), occur along the wake-induced trajectory W in which transition is completed farther forward. Trajectory W corresponds to the region of increased Tu seen in Fig. 6.7. Along trajectory Y and Z where transition was completed farther aft, the more newly formed turbulent layers at 0.56 s/S_0 have momentum Reynolds numbers of 650. In contrast at the same location, those along wake-induced trajectory W are 950.

6.3.1.2 Near Stall

Ensemble-average velocity profiles (Fig. 6.8) obtained at $\phi = 0.400$, along with the calculated integral parameters (Fig. 6.9) for one blade passing period are discussed in this section. Shown in the figures are the same four time instances described above.

At 0.25 s/S_0 for $\phi = 0.450$ and 50% span the velocity profiles and integral parameters showed evidence that the boundary layer was intermittently turbulent. Trajectories away

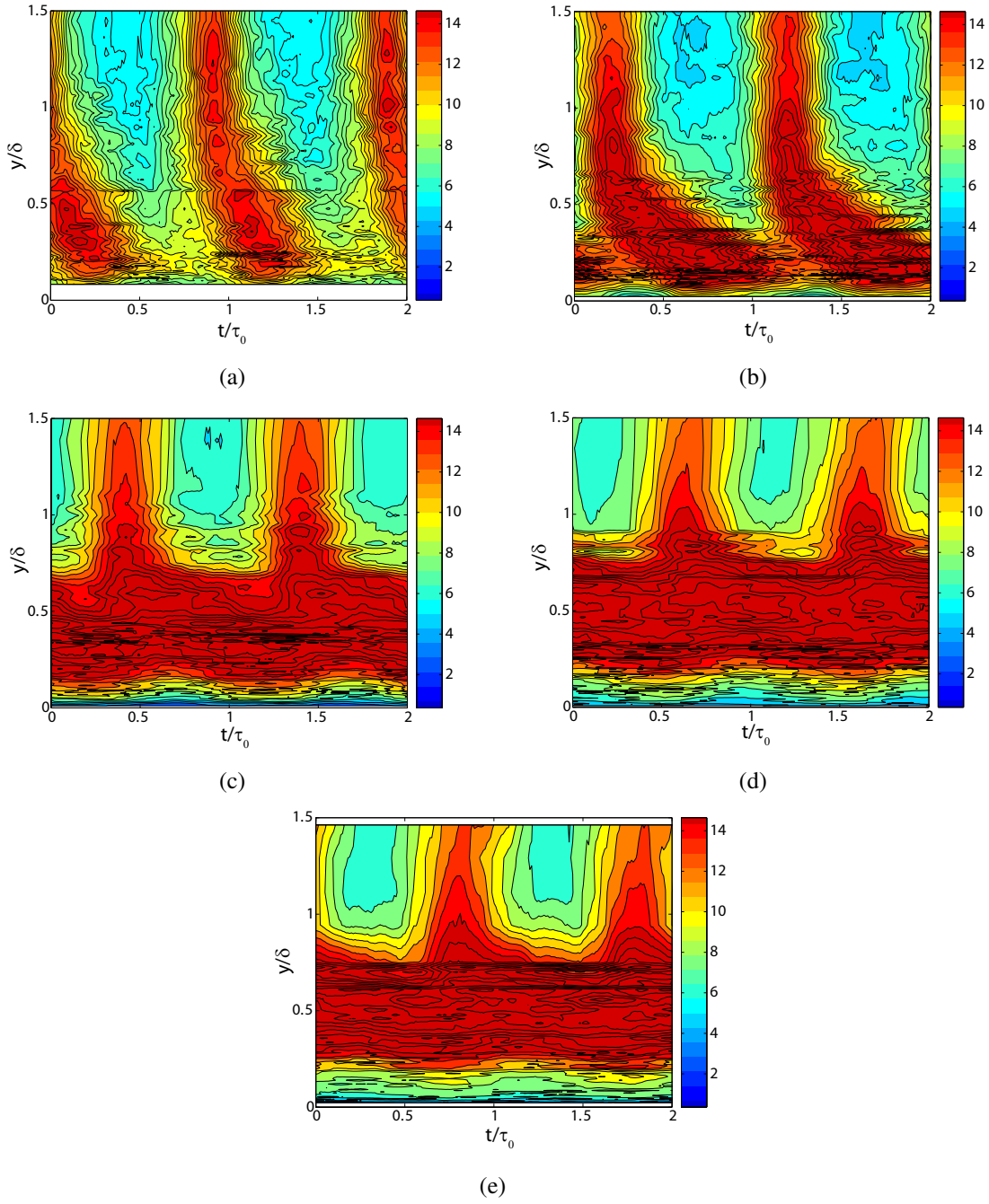

Figure 6.10: Random unsteadiness, Tu, through the boundary layer at 50% span and $\phi = 0.400$: a) 0.25 s/S_0, b) 0.35 s/S_0, c) 0.44 s/S_0, d) 0.50 s/S_0, e) 0.56 s/S_0

from the wake path had shape factors that were typically associated with laminar boundary layers and a momentum thickness Reynolds below the critical value of 163 after Abu-Ghannam and Shaw (1980). Towards off design, $\phi = 0.400$ the picture of boundary layer development at 50% span changes completely. Profiles W and X in Fig. 6.8(a) and Fig. 6.9 are thicker than profiles Y and Z by a factor of nearly 2, but all four trajectories posses momentum thickness Reynolds greater than the minimum value required for the inception of transition. Profiles Y and Z have lower momentum thickness Reynolds number and a higher shaper factor compared to profiles W and X suggesting that upstream of this location the transition process was influenced by the propagation of the upstream wake.

The velocity profiles at 0.35 s/S_0 show very little variation across the blade passing period. The velocity profiles become increasingly steady towards 0.56 s/S_0. This is also evident in the distribution of the integral parameters across the period. At 0.44 s/S_0 the shape factor is continuously greater than 2.5. The velocity profiles in Fig. 6.8(c) start to show signs of an inflexion. The single element hotwire probe is unable to provide information on direction of the flow and is therefore unable to produce a velocity profile with a negative velocity. Any regions of negative flow will therefore, be seen as regions of positive flow by the hotwire. The flow visualisation shown in Fig. 6.2 and velocity distribution presented in Fig. 6.1 at $\phi = 0.400$ show the boundary layer to be separated from approximately 0.5 s/S_0. This agrees with the velocity profile measured at 0.44 s/S_0. The velocity profiles at 0.50 s/S_0 and 0.56 s/S_0 (Fig. 6.8(d) and (e)) clearly have a point of inflexion and therefore show the boundary layer to be separated.

At off design, like peak efficiency, the peak values of displacement, momentum thickness and momentum Reynolds number, in Figs. 6.9(a)-(c), occur along the wake-induced trajectory W in which transition was completed farther forward. But unlike peak efficiency the off design profiles become increasingly steady in time. This is caused by the separated boundary layer, where the response of the boundary layer is damped due to reduced convection speeds caused by the lower momentum of the flow.

Transition appears to have been either completed or in the later stages of completion by 0.25 s/S_0, suggesting that the location of transition has propagated forward with throttling and or the length of transition has reduced due to increased spot spreading rate. This is nothing new and was noted by Halstead et al. (1997a) and Mailach and Vogeler (2003), who both showed that as the compressor is throttled the location of transition moves farther upstream. Abu-Ghannam and Shaw (1980) suggested that the end of transition can be estimated by $\mathrm{Re}_{\theta_{xe}} = 2\mathrm{Re}_{\theta_{xs}}$. Assuming transition started at $\mathrm{Re}_{\theta_{xs}} = 163$, then transition would have been completed by $\mathrm{Re}_{\theta_{xe}} = 326$. Trajectory Z at 0.25 s/S_0 has a $\mathrm{Re}_\theta = 313$ which is close to the minimum value suggested for end of transition.

Ensemble-average Tu through the boundary layer is presented in Fig. 6.10 for the same

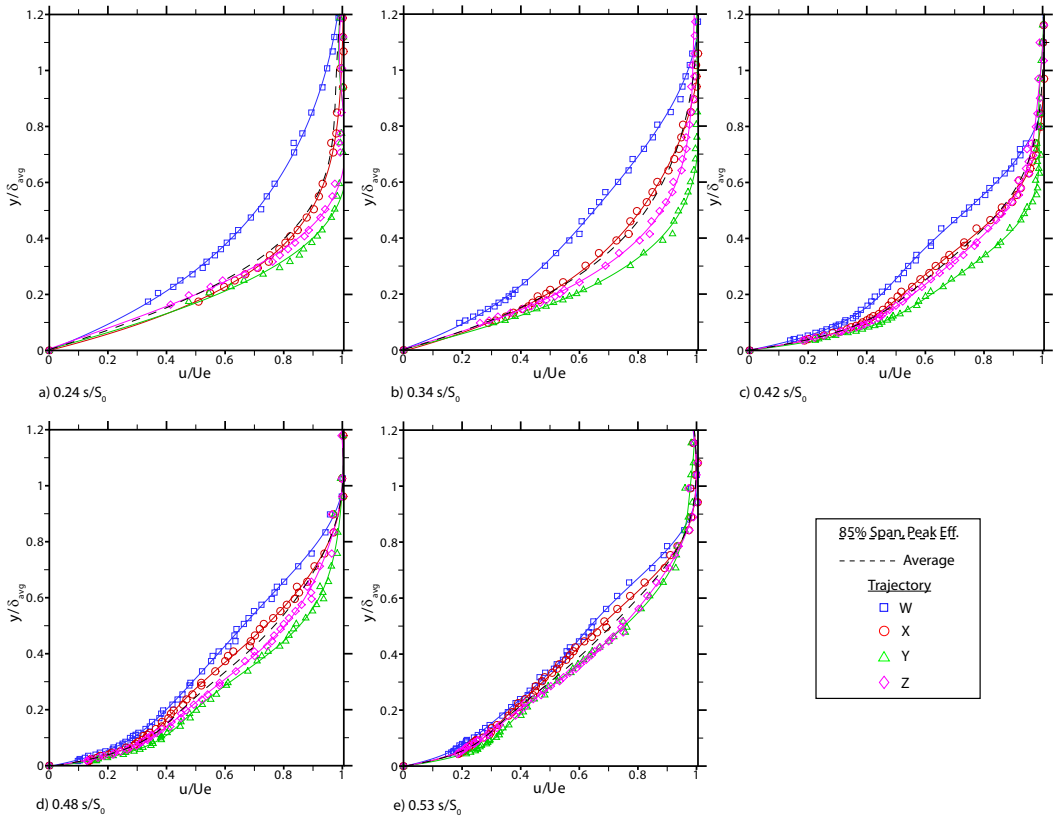

Figure 6.11: Boundary layer profiles for Stator 3 suction surface at 85% span. Trajectories W, X, Y and Z shown. Profiles normalised by time-average boundary layer thickness; $\phi = 0.450$.

streamwise locations presented in Figs. 6.8 and 6.9. In Chapter 5 it was shown that the wake width and Tu of the incoming wake increases towards $\phi = 0.400$. This effect can be seen when comparing Figs. 6.7(a) and 6.10(a). At this streamwise location the Tu in the wake outside of the boundary layer has increased from 10% to 15% and the width of the wake has increased from approximately 0.20 t/τ_0 to 0.38 t/τ_0. By 0.35 s/S_0 the increased Tu associated with the wake appears throughout the blade passing period. It is clear when comparing Figs. 6.7 and 6.10 that transition has occurred farther forward for the $\phi = 0.400$ than at $\phi = 0.450$, but the boundary layer still shows evidence that the transition process will have been an unsteady one, tied to the blade passing cycle. By 0.44 s/S_0 the flow has separated from the suction surface. The increased loss associated with a separated boundary layer can be seen through Figs. 6.10(c)-(e) as the band of $Tu > 15\%$ that occurs continuously across the period.

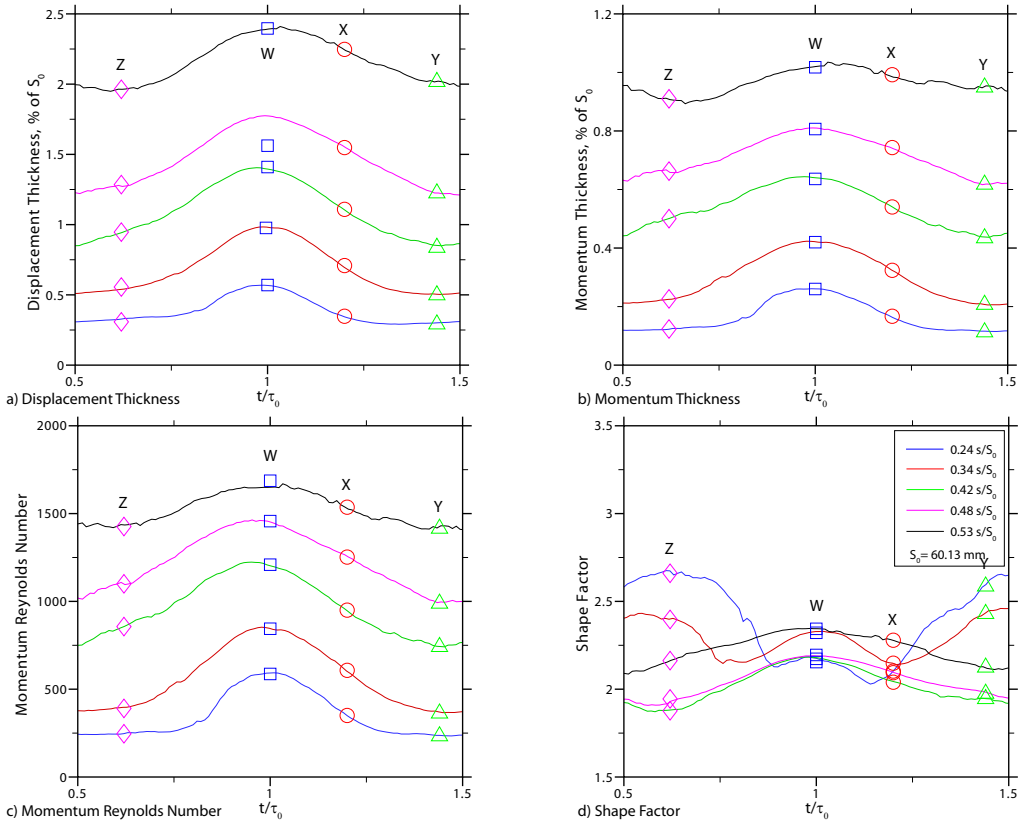

Figure 6.12: Variation of integral boundary layer parameters across wake passing period for Stator 3 suction surface at 85% span. Trajectories W, X, Y and Z are highlighted; $\phi = 0.450$.

6.3.2 Response of Boundary Layer at 85% Span

6.3.2.1 Peak Efficiency

Ensemble-average velocity profiles (Fig. 6.11) obtained at 85% span and $\phi = 0.450$, along with the calculated integral parameters (Fig. 6.12) for one blade passing period are discussed in this section. Shown in the figures are the same four time instances, W, X, Y and Z described in § 6.3.1.1.

Transitional and turbulent profiles can be observed to occur across a wake-passing period at 0.24 s/S_0 (see Fig. 6.11(a)). Profiles Y and Z posses shape factors of approximately 2.5 and a momentum thickness Reynolds number of approximately 250. The increased Re_θ compared to that at 50% span suggests that these profiles are more likely to be transitional. Profile W, again lies within the wake-induced strip and is turbulent. Profile X lies on the edge of the wake-induced strip and owing to its increased Re_θ above that of Profile Y and Z is also most probably turbulent or at the later stages of transition. Profile W in Fig. 6.11(a) and Fig. 6.12(a)(b) is thicker than the others and is clearly distinguishable from them.

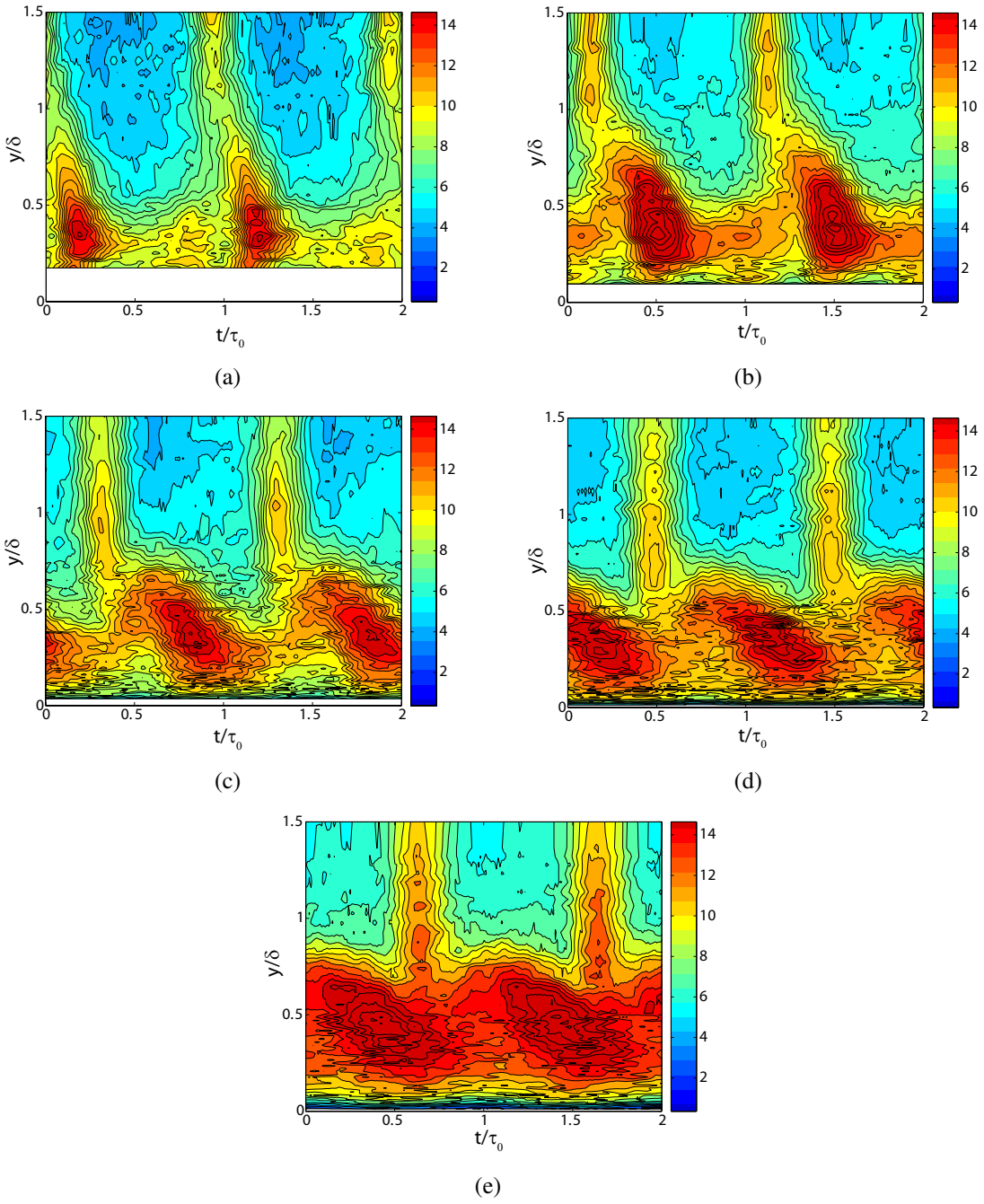

Figure 6.13: Random unsteadiness, Tu, through the boundary layer at 85% span and $\phi = 0.450$: a) 0.24 s/S_0, b) 0.34 s/S_0, c) 0.42 s/S_0, d) 0.48 s/S_0, e) 0.53 s/S_0

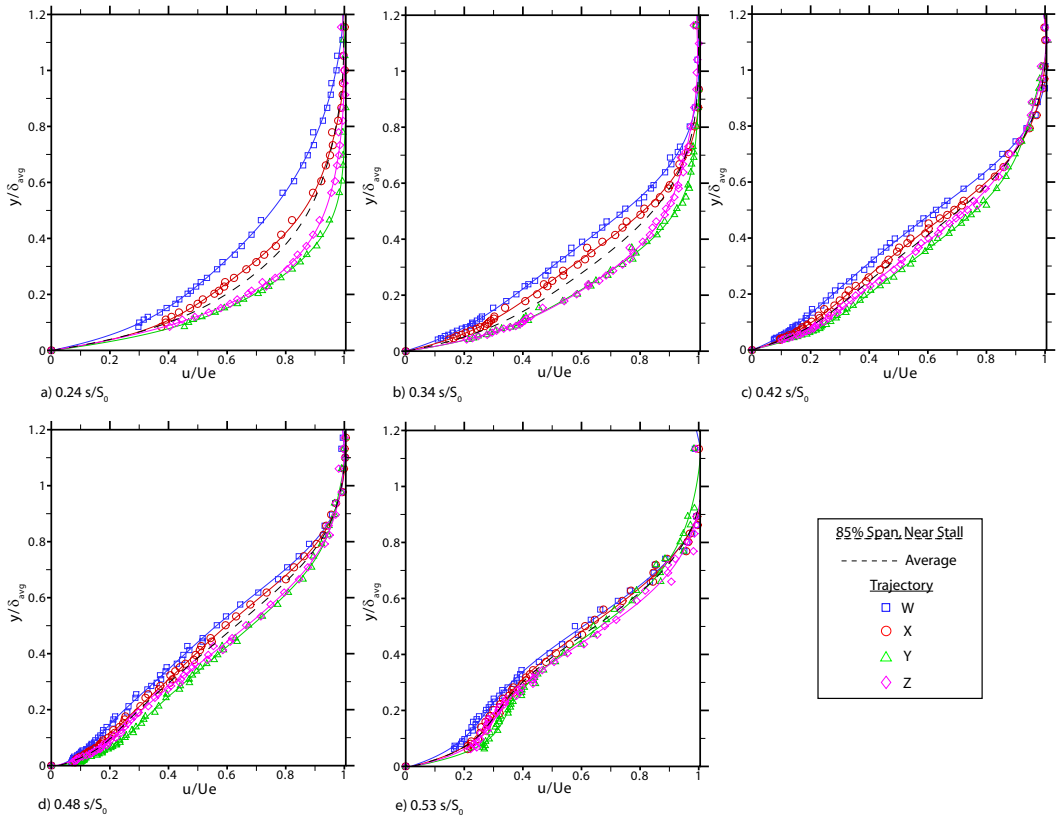

Figure 6.14: Boundary layer profiles for Stator 3 suction surface at 85% span. Trajectories W, X, Y and Z shown. Profiles normalised by time-average boundary layer thickness; $\phi = 0.400$.

For Profiles 0.34 and 0.42 s/S_0 the wake-induced profiles W remain clearly distinguishable from the others in Figs. 6.11(b)(c) as at 50% span. These profiles are filling with lower momentum fluid and are seen in Figs. 6.12(a)(b) to occupy a larger percentage of the wake passing period. Their shape factors in Fig. 6.12(d) have only slightly increased from those at 0.24 s/S_0, compared to the other trajectories. The shape factor for profiles Y and Z have started to relax down to a more turbulent value. At 50% span the shape factor had continued to increase and reached a value that was close to laminar separation. This substantiates the transitional nature of profile Y and Z at this height compared to the more laminar like profiles at 50% span.

By 0.48 s/S_0 the four velocity profiles in Fig. 6.11(d) have started to merge to the time-average profile (dashed-line in Fig. 6.11) and little variation is seen across the wake passing period by 0.53 s/S_0. At this location all four profiles start to fill with lower momentum fluid as they respond to the adverse pressure gradient. The reduction of unsteadiness seen at this streamwise location is linked to the casing-corner separation, seen in the flow visualisation (see Fig. 6.2). This is apparent by the high shape factor seen across the cycle, Fig. 6.12(d).

As at 50% span the ensemble-average random unsteadiness, Tu, is shown in Fig. 6.13

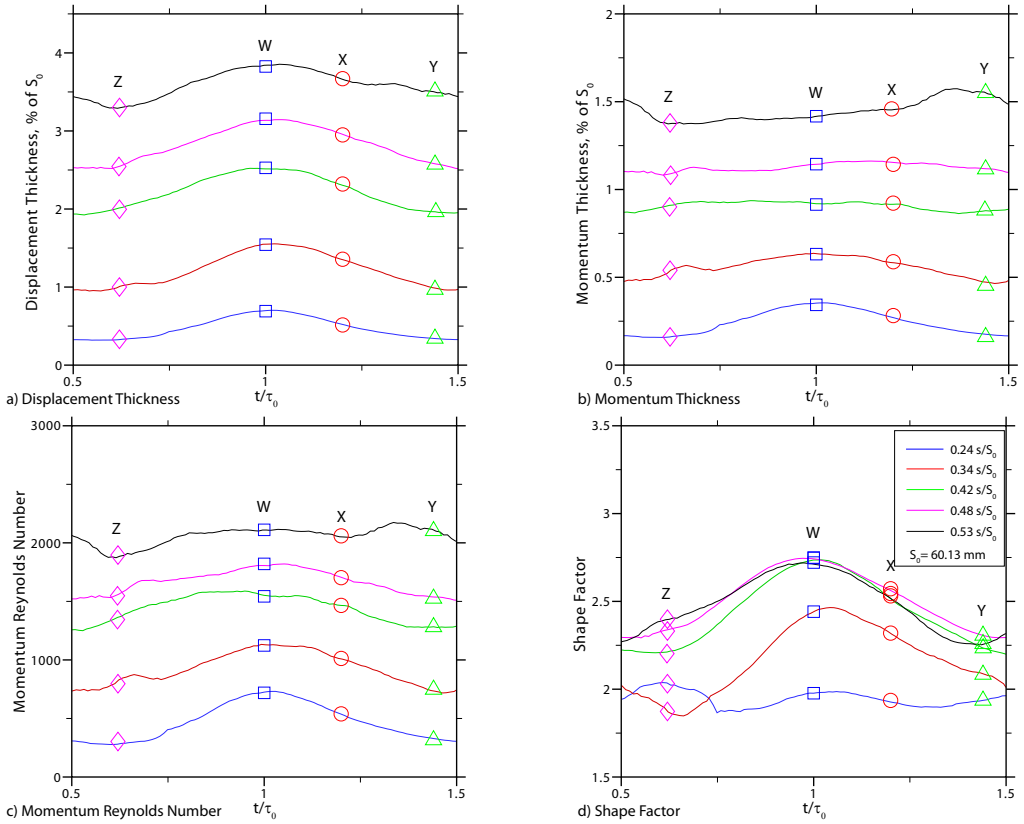

Figure 6.15: Variation of integral boundary layer parameters across wake passing period for Stator 3 suction surface at 85% span. Trajectories W, X, Y and Z are highlighted; $\phi = 0.400$.

for 85% span. Comparing Fig. 6.7(a) with Fig. 6.13(a) it can be observed that the peak Tu in the wake has increased to 15% compared to 10% and that the unsteadiness between wake passing periods has also increased, 10% compared to 7/8%, but the wake width is comparably to that at 50% span. By Fig. 6.13(b) the Tu occupies a significant fraction of the blade passing period suggesting that the boundary layer flow is in the later stages of transition. The same phenomenon seen at $\phi = 0.450$ of the peak Tu associated with the wake in the boundary convects at a reduced velocity compared to the propagation velocity of the free-stream.

6.3.2.2 Near Stall

Ensemble-average velocity profiles (Fig. 6.14) obtained at $\phi = 0.400$, along with the calculated integral parameters (Fig. 6.15) for one blade passing period are discussed in this section. Shown in the figures are the same four time instances described above.

Profile W, the wake-induced strip is clearly distinct from the other three profiles in Fig. 6.14(a). Its shape factor is similar to profiles X, Y and Z, but its momentum thickness

Reynolds number is approximately double that of trajectories Y and Z. Due to its higher momentum thickness Reynolds number compared to the other trajectories it is believed that trajectory W transitioned earlier.

By Fig. 6.14(b) trajectory X has begun to match trajectory W profile. Looking at profile X integral parameters it can be seen that these are approaching similar values to that of trajectory W. As the boundary layer develops downstream, Fig. 6.14(c)-(e), the differences between the profiles starts to decrease. This coincides with the profiles becoming inflectional as they respond to the increasingly adverse pressure gradient. Flow visualisation and surface velocity distribution indicates that complete separation of the boundary layer flow by approximately 0.5 s/S_0. The shape factor (Fig. 6.15(d)) shows a sharp increase in value for all four trajectories from 0.24 s/S_0.

Ensemble-average Tu through the boundary layer is presented in Fig. 6.16 for the same streamwise locations presented in Figs. 6.14 and 6.15. Comparing the distribution of Tu at peak efficiency with that at off design, it is clear that the level of unsteadiness in the boundary layer and the level in the wake has increased. The combined effect of increased loading and unsteadiness in the incoming flow, is likely to result in earlier and rapid transition of the boundary layer flow from laminar to turbulent. The wake occupies approximately 0.2 t/τ_0 at $\phi = 0.450$ and increases to 0.35 t/τ_0 at $\phi = 0.400$ in the free-stream. The increased Tu associated with the wake in the boundary layer has increased significantly with throttling the rig. The region of peak Tu in the boundary layer at $\phi = 0.450$ occupies approximately 0.35 t/τ_0 increasing to 0.50 t/τ_0 at $\phi = 0.400$. By Fig. 6.16(b) the boundary layer flow contains continuously high Tu. The effect of the boundary layer flow separation can be seen in Fig. 6.16(e).

6.4 Comparison of Experimental and Computational Results

6.4.1 Steady Integral Parameters

A comparison of measured and computed integral values for Stator 3 suction surface is shown in Fig. 6.17 for $\phi = 0.450$ at 50% and 85% span and Fig. 6.18 for $\phi = 0.400$ also at 50% and 85% span. Calculations from the two-dimensional unsteady calculation at $\phi = 0.450$ were obtained from a time-average of the unsteady solutions. The computed quantities are shown as lines in Figs. 6.17 and 6.18, whilst the time-average measured quantities are shown as symbols (blue for $\phi = 0.450$ and red of $\phi = 0.400$) for the streamwise locations where boundary layer traverses were made. In addition to the measured time-average quantity, the maximum and minimum measured value at that streamwise lo-

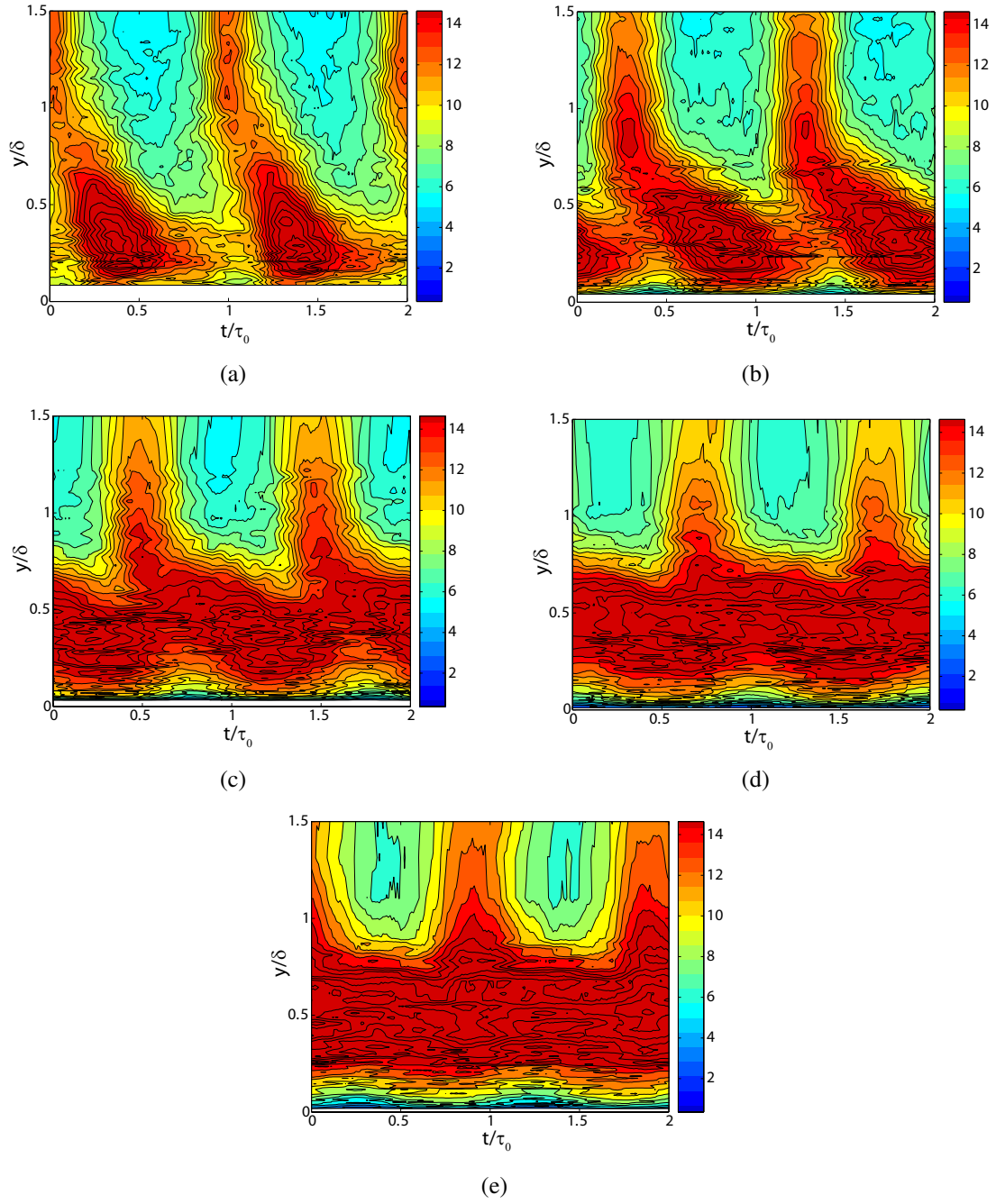

Figure 6.16: Random unsteadiness, Tu, through the boundary layer at 85% span and $\phi = 0.400$: a) 0.24 s/S_0, b) 0.34 s/S_0, c) 0.42 s/S_0, d) 0.48 s/S_0, e) 0.53 s/S_0

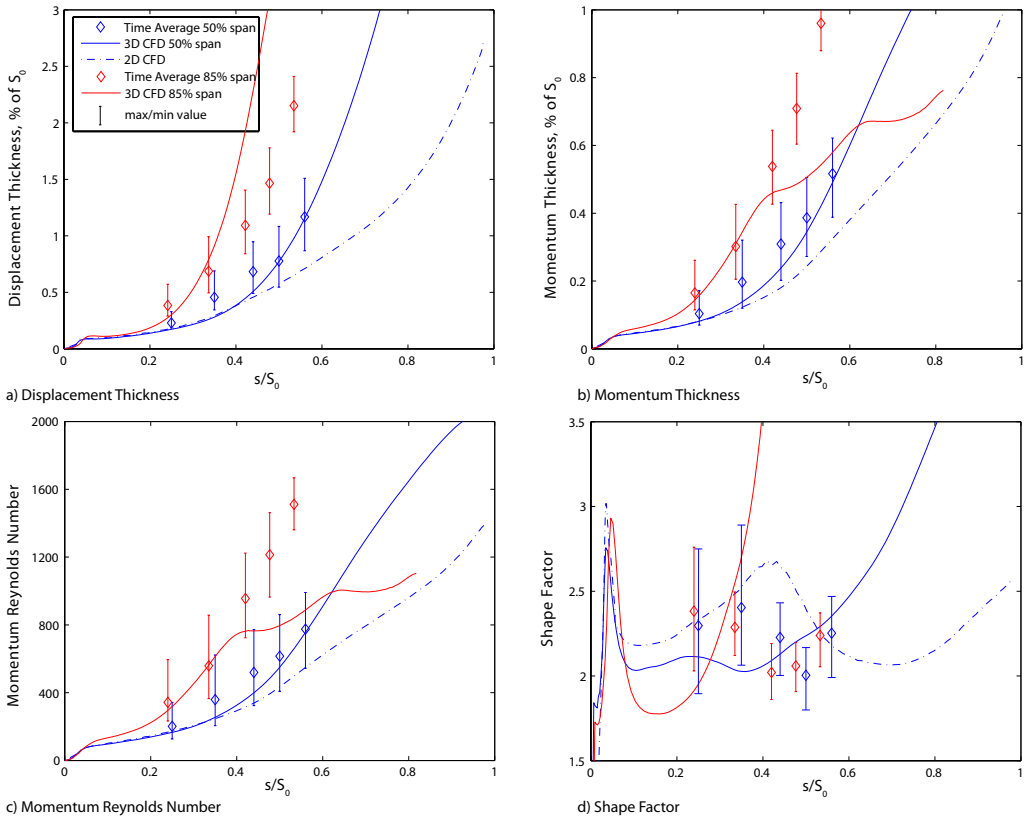

Figure 6.17: Comparison of measured and predicted integral boundary layer parameters for Stator 3 suction surface at 50% and 85% span; $\phi = 0.450$.

cation are shown to illustrate the variation of the unsteady about the mean.

The computed values at 50% span and $\phi = 0.450$ for the steady-state calculation are in quite good agreement with the measured boundary layer values Fig. 6.17(a)-(d). The computed two-dimensional time-average values (dashed-blue line) show similar trends to the three-dimensional calculation up to approximately 0.4 s/S_0. The comparison between the measured boundary layer values and calculated at 85% span are not as good. The first two steamwise locations agree well with the computed values, but after 0.35 s/S_0 the gradient in δ^* appears to be over-predicted, Fig. 6.17(a). In Fig. 6.17(b)-(c) the computed values show a decrease for θ and Re_θ. The decrease in these quantities are due to the excessive separation predicted by the calculations. This excessive separation is believed not to be physical, as the measured boundary layer profiles (Fig. 6.11) and surface velocity profiles (Fig. 6.1(a)) do not show the boundary layer to be separated at these streamwise locations. This over-estimation in the boundary thickness and loss is also observed in the contours of total pressure at exit of Stator 3 (see Figs. 4.9 and 4.10).

The difference in the nature of transition between the measured and computed boundary layers is shown by the variation of shape factor, Fig. 6.17(d). The implemented transition model accounts for the length of transition, by using an intermittency transport equa-

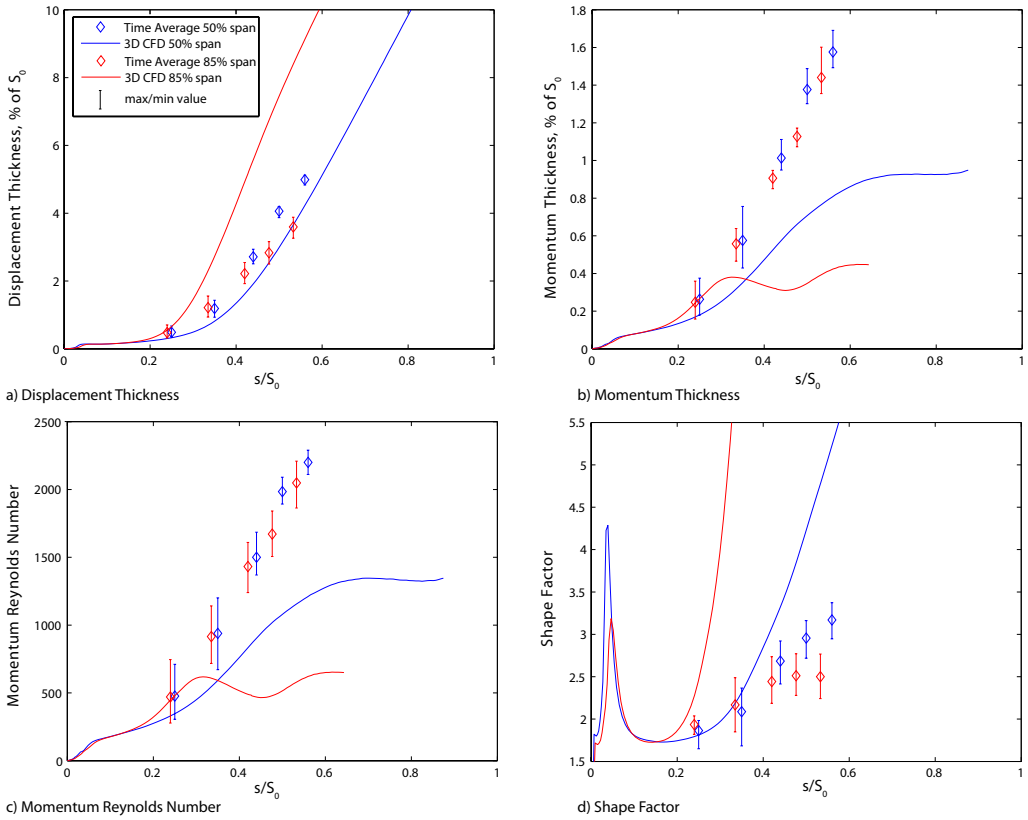

Figure 6.18: Comparison of measured and predicted integral boundary layer parameters for Stator 3 suction surface at 50% and 85% span; $\phi = 0.400$.

tion. This explains the absence of a sudden change in shape factor which is characteristic of a point transition model, typical in boundary layer codes. The second peak in computed shape factor (the first being associated with the leading edge spike) for 50% span appears to be forward to that of the experiment, suggesting that transition was completed earlier. The time-average γ_{pk} showed transition to be completed by 0.48 s/S_0, whereas the computed transition location is approximately 0.35 s/S_0. The computed shape factor, then increases rapidly, indicating turbulent separation. The two-dimensional unsteady calculation better captures the trend of the measured time-average data. This calculation predicts a peak time-average shape factor of 2.6-2.7 at approximately 0.4 s/S_0 indicating that on average the boundary layer is close to separation. The shape factor can then be observed to decrease to approximately 0.6 s/S_0 where is starts to increase again indicating turbulent separation close to the trailing edge. The unsteady calculation predicts transition to occur farther aft than the steady state calculation and this explains the divergence of the computed quantities after 0.4 s/S_0 in Fig. 6.17(a)-(c).

The computed values at 50% and 85% span for $\phi = 0.400$ are not in good agreement with the measured boundary layer values Fig. 6.18(a)-(d). The flow visualisation, Fig. 6.2(c) showed complete flow separation across the span close to 0.5 s/S_0. As the

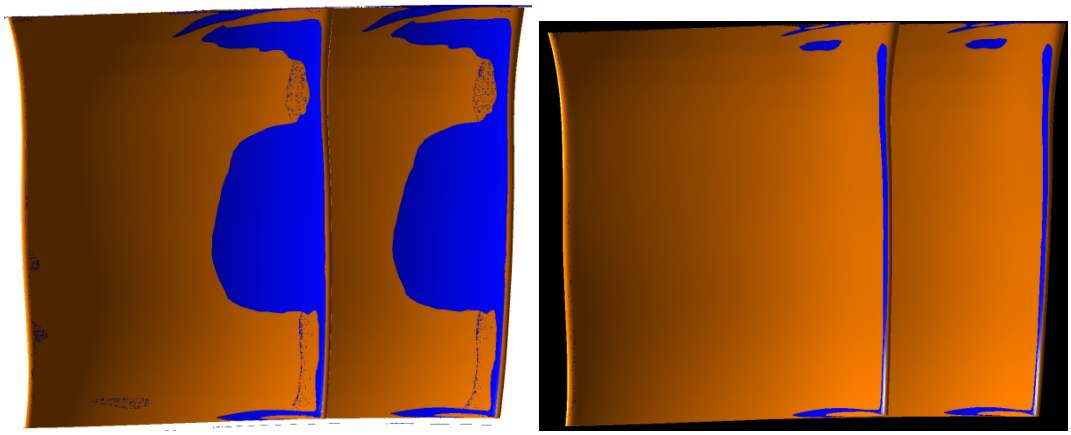

(a) (b)

Figure 6.19: Calculated iso-surface of laminar flow, blue regions, on Stator 3 suction surface: a) $\phi = 0.450$, b) $\phi = 0.400$. Flow direction is from right to left.

hotwire probe cannot differentiate between forward and reverse flow, the measured momentum thickness, is likely to be over-estimated in regions of reverse flow. This can be seen comparing Fig. 6.18(a), where the growth of displacement thickness at 50% span is well predicted, with the growth of momentum thickness, Fig. 6.18(c)-(d). Here the momentum thickness rate of growth decreases after the flow separates (0.3 s/S_0), causing the measured and computed values to diverge. Comparing the range of measured maximum and minimum quantities at a streamwise location at $\phi = 0.450$ with those at $\phi = 0.400$ it is immediately obvious that the period-to-period variation at off design is significantly lower than that at peak efficiency. The reduced variation is likely to be caused by the complete flow separation seen at this flow coefficient.

An illustration of the size of the laminar flow region on Stator 3 suction surface for $\phi = 0.450$ and $\phi = 0.400$ is given in Fig. 6.19(a)(b). The flow direction is from right to left. At off design the laminar flow region is confined to the leading edge region and is most likely terminated through the large leading edge spike present at this flow coefficient. At $\phi = 0.450$, large regions of laminar flow are calculated in the midspan region (25-75% span) extending approximately to 0.35 s/S_0. Towards the endwalls the laminar flow regions are terminated close to the leading edge. In this region the CFD predicts a large streamwise pressure gradient, which will cause the flow to possibly prematurely transition. Better grid resolution around the leading edge region might better capture these large gradients and therefore delay transition.

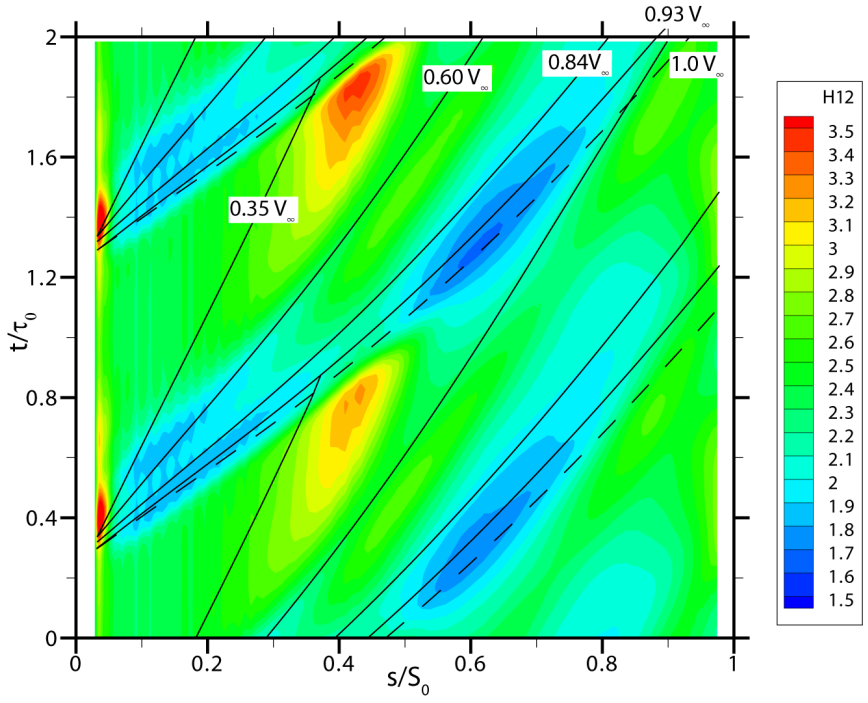

(a)

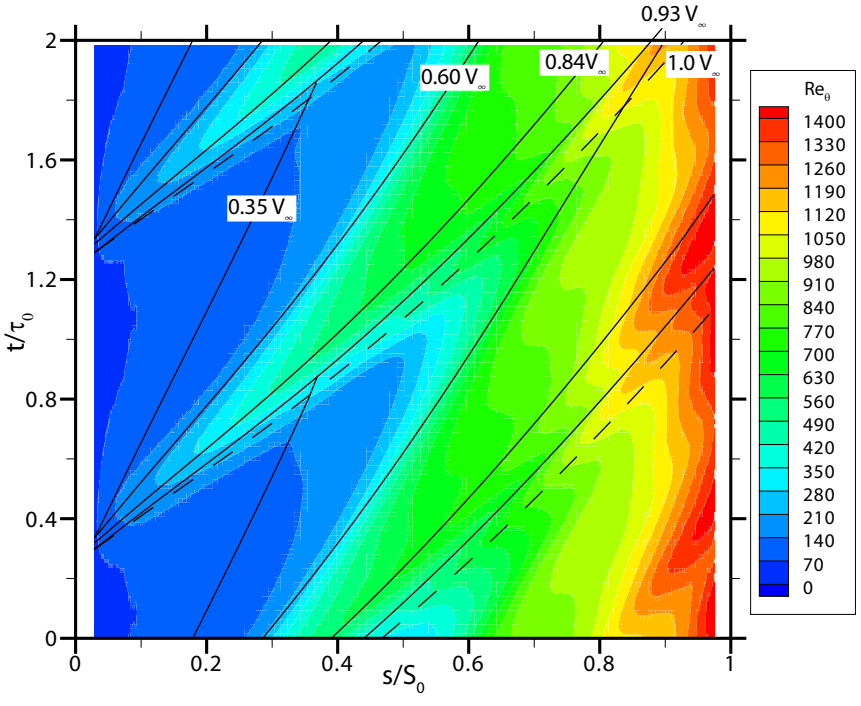

(b)

Figure 6.20: Calculated S-T diagram for Stator 3 suction surface at 50% span and $\phi = 0.450$: a) H_{12}, b) Re_θ.

6.4.2 Unsteady Boundary Layer Development at Midspan

Unsteady boundary layer calculations were obtained using a two-dimensional slice at 50% span of the third stage rotor, stator and the fourth stage rotor. Details of the computational set-up are described in Chapter 3.

Computed S-T diagrams of shape factor and momentum thickness Reynolds number along the suction surface are shown in Figs. 6.20(a)(b) for the third-stage stator at 50% span and $\phi = 0.450$. Five trajectories, labelled $1.0V_\infty$, $0.93V_\infty$, $0.84V_\infty$, $0.60V_\infty$ and $0.35V_\infty$ are drawn. The first trajectory, represents the convection speed of the free-stream. Trajectory $0.93V_\infty$ and $0.60V_\infty$ are the calculated celerities of the leading and trailing boundary of the thickened momentum thickness, and as such represents the wake-induced strip. Halstead et al. (1997a) calculated the leading and trailing boundaries of a turbulent spot at 0.88 and 0.5 of the free-stream velocity. Wheeler et al. (2006) calculated the celerities of a thickened boundary layer at 0.7 and 0.6 of the free-stream velocity. Whereas Mailach and Vogeler (2003) calculated a leading boundary of 0.95 of the free-stream velocity. The calculated celerities compare favourably with the measured values quoted in the literature. Trajectory $0.84V_\infty$ is the centreline velocity of the peak momentum thickness and $0.35V_\infty$ is a typical value quoted for the convection of the calmed region.

The shape factor, Fig. 6.20(a), gives a clear characteristic of the boundary layer profile, and as such is a measure of the boundary layer state. As seen earlier turbulent boundary layers profiles are fuller than laminar profiles and therefore, typically have a lower shape factor. Shape factor along with the momentum thickness Reynolds can be used to discretise the suction surface into distinct regions.

Trajectory $1.0V_\infty$ and $0.60V_\infty$ carves out a region of low shape factor ($H_{12} < 2$) and high momentum thickness Reynolds number ($\mathrm{Re}_\theta > 300$). This region, corresponds to the wake-induced strip. Between trajectory $0.6V_\infty$ and $0.35V_\infty$ the shape factor is quite high ($2.5 < H < 3.5$) with a low momentum thickness Reynolds number ($\mathrm{Re}_\theta < 250$). This region corresponds to laminar like flow that trails the wake-induced strip. At approximately $0.4\ s/S_0$ and at $t/\tau_0 = 1.8$ the maximum shape factor is seen. This region corresponds to a laminar separation bubble. The bubble is terminated in time by the reappearance of the wake-induced strip. Left of trajectory $0.35V_\infty$ the flow can be classified as laminar.

Figure 6.21 provides a close-up region of Stator 3 suction surface leading edge region, covering one blade passing period. The five trajectories shown in Fig. 6.20 are redrawn. The contours of momentum thickness Reynolds number in Fig. 6.21(b) have been cutoff at 200. This is to highlight regions that are most likely to be turbulent. The rotor wake strikes the suction surface at approximately $0.35\ t/\tau_0$. The induced incidence caused by the wake generates a region of high shape factor (Fig. 6.21(a), indicating laminar separation. The shape factor then relaxes to a value of approximately 1.9. The momentum thickness

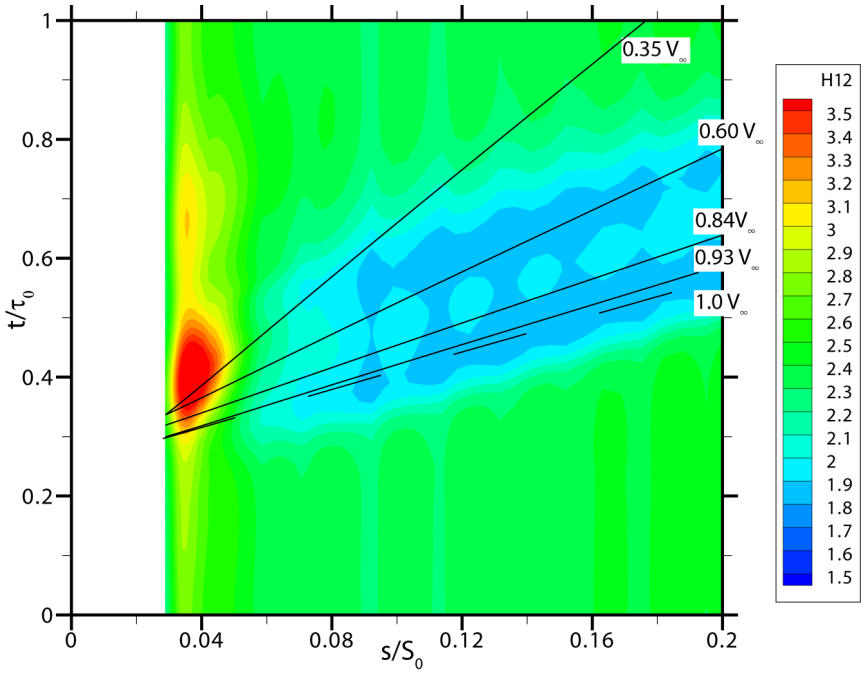

(a)

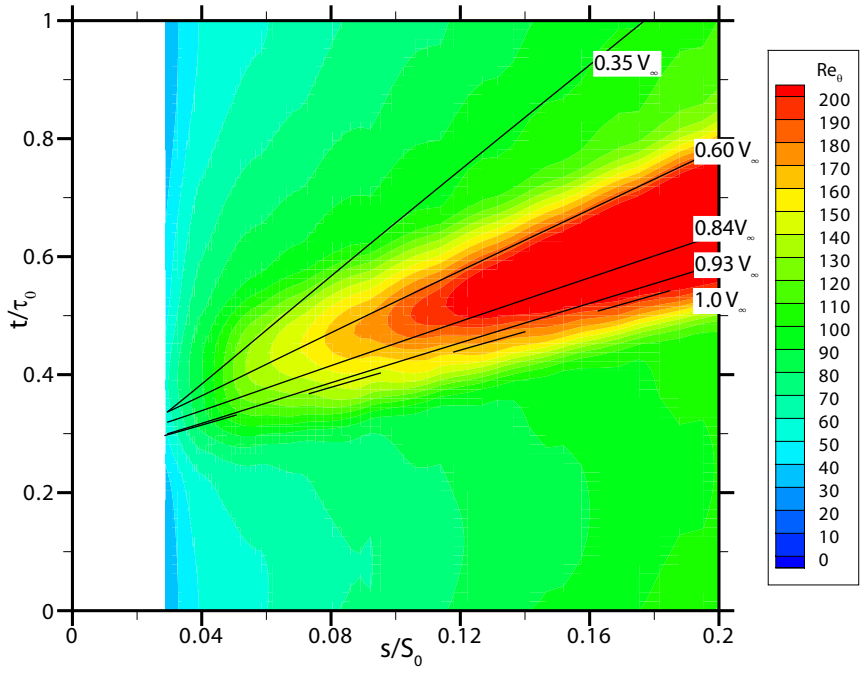

(b)

Figure 6.21: Calculated S-T diagram of Stator 3 suction surface; leading edge region at 50% span and $\phi = 0.450$: a) H_{12}, b) Re_θ.

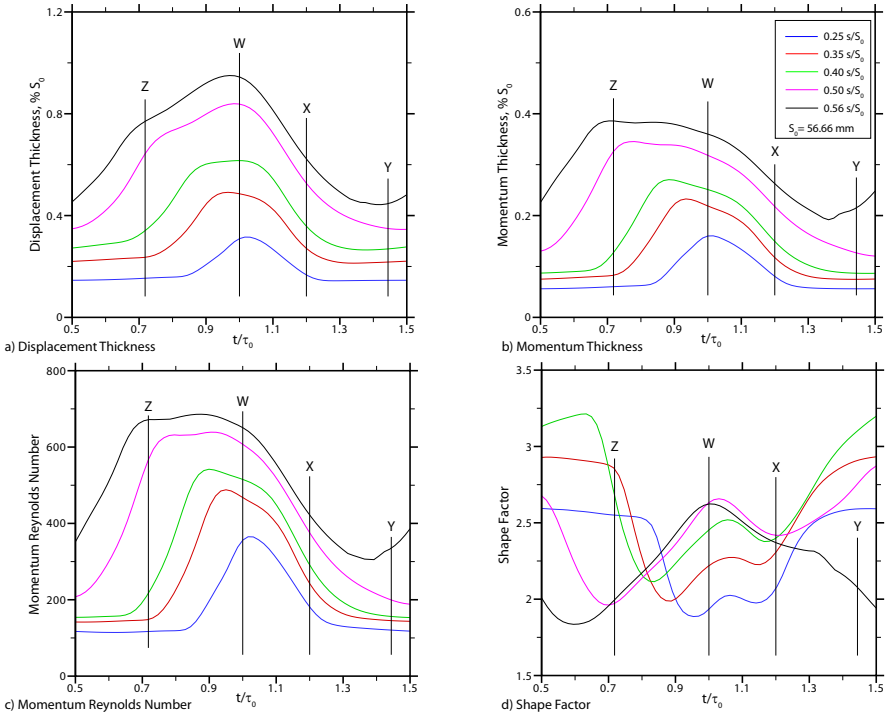

Figure 6.22: Variation of computed integral boundary layer parameters across wake passing period for Stator 3 suction surface at 50% span. Trajectories W, X, Y and Z are highlighted; $\phi = 0.450$.

Reynolds number in this region are significantly higher than the surrounding flow, indicating turbulent re-attachment of the flow. Between wake passing the shape factor and momentum thickness Reynolds number are indicative of an attached laminar boundary layer flow.

Computed boundary layer parameters across one wake passing period are shown in Fig. 6.22 for the same five streamwise locations where traverse measurements were shown in Fig. 6.6. The unsteady computations exhibit some of the general features of the measurements. The computations of δ^*, θ, and Re_θ show a periodic variation with peak values occurring along the wake-induced region. Other unsteady computations have shown a more sinusoidal pattern such as (Halstead et al., 1997d).

The computed shape factors show a more pronounced peak along trajectory Z indicating that the flow is on the verge of separation at 0.40 s/S_0. In the measurements the shape factor has already started to relax down to a more turbulent value. This could be due to the effect of the two-dimensional domain not allowing for redistribution or the effect of the turbulence model. The unsteady calculations were performed at a slightly reduced blade count, which would have meant that the loading would have increased slightly. Values of shape factor along the wake-induced region are comparable with those measured, Fig. 6.6(d), indicating that the transitional turbulence model has performed well in predict-

ing the unsteady influence of the impinging wakes.

6.5 Chapter Closure

Boundary layer traverses along with numerical calculations were performed on Stator 3 suction surface of the Cranfield rig at two operating points: $\phi = 0.450$ and $\phi = 0.400$ and at two spanwise locations: 50% and 85% span, in order to understand the unsteady development of a boundary layer in a multistage environment. The following summary can be drawn from the results.

The flow at midspan and peak efficiency showed that the peak values of δ^* and θ (and hence Re_θ) occurred along the wake-induced trajectory in which transition is completed farther forward. The unsteady computations highlighted a possible explanation for the interaction of an upstream wake and a laminar boundary layer. The impingement of an upstream wake onto the suction surface temporarily caused the laminar boundary layer to separate. The boundary layer flow then reattaches as a turbulent boundary layer and propagates downstream. The leading front of which convected at a 0.93 of the free-stream velocity. Away from the wake-induced strip laminar like flow was measured up to approximately 0.35 s/S_0. Towards the casing at peak efficiency similar trends were observed to that at midspan. Transition completion was found to have moved farther forward towards the leading edge, whilst the boundary layer thickness was approximately 1.5 times larger than that at midspan. The increase in boundary layer thickness is caused by the casing corner separation.

The picture of boundary layer development changes completely as the rig is throttled towards stall. The flow is completely turbulent by the first measurement location at both midspan and close to the casing. Although the flow is already fully turbulent by 0.25 s/S_0 the boundary layer flow showed evidence of fluctuations with rotor passing. These fluctuations were damped out by the large separation that occurred at stall.

The capability of the steady CFD codes to predict the integral parameters were affected by the single stator calculation. It is expected that with an upstream rotor and possibly a downstream one would provide better agreement. The unsteady calculation successfully captured general unsteady features that were observed experimentally.

Chapter 7

Conclusion and Recommendations for Future Work

7.1 Introduction

This study set out to investigate the highly unsteady and three-dimensional environment of an embedded axial compressor stage of three-dimensional blade design. This chapter provides a review of the salient findings from the work. The final section provides recommendations for how the author believes this work should be further exploited.

7.2 Embedded Stage Flow Field

The third-stage flow field of an embedded axial compressor with three-dimensional blade design was measured using three-hole pressure probes in the stationary and rotating frames-of-reference. The three-dimensionality and unsteadiness of the flow field in the third-stage was measured using a slanted hotwire. The results downstream of Rotor 3 showed that the hub-corner separation had a major impact on the stator inlet angle profile due to its effects on the rotor exit axial velocity. Throttling of the rig increased the incidence angle onto the downstream stator and hence loading. The deviation at exit of the rotor was observed to increase by 10° with reduction of flow coefficient. The leakage over the rotor tip results in a region of low axial momentum which governs the stator inlet angle profile close to the casing. It can therefore, be clearly seen that the inlet conditions to the downstream stator bladerow vary considerably along the span, which is a significant consideration in blade design toward the hub and casing region. Strong variations are present in the endwall regions where corner stall and corner vortex and tip clearance flows dominate. The secondary flow field showed considerable cross-passage and spanwise fluid motion. Radially inward velocities were observed along the stator trailing edge which would transport the

low momentum fluid near the casing towards midspan. Radially outward velocities were found in the rotor wakes, indicating wake centrifugation.

The time-resolved measurements downstream of Rotor 3 showed that the rotor wake was characterised by high levels of random unsteadiness and increased incidence. The increase in incidence across the wake was 2-3 times that experienced with change in flow coefficient. Therefore the increased incidence and turbulence in a rotor wake will have a significant influence on the unsteady development of a downstream boundary layer. The properties of the rotor wake were found not to be constant, but with local intense regions of elevated unsteadiness that form at the intersection of the remains of the second stage stator wake streets and those of third-stage rotor wakes.

Stator 2 wake street was measured at the inlet plane to Stator 3. The circumferential position of stator 2 wake street varied with span and loading. At 80% span, peak efficiency and 50% and 80% span at near stall, stator 2 wake street was aligned with stator 3 leading edge. This had the effect of artificially elevating the background turbulence. The level of free-stream turbulence will have a significant effect on wake dispersion and ultimately boundary layer transition.

Exit traverses downstream of Stator 3 showed significant variation in terms of wake depth and width with passage of the rotor. The casing-corner separation was forced into unsteady periodic motion due to incoming wakes. This in turn, amplified the stator wake deficit, which will be ultimately transported further downstream. This will have serious implications for a downstream rotor with regards to forcing and critically stall. The results show that fluctuations in the measured random unsteadiness occur in the stator wake at the frequency of blade passing. This is caused by periodic increases in boundary layer thickness caused by the wake boundary layer interactions and point to periodic fluctuations in stator profile loss.

Numerical predictions of a two-dimensional rotor wake propagation through the stator bladerow, confirmed that the wake fluid is, re-orientated, elongated and stretched. The wake's induced velocities at the leading and trailing boundary, altered the velocity distribution over the first 20% of the stator's suction surface. As the wake convected through the downstream bladerow the magnitude of the unsteadiness continually declined from the leading edge to the trailing edge. The damping of the unsteadiness is due to viscous dissipation and turbulence. The numerical calculations predicted a phenomena that was similar to the thickened boundary layer as measured by Wheeler et al. (2006), and was characterised by increased boundary layer thickness, turbulence and negative perturbation velocity.

7.3 Multistage Boundary Layers

Measurements of the wake boundary layer interaction of an embedded stator were made using boundary layer traverses over the mid-chord region. These measurements were made at 50% and 85% span and at two operating points: $\phi = 0.450$ and $\phi = 0.400$.

The results at midspan and peak efficiency show that the peak values of the integral quantities (displacement and momentum thickness) occurred along the wake-induced strip in which transition is completed farther forward. The unsteady computations highlighted a possible explanation for this. The impingement of a wake into the newly developing laminar boundary temporarily causes the boundary layer to separate. This is partly brought about by the increase in induced incidence. The boundary layer flow then reattaches in a turbulent state.The leading front of the wake-induced strip was convected at 0.93 of the free-stream velocity. Away from the wake-induced strip, laminar-like flow was measured up to approximately 0.35 s/S_0 and completion by 0.5 s/S_0. This corresponded to the location where the shape factor (for an attached flow) was the highest, that is where the boundary layer is laminar for the longest distance. This is close to the location where the trailing boundary of a wake-induced strip meets the leading boundary of the next one. Therefore regions of laminar flow are terminated by the boundaries of successive turbulent strips. The trailing boundaries of these propagate at a lower convection speed and their footprint grows as the strip convects downstream. Towards the casing at peak efficiency similar trends were observed to that at midspan. Transition completion was found to have moved farther forward towards the leading edge to approximately 0.35 s/S_0. This is caused by the increased spreading rate of the turbulent strips brought about by the higher loading close to the casing. Differences in the thickness of the boundary layer were measured and computed between the two spanwise locations. The measured boundary layer thickness close to the casing was approximately 1.5 times larger than that at midspan. The increase in boundary layer thickness is caused by the casing corner separation and the increased adverse pressure gradient.

The picture of boundary layer development changes completely as the rig is throttled towards stall. The flow is completely turbulent by the first measurement location at both midspan and close to the casing. Although the flow is already fully turbulent by 0.25 s/S_0 the boundary layer flow showed evidence of fluctuations with rotor passing, but these fluctuations were damped out the farther downstream the boundary layer went and were significantly smaller in magnitude to the ones measured at peak efficiency. This was due to the lower momentum of the fluid and the large boundary layer separation that occurred at stall. The numerical calculations show that the boundary layer transitions close to the leading edge over the complete span.

The capability of the steady CFD codes to predict the integral parameters were affected

by the single stator calculation. It is expected that with an upstream rotor and possibly a downstream rotor, better agreement between the two data set would be possible to obtain. The unsteady calculation successfully captured the general unsteady features that were observed experimentally at midspan.

7.4 Recommendations for further work

The following areas for future work are recommended.

- The results have shown that the effect of wakes from the preceding stator row were still present at the inlet to the stator row. These wakes interacted with the wake streets from the rotor causing fluctuations in the level of turbulence and re-orientation of the wake. In addition due to the three-dimensional design of the blading, these wake streets impinged onto the leading edge of the stator row, but only a certain spanwise locations. Research into clocking has been carried out by a number of authors but all this research was performed on conventional blading. It is recommended, therefore, to study the stator-stator and rotor-rotor clocking on modern three-dimensional blading. Correct alignment of bladerows would allow for gains in compressor efficiency. This could be carried out in a computational study where the effects of compressibility, Mach number and engine representative Reynolds number could be achieved. Low speed testing could also be performed but this suffers from the low Mach numbers, Reynolds number and low speed compressor rigs tend to be equipped with equal number of blades in each row.

- The current work has shown that the transition model implemented in the ANSYS-CFX code was capable of predicting the general unsteady features that were observed experimentally. In contrast the three-dimensional results were adversely affected due to the lack of appropriate boundary conditions. It is suggested that efforts are made to model a full three-dimensional calculation, with a minimum of three bladerows using the transition model. A comparison should also be performed between a steady-state calculation and the time-average of the unsteady solutions. From this data it would be possible to ascertain if the mixed-out assumption is valid for the design of compressors.

- Work by Wheeler et al. (2006, 2007) and Henderson and Walker (2007) has shown that the leading edge is the key receptivity site for boundary layer transition, through the creation of an initially thickened laminar boundary layer that provides a favourable site for the production of turbulent spots. The limitation of their work apart from the

low speed aspect is that the research was carried out in a one and half stage compressor of two-dimensional blading. Unsteady data in this thesis has shown that wakes from the previous stator row are still evident and that the boundary layer development varies in the spanwise direction. It is recommended therefore, to perform a series of experiments using surface mounted hotfilms around the leading edge of the Stator 3 at a number of spanwise heights. In addition a traverse gear capable of traversing the leading and trailing edge should be designed. This will allow calculation of integral parameters and trailing edge loss estimates to be performed. The subsequent data set would provide a database for numerical validation of turbulence models.

- The surface flow visualisation showed a significant flow separation at the near stall operating point. It is suggested that this flow separation should be investigated further. This would require more testing to be performed at a number of flow coefficients close to the stall point in order to understand if this is a sudden or gradual event and whether this occurs on other stator bladerows. In addition the influence of the separation should be investigated with regards to downstream bladerows.

Bibliography

Abu-Ghannam, B. J. and Shaw, R. (1980). Natural transition of boundary layers–the effect of turbulence, pressure gradient and flow history. *Journal of Mechanical Engineering Science*, Vol. 22(5):pp. 213–228.

Adachi, T. and Murakami, Y. (1979). Three-dimensional velocity distribution between stator blades and unsteady force on a blade due to passing wakes. *Bulletin of the JSME*, Vol. 22:pp. 1074–1082.

Anderson, J. D. (1995). *Computational fluid dynamics. The basics with applications*. McGraw-Hill.

ANSYS (2005). *ANSYS CFX 10 Manual*.

Aurifeille, E. V. J. (2003). CFD simulations of the ANT1 low speed rig compressor tested at Cranfield University. Multistage and single row calculations using JACC, HYDRA and Multip (standard and fine mesh) programs. Technical Report DNS 94811, Rolls-Royce.

Barlow, J. B., Rae, W. H., and Pope, A. (1999). *Low Speed Wind Tunnel Testing*. Wiley & Sons, 3rd edition.

Barth, T. J. and Jesperson, D. C. (1989). The design and application of upwind schemes on unstructured meshes. In *AIAA Paper*, 89-0366. AIAA.

Bradshaw, P. (1978). *Turbulence*. Springer.

Camp, T. R. and Shin, H. W. (1995). Turbulence intensity and length scale measurements in multistage compressor. *ASME Journal of Turbomachinery*, Vol. 117:pp. 38–46.

Chow, Y. Uzol, O. and Katz, J. (2003). On the flow and turbulence within the wake and boundary layer of a rotor blade located downstream of an IGV. In *ASME Turbo Expo*, GT2003-38599.

Chow, Y., Uzol, O., and Katz, J. (2002). Flow nonuniformities and turbulent ”hot spots” due to wake-blade and wake-wake interactions in a multi-stage turbomachiner. *Jornal of Turbomachinery*, 124.

Coldrick, S. (2003). *Influence of blade row aerodynamics on pneumatic gas turbine instrumentation*. PhD thesis, Cranfield University, Cranfield Bedfordshire.

Cumpsty, N. A. (1989). *Compressor aerodynamics*. Lomgman Scientific & Technical, New York, U.S.A.

Cumpsty, N. A., Dong, Y., and Li, Y. S. (1995). Compressor blade boundary layers in the presence of wakes. In *ASME Turbo Expo*, 95–GT–443. ASME.

Dawes, W. N. and Cant, R. S. (2005). 4A2 computational fluid dynamics. University of Cambridge Lecture Notes.

Denton, J. D. (1993). Loss mechanisms in turbomachines. In *ASME Turbo Expo*, 93-GT-435.

Dhawan, S. and Narasimha, R. (1958). Some properties of boundary layer flow during transition from laminar to turbulent motion. *Journal of Fluid Mechanics*, 3.

Dong, Y. (1988). *Boundary layers on compressor blades*. PhD thesis, University of Cambridge.

Dong, Y. and Cumpsty, N. A. (1990a). Compressor blade boundary layers: Part 1–test facility and measurement with no incident wakes. *ASME Journal of Turbomachinery*, Vol. 112(2):pp. 222–230.

Dong, Y. and Cumpsty, N. A. (1990b). Compressor blade boundary layers: Part 2–measurements with incident wakes. *ASME Journal of Turbomachinery*, Vol. 112(2):pp. 231–240.

Dong, Y., Gallimore, S. J., and Hodson, H. P. (1987). Three-dimensional flows and loss reduction in axial compressors. *Journal of Turbomachinery*, Vol. 109.

D'Ovidio, A., Harkins, J. A., and Gostelow, J. P. (2001a). Turbulent spots in strong adverse pressure gradients part 1 - spot behavior. In *ASME Turbo Expo 2001*, 2001-GT-0194, New Orleans, Lousisiana. ASME.

D'Ovidio, A., Harkins, J. A., and Gostelow, J. P. (2001b). Turbulent spots in strong adverse pressure gradients part 2 - spot propagation and spreading rates. In *ASME Turbo Expo 2001*, 2001-GT-0406, New Orleans. ASME.

Dring, R. P., Joslyn, H. D., and Wagner, J. H. (1983). Compressor rotor aerodynamics. In *Viscous Effects in Turbomachines*, AGARD-CP-351.

Durbin, P. A., Jacobs, R. G., and Wu, X. (2002). *Closure strategies for turbulent and transitional flows*, chapter DNS of bypass transition, pages 449–463. Cambridge University Press.

Emmons, H. W. (1951). The laminar-turbulent transition in a boundary layer–part 1. *Journal of Aero. Sciences*, Vol. 18(7):pp. 490–498.

Evans, R. L. (1978a). Boundary layer development on an axial-flow compressor stator blade. *Journal of Engineering for Power*, Vol. 100.

Evans, R. L. (1978b). Turbulence and unsteadiness measurements downstream of a moving blade row. *Journal of Engineering for Power*, Vol. 100.

Ferziger, J. H. and Peric, M. (2002). *Computational Method for Fluid Dynamics*. Springer, 3 edition.

Gallimore, S. J. (1998). Axial flow compressor design. In *The Successful Exploitation of CFD in Turbomachinery Design*, IMechE Seminar.

Gaster, M. (1969). The structure and ehaviour of laminar separation bubbles. Technical Report RM No. 3595, Ministry of Technology - Aeronautical Research Council Reports and Memoranda.

Gbadebo, S., Cumpsty, N., and Hynes, T. (2005). Three-dimensional separation in axial compressors. *Journal of Turbomachinery*, Vol. 127.

Gostelow, J. P. (1977). A new approach to the experimental study of turbomachinery flow phenomena. *Journal of Engineering for Power*, pages pp. 97–105.

Gostelow, J. P., Blunden, A. R., and Walker, G. J. (1994). Effects of free-stream turbulence and adverse pressure gradients on boundary layer transition. *Journal of Turbomachinery*, Vol. 116:pp. 392–404.

Gostelow, J. P., Hodson, H. P., and Walker, G. J. (1999). Comparisons between triggered turbulent spots and unsteady transition phenomena on compressor and turbine blading. In *Laminar-Turbulent Transition*, Proceddings IUTAM Symposium.

Gostelow, J. P., Melwani, N., and J., W. G. (1996). Effects of streamwise pressure gradients on turbulent spot development. *ASME Journal of Turbomachinery*, Vol. 118(4):pp. 737–743.

Gostelow, J. P. and Thomas, R. L. (2005). Response of a laminar separation bubble to an impinging wake. *Journal of Turbomachinery*, Vol. 127.

Gostelow, J. P., Thomas, R. L., and Adebayo, D. S. (2007). On the response of a strongly diffusing flow to propagating wakes. In *ASME Turbo Expo*, GT2007-28237.

Grotjans, H. and Menter, F. R. (1998). Wall functions for general application CFD codes. In *Proceedings of ECCOMAS*.

Gutmark, E. and Blackwelder, R. F. (1987). On the structure of a turbulent spot in a heated laminar boundary layer. *Experiments in Fluids*, Vol. 5.

Hah, C. and Loellbach, J. (1999). Development of hub corner stall and its influence on the performance of axial compressor blade rows. *Journal of Turbomachinery*, Vol. 121.

Halstead, D. E., Wisler, D. C., Okiishi, T. H., Walker, G. J., Hodson, H. P., and Shin, H. W. (1997a). Boundary layer development in axial compressors and turbines: Part 1 of 4–composite picture. *ASME Journal of Turbomachinery*, Vol. 119(1):pp. 114–127.

Halstead, D. E., Wisler, D. C., Okiishi, T. H., Walker, G. J., Hodson, H. P., and Shin, H. W. (1997b). Boundary layer development in axial compressors and turbines: Part 2 of 4–compressors. *ASME Journal of Turbomachinery*, Vol. 119(3):pp. 426–444.

Halstead, D. E., Wisler, D. C., Okiishi, T. H., Walker, G. J., Hodson, H. P., and Shin, H. W. (1997c). Boundary layer development in axial compressors and turbines: Part 3 of 4– turbines. *ASME Journal of Turbomachinery*, Vol. 119:pp. 225–237.

Halstead, D. E., Wisler, D. C., Okiishi, T. H., Walker, G. J., Hodson, H. P., and Shin, H. W. (1997d). Boundary layer development in axial compressors and turbines: Part 4 of 4– computations and analysis. *ASME Journal of Turbomachinery*, Vol. 119(1):pp. 128–139.

Haselbach, F., Schiffer, H.-P., Horsman, M., Dressen, S., and Harvey, N. (2001). The application of Ultra high Lift Blading in the BR715 LP Turbine. In *Proceedings of the ASME TURBO EXPO 2001*, 2001-GT-0436.

Henderson, A., Walker, G. J., and Hughes, J. (2006). Unsteady transition phenomena at a compressor leading-edge. In *ASME Turbo Expo*, GT2006-90641.

Henderson, A. D. and Walker, G. J. (2007). Observations of transition phenomena on a controlled diffusion compressor stator with a circular arc leading edge. In *ASME Turbo Expo*, GT2007-27612.

Hirsch, C. (1988). *Numerical Computation of Internal and External Flows Volume 1: Fundamentals of Numerical Discretization*. Wiley.

Ho, Y.-H. and Lakshminarayana, B. (1995). Computation of unsteady viscous flow through turbomachinery bladerow due to upstream rotor wakes. *Journal of Turbomachinery*, Vol. 117.

Hodson, H. P. (1984). Boundary layer and loss measurements on the rotor of an axial-flow turbine. *Journal of Engineering for Power*, Vol. 106.

Hodson, H. P. (1998). Bladerow interactions in low pressure turbines. In *VKI Lecture Series No. 1998-02*. Von Karman Institute.

Hodson, H. P. and Howell, R. K. J. (2005). The role of transition in high-lift low-pressure turbines for aero-engines. *Progress in Aerospace Sciences*, Vol. 41.

Hodson, H. P., Huntsman, I., and Steele, A. B. (1994). An investigation of boundary layer development in a multistage LP turbine. *ASME Journal of Turbomachinery*, Vol. 116(3):pp. 375–383.

Honen, H. and Gallus, H. E. (1995). Monitoring of aerodynamic load and detection of stall in multistage axial compressors. *Journal of Turbomachinery*, Vol. 117.

Horlock, J. H., Lewis, J. F., Percival, P. M. E., and Lakshminarayana, B. (1966). Wall stall in compressor cascade. *Journal of Basic Engineering*.

Howell, R. J., Hodson, H. P., Schulte, V., Schiffer, H.-P., Haselbach, F., and Harvey, N. (2001). Boundary layer development on the BR710 and BR715 LP Turbines - the implementaion of High Lift and Ulta High Lift concepts. In *Proceedings of the ASME Turbo Expo 2001*, 2001-GT-0441, New Orleans.

Howell, R. J., Ramesh, O. N., Hodson, H. P., Harvey, N. W., and Schulte, V. (2000). High Lift and Aft loaded profiles for LP Turbines. In *Proceedings of the ASME Turbo Expo 2000*, 2000-GT-261.

Hughes, J. D. and Walker, G. J. (2001). Natural transition phenomena on an axial compressor blade. *ASME Journal of Turbomachinery*, Vol. 123.

Inoue, M. and Kuroumaru, M. (1989). Structure of tip clearance flow in an isolated axial compressor rotor. *Journal of Turbomachinery*, Vol. 111.

Johnson, M. W. and Ercan, A. H. (1996). A boundary layer transition model. In *Presented at the International Gas Turbine and Aeroengine Congress & Exhibition*, 96-GT-444, Birmingham, UK.

Joslyn, H. D. and Dring, R. P. (1985). Axial compressor stator aerodynamics. *Journal of engineering for gas turbines and power*, Vol. 107:pp. 485–493.

Kang, C. S. (1996). *Vaned recess anti-stall for axial-flow fans and compressors*. PhD thesis, Cranfield University, Cranfield, Bedfordshire.

Kemp, N. H. and Sears, W. R. (1955). The unsteady forces due to viscous wakes in turbomachines. *Journal of Aeronatuical Sciences*, Vol. 22.

Kerrebrock, J. L. and Mikolajczak, A. A. (1970). Intra-stator transport of rotor wakes and its effects on compressor performance. *Journal of Engineering for Power*, page pp. 359.

Klebanoff, P. S., Tidstrom, K. D., and Sargent, L. M. (1962). The three-dimensional nature of boundary layer instability. *Journal of Fluid Mechanics*, Vol. 12.

Lange, C. F., Durst, F., and Breuer, M. (1999). Wall effects on heat loss from hot-wires. *Journal of Heat and Fluid Flow*, Vol. 20:pp. 34–47.

Langtry, R. B. (2006). *A correlation-based transition model using local variables for unstructured parallelized CFD codes*. PhD thesis, University Stuttgart.

Langtry, R. B. and Menter, F. R. (2005). Transition modelling for general CFD applications in aeronautics. In *AIAA Paper*, 2005-522.

Langtry, R. B., Menter, F. R., Likki, S. R., Suzen, Y. B., Huang, P. G., and Volker, S. (2004). A correlation based transition model using local variables part 2 - test cases and industrial applications. In *ASME Turbo Expo*, GT2004-53452, Vienna, Austria. ASME.

Lee, D. Y. (2001). Wake affected boundary layer flows within an embedded stage of a multi-stage axial compressor. Master's thesis, Cranfield University, Cranfield, Bedfordshire.

Lefcort, M. D. (1965). An investigation into unsteady blade forces in turbomachines. *Journal of Engineering for Power*, Vol. 87.

Lei, V.-M., Spakovszky, Z. S., and Greitzer, E. M. (2006). A criterion for axial compressor hub corner stall. In *ASME Turbo Expo*, GT2006-91332.

Livesey, J. L. (1956). The behaviour of transverse cylindrical and forward facing total pressure probes in transverse total pressure gradients. *Journal of the Aeronautical Sciences*.

Lockhart, R. C. and Walker, G. J. (1974). The influence of viscous interactions on the flow downstream of an axial compressor stage. In *Proceedings of the 2nd International Symposium on Air-Breathing Engines*, Sheffield, United Kingdoms.

Lomas, C. G. (1986). *Fundamentals of hot-wire anemometry*. Cambridge University Press, Cambridge, U.K.

Lyes, P. A. and Ginder, R. B. (1998). Experimental evaluation of the high-to-low speed transformation process for a highly loaded core compressor stage. In *International Gas Turbine & Aeroengine Congress & Exhibition*, 98-GT-334, Stockholme, Sweden. ASME.

MacBurnie, E. (2005). Annual review of civil avaition 2005. *ICAO Journal*, Vol. 61(5).

Madden, D. S. (2001). Aerodynamic design of the increased loading low speed research compressor ANT1 to be tested at Cranfield University (Brochure B1C1–1489 DT). Technical Report RR Report DNS 82539, RCR 91358, Rolls-Royce.

Madden, D. S. (2003). Analysis of the increased loading low-speed research compressor ANT1 tested at cranfield university. Technical Report RR Report DNS 96785, RCR 91392, Rolls-Royce.

Mailach, R., Lehmann, I., and Vogeler, K. (2007a). Periodical unsteady flow within a rotor blade row of an axial compressor - Part i: flow field at midspan. In *ASME Turbo Expo*, GT2007-27210.

Mailach, R., Lehmann, I., and Vogeler, K. (2007b). Periodical unsteady flow within a rotor blade row of an axial compressor - Part ii: tip clearance vortex interaction. In *ASME Turbo Expo*, GT2007-27211.

Mailach, R. and Vogeler, K. (2003). Aerodynamic blade row interactions in an axial compressor part i: Unsteady boundary layer development. In *Proceedings of ASME Turbo Expo 2003*, GT2003-38765, Atlanta, Georgia, USA. ASME.

Mailach, R. and Vogeler, K. (2004). Rotor-stator interactions in a four-stage low speed axial compressor - Part i: unsteady profile pressures and the effect of clocking. In *ASME Turbo Expo*, GT2004-53098.

Mayle, R. E. (1991). The role of laminar-turbulent transition in gas turbine engines. *ASME Journal of Turbomachinery*, Vol. 113(4):pp. 509–537.

Mayle, R. E. and Dullenkopf, K. (1989). A theory for wake-induced transition. *Journal of Turbomachinery*, Vol. 111.

Mayle, R. E. and Schulz, A. (1997). The path to predicting bypas transition. *Journal of Turbomachinery*, Vol. 119:pp. 405–411.

Menter, F. R. (1992). Influence of freestream values of k-omega turbulence model predictions. *AIAA*, Vol. 30:pp. 1657–1659.

Menter, F. R. (1994). Two-equation eddy-viscosity turbulence models for engineering applications. *AIAA*, Vol. 32(8):pp. 1598–1605.

Menter, F. R., Langtry, R., and Hansen, T. (2004a). CFD simulation of turbomachinery flows - verfication, validation and modelling. In *European Congress on Computational Methods in Applied Sciences and Engineering*, Jyvaskyla.

Menter, F. R., Langtry, R. B., Likki, S. R., Suzen, Y. B., Huang, P. G., and Volker, S. (2004b). A correlation-based transition model using local variables part 1-model formulation. In *ASME Turbo Expo 2004*, GT2004-53452, Vienna, Austria. ASME.

Merzkirch (1974). *Flow Visualisation*. Academic Press, 1st edition.

Meyer, R. X. (1985). The effect of wakes on the transient pressure and velocity distributions in turbomachines. *Transactions of the ASME*, Vol. 107.

Mohammadi, B. and Pironneau, O. (1994). *Analysis of the k-Epsilon Turbulence Model*. Wiley.

Moore, X. X. and Richardson, Y. Y. (1957). Skewed boundary layer flow near endwalls of a compressor cascade. *Trans. ASME*, Vol. 79.

Narasimha, R. (1957). On the distribution of intermittency in the transition region of a boundary layer. *Journal of Aerospace Science*, Vol. 24:pp. 711–712.

Orth, U. (1993). Unsteady boundary layer transition in flow periodically disturbed by wakes. *Journal of Turbomachinery*, Vol. 115.

Ottavg, X., Vilmin, S., Hodson, H. P., and Gallimore, S. (2004). The effects of wake passing unsteadiness over a highly-loaded compressor-like flat plate. *Journal of Turbomachinery*, Vol. 126.

Patankar, S. V. (1980). *Numerical heat transfer and fluid flow*. Computational Methods in Mechanics and Thermal Sciences. Hemisphere Publishing Corporation.

Peacock, R. E. (1982). A review of turbomachinery tip gap effects. Part 2: Rotating machinery. *International Journal of Heat and Fluid Flow*, Vol. 4.

Penner, J. E. (1999). *Aviation and the Global Atmosphere*. Intergovernmental Panel on Climate Change.

Pfeil, H. and Herbst, R. (1979). Transition procedure of instationary boundary layers. In *ASME Turbo Expo*, 79-GT-128.

Pfeil, H., Herbst, R., and Schroder, T. (1983). Investigation of laminar boundary layers disturbed by wakes. *Journal of Engineering for Gas Turbines and Power*, Vol. 105.

Rayleigh, L. (1880). Scientific papers. *Dover, New York, 1964*, Vol. 1:pp. 474–487.

Rhie, C. M. and Chow, W. L. (1982). A numerical study of the turbulent flow past an isolated airfoil with trailing edge separation. In *AIAA Paper 82-0998*.

Robinson, C. J. (1991). *End-wall flows and blading design for axial flow compressors*. PhD thesis, Cranfield University, Cranfield, Bedfordshire.

Salvage, J. W. (1974). Investigation of secondary flow behaviour and endwall boundary layer development through compressor cascades. Technical Report TN 107, von Karman Inst.

Savill, A. M. (1993a). *Further progress in the turbulence modelling of by-pass transition*. Engineering Turbulence Modeling and Experiments 2. Elsevier Science Publishers.

Savill, A. M. (1993b). *Some recent progress in the turbulence modelling of by-pass transition*. Near-Wall Turbulent FLows. Elsevier Science Publishers.

Schlichting, H. (1959). Application of boundary-layer theory in turbomachinery. *ASME series D. Journal Basic Engg.*, Vol. 81(4):pp. 543–551.

Schlichting, H. T. (1967). *Boundary layer theory*. McGraw-Hill Education.

Schubauer, G. B. and Klebanoff (1955). Contributions on the mechanics of boundary layer transition. Report 1289, NACA.

Schubauer, G. B. and Skramstead, H. K. (1948). Laminar-boundary-layer oscillations and transition on a flat plate. 34th Annual Report 909, NACA.

Schulte, V. and Hodson, H. P. (1998). Unsteady wake-induced boundary layer transition in high lift LP turbines. *ASME Journal of Turbomachinery*, Vol. 120:pp. 28–35.

Schulz, H. D. and Gallus, H. E. (1988). Experimental investigations of the three-dimensional flow in an annular compressor cascade. *ASME Journal of Turbomachinery*, Vol. 110:pp. 467–478.

Schulz, H. D., Gallus, H. E., and Lakshminarayana, B. (1990). Three-dimensional separated flow field in the endwall region of an annular compressor cascade in the presence of rotor-stator interaction: Part 2 - unsteady flow and pressure field. *Journal of Turbomachinery*, Vol. 112.

Shaw, C. T. (1992). *Using computational fluid dynamics*. Prentice Hall.

Shin, Y. H., Elder, R. L., and Bennett, I. (2003). Boundary layer measurement on the blade surface of a multi-stage axial flow compressor. In *Proceedings of ASME Turbo Expo 2003*, GT2003-38183, Atlanta, Georgia, USA. ASME.

Smith, L. H. (1966). Wake dispersion in turbomachines. *Journal of Basic Engineering*.

Smith, L. H. (1969). Casing boundary-layers in multistage compressors. In Dzung, L. S., editor, *Proceedings of the Symposium on flow research on blading*, flow research on blading, Baden, Switzerland. Brown Boveri & Co. Ltd, Elsevier Publishing Company.

Solomon, W. J. and Walker, G. J. (2000). Incidence effects on wake-induced transition on an axial compressor blade. *Journal of Propulsion and Power*, Vol. 16.

Solomon, W. J., Walker, G. J., and Gostelow, J. P. (1996). Transition length predictions for flows with rapidly changing pressure gradients. *Journal of Turbomachinery*, Vol. 118:pp. 744–751.

Solomon, W. J., Walker, G. J., and Hughes, J. D. (1999). Periodic transition on an axial compressor stator: Incidence and clocking effects: Part II – transition onset predictions. *Journal of Turbomachinery*, Vol. 121.

Speziale, C. G. (1991). Analytical methods for the development of Reynolds-stress closures in turbulence. *Annual Review of Fluid Mechanics*, Vol. 23:pp. 107–157.

Squire, L. C. (1962). The motion of a thin oil sheet under the boundary layer on a body. In Maltby, R. L., editor, *Flow Visualisation in Wind Tunnels Using Indicators*, pages pp. 7–28. AGARDograph 70.

Storer, J. (1991). *Tip clearance flows in axial compressor*. PhD thesis, University of Cambridge.

Suzen, Y. B., Huang, P. G., S., H. L., and Ashpis, D. E. (2003). Predictions of separated and transitional boundary layers under low-pressure turbine airfoil conditions using an intermittency transport equation. *Journal of Turbomachinery*, Vol. 125:pp. 455–464.

Thomas, R. L. and Gostelow, J. P. (2005). The pervasive effect of the calmed region. In *ASME Turbo Expo*, GT2005-69125.

Thwaites, B. (1949). Approximate calculation of the laminar boundary layer. *Aeronautical Quar.*, Vol. 7:pp. 245–280.

Tobak, M. and Peake, D. J. (1979). Topology of two-dimensional and three-dimensional flows. In *AIAA*, 79-1480.

Tobak, M. and Peake, D. J. (1982). *Annual Review of Fluid Mechanics*, volume 14, chapter Topology of three-dimensional separated flows, pages pp 61–85. Annual Reviews INC, 4139 El Camino Way, Palo Alto, California, 94306, USA.

Valkov, T. and Tan, C. S. (1995). Control of the unsteady flow in a stator blade row interacting with upstream moving wakes. *Journal of Turbomachinery*, 117.

Van Zante, D. E., Adamczyk, J. J., Strazisar, A. J., and Okiishi, T. H. (2002). Wake recovery performance benefit in a high-speed axial compressor. *Journal of Turbomachinery*, 124.

Versteeg, H. K. and Malalasekera, W. (1995). *An introduction to computational fluid dynamics: The finite volume method*. Pearson Eduction Limited.

Walker, G. J. (1968). The prediction of boundary-layer development on axial flow turbomachinery blades. In *Proceedings of 3rd Australasian Conference on Hydraulics and Fluid Mechanics*, Sydney, Australia.

Walker, G. J. (1974). The unsteady nature of boundary layer transition on an axial compressor blade. In *ASME Turo Expo*, 74-GT-135.

Walker, G. J. (1989). Transitional flow on axial turbomachine blading. *AIAA Journal*, Vol. 27:pp. 595–602.

Walker, G. J. (1993). The role of laminar-turbulent transition in gas turbine engines: A discussion. *Journal of Turbomachinery*, Vol. 115:pp. 207–217.

Walker, G. J., Hughes, J. D., and Solomon, W. J. (1999). Periodic transition on an axial compressor stator: Incidence and clocking effects: Part 1–Experimental Data. *ASME Journal of Turbomachinery*, Vol. 121:pp. 398–407.

Walker, G. J. and Wu, J. (1991). Turbulence intermittency measurement for turbomachinery flows. In *1st Proceedings of the Symposium on Boundary layer stability and transition to turbulence*, Portland, USA.

Walraevens, R. E. and Cumpsty, N. A. (1995). Leading edge separation bubbles on turbomachinery blades. *Journal of Turbomachinery*, Vol. 117.

Wheeler, A. P. S. (2007). *The effect of unsteady flows on compressor performance*. PhD thesis, Cambridge Univeristy.

Wheeler, A. P. S., Miller, R. J., and Hodson, H. P. (2006). The effect of wake induced structures on compressor boundary layers. In *ASME Turbo Expo*, GT2006-90892.

Wheeler, A. P. S., Sofia, A., and Miller, R. J. (2007). The effect of leading-edge geometry on wake interactions in compressors. In *ASME Turbo Expo*, GT2007-27802.

White, F. M. (2006). *Viscous Fluid Flow*. McGraw-Hill inc.

Whitfield, C. E., Kelly, J. C., and Barry, B. (1972). A three-dimensional analysis of rotor wakes. *Aeronautical Quarterly*, pages pp. 285–300.

Wilcox, D. C. (1988). Reassessment of the scale-determining equation for advanced turbulence models. *AIAA Journal*, Vol. 26(11):pp. 1299–1310.

Wisler, D. C. (1985). Loss reduction in axial-flow compressors through low-speed model testing. *ASME Journal of Engineering for Gas Turbines and Power*, Vol. 107:pp. 354–363.

Wisler, D. C., Bauer, R. C., and Okiishi, T. H. (1987). Secondary flow, turbulent diffusion and mixing in axial-flow compressors. *ASME Journal of Turbomachinery*, Vol. 109:pp 455–482.

Youngren, H. and Drela, M. (1991). Viscous-inviscid method for preliminary design of transonic cascades. In *AIAA Paper No. 91-2364*.